Cavity QED with Atomic Ensembles

A dissertation presented

by

Jonathan Simon

to

The Department of Physics

in partial fulfillment of the requirements

for the degree of

Doctor of Philosophy

in the subject of

Physics

Harvard University

Cambridge, Massachusetts

May 2010

Thesis advisor   Author

Vladan Vuletic   **Jonathan Simon**

Cavity QED with Atomic Ensembles

Abstract

Cavity Quantum Electrodynamics has long been a proving grounds for the study
of the interaction of light with matter. Historically the objective has typically been
to couple one atom to one photon as strongly as possible. While this endeavor has
yielded a variety of beautiful and groundbreaking results, we take a different approach.

Inspired by the quantum repeater scheme of Duan, Lukin, Cirac and Zoller, we
have built a cavity-ensemble experiment, where the strong coupling between the light
and the matter is achieved via the combination of the resonant enhancement of a
cavity and a collective enhancement of an ensemble. We investigate the capabilities
and limitations of such an approach through a number of experiments.

The first experiment we describe is a very-high-quality source of photon pairs
of opposite polarization, but otherwise nearly-identical spectral properties. We pro-
ceed to a high-fidelity single photon source, and carefully investigate the decoher-
ence mechanisms that limit the performance of such a system. Next we present the
cavity-mediated transfer of a single collective excitation between atomic ensembles,
and deterministic entanglement generation. Lastly, we present a heralded, polariza-
tion preserving quantum memory. All of these experiments depend critically on the
strong light-matter coupling afforded by the cavity-ensemble interaction, and require

increasingly more sophisticated state control of the atoms.

Finally, we describe our new apparatus, combining a relatively long, high-finesse optical resonator with a 2μm dipole trap. We focus on the technical details of stabilizing the narrow resonator, and discuss briefly a proposal for high efficiency Quantum Non-Demolition photon detection. We conclude with preliminary data demonstrating single-atom detection.

Contents

Acknowledgments

When I began my PhD I viewed scientific research as a solitary and personal endeavor. Six years of graduate school have taught me many things, but most importantly that no physicist is an island. I have discussed with and learned from, worked with and for, and been supported and guided by a number of wonderful people. This thesis would not have been possible without them.

Ellenor Barish made me feel at home from day one. Maternity leave saw her replaced by Joanna Keseberg, whose smile was the first that I saw most mornings. Both were patient and helpful in dealing with the logistical issues associated with being a member of the CUA. Sheila Ferguson did a fantastic job keeping tabs on me and ensuring that I made it past all of the logistical hurdles Harvard threw my way. Whenever I needed help in the machine shop, Mark Belanger was there with excellent advice.

Over the years I have had the privilege of working with a variety of fine undergraduates. Huanqian Loh was already working on the experiment when I arrived, and was a phenomenal lab-mate and friend. I will never forget the nights (and early mornings!) spent measuring photon-linewidth data together. Jake Bernstein built us a treasure trove of photodiodes and breakout boxes that we use to this day. Ben Bloom worked with tremendous fervor on our recent quantum memory project, and welcomed me into his home for Passover. Alexander Papageorge did a bang-up job with the transfer cavity, and many other crucial tasks in the preparation of the new apparatus, and has been a fine lifting partner and conversationalist.

As a member of the Vuletic group I have worked with and around many brilliant and kind scientists. Adam Black, Yu-ju Lin and Igor Teper formed the first generation

of the group- they were always happy to provide me with direction and guidance as I tested the waters of AMO physics. Marko Cetina, Andrew Grier, Ian Leroux, and Monika Schleier-Smith are all excellent physicists, and I have enjoyed learning and discussing physics together with them over the years. Sebastian Hofferberth, Thibault Peyronel and Michal Bajcsy were only a floor away, and always happy to talk science and share equipment. Overflowing with ideas and irrepressible enthusiasm, our postdoc Saikat Ghosh was a true pleasure to collaborate with and learn from. Though they are still at the beginning of their graduate careers, I am expecting great and wonderful things from our apparatus under the direction of Wenlan Chen and Renate Landig.

The three scientists to whom I am most indebted are Vladan Vuletic, Haruka Tanji, and James Thompson. From day one, James Thompson was my mentor. Together we built an apparatus which has produced wonderful results long after his departure for JILA. He taught me the value of organization, and how critical it is to develop simple physical pictures. I admire James for his precise, thorough approach to science, and his grace in dealing with the bumps along the way.

Haruka has been my partner in crime since almost the beginning. Together we learned to master magnons, time transfers, and query quantum memories. Sharing and testing ideas with Haruka has been among the most memorable experiences of my PhD. We could not be more different in our approaches, and those differences have made us a great team. Her insistence on doing things carefully has been invaluable every step of the way, and is the reason that the new apparatus is under vacuum and working as beautifully as it is. She has been a great friend and a fantastic

labmate. There is no doubt in my mind that exquisite results are forthcoming under her guidance.

Working for Vladan has been a truly wonderful experience. He is an unending wellspring of ideas, and I strive daily to emulate his cut-to-the-chase approach to science. Time and again I have seen him pull signals out of thin air, armed with the same tools that the rest of us had, but also his deep understanding of the laws of physics. He has insisted upon my best, but never held me to a standard I could not achieve. He is a constant source of inspiration and excitement, advice and guidance. He is a great tango instructor, and dancing with him was not so terrible either.

Beyond the lab, I have been supported by more people than I can possibly name. My parents Richard and Caroline have encouraged and loved me unconditionally. They have also set fantastic examples of what it is to be devoted to and passionate about your profession. I strive daily to ensure that I am as excited about physics as they are about biostatistics and psychology. I am most fortunate to have a brother who is both caring and brilliant; I have come to depend upon Noah for friendship, witty banter, and the occasional huge television. Lastly, I would like to thank my housemates Mike Lazarus, Cliff Cheung, Chris Murphy, and Evan Bullock for their friendship and company after long days in lab.

In science, hindsight is often 20/20. Given the chance I might have tuned my lasers differently, but I could not possibly hope to be surrounded by more wonderful people as I did it.

Dedicated to my father Richard,
my mother Caroline,
and my brother Noah.

Chapter 1

Introduction

Quantum mechanics is one of the most complex and beautiful successes of the 20th century. It teaches us that an object can behave as both a particle and wave, and that its state cannot necessarily be described without reference to the states of other objects. The laws were formulated to satisfy observations performed on natural systems, and indeed, quantum mechanics has been one of the most tested and successful theories of all time.

Having built quantum mechanics from the ground up, one of the objectives moving forward is to tear it down, and an effort spanning disciplines seeks to probe the universe on length scales so fine that quantum mechanics falls apart. The approaches to this endeavor range from high energy supercolliders[37] to precision measurements[86].

Another effort seeks to build *artificial* systems whose very existence depends critically upon the mysterious laws of quantum mechanics. This push for *Quantum State Engineering* has gained momentum in recent decades, with its most triumphant moment coming with the creation of a ground-state matter-wave known as a Bose-

Einstein Condensate[24, 2]. Among the many other early successes are the creation of squeezed states of light[62], and the generation of entanglement between photons[44].

As time has passed, the efforts towards Quantum State Engineering have grown in scale. Fueled by a proposal to use computers exhibiting quantum coherence for efficient factorization[110], efforts have taken off to exact ever increasing coherent control over the quantum states of individual particles, and the correlations between them. Work in ion-traps has demonstrated first two[119], then four[99] and six[70] particle entanglement.

Replacing atoms with photons, there exists a large body of work in quantum optics. One of the earliest approaches to generating nonclassical light is the parametric downconverter[109]. The localization and control of single atoms[82, 66], and single ions[59] within the waist and standing wave structure of a cavity has permitted beautiful realizations of single-photon sources. Surface plasmon modes of gold nano-wires have been coupled to quantum dots to efficiently capture and transport single photons[1]. Quantum dots have also been efficiently coupled to photonic crystal cavities for the generation of single photons[101] and nonlinear optics[38].

A parallel and closely related line of research has worked from the top down, attempting to build quantum mechanical states from large ensembles of atoms. Following the creation of the Bose-Einstein condensate, the Mott insulator[50] and Fermi degenerate gas[28] are some of the most stunning, though by no means only developments in this direction.

Employ the same top-down approach with thermal atoms, quantized collective excitations (magnons) of atomic ensembles have been interfaced with optical photons. A

prescription for entanglement distribution over lossy channels[34] using the magnons for photon generation and storage, in combination with a proposal to perform quantum computations using only linear optics[63], has created a lot of excitement about the generation and control of single photons. It is into this honey-pot that I dipped my paws for my doctoral research.

The proposal in [34], henceforth the DLCZ proposal, outlines a method to probabilistically build up entanglement between distant nodes by generating magnons entangled with single photons. In addition to the possibilities for the generation of truly delocalized entanglement resources, this scheme connected electromagnetically induced transparency[74] to quantum optics in an experimentally realizable way. EIT provides a method of using lasers to coherently convert optical excitations into atomic ground-state coherences (magnons) for storage, and back. While there existed a proposal[42] to efficiently manipulate single photons with EIT, DLCZ provided both a simple method to *create* such photons, and a practical application for them.

In the years since the DLCZ proposal, there has been an explosion of exciting work using atomic ensembles to generate, manipulate, and store single photons. In the earliest demonstration of the technique[68], the single photons were generated with very low efficiency, and the corresponding magnons were short-lived. In the years that followed, the entanglement within the atomic ensembles was better understood, and efficiencies[69, 3] and storage times[26, 35] increased.

The method of [34] was used in combination with quantum feedback in efforts to generate single photons on demand[40, 77]. Using EIT, the Kuzmich group stopped

a single photon and then restarted it after a programmable delay[15]. In the vein of the original proposal, some of the most exciting work involves the generation of entanglement *between* atomic ensembles, generated in either a heralded[19], or deterministic[18] manner.

We entered this burgeoning field near, though not at, the beginning. While many other groups focused on developing the fundamental building blocks of quantum repeaters, we initially focused on the fundamental physics underlying the magnon-photon interface. By working in a cavity instead of free-space, we simplified the light-matter interactions while at the same time achieving a number of technical benefits. This has allowed us to build the highest efficiency atomic-ensemble single photon source to date[114], and to put forth some of the most convincing data describing the time dependence of magnon decoherence. In our more recent work we have scaled up our efforts, working with two samples in our cavity. We have transferred single excitations between the two samples[113], and used them together as a quantum memory for photon polarization[117]. Along the way, we have developed tricks for optically pumping a sample in a (spatially) rotating frame, and adiabatically transferring a single photon between atomic ensembles, through a cavity field. This thesis documents that journey.

Chapter (2) serves as an overview of the formalism used to describe the cavity QED and collective effects relevant to all of the experiments discussed in the thesis. Chapter (3) motivates the use of cavities and atomic ensembles for the creation of single photon sources, and describes an important benchmark for such sources. In chapter (4) we proceed to a description of the experimental apparatus used for all

but the last experiment in this document. Chapters (5) - (8) motivate and then describe in detail four different experiments performed on this apparatus. The first is a spectrally narrow source of polarization separated photon pairs. The second is a study of the temporal and spatial coherence properties of the magnons, culminating in a very high fidelity source of single photons. The third is a demonstration of cavity mediated transfer of a single magnon between two atomic ensembles, and inter-ensemble entanglement generation. The fourth is a heralded, polarization preserving quantum memory. Chapter (9) describes a new hybrid apparatus, built over the last year and a half of my PhD. This apparatus includes a lens for achieving $2 \ \mu m$ spatial resolution of the atomic cloud, as well as a high finesse cavity. I describe both the technical challenges of designing, implementing and controlling the new apparatus, as well as some preliminary results and the myriad new, exciting problems this new apparatus has the potential to tackle. Chapter (10) concludes.

Chapter 2

Single Photons, Cavity QED and Collective Effects

We begin with a brief introduction to cavity quantum electrodynamics (cQED) as it applies to the experiments performed in this thesis. Throughout this thesis we use non-hermitian Hamiltonians to model our real system, including dissipation. We find this approach to be more intuitive than a master equation, although it must be employed with care as non-hermitian Hamiltonians yield non-physical results in situations where the actual physical system may be re-excited after a quantum jump[75, 85].

Having acquired a handle on writing down Hamiltonians for cQED systems, this chapter continues with a prescription for figuring out which of the myriad states allowed by the Hamiltonian are actually relevant for the dynamics of interest. Finally we introduce the many-atom Hamiltonian, and apply the prescription to the calculation of the cavity transmission. In the process we come across collective states for

the first time. *If you get one thing out of this chapter, this should be it!*

2.1 Cavity QED

We first derive the Jaynes-Cummings Hamiltonian in the absence of dissipation, and from it the vacuum Rabi splitting and the cavity shift. We next introduce dissipation into the system, and derive the Wigner-Weisskopf limit as motivation for the phenomenological Hamiltonian used thereafter. Finally we add additional atomic levels to the Hamiltonian which are *not* coupled to the cavity mode, and investigate briefly how they affect the Hamiltonian for the system.

2.1.1 The Jaynes-Cummings Hamiltonian

It seems a bit pedantic to start with the procedure for second quantization of the electromagnetic field, and so instead we will begin with fields quantized inside of a 1-D box of length $2L$, and periodic boundary conditions. This box will be our cavity, and we will (for now) consider only one of the two polarizations states, and ignore the two transverse dimensions. The higher order transverse modes may be ignored because our cavity is not confocal, and hence these modes are not degenerate in frequency with the TEM_{00} mode. As such we can selectively address our mode of interest with appropriate choice of laser frequencies, and cavity tuning relative to atomic resonance. Additionally, our cavity subtends a very small solid angle of 120μsr, and so the spontaneous lifetime of atomic excited state due to free-space continuum coupling is not impacted by a Purcell-type effect[92].

The Hamiltonian for the cavity is:

$$H_{cav}/\hbar = \sum_j \omega_j^{cav} a_j^\dagger a_j \tag{2.1}$$

Where a_j (a) is the creation (annihilation) operator for a photon in mode j, with energy $\omega_j^{cav} = \frac{c}{2L} j$. The operator for creation of a photon at position x, $a_x^\dagger$, is, accordingly:

$$a_x^\dagger = \sum_j e^{i k_j x} a_j^\dagger \tag{2.2}$$

with $\omega_j^{cav}/k_j = c$. For convenience, we will choose $\hbar = 1$ from now on, except when explicitly computing numerical values, in which case we will use SI units. It should be noted that equation (2.2) actually defines the spatial "wavefunction" of the photon.

Things become interesting when we add an atom to the system. The atom has many energy levels with highly non-uniform spacing, and so we will denote these levels for now by $|j\rangle$ with energy ω_j^{at}. The atom Hamiltonian is then:

$$H_{at} = \sum_j \omega_j^{at} |j\rangle \langle j| \tag{2.3}$$

Here ω_j^{at} is the energy of the eigenstate $|j\rangle$. For alkali atoms the light-matter interaction is almost exclusively between the single valence electron and the electromagnetic field. We write the position operator for this electron as $\vec{r}_e = \vec{r}_0 + \vec{r}$, where $\vec{r}_0$ is the location of the atom center of mass, and $\vec{r}$ is the offset to the location of the valence electron. Because the extension of the electron wavefunction is much smaller than the wavelength of the optical field ($r \sim a_b \ll \lambda$) we may make the electric dipole approximation[100], and the interaction Hamiltonian may be written to lowest order in $\vec{r}_0$ as[108]:

$$H_{int} = -e\vec{r} \cdot \vec{E}(\vec{r}_0) \tag{2.4}$$

Where $\vec{E}(\vec{r}_0)$ is the electric field within the cavity at the location $\vec{r}_0$ of the atom, and is given by:

$$\hat{\vec{E}}(\vec{r}_0) = \sum_j \vec{E}_j^0 (a_j^\dagger e^{-i\vec{k}\cdot\vec{r}_0} + a_j e^{i\vec{k}\cdot\vec{r}_0}) \tag{2.5}$$

E_j^0 is defined such that the field is normalized to one photon energy[1] $:|E_j^0| = \sqrt{\frac{\hbar\omega_j}{\epsilon_0 V}}$.

The total Hamiltonian is now given by:

$$
\begin{aligned}
H_{tot} &= H_{at} + H_{cav} + H_{int} \\
&= \sum_j \omega_j^{at} |j\rangle\langle j| + \sum_j \omega_j^{cav} a_j^\dagger a_j \\
&+ e \sum_{k,l} |k\rangle\langle k| \vec{r} |l\rangle\langle l| \cdot \sum_j \vec{E}_j^0 (a_j^\dagger e^{-i\vec{k}\cdot\vec{r}} + a_j e^{i\vec{k}\cdot\vec{r}})
\end{aligned}
\tag{2.6}
$$

The above equation includes the interactions of many optical modes with many atomic levels. In practice our atoms will be cold relative to the lowest optical transition, since $852\text{nm} \leftrightarrow 17000\text{K} \gg$ Room Temperature. As such, our atoms will only populate the lowest energy level[2], $|G\rangle \equiv |j = 0\rangle = |6^2 S_{1/2}\rangle$ for Cs. This allows us to consider solely the interactions between the ground state atom, and a particular optical mode of interest, correspond to a particular excited state $|E\rangle = |6^2 P_{3/2}\rangle$. We label the cavity mode under consideration of energy ω_c with creation operator $a^\dagger$. Ignoring the impact of all other cavity modes and atomic energy levels, and dropping the spatial

---

[1] Including the full spatial structure of the mode, the normalization is: $\int \frac{1}{2}\epsilon_0 |E_j^0|^2 \, dV = \frac{1}{2}\hbar\omega_j$. The factor of $\frac{1}{2}$ on the right side of the equation arises because half of the photon energy is stored in the electric field, and half in the magnetic field.

[2] We are ignoring hyperfine structure.

phase factor whose role is to induce recoil upon scattering (important later), we find:

$$H_{1mode1transition} = \omega_a \left| E \right\rangle \left\langle E \right| + \omega_c a^\dagger a + g(\left| G \right\rangle \left\langle E \right| + \left| E \right\rangle \left\langle G \right|)(a^\dagger + a) \qquad (2.7)$$

Where we have defined $g \equiv \vec{d} \cdot \vec{E_0}$, $\vec{d} \equiv \left\langle E \right| e\vec{r} \left| G \right\rangle$, and have chosen $\vec{d} = \vec{d^*}$ without loss of generality. Dropping counter-rotating terms we are left with:

$$H_{JC} = \omega_a \left| E \right\rangle \left\langle E \right| + \omega_c a^\dagger a + g(a^\dagger \left| G \right\rangle \left\langle E \right| + a \left| E \right\rangle \left\langle G \right|) \qquad (2.8)$$

This is the famous Jaynes-Cummings Hamiltonian of quantum optics[108].

Vacuum Rabi Splitting and Cavity Shift: Quantum Picture

When $g = 0$, the Hamiltonian is easily diagonalized giving near-degenerate pairs $\left| E, N \right\rangle$, $\left| G, N+1 \right\rangle$, with energies $(N+1)\omega_c - \delta_{ac}$ and $(N+1)\omega_c$ respectively[3], with $\delta_{ac} = \omega_c - \omega_a$. When $g \neq 0$ the interaction couples only the states within each pair, and the eigenstates are somewhat more complicated:

$$\begin{aligned}
\left| +, N \right\rangle &= \cos\frac{\theta_N}{2} \left| G, N+1 \right\rangle + \sin\frac{\theta_N}{2} \left| E, N \right\rangle \\
\left| -, N \right\rangle &= -\sin\frac{\theta_N}{2} \left| G, N+1 \right\rangle + \cos\frac{\theta_N}{2} \left| E, N \right\rangle \\
E_{\pm,N} &= (N+1)\omega_c + \frac{1}{2}(-\delta_{ac} \mp \sqrt{4g^2(1+N) + \delta_{ac}^2})
\end{aligned} \qquad (2.9)$$

Where $\tan\theta_N = \frac{2g\sqrt{1+N}}{\delta_{ac}}$. Note also that $\left| G, 0 \right\rangle$ is unperturbed by the coupling to the cavity. From here it is straightforward to consider two limits[4]:

$|\delta_{ac}| \gg g$: Here $\left| +, N \right\rangle \approx \left| G, N+1 \right\rangle$, and $\left| -, N \right\rangle \approx \left| E, N \right\rangle$, for $\delta_{ac} > 0$. The primary

effect is a shift of the cavity and atomic resonance frequencies:

---

[3] $\left| \alpha, N \right\rangle$ denotes that the atom is in state $\left| F = \alpha \right\rangle$, and the cavity contains N photons

[4] The situation is more complicated in the (unavoidable) presence of dissipation, as described in the next section.

$$E_{+,N} \approx (N+1)\omega_c - \delta_{ac} - \frac{(1+N)g^2}{\delta_{ac}}$$

$$E_{+,N} \approx (N+1)\omega_c + \frac{(1+N)g^2}{\delta_{ac}}$$

These shifts are analogous to the stark shift an atom experiences in the presence of an off-resonance laser beam[12], and exist even for the $N=0$ manifold. In other words, probing the cavity with a laser will reveal a shift in the transmission resonance of $\frac{g^2}{\delta}$[5]. Observing the atomic scattering into free-space will reveal a similar shift. As we will see, the optimal ratio of cavity-to-free-space scattering will not reflect this shift, as it occurs on the so-called EIT resonance, rather than the 2-photon resonance.

$|\delta_{ac}| \ll g$: Here $|\pm, N\rangle \approx \frac{|E,N\rangle \pm |G,N+1\rangle}{2}$, with $E_{\pm,N} = \mp g\sqrt{1+N}$. The $N=0$ manifold forms the vacuum rabi doublet, which reveals itself when the cavity is probed in transmission as described in the next section.

2.1.2 Dissipation

If we wish to calculate cavity transmission spectra, or in fact how *any* of the actual experiments performed in our lab take place, we need to learn how to include dissipation in our models. This may seem like a technical detail, but in fact it is quite fundamental. In order to probe a quantum-mechanical system, it must somehow interact with the measurement apparatus, which is a classical device and hence has many (a continuum of!) accessible modes. What this means is that the measurement process is always dissipative, and hence irreversible. We knew this anyway from

---

[5]In the single-atom weak coupling limit it turns out that the observed cavity shift is independent of intra-cavity photon number N_γ, so long as $N_\gamma \ll \frac{8g^2}{\Gamma^2}$.

the collapse postulate, but we will find that for our experiments we rarely have to apply the collapse postulate to anything but continua, which we map back to discrete quantities using statistical inference.

In contrast, in recent experiments with Rydberg atoms in microwave cavities[47, 27], the measurement is performed on the atom after it has already left the cavity. In these experiments the finite cavity lifetime κ is not critical for the measurement process. Because we collect our data as photon leakage from the cavity, we are in fact dependent upon dissipation (finite κ) for data collection.

Cavity Loss

We will begin by removing the atom from the system, and considering the effect of coupling the cavity mode to the outside world through transmission of a single cavity mirror. The outside world will be modeled via a continuum of modes of a much larger cavity. This derivation closely follows reference[108].

The cavity mirror may be thought of as beamsplitter, and so it is clear that the equations defining the effect of the interface must essentially be beamsplitter relations. We will consider a single mode of the cavity with destruction operator a, and a continuum of modes b_j outside of the cavity, coupled to the cavity mode with a coupling constants g_j. The Hamiltonian for the system is then:

$$H = \omega_c a^\dagger a + \sum_j [\omega_j b_j^\dagger b_j + g_j(a^\dagger b_j + b_j^\dagger a)] \tag{2.10}$$

The Heisenberg[6] equations of motion are:

$$\dot{a} = i\omega_c a + \sum_j g_j b_j \tag{2.11}$$

$$\dot{b}_j = iw_j b_j + ig_j a \tag{2.12}$$

Formally integrating the second equation and plugging it into the first yields:

$$\dot{a} = i\omega_c a - \int_0^\infty d\tau \sum_j e^{i\omega_j \tau} g_j^2 a(t - \tau) + F(t) \tag{2.13}$$

$$F(t) = i \sum_j g_j b^j(t = 0) e^{i\omega_j t} \tag{2.14}$$

Moving to the continuum limit, and going into a frame rotating at ω_c for a yields:

$$\dot{\tilde{a}} = -\int_0^\infty d\tau \int_0^\infty d\omega \rho(\omega) g(\omega)^2 e^{i(\omega - \omega_c)\tau} \tilde{a}(t - \tau) + F(t) \tag{2.15}$$

$$\tilde{F}(t) = i \int d\omega\, g(\omega)\rho(\omega) e^{i(\omega - \omega_c)t} b_\omega(t = 0) \tag{2.16}$$

We now note that, for the first expression, the exponential factor oscillates very rapidly away from $\omega \approx \omega_c$. As such we approximate $\rho(\omega)g(\omega)^2 \approx \rho(\omega_c)g(\omega_c)^2$, extend the limits of the ω integration from $[0, \infty)$ to $(-\infty, \infty)$, and then note that the integral yields a delta function. This limit is called the Wigner-Weisskopf approximation[108] and leaves us with (upon leaving the rotating frame):

$$\dot{a} = i(\omega_c + i\frac{\kappa}{2})a(t) + F(t) \tag{2.17}$$

$$F(t) = i \int d\omega\, g(\omega)\rho(\omega) e^{i\omega t} b_\omega(t = 0) \tag{2.18}$$

$$\kappa = 2\pi\rho(\omega_c)g(\omega_c)^2 \tag{2.19}$$

$$\tag{2.20}$$

---

[6]This calculation could equally well be performed in the Schrodinger picture. We wish to show that the result holds true for the entire harmonic oscillator ladder, and not just the first excited manifold, and time evolving all relevant wavefunction amplitudes is more cumbersome than simply working in the Heisenberg picture.

We see that κ is the spontaneous emission rate, consistent with Fermi's Golden Rule[100]. The classical analysis (see appendix (D)) reveals trivially that $\kappa = 2\pi \times \frac{c}{2L}/\mathcal{F}$, where the cavity finesse $\mathcal{F} = \frac{2\pi}{L_{rt}}$, with L_{rt} the cavity round trip power losses.

It is interesting to note that the spontaneous emission enters into these equations of motion as an imaginary contribution to the energy. We will be working in the Schrodinger picture for much of the remainder of this thesis, and will put this imaginary contribution to the energy into the Hamiltonian. This turns out to be equivalent to the Quantum-Monte-Carlo Wavefunction approach to Hamiltonian evolution in the presence of dissipation[85, 75]. It is valid in the limit that either a)the total quantum jump probability over the evolution time is small, or b)the decay process leaves the system in a state from which in cannot be re-excited into the manifold of interest[7].

In the absence of photons initially in the modes $b(\omega)$, $F(t)$ is a Langevin noise operator which does not contribute to expectation values of normally ordered operators[108]. If there are initially photons in the mode, $F(t)$ also incorporates their effect upon the system. We consider here a coherent drive field of amplitude[8] $\Omega(t)e^{i\omega t}$, which yields, after a brief calculation (and ignoring the noise contribution which will drop out of measurements):

$$\dot{a} = i(\omega_c + i\frac{\kappa}{2})a(t) + \frac{\Omega(t)}{2}e^{i\omega t} \qquad (2.21)$$

---

[7]One might worry that insisting that the decay probability be small means that we may as well drop the loss term, as we are insisting it not impact the dynamics. It turns out that, through a sort of quantum-zeno effect, the decay can impact the dynamics *even in the absence of a quantum jump*. This strange effect is discussed in detail in reference [75].

[8]This does not correspond to a $d \cdot E$, as we are speaking here of driving the cavity *directly*, in the absence of an atom, and hence there is no d to speak of.

Moving to a frame rotating with ω and finding the steady state solution $\dot{a} = 0$ yields:

$$E_{out}^+ \propto \langle a^\dagger \rangle = \frac{\frac{\Omega_c/2}{\kappa/2}}{1 - i\frac{\omega_c - \omega}{\kappa/2}} \tag{2.22}$$

Atomic Loss

We may follow the same procedure to add atomic loss, and arrive at the final Hamiltonian, including both cavity and atomic loss, as well as cavity and atomic driving:

$$\begin{aligned} H_{JC} &= (\omega_a + i\frac{\Gamma}{2})|E\rangle\langle E| + (\omega_c + i\frac{\kappa}{2})a^\dagger a + g(a^\dagger |G\rangle\langle E| + a|E\rangle\langle G|) \quad (2.23)\\ &+ \Omega_c(t)(a^\dagger + a) + \Omega_a(t)(|G\rangle\langle E| + |E\rangle\langle G|) \quad (2.24) \end{aligned}$$

In the interest of notational simplicity we will define $\sigma_{AB} \equiv |A\rangle\langle B|$, which yields:

$$H_{JC} = (\omega_a + i\frac{\Gamma}{2})\sigma_{EE} + (\omega_c + i\frac{\kappa}{2})a^\dagger a + g(a^\dagger \sigma_{GE} + a\sigma_{EG}) + \Omega_c(t)(a^\dagger + a) + \Omega_a(t)(\sigma_{GE} + \sigma_{EG}) \tag{2.25}$$

Here, Γ is the atomic spontaneous emission linewidth due to coupling to the free-space continuum. The Wigner-Weisskopf process and Fermi's Golden rule both yield $\Gamma = \frac{\omega_a^3 d^2}{3\pi\epsilon_0 \hbar^3 c}$.

One can use the perturbative methods from appendix (B) to compute a cavity transmission spectrum in the weak-driving limit:

$$E_{out}^+ \propto \langle a^\dagger \rangle = \frac{\frac{\Omega_c}{\kappa/2}}{1 + i\frac{\delta_{lc}}{\kappa/2} + \frac{\eta}{1 + i\frac{\delta_{la}}{\Gamma/2}}} \tag{2.26}$$

Where $\delta_{lX} \equiv \omega - \omega_X$ are the laser-cavity ($X = C$) and laser-atom ($X = A$) detunings, and $\eta \equiv \frac{4g^2}{\kappa\Gamma}$ is the (unitless) single atom cooperativity parameter, discussed later. A sample plot for $\delta_{ac} = 0$, demonstrating the vacuum Rabi-splitting is shown in figure (2.1).
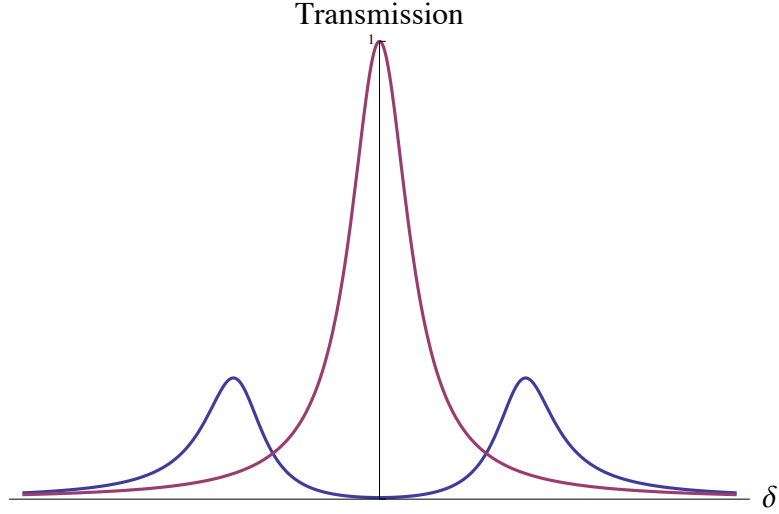
Figure 2.1: Cavity transmission spectrum with, and without an atom. The magenta curve is the cavity transmission spectrum as the laser is swept across the cavity resonance, in the absence of an atom. The blue curve is the cavity transmission spectrum in the presence of a single atom with $\kappa = \Gamma = \frac{g}{2}$. The cavity resonance has been tuned to coincide with the atomic resonance.

In the strong coupling limit the dressed atom-photon eigenstates remain $|\pm, N\rangle$, as defined in the absence of dissipation. These eigenstates now have lifetimes $(N-1)\kappa + \frac{\kappa + \Gamma}{2}$, reflecting the fact that the states are equal mixtures of (N photons and a ground-state atom), and ($N-1$ photons and an excited state atom), with corresponding decay rates. This may be computed either by explicit diagonalization of the Nth excited manifold of equation (2.25), or by analysis of the transmission spectrum, equation (2.26).

2.1.3   Adding Additional Atomic Levels

Thus far we have considered a single two level atom coupled to a single mode of an optical cavity. The experiments we actually perform involve atoms with three or more relevant levels, although typically one of them is not directly coupled to the

cavity[9] Including these additional levels is trivial. For now we will simply add a single metastable ground atomic level $|F\rangle$ of energy $\hbar\omega_F$ coupled to the atomic excited state $|E\rangle$ via a separate laser beam of Rabi-frequency Ω_P:

$$
\begin{aligned}
H_{JC} &= (\omega_a + i\frac{\Gamma}{2})\sigma_{EE} + \omega_F\sigma_{FF} + (\omega_c + i\frac{\kappa}{2})a^\dagger a + g(a^\dagger\sigma_{GE} + a\sigma_{EG}) \\
&+ \Omega_c(t)(a^\dagger + a) + \Omega_a(t)(\sigma_{GE} + \sigma_{EG}) + \Omega_P(t)(\sigma_{EF} + \sigma_{FE}) \qquad (2.27)
\end{aligned}
$$

2.2 Which States Are Relevant?

Throughout this thesis we will be working with systems of many atoms (introduced shortly), each interacting with laser beams, and cavity modes, not to mention magnetic and microwave fields. It may initially seem quite daunting to determine which states of the myriad many-body states are actually relevant for the physics. A system of N 3-level atoms has 3^N total states, and yet the physics I will describe typically only requires 3 of them. How could we possibly have known that *those three* levels would be the ones that mattered?

I would like to share a relatively simple prescription which has served me very well over the years. I do not know if this is how the pro's do it, but it seems intuitive. It stems from the fact that the time evolution of any arbitrary initial state $|A\rangle$ is given by $e^{-iHt}|A\rangle$, so Taylor expansion reveals that the accessible subspace is limited to the set $\bigcup_{N\in\mathsf{Z}}\{H^N|A\rangle\}$[10].

---

[9]Strictly speaking, all levels are coupled to the cavity, if off-resonantly. If the coupling is far enough off-resonance that I know it will not affect the dynamics, I just ignore the coupling. When in doubt compute the scattering rate and cavity shift due to an atom in that state!

[10]For Hamiltonians with time dependence this is not so obvious. In that case one computes the subspace $\{S_0\}$ generated for $H|_{t=0}$, and computes a subspaces $S_M \equiv \bigcup_{N\in\mathsf{Z}}\{H|_{t=M\delta}{}^N S_{M-1}\}$. For H with relatively simple symmetry, this will not be different from S_0

2.2.1 Recipe

1. Write Out the Hamiltonian: Write out the full Hamiltonian for the system. If there are many atoms do not try to figure out which collective states are relevant, just write out everything in the uncoupled basis.

2. Define Your Initial State: Your experiment presumably begins with an optical pumping step. What state does your system start in? This is your initial state. I will typically denote this state $|0\rangle$, or in an effort to be as confusing as possible $|G\rangle$. Context and common sense may be the only tools at your disposal to determine if $|G\rangle$ refers to the state of a particular atom, or to the state of the system as a whole.

3. Gram-Schmidt Branching Procedure: Apply H repeatedly to $|0\rangle$, and determine the state-space spanned by infinite iteration. Use the Gram-Schmidt procedure to generate ortho-normal states $|j\rangle$. It is easy to show that the Hamiltonian for the full system may now be written in a convenient matrix form:

$$\{H_{reduced}\}_{ij} \equiv \langle i| H |j\rangle \tag{2.28}$$

It bears mentioning that I will often choose states $|j\rangle$ with physical significance, rather than blindly applying the Gram-Schmidt procedure. Typically this amounts to applying the orthnormalization procedure after each application of the H, and choosing to define a state coupled by a laser beam as a separate state from one coupled by a cavity emission. Applying this procedure carefully will even yield the relevant collective states *directly*, as detailed below.

Lastly, we will almost always make the rotating wave approximation for all coherent drives, and then move into frames that rotate with the drive fields. This has the effect of removing the optical time-dependence from the Hamiltonian, and replacing optical energy differences with detunings[108].

2.3   Many Atoms in the Cavity

Suppose we would like to calculate the cavity transmission spectrum in the presence of an ensemble of atoms. We now introduce the Hamiltonian for many atoms within a cavity[127]. We then derive the collective states, leaving further explanation of their significance to later chapters.

2.3.1   Many Atom Hamiltonian

If we have many atoms within a cavity, each interacting with the cavity mode the effect is simply to add an index to the atomic operators which we must sum over. For the time-scales, temperatures, and densities we are considering ($\leq 10\mu$s, $\geq 10\mu$k, and $\leq 10^{11}/cm^3$, respectively), direct ground state atom-atom interactions may be ignored[120]. The Hamiltonian for two-level atoms interacting with a cavity in the presence of a cavity probe beam, but no atom-pump, yields:

$$
\begin{aligned}
H_{JC} &= \sum_m \{(\omega_a + i\frac{\Gamma}{2})\sigma_{EE}^m + g_m(a^\dagger \sigma_{GE}^m + a\sigma_{EG}^m)\} \\
&+ (\omega_c + i\frac{\kappa}{2})a^\dagger a + \Omega_c(t)(a^\dagger + a)
\end{aligned}
\tag{2.29}
$$

It turns out that this Hamiltonian may be partially diagonalized very simply, by

defining *collective* excitation operators $\Sigma_{AB} \equiv \frac{1}{g_{coll}} \sum_m g_m \sigma_{AB}^m$, $g_{coll} \equiv \sqrt{\sum_j g_j^2}$:

$$
\begin{aligned}
H_{JC} &= (\omega_a + i\frac{\Gamma}{2})\Sigma_{EE} + g_{coll}(a^\dagger \Sigma_{GE} + a\Sigma_{EG}) \\
&+ (\omega_c + i\frac{\kappa}{2})a^\dagger a + \Omega_c(t)(a^\dagger + a) \\
&+ (\omega_a + i\frac{\Gamma}{2})\Upsilon_{EE}
\end{aligned} \tag{2.30}
$$

Here $\Upsilon_{EE} \equiv [\sum_m \sigma_{EE}^m] - \Sigma_{EE}$ gives the number of *non-collective* excitations. The interesting point here is that if we begin in state $|0\rangle$ and apply H repeatedly according to the iterative procedure of the previous section, we *never* create any non-collective excitations– we can drop that term from the Hamiltonian without affecting anything! In the limit that all atoms have equal coupling strength to the cavity $g_j = g$, $g_{coll} = \sqrt{N}g$ is the collective coupling, and we are left with:

$$
\begin{aligned}
H &= (\omega_a + i\frac{\Gamma}{2})\Sigma_{EE} + g\sqrt{N}(a^\dagger \Sigma_{GE} + a\Sigma_{EG}) \\
&+ (\omega_c + i\frac{\kappa}{2})a^\dagger a + \Omega_c(t)(a^\dagger + a)
\end{aligned} \tag{2.31}
$$

Thus we see that the collective excitations are coupled to the cavity with a rabi frequency of $g\sqrt{N}$, which is $\sqrt{N}$ times larger than the single atom coupling.

It is straightforward to show that $[\Sigma_{GE}, \Sigma_{GE}^\dagger] = (1 - \frac{N_e}{N})$. What this means is that as long the majority of the atoms are in the ground state ($N_e \ll N$), the collective excitations of the ensemble essentially behave as a classical harmonic oscillator[127]: $[\Sigma_{GE}, \Sigma_{GE}^\dagger] \approx 1$. This is equivalent to the classical picture, as can be seen either by the perturbative method of appendix (B), or by moving to the Heisenberg picture. In the low excitation limit, the latter technique yields the equations of motion:

$$
\begin{aligned}
\dot{a} &= i(\omega_c + i\frac{\kappa}{2})a(t) + ig\sqrt{N}\Sigma_{GE} + \Omega_c(t) \\
\dot{\Sigma}_{GE} &= i(\omega_a + i\frac{\Gamma}{2})\Sigma_{GE} + g\sqrt{N}a
\end{aligned} \tag{2.32}
$$

Setting $\Omega_c(t) = \Omega_c e^{i\omega_l t}$, and solving for the steady state response in a frame rotating with ω_l, we arrive at 2.26 for the cavity transmission, with $\eta \to N\eta$.

One might wonder why we chose not to compute the transmission spectrum for a single atom in a cavity this way as well. The key point is that $[\sigma_{GE}^\dagger, \sigma_{GE}] \neq \mathbf{1}$, and so a single atom is explicitly *not* a harmonic oscillator. Had we attempted to use the Heisenberg picture we would have ended up with extra terms corresponding to the saturation of the atom that we did not want, and made calculation difficult. Dropping those terms is equivalent to the assumption that the atom is mostly in its ground state, which is precisely the weak (typically $\ll 1$ photon) driving limit which we computed perturbatively using the method of appendix (B).

It bears mentioning that we eventually became interested in *precisely* the anharmonicity arising from the excitation of a single atom. An ensemble-cavity system behaves like two masses coupled by a spring, and so reacts the same way, in proportion to the drive, no matter how strongly or weakly it is driven. A single atom coupled to a cavity has the potential to behave as a highly anharmonic oscillator coupled to a mass. This system can be so nonlinear that it reacts differently to a single photon drive than two photon drive. This nonlinear behavior is the basis of photon blockade[5] and two-photon filter[65] experiments, among a rich variety of others, and forms part of our motivation for building a new system.

Chapter 3

Controlling Single Photons

Building upon the theory from the preceding chapter on cQED, this chapter will begin with a discussion of ways to efficiently couple single photon to matter. Beginning with a geometrical picture of the collection efficiency of a high NA lens, we will build an understanding of why cavities enhance the emission/absorption probability beyond the subtended solid angle. We will connect both the quantum and classical pictures to the unitless single-atom cooperativity parameter which determines how efficiently a cavity (or freespace) detection system can hope to collect a single emitted photon. We will then turn to the collective absorption and emission of radiation by an atomic ensemble.

Finally, we discuss the intensity-intensity autocorrelation function $g_2(\tau)$, a quantity which is ubiquitous in quantum optics, and specifically in the characterization of single photon sources. This quantity is crucial for understanding both the time dependence of the quantum dynamics, as well as the behavior of the source in the presence of backgrounds.
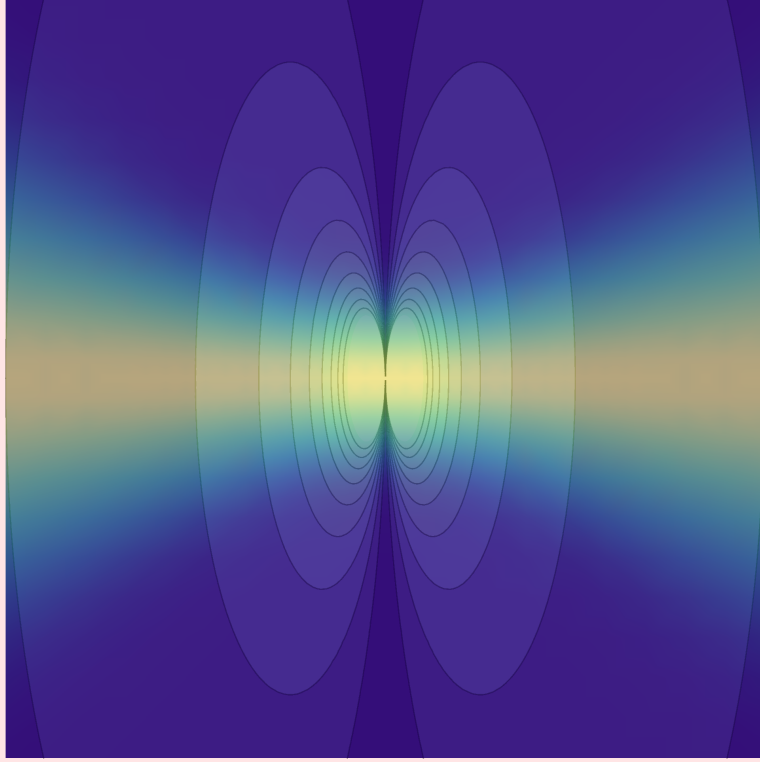
Figure 3.1: Schematic of overlap between optical detection mode and atomic emission mode. The optical detection mode is depicted in the density plot, and the atomic dipole emission pattern as a contour plot.

3.1   Single Photon Interfaces

Imagine that one wants to make a single photon source. A single-atom is excited via a π pulse, and allowed to spontaneously decay, emitting a single-photon. This photon will be emitted according to a dipole pattern, with the maximum collection efficiency into a mode of waist w_0 given by the overlap of the emission and detection patterns (see figure (3.1)):

$$P_{det} = \left| \int \vec{A}_{dip}(\hat{n}) \cdot \vec{A}^*_{det}(\hat{n}) \, d\Omega \right|^2 \approx \frac{6}{(kw_0)^2} \tag{3.1}$$

Here $\vec{A}_{dip}(\hat{n})$ and $\vec{A}_{det}(\hat{n})$ are the normalized atomic-dipole emission and detection
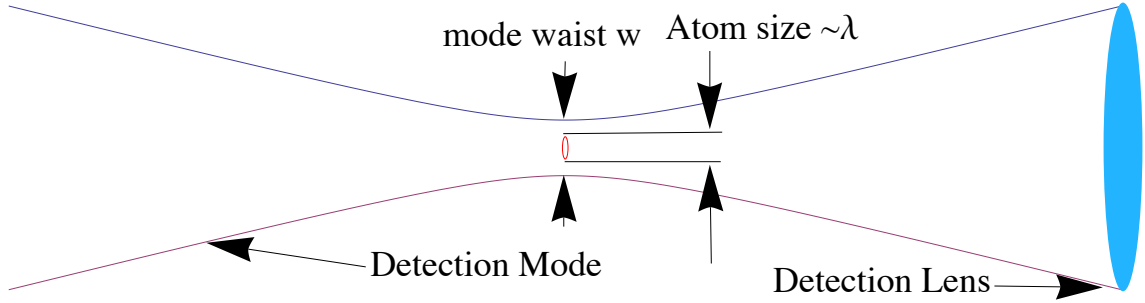
Figure 3.2: Schematic of the detection of light emitted by a single atom. The detection problem may be understood in terms of its time-reverse: absorption of light by the atom. The atom has a resonant absorption cross section of $\sigma \sim \lambda^2$, and the optical field has been focused by the detection lens to a waist w. It is then clear from geometrical considerations that the absorption probability, per photon, ought to scale like λ^2/w^2.

mode-functions, respectively. The above expression reveals that even when using a lens which can generate a 1μm focal spot, only 10% of the light an atom emits will be captured by the detection mode (at 852nm). Up to numerical factors, this is purely an issue of solid-angles: To achieve anywhere near 4π collection efficiency requires sub-wavelength resolution, and hence tremendously high quality lenses[1]. *How can we do better?*

The answer is nicely motivated by first understanding the time-reversed process: absorption. $P_{abs} = P_{det}$, in the case of an optical pulse that fits spectrally within the atomic resonance. This can be shown in a variety of ways, but most simply using the atomic absorption cross section (see figure (3.2)):

$$\sigma_{res} = \frac{3}{2\pi}\lambda^2 = \frac{6\pi}{k^2} \tag{3.2}$$

One can then see that for a pulse of spatial cross section $\sigma_{pulse} = \pi w_0^2$, the absorption

---

[1]There has recently been very promising work using ellipsoidal mirrors for efficient light collection[10]

probability will be: $P_{abs} = \frac{\sigma_{res}}{\sigma pulse} = \frac{6}{(kw_0)^2} = P_{det}$.

There are then two obvious ways to increase the absorption probability that we will consider separately: 1) Increasing the number of interactions between the light and the atom, and 2) increasing the atom number. We will see that under appropriate circumstances, it is not only the absorption probability, but also the emission probability that may be enhanced in this manner. The former approach is the realm of cavity QED. The latter is the realm of collective excitation of atomic ensembles.

3.1.1 Multiple Interactions between Light and Matter: The Cavity Approach

An optical pulse within a cavity[2] will make on average $\frac{\mathcal{F}}{2\pi}$ round trips[3] before leaving the resonator. Due to the resonator standing-wave structure, the intensity is enhanced fourfold at anti-nodes of the standing-wave field, and the photon may be emitted into the resonator in either of two directions. As such the absorption probability ought to be enhanced by a factor of $\frac{\mathcal{F}}{2\pi} \times 4 \times 2$:

$$P_{abs}^{cav} = \eta \equiv \frac{24\mathcal{F}}{\pi} \frac{1}{(kw_0)^2} \tag{3.3}$$

We have now defined the very important and unitless cooperativity parameter $\eta \equiv \frac{24\mathcal{F}}{\pi} \frac{1}{(kw_0)^2}$. It is clear that equation (3.3) is only valid for $\eta < 1$. As we will see

---

[2]Strictly speaking, this is a poor analogy. An optical pulse which fits spatially within a cavity must by definition drive many cavity longitudinal modes. This means that for any practical cavity length, most of the pulse will be spectrally outside of the absorption line. We ignore this fact for now, as it does not impact the conclusions, which can be derived more properly later.

[3]$N_{roundtrips} = \sum_{n=0}^{\infty} P_n = \sum_{n=0}^{\infty}(1 - L_{RT})^n = \frac{\mathcal{F}}{2\pi}$

1 Atom   Finesse $\longrightarrow$ ~ 11Atoms

Cavity
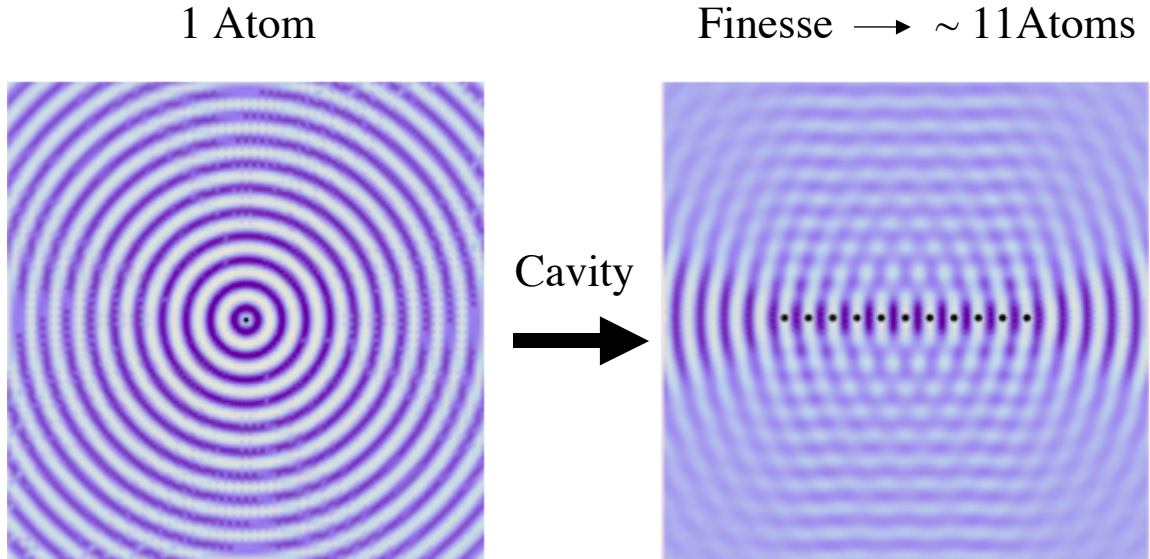
Figure 3.3: The increased directionality of a dipole radiator placed inside of a resonator. **Left**: Dipole radiator in freespace, demonstrating isotropic radiation. **Right**: Dipole radiator in a resonator, modeled by 10 "image" oscillators, and demonstrating increased directionality.

shortly, in general:

$$P_{abs} = \frac{\eta}{1 + \eta} \qquad (3.4)$$

Having understood that absorption may be enhanced by a cavity, one might wonder what role a cavity could possibly have in enhancing emission. One explanation is that the cavity mirrors generate image dipoles which, if they oscillate with the proper phase, will enhance the radiation into the cavity mode (see figure (3.3)). Another explanation, which is more quantum mechanical in nature, is that the cavity enhances the density of states, at particular frequencies, into the direction of the cavity mode, and that this stimulates emission into the cavity. Both of these pictures are valid, and both reveal that the atom will only have enhanced emission into the cavity at particular frequencies. In the former case this is because the image dipoles must be phased up, and in the latter case because the mode density only bunches up near the
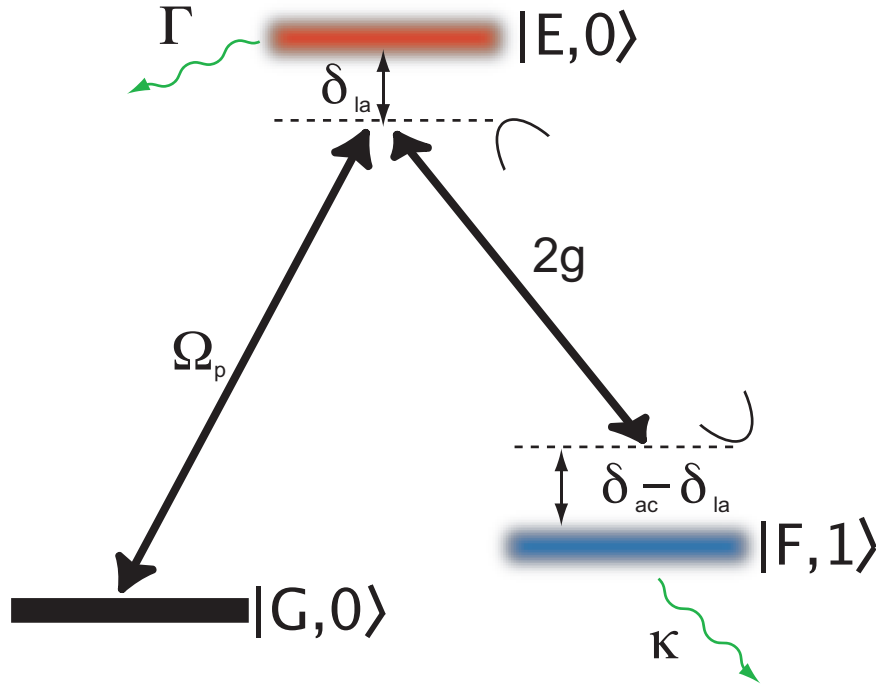
Figure 3.4: Level Diagram for Single Atom Single Photon Source using a Cavity. A laser beam generates the $|G\rangle \leftrightarrow |E\rangle$ transition, while the cavity is near-resonant with the $|E\rangle \leftrightarrow |F\rangle$ transition. The states shown in the diagram are the full states of the atom cavity system: $|X, N\rangle$, where $X \in \{G, E, F\}$ is the atomic state and N is the number of intra-cavity photons.

cavity resonant frequencies.

In order to *derive* the proper scaling of the emission into the cavity, we will resort to a bit of quantum mechanics. We will analyze what happens when a Λ-type 3-level atom undergoes a spontaneous Raman transition within the mode of a cavity, and compute the cavity and free-space emission probabilities for the first scattered photon[4]:

Consider a 3-level atom as in figure (3.4), whose $|F\rangle \leftrightarrow |E\rangle$ transition is near

---

[4]alternatively if the spontaneous emission nearly always results in the atom being transferred to a state other than $|G\rangle$, then we may be assured that the system will only emit one photon.

resonantly coupled to the mode of an optical resonator mode with detuning δ_{ac}. Suppose the system is initialized in the state $|G, 0\rangle$, that is, with the atom in the state $|G\rangle$, and the cavity mode in its vacuum state $|0\rangle$. A laser beam drives the $|G\rangle \leftrightarrow |E\rangle$ transition detuned from resonance by δ_{la}, with a rabi-frequency Ω_p. The non-hermitian Hamiltonian for the system, in matrix form, is:

$$H = \begin{bmatrix} 0 & \frac{\Omega_p}{2} & 0 \\ \frac{\Omega_p}{2} & I\frac{\Gamma}{2} + \delta_{la} & g \\ 0 & g & I\frac{\kappa}{2} + (\delta_{la} - \delta_{ac}) \end{bmatrix} \tag{3.5}$$

Using the perturbative methods of appendix (B), we can compute the steady-wavefunction in the limit that Ω_p is small[5]. In the notation of the appendix, the "strongly coupled manifold" is formed by the states $|E, 0\rangle$ and $|F, 1\rangle$, and its Hamiltonian is accordingly given in matrix form, as:

$$H_0 = \begin{bmatrix} I\frac{\Gamma}{2} & g \\ g & I\frac{\kappa}{2} - \delta_{ac} \end{bmatrix} \tag{3.6}$$

The perturbation is given by $V = \frac{\Omega_p}{2} |G, 0\rangle \langle E, 0| + H.C.$, and the initial state $\psi_0 = |G, 0\rangle$. We may shift the laser detuning onto the energy of the ψ_0: $E_0 = -\delta_{la}$. We may now apply the method from appendix (B) to reach the result that:

$$P(\textbf{Scattered to Cavity}) = \frac{\Gamma_{cav}}{\Gamma_{cav} + \Gamma_{fs}} = \frac{\tilde{C}}{1 + \tilde{C}} \tag{3.7}$$

---

[5] "Small" here is in comparison to detunings, energy splittings, line-widths, and coupling strengths.

where

$$\tilde{C} = \frac{\frac{4g^2}{\kappa\Gamma}}{1 + \frac{(\delta_{ac} - \delta_{la})^2}{\kappa/2}}$$

$$\Gamma_{cav}\big|^{\delta_{ac}=\delta_{la}} = \frac{\Omega_p^2}{\Gamma} \frac{\eta}{(1+\eta)^2 + (\frac{\delta_{la}}{\Gamma/2})^2}$$

$$\Gamma_{fs}\big|^{\delta_{ac}=\delta_{la}} = \frac{\Omega_p^2}{\Gamma} \frac{1}{(1+\eta)^2 + (\frac{\delta_{la}}{\Gamma/2})^2} \tag{3.8}$$

So we see that when the laser is tuned to Raman scatter into the cavity, $\delta_{ac} = \delta_{la}$, the probability that the atom will scatter into the cavity is given by $\frac{\frac{4g^2}{\kappa\Gamma}}{1 + \frac{4g^2}{\kappa\Gamma}}$. This equation would be the same as equation (3.4), if only:

$$\frac{4g^2}{\kappa\Gamma} \overset{?}{=} \eta \equiv \frac{24\mathcal{F}}{\pi} \frac{1}{(kw_0)^2} \tag{3.9}$$

The amazing fact is that one can show that equation (3.9) is true! To do so g, Γ and κ must all be written in terms of the atomic dipole matrix element d, and the relevant cavity parameters. This shows that the quantum mechanical calculation of scattering probability into the cavity gives a result which is not inherently quantum mechanical at all, but rather depends only upon cavity geometry, and mirror quality! We anticipated this on qualitative grounds, but it is neat to see it borne out by calculation.

It must be mentioned that g and Γ may have different dipole matrix elements d depending upon the branching ratio of the excited state. Put another way, an atom only has the maximal resonant absorption cross section given by equation (3.2) for the strongest transition ($|F_g = 4, m_F = 4\rangle \rightarrow |F_e = 5', m_F = 5\rangle$ for the Cs D2 line). One may observe the maximal cross section scaled down by $(\frac{\delta_{la}}{\Gamma/2})^2$ once Rayleigh scattering dominates, eg δ_{la} is greater than Δ_{fine}, the excited state fine structure.

This occurs due to a sum rule on the coupling matrix elements requiring the sum of squares equal the maximal value for any ground state, if excited state fine- and hyper-fine structures are summed over[116].

Detuning Independence of the Cavity Enhancement

Perhaps the most important message to take away from this section is that an atom may efficiently scatter into a cavity at *any* detuning from atomic resonance, as long as the cavity is tuned to the two-photon resonance $\delta_{ac} = \delta_{la}$. We proved this in the general case, above, but it is informative to consider the detuned and resonant limits separately:

Detuned Scattering: In the large detuning limit, the effect of the cavity is to enhance the scattering rate into the resonator mode by a factor of η, compared to the freespace scattering rate, $\Gamma_{sc} = \frac{\Omega_p^2}{4\delta_{la}^2}\Gamma$. We can show this by treating the detuned scattering process as a two-photon rabi frequency coupling the $|G,0\rangle \rightarrow |F,1\rangle$, with a rabi frequency $\Omega_2 = \frac{2\Omega_p g}{2\delta_{la}}$. $|F,1\rangle$ has a linewidth κ, and so the effective two-photon scattering rate is $\frac{\Omega_2^2}{\kappa} = \eta\Gamma_{sc}$, once we identify $\eta \equiv \frac{4g^2}{\kappa\Gamma}$.

Comparing rates, this means that the atom will Raman scatter into the cavity with a probability $\frac{\eta}{1+\eta}$, as we calculated before.

Resonant Scattering: In the on-resonant case, the cavity g-coupling opens an electromagnetically induced transparency window such that the freespace scattering is suppressed by a factor $\frac{1}{(1+\eta)^2}$ compared to what it would be in the absence of the cavity $\Gamma_{sc} = \frac{\Omega_p^2}{\Gamma}$. The cavity scattering, on the other hand, is only suppressed by a

factor of $\frac{\eta}{(1+\eta)^2} \approx \eta^{-1}$ compared with Γ_{sc}.

We can show this by directly (in the limit $\eta \gg 1$) computing the dark state, and its linewidth. The dark state of the system (in the weak pumping limit) will be $|G, 0\rangle - \frac{\Omega_p}{2g} |F, 1\rangle$. This state decays out of the cavity at a rate $\left(\frac{\Omega_p}{2g} \right)^2 \kappa = \frac{\Gamma_{sc}}{\eta}$. This population must be scattered out of the atomic excited state population P_E, so we must have $P_E \times \frac{4g^2}{\kappa} = \frac{\Gamma_{sc}}{\eta}$. The free-space loss rate $P_E \times \Gamma$ is thus given by $\frac{\Gamma_{sc}}{\eta^2}$. Again comparing rates, we arrive at a cavity scattering probability of $\frac{\eta}{1+\eta}$.

If the on-resonant process is performed at a time-varying intensity which begins low and ends higher than g, we enter the so called dark-state rotation limit. As long as the rotation is performed adiabatically, the expected retrieval efficiency remains the same: $\frac{\eta}{1+\eta}$.

That the cavity enhancement works at all detunings from the atomic turns out to be critically important in practice. This is because we will often need two different scattering processes to emit photons into the cavity– one for a Raman transition from $F = 3 \to F = 4$, and one for $F = 4 \to F = 3$. While both processes turn out to be *near* atomic resonance, they will differ in detuning by $\Delta_{HF} - 4\nu_{FSR} = 130\text{MHz}$. If we were forced to work on atomic resonance to reach the strong atom-cavity coupling regime, we would not be able to use these two transitions simultaneously.

Cavities and Causality– Action at a Distance?

It may seem almost *magical* that a cavity can affect the emission properties of an atom. The atom, after all, does not even know that the cavity mirrors are there

when it begins emitting. The key is that the image dipoles take a time κ^{-1} to build

up: the cavity is expected to generate of order $\frac{\mathcal{F}}{2\pi}$ image dipoles, and one dipole is

generated per cavity round trip. Each cavity roundtrip requires a time $\frac{2L}{c}$, and so

the image dipoles begin radiating after a time $\frac{\mathcal{F}}{2\pi}\frac{2L}{c} = \kappa^{-1}$. This is another way to

understand that the enhancement window is only κ wide in frequency, and reveals why

the resonant enhancement of the cavity (compared to a free-space mode of identical

waist) depends only upon the cavity finesse, and not κ or Γ explicitly.

In light of this understanding it is clear that exciting an atom as described at the

beginning of this chapter by a π pulse would *not* result in the enhancement of cavity

scattering, unless $\kappa > \Gamma$, as the excitation process would be too rapid and the image

dipoles would not have time to build up. This would of course be borne out directly

by time evolution of the quantum state under the hamiltonian (3.6). According to

[23] the result is: $P(\textbf{Scattered to Cavity}) = \frac{\eta}{1+\eta}\frac{\kappa}{\kappa+\Gamma}$, which can be understood as

rapid rabi-flopping in and out of the cavity. The probability of losing the excitation

into freespace is then set by the rate of freespace loss relative to the rate of cavity

leakage.

3.1.2 Atomic Ensembles and Super-Radiance: An Introduction to Magnons

A simple (classical) counting argument reveals that if a single-atom has a prob-

ability $P_1 \ll 1$ of absorbing a single photon which is passing it, N atoms will have

a probability $P_N \approx 1 - e^{-NP_1}$. Running the process backwards, it seems that an

atomic ensemble may be stimulated to emit a single photon with very high probabil-

ity into a particular spatial mode. Is this true, or have we been fooled by the inherent irreversibility of dissipative processes?

It has long been known that a Bragg reflector made of crystalline planes can scatter light from a particular mode into another well-defined mode. This phenomenon results from the (classical) constructive interference of the wavelets produced by periodically located scattering sites. What remains unclear, then, is how to prepare an ensemble of atoms such that it can emit precisely *one* photon, while maintaining the crystalline, directional properties a Bragg grating.

In 1956, R.H. Dicke predicted a phenomenon called called super-radiance[30] wherein an ensemble of atoms confined to within a radiation wavelength will radiate either more or less strongly depending upon the quantum phases between the different excited atoms[6]. In a subsequent paper[31], he predicted that radiation into a particular *mode* could be enhanced or suppressed for a spatially extended sample, depending upon the relative phases of the atoms. By properly choosing which superposition of atoms is excited, one may enforce that the sample emit into a desired (and optically thick) direction. This physics was observed experimentally in a number of systems[94, 104]. Although the Dicke papers focus on spontaneously occurring super-radiant pulses in the absence of any quantum-state engineering, what they essentially describe is the quantum analog of a Bragg grating. We will call these quanta magnons, because the phase information of these collective excitations is stored in electron and nuclear spin.

---

[6]Strictly speaking, it was the quantum phases between the states of the system where different subsets of atoms were excited

Magnon Readout

The essential physics is actually *very* similar to the enhanced directionality of a single atom scattering into an optical resonator, except that the phased up dipoles are real, rather than images generated by the cavity mirrors. For a more detailed understanding we consider a system which is in a state [7] $\alpha^\dagger(\delta_k)\ket{\Omega}$, where $\ket{\Omega} = \ket{GG.....G} \otimes \ket{0}_c$ is the "vacuum" state, with no atoms excited, and no photons in the cavity. $\alpha^\dagger(\delta_k)$ is the magnon creation operator:

$$\alpha^\dagger(\delta_k) = \frac{1}{\sqrt{N}} \sum_{j=0}^{N} e^{i\vec{\delta_k}\cdot\vec{x}_j} \sigma_{FG}^j \qquad (3.10)$$

We expect that this state will act as a quantum Bragg grating capable of imparting a momentum $\hbar\vec{\delta_k}$ to a *single* Raman-scattered photon, when driven by a laser on the $\ket{F} \leftrightarrow \ket{E}$ transition. This phenomenon may be analyzed quantitatively[34, 49], but qualitatively one sees that the scattered field amplitude for a system initialized into the state $\ket{\psi}$ is a superposition of the scattering amplitudes for each atom separately[8], adjusted for the phase of the incoming (pump) beam, and the outgoing(scattered) photon.

If each atom separately scatters with an amplitude $A(\hat{n})$ into the direction $\hat{n}$, then the total scattering amplitude is:

$$A_{tot}(\hat{n}) = \frac{1}{\sqrt{N}} \sum_{j=0}^{N} e^{i(\vec{\delta_k}+\vec{k}_{pump}-\hat{n}k)\cdot\vec{x}_j} A(\hat{n}) \qquad (3.11)$$

It is clear that in the limit of a sample of infinite spatial extent, the terms from all of

---

[7]How it arrived in this state will be discussed shortly.

[8]Technically, we should include reabsorption in our calculation. We do so in the analysis for our cavity-ensemble system, both later in this chapter, and in chapters (5) to (8). This is unnecessary for our qualitative understanding here.

the atoms interfere constructively only for $\hat{n}k = k_r^{\hat{det}} = \frac{\vec{k}_{pump} + \vec{\delta_k}}{k}$, that is:

$$\vec{k}_w^{pump} - \vec{k}_r^{pump} = \vec{k}_w^{det} - \vec{k}_r^{det} \tag{3.12}$$

When this *phase-matching* condition is met, the collectively enhanced scattering amplitude is given by:

$$|A_{tot}(\hat{n}_{read})|^2 = N \, |A(\hat{n}_{read})|^2 \tag{3.13}$$

Hence we have an N-fold enhancement in the scattering rate in this direction. In all other directions, the various terms interfere destructively, leaving:

$$|A_{tot}(\hat{n} \neq \hat{n}_{read})|^2 = |A(\hat{n})|^2 \tag{3.14}$$

Thus we see that the ratio of scattering into the mode of interest, to the rest of 4π is enhanced by a factor of N. A proper calculation for an atomic ensemble with finite extent yields that the ratio of scattering into the mode of interest, compared with the rest of 4π, is $\frac{6N}{(kw_0)^2}$. With enough atoms this may be made $\gg 1$, and the sample will almost always scatter the single photon into our mode of interest. Suffice it to say that by preparing this *super-radiant* state one can induce an ensemble to scatter a single photon into the preferred direction with high probability.

Magnon Generation

Having successfully described the enhanced directionality of magnon readout, the remaining question is how to *prepare* a magnon $|\psi_{MAGNON}\rangle$. The solution to this problem was provided by Duan, Lukin, Cirac, and Zoller[34]. Beginning with a system optically pumped into the state $|GG...G\rangle$, a laser beam is applied on the $|G\rangle \leftrightarrow |E\rangle$ transition with wavevector $\vec{k}_{write}$. The atoms will begin to scatter on the $|G\rangle \rightarrow$

$|E\rangle \rightarrow |F\rangle$ transition, and detection of a photon scattered into the $\vec{k}_{det}$ direction does not definitively reveal which atom made the transition, only that the system has been projected into the state $|\psi_{MAGNON}\rangle$, with $\delta_k = \vec{k}_{write} - \vec{k}_{det}$. This is precisely the collective state, or magnon, that we wanted to generate.

One might worry about the impact of atoms scattered on the $|G\rangle \rightarrow |E\rangle \rightarrow |F\rangle$ transition into *other* directions than $\vec{k}_{det}$. This will be addressed thoroughly in chapter (6), but it suffices to say that these scattering events do not produce collective excitations which will be efficiently read-out into the $\hat{n}_{read}$ direction, and serve only to reduce the participating atom-number. A serious concern arises only when enough atoms are scattered into the $|F\rangle$ state that they begin to absorb strongly. As long as $\frac{6}{(kw_0)^2} \ll 1$, this requires many atoms and there exists a regime where it is not a concern[9].

3.1.3   Combining Cavities *and* Ensembles

For a variety of reasons, some of them historical, we chose to enhance our light-matter interaction using the *combination* of a cavity and an ensemble. This has a number of benefits which will be described in more detail in the upcoming chapters:

1. Lower Necessary Single-Atom Cooperativity: We can tolerate $\eta \ll 1$, so long as $N\eta > 1$. This substantially mitigates the formidable technical requirements typical of making a high-finesse, small-waist resonator sufficient for single-atom strong-coupling.

---

[9]It turns out that the optical depth in the $|F\rangle$ state is given by n_w, the number of photons scattered into the mode of interest, up to a numerical factor. As a consequence n_w must be kept far below 1 to avoid absorption effects.

2. Less Spatial Localization: Single atom Cavity QED experiments obtain stable strong coupling by localizing the atom to a cavity anti-node. With an ensemble one makes use of the average coupling and so localization is at least initially not required.

3. Less Stringent Atom Number/Density Requirements: Preparing a MOT which is optically thick is complicated by radiation trapping effects. When much of the optical depth comes from the cavity finesse enhancement, one can make due with a far less optimized MOT.

4. Optical Pumping: Because the sample is optically thin in all directions except along the cavity axis, high quality optical pumping of the entire sample may be achieved without being limited by reabsorption.

5. Theoretical Simplicity: The basic model of this system requires only a 3-state hamiltonian[48]. In contrast, the comparable free-space system must be modeled by coupled differential equation[3, 74]. The physics is very much the same, but the cavity model is in some ways conceptually simpler, as it deals only with time dependent, and not spatially and time dependent fields.

Preparation of Intra-Cavity Magnon: The *Write* Process

The procedure for preparing a collective excitation of an atomic ensemble within a cavity (see figure (3.5)) closely mimics the procedure in free-space. The ensemble is initially optically pumped such that all of the atoms are in the state $|G\rangle$. The so-called write beam is applied on the $|G\rangle \leftrightarrow |E\rangle$ transition, with the cavity tuned to
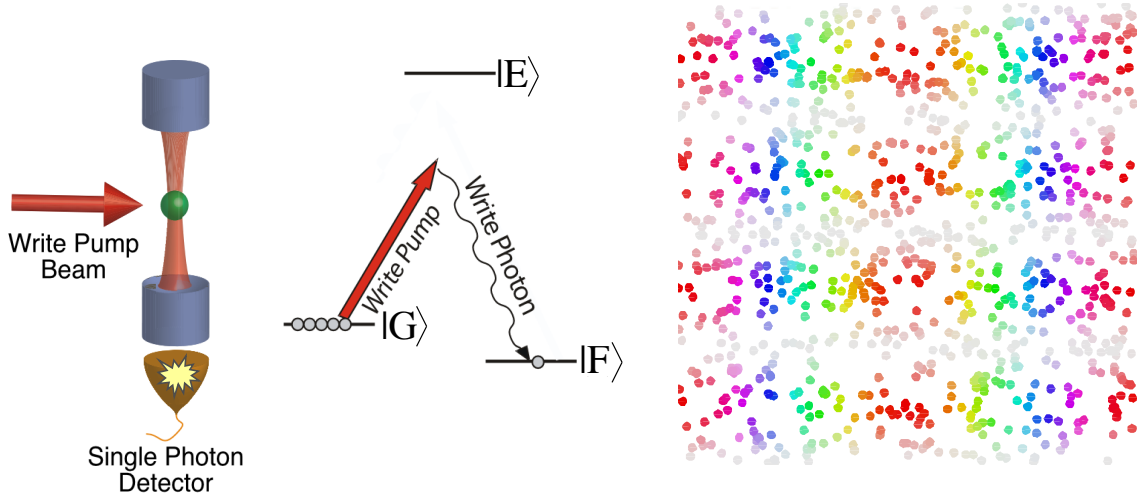
Figure 3.5: Schematic of Magnon Generation Process. An optically pumped sample, prepared in the state $|G\rangle$, is illuminated with a weak laser beam (**left**) on the $|G\rangle \rightarrow |E\rangle$ transition (**center**). While most photons are scattered into free-space, detection of a photon Raman-scattered into the cavity mode on the $|G\rangle \rightarrow |E\rangle \rightarrow |F\rangle$ transition heralds the creation of a magnon (**right**). In the magnon diagram, the color reflects the phase written into the atom (arising from the pump phase), while the intensity reflects the amplitude (arising from the cavity standing wave).

the $|E\rangle \leftrightarrow |F\rangle$ transition. A photon scattered into the resonator mode which leaks through an end-mirror and is detected reveals that an atom has been transferred $|G\rangle \rightarrow |E\rangle \rightarrow |F\rangle$, but does not reveal which atom, projecting the system into the state $\alpha^\dagger(\delta_k) |\Omega\rangle$. As before $\alpha^\dagger(\delta_k)$ is the magnon creation operator. Now $\delta_k = \vec{k}_w - \vec{k}_c$, with $\vec{k}_c$ the cavity direction[10], and $\vec{k}_w$ the direction of the write pump beam.

Because the write-process is not collective, the probability that any particular photon scattered on the write transition will go into the cavity mode is given by $\frac{\eta}{1+\eta} \approx \eta$, for $\eta \ll 1$. The write process thus creates magnons randomly (and infrequently), but heralded by a single photon scattered into the cavity mode.

---

[10]For now we are assuming a running wave cavity for simplicity. This will be corrected in chapter (6).

Readout of Intra-Cavity Magnons: The *Read* Process

Having initialized the system in the state $\alpha^\dagger(\delta_k)\,|\Omega\rangle$, we now read it out. A readout laser is applied on the $|F\rangle \leftrightarrow |E\rangle$ transition, and the cavity tuned to the $|E\rangle \leftrightarrow |G\rangle$ transition. The Hamiltonian for the system is:

$$
\begin{aligned}
H &= (\omega_a + i\frac{\Gamma}{2})\Sigma_{EE} + g\sqrt{N}(a^\dagger\Sigma_{GE} + a\Sigma_{EG}) \\
&+ (\omega_c + i\frac{\kappa}{2})a^\dagger a + \Omega_P(t)(\Sigma_{FE} + \Sigma_{EF}))
\end{aligned}
\tag{3.15}
$$

Here the collective creation operators are:

$$
\Sigma_{EG} = \frac{1}{\sqrt{N}}\sum_j e^{i\vec{k}_r\cdot\vec{x}_j}\sigma_{EG}
$$

$$
\Sigma_{EF} = \frac{1}{\sqrt{N}}\sum_j e^{i\vec{k}_c\cdot\vec{x}_j}\sigma_{EG}
\tag{3.16}
$$

Beginning in the state $\alpha^\dagger(\delta_k)\,|\Omega\rangle$ and generating the manifold of coupled states, as per chapter (2), we discover that as long as $\vec{k}_w + \vec{k}_r = 0$, there are only three coupled states:$|f\rangle \equiv \sigma_{FE}\sigma_{EG}\,|\Omega\rangle, |e\rangle \equiv \sigma_{EG}\,|\Omega\rangle$, and $|\Omega\rangle$. Noting that, as discussed above, the free-space scattering sees no-collective enhancement and proceeds at the single-atom rate, we arrive at the hamiltonian:

$$
H = \begin{bmatrix} 0 & \frac{\Omega_p}{2} & 0 \\ \frac{\Omega_p}{2} & I\frac{\Gamma}{2} + \delta_{la} & \sqrt{N}g \\ 0 & \sqrt{N}g & I\frac{\kappa}{2} + (\delta_{la} - \delta ac) \end{bmatrix}
\tag{3.17}
$$

This is precisely the same Hamiltonian that describes a single atom scattering into a cavity, except that $g \to \sqrt{N}g$ and so we expect the single photon retrieval efficiency
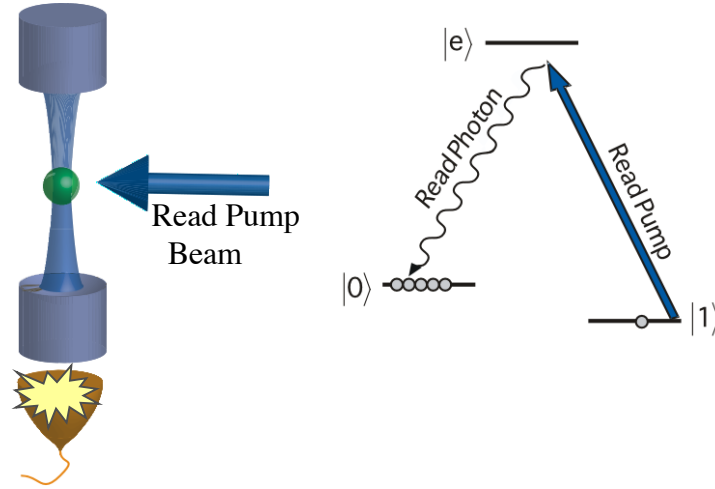
Figure 3.6: Schematic of Magnon Readout Process. Applying a phase matched read pump on the $|F\rangle \leftrightarrow |E\rangle$ transition allows the magnon prepared in the write process to collectively scatter a single photon into the cavity on the $|F\rangle \rightarrow |E\rangle \rightarrow |G\rangle$ transition. The collective enhancement is essential because the single-atom cooperativity is low, so a single atom in the $|F\rangle$ state would Raman-scatter into the cavity with probability $\eta \ll 1$.

on Raman resonance to be[11]:

$$P(\textbf{Scattered to Cavity}) = \frac{N\eta}{1 + N\eta} \tag{3.18}$$

One may view this expression as compensation for small η by large N, *or* compensation for small N by large $\mathcal{F}$[12]. In practice we take the middle ground- we use moderate $\mathcal{F}$ and moderate N to get near unity probability for scattering into the cavity!

It is also interesting to note that equation (3.17) is actually a *better* approximation

---

[11]We also expect that the retrieval efficiency should be independent of detuning from atomic resonance δ_{la}, just as in the single atom case.

[12]It might appear that reducing w_c would be helpful as well, but this is not the case as long as the atom cloud is larger than the cavity waist. In that limit $N \approx \pi w_c^2 L \rho_{at}$, so $N\eta \approx \frac{24\mathcal{F}L\rho_{at}}{k^2}$, which is independent of the cavity waist!

for a collective excitation strongly coupled to a cavity than it is for a single atom strongly coupled to a cavity. This is because after a free-space scattering event, the collective excitation is *destroyed*[13], leaving only the non-collective atom-cavity interaction, which is negligible for $\eta \ll 1$. In contrast, a single atom with $\eta \geq 1$ will still be strongly coupled to the cavity mode, even after a free-space scattering event, and so a master equation needs to be used, rather than a non-Hermitian Hamiltonian.

3.2 An Introduction to $g_2(\tau)$: Verifying Anti-Bunching of a Light Field

Given the variety of different systems which may act as single-photon sources, it is imperative to come up with consistent ways to characterize such sources that apply to as many different physical realizations as possible. In later chapters we will investigate such properties as spectral width, repetition rate, retrieval efficiency, and indistinguishability, among others. There is one specification, however, which is often misunderstood and deserves a separate explanation. That specification is the intensity-intensity autocorrelation function, denoted $g_2(\tau)$, defined according to[108]:

$$g_2(\tau) \equiv \frac{\langle : I(t)I(t+\tau) : \rangle}{\langle I(t) \rangle^2} \tag{3.19}$$

This function describes how the intensity of a beam $I(t)$ is correlated with itself, from one moment to the next. $\langle : B : \rangle$ denotes the expectation of the normal ordering of B,

---

[13]Free-space scattering destroys collective excitations as a consequence of the random phase imparted on the atom by the scattering process, or alternatively the entanglement of the scattering atom with the scattered field, with different phases for different atoms.

with respect to the photon creation and annihilation operators. Any classical beam must satisfy[97, 83]:

$$g_2(0) \geq 1 \tag{3.20}$$

$$g_2(\tau) \leq g_2(0) \tag{3.21}$$

We will focus primarily on the former equation. Classically, this equation says that when a classical beam is split on a beam-splitter, fluctuations above the mean on one output port will be accompanied by fluctuations above the mean on the other output port. This is to be contrasted with a source of single photons: when a single photon impinges upon a beamsplitter it must chooses to go one way or the other, and so the two output ports will be anti-correlated. Practically, it turns out that assuming that $I(t)$ is a non-negative real valued function $I(t) \in \mathbb{R}$ is sufficient to prove the above inequalities: this says that any violation comes explicitly from the *quantized* nature of the electromagnetic field.

3.2.1 Proof of Equation 3.20 in the Case of Classical Light

We begin by defining the variance of $I(t)$, averaged over n experimental realizations $I_j(t)$, to be:

$$\sigma_{I(t)}^2 \equiv \frac{1}{N} \sum_j [I_j(t) - \frac{1}{N} \sum_k I_k(t)]^2 \tag{3.22}$$

It is clear that $\sigma_{I(t)}^2 \geq 0$, and so expanding the right side of equation (3.22) we arrive at:

$$\frac{1}{N} \sum_j I_j(t)^2 + \frac{1}{N} \sum_k I_k(t)^2 - \frac{2}{N^2} \sum_j I_j(t) \sum_k I_k(t) \geq 0 \tag{3.23}$$

Collecting terms yields:

$$\frac{1}{N} \sum_j I_j(t)^2 \geq [\frac{1}{N} \sum_j I_j(t)]^2 \tag{3.24}$$

Identifying $\langle I(t)^2 \rangle \equiv \frac{1}{N} \sum_j I_j(t)^2$, and $\langle I(t) \rangle \equiv \frac{1}{N} \sum_j I_j(t)$, , and dividing through by the second term squared, we find:

$$\frac{\langle I(t)^2 \rangle}{\langle I(t) \rangle^2} \geq 1 \tag{3.25}$$

We have thus proven equation (3.20), assuming only that the intensity of the light field is a real quantity $I(t)$.

3.2.2 Equation 3.20 in the Case of Squeezed Light

Before attempting to understand why equation(3.20) may be violated by squeezed light, it seems sensible to attempt to justify the form of the equation– specifically the normal ordering. To do this, it is simplest to think about how one would attempt to distinguish a single photon from a weak coherent beam. The simplest way to do this is with a Hanbury-Brown-Twiss (HBT) interferometer[62], as shown in figure (3.7).

The operating principle of an HBT interferometer relies upon the fact that if a single photon impinges on a beam-splitter, it choose to either be transmitted or reflected, but not both. As such, one of the two detectors will click, but never both– detection events are anti-correlated. In contrast, when a coherent beam impinges upon a beamsplitter, both of the output arms contain an attenuated coherent beam, and detection events in the two output arms are uncorrelated.

a) **Coherent State**

b)

Fock State

–OR–
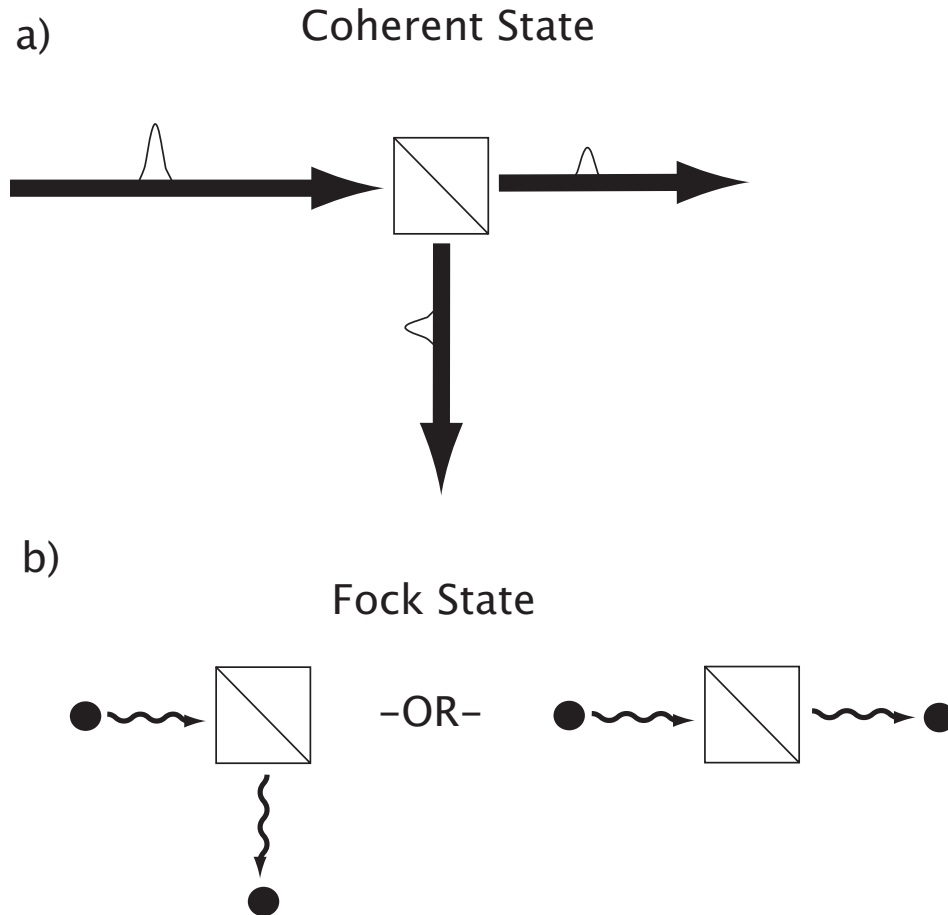
Figure 3.7: Schematic of a Hanbury-Brown Twiss Interferometer. **(a)** When a coherent state is incident on the beamsplitter, the classical wave properties of the coherent state ensure that unentangled coherent states of reduced amplitude leave through the two output ports, resulting in no correlation between the output arms. **(b)** When a single photon Fock state is incident on the beam splitter, a simple calculation reveals that the photon must go one way or the other, and so the output arms are anti-correlated. This is a reflection of the fact that a Fock state in an HBT interferometer behaves like a classical *particle*, while a coherent state behaves like a classical *wave*.

In order to quantify this, let us compute the the rate of coincidences between the two arms into a bin of size T, $R_{1\&2}$, and compare it with the rate of coincidences expected for uncorrelated beams, $R_1 R_2 T$. One may show that in the limit $T \to 0$, the ratio may be expressed as:

$$g_{BC} \equiv \frac{\langle b^\dagger b c^\dagger c \rangle}{\langle b^\dagger b \rangle \langle c^\dagger c \rangle} \tag{3.26}$$

Where $b^\dagger$ ($c^\dagger$) creates a photon in the transmitted (reflected) mode, at the location of the photon counting module. We could continue to work in the output modes, which would allow us to show that an incident coherent state is converted into unentangled coherent states in the output arms. Instead, we will compute g_{BC} by referencing back to the input mode of the beamsplitter. Using beamsplitter relations and assuming that the beamsplitter is lossless and couples the input mode equally into the transmitted and reflected modes, we may make the transformation:

$$b^\dagger = \frac{1}{\sqrt{2}}(a^\dagger + v^\dagger)$$
$$c^\dagger = \frac{1}{\sqrt{2}}(a^\dagger - v^\dagger) \tag{3.27}$$

Here a and v destroy photons in the two output modes of the beam-splitter. This transformation yields (with the additional assumption that the mode v is in a vacuum state) the relation:

$$g_{BC} = \frac{\langle a^\dagger a^\dagger a a \rangle}{\langle a^\dagger a \rangle^2} \tag{3.28}$$

Which is precisely the expression given in equation (3.20). Thus we see that the quantity that we were naively interested in measuring, relating to whether a single photon goes one way on a beamsplitter, corresponds directly to the inequality (3.20). We can now compute g_{BC} for a variety of input states:

$$\textbf{Coherent State} \, |\alpha\rangle : \qquad\qquad g_{BC} = 1 \qquad\qquad (3.29)$$

$$\textbf{Fock State} \, |N\rangle : \qquad\qquad g_{BC} = 1 - \frac{1}{N} \qquad\qquad (3.30)$$

In spite of the fact that the math works out, one might still wonder why it is *physically* that the numerator of the correlation function is $a^\dagger a^\dagger a a = \hat{n}^2 - \hat{n}$, rather than $a^\dagger a a^\dagger a = \hat{n}^2$, as would be naively expected from the expression in the output (transmitted and reflected) basis of the beamsplitter. The reason is that the former expression prevents us from double-counting single-photon events. If, for example, the state of the optical field were given by:

$$|\psi\rangle = A_0 \, |0\rangle + A_1 \, |1\rangle + A_2 \, |2\rangle \qquad\qquad (3.31)$$

Then the numerator would be $2P_2$ in the former case, and $4P_2 + P_1$ in the latter case, with $P_j \equiv |A_j|^2$. Since the numerator was designed to count coincidences, the latter expression is clearly wrong! The g_2 of a weak pulse, where equation (3.31) applies, is thus given by:

$$g_2(\tau = 0) = \frac{P_2}{\frac{1}{2}P_1^2} \qquad\qquad (3.32)$$

This expression will be applied extensively to the data analyzed in the succeeding chapters.

3.2.3   Insensitivity of the g_2 Function to Losses

Here we will show that the value of the g_2 function is insensitive to losses in the detection path[14] This is convenient because it means that one can demonstrate that a given light-source is non-classical in spite of the inevitable losses arising from finite detector quantum efficiency, fiber coupling, cavity out-coupling, interference filters and so forth.

An attenuator may be modeled as a beamsplitter inserted into the mode[14]. If the mode to be attenuated has creation operator $a^\dagger$, then the transformation is:

$$u^\dagger = \frac{1}{\sqrt{2}}(\sqrt{\epsilon}a^\dagger + \sqrt{1-\epsilon}b^\dagger)$$
$$l^\dagger = \frac{1}{\sqrt{2}}(\sqrt{1-\epsilon}a^\dagger - \sqrt{\epsilon}b^\dagger) \tag{3.33}$$

Where $u^\dagger$ creates a photon in the output mode, after the loss, $l^\dagger$ creates a photon in the loss channel, and $b^\dagger$ creates a photon in the dark port. Here ϵ is the power transmission coefficient of the attenuator. The g_2 of the output mode is given by:

$$g_2^{output} = \frac{\langle u^\dagger u^\dagger u u \rangle}{\langle u^\dagger u \rangle^2} \tag{3.34}$$

Substituting equation (3.33) into equation (3.34), and assuming that the dark port of the beam splitter is in the vacuum state, yields that:

$$g_2^{output} = g_2^{input} \tag{3.35}$$

That is, we have shown that losses do not affect the value of g_2. Assuming that the dark port of the beam splitter is in the vacuum state corresponds to the assumption

---

[14]The expected value is unbiased by detection path losses, however the measured variance *is* sensitive to path losses– the amount of time necessary to acquire good enough statistics scales as l^{-n}, where l is the loss per photon, and n is the number of coincident photons necessary to make the measurement. This time requirement is one of the primary limitations upon what experiments we can perform.

that no light is coupled *into* the output mode from whatever the attenuating element is. We use interference filters and various other light insulation procedures to ensure that this is in fact the case.

The above conclusion may be reached from the more intuitive expression for g_2, equation (3.32). In the presence of an attenuator, one can easily show that to lowest order in P_2/P_1: $P_1 \rightarrow \epsilon P_1$, $P_2 \rightarrow \epsilon^2 P_2$. Inserting this into equation (3.32) yields that $g_2 \rightarrow g_2$, as we have just shown.

It is worth mentioning that in the presence of backgrounds that enter *after* the loss channel, and hence disturb the state of the optical field, the g_2 function is not insensitive to losses. This will be elucidated in chapter (6).

3.2.4 Experimental Measurement of the g_2 Correlation Function

In practice, g_2 is measured with the two-detector Hanbury-Brown-Twiss configuration described previously. The two main reasons the for this are detector dead-time, and detector after-pulsing.

After a single photon counting module detects a photon, the avalanching medium needs to be actively quenched for some period of time before it can detect another photon. For the Perkin-Elmer SPCM's that we use, this *dead*-time is 50ns. What this means practically is that when measuring with a single detector, the light *always* looks perfectly anti-bunched ($g_2 = 0$) on a 50ns time scale, because the detector simply cannot click twice during this time interval. Using two detectors and looking for coincidences between them bypasses this concern.

The other concern is detector after-pulsing. When a single photon triggers an avalanche in an SPCM, this avalanche must be actively quenched, as mentioned above. Sometimes this active quenching leaves trapped charges in the active region of the photodiode which subsequently initiate further avalanching. This typically occurs with a probability of approximately $1 \sim 2\%$ over a period of about $1\mu s$ [81]. These after-pulsing events may easily be mistaken for a two-photon coincidence, enhancing g_2. Again looking for coincidences between two separate detectors is a good way to circumvent this difficulty.

There used to be a concern about the broadband light-pulse emitted by an SPCM during detection inducing false correlations. This effect has been strongly suppressed by the use of single mode fibers and interference filters such that we do not worry about it any more.

Chapter 4

Experimental Setup

4.1 Magneto-Optical Trap

The work I will present in this thesis only requires micro-kelvin temperatures to operate, not the nanokelvin temperatures typically necessary for a degenerate-gas experiment. What this means is that the Cesium atoms used may be captured in a magneto-optical trap[93] and polarization gradient cooled, and are then at a low enough temperature for the experiment to proceed.

The MOT runs on the $|F_g = 4\rangle \rightarrow |F_e = 5\rangle$ transition of the Cesium D_2 line $\left|6^2 S_{\frac{1}{2}}\right\rangle \rightarrow \left|6^2 P_{\frac{3}{2}}\right\rangle$ at 852nm. This transition has the benefit of being closed, and lacking a dark state, so cooling proceeds uninterrupted until an atom is scattered off-resonantly to the $F_g = 3$ ground state via the $F_e = 4$ excited state. The MOT beams are detuned ~2 atomic linewidths ($\Gamma = 2\pi \times 5.2$MHz) below the atomic resonance, in a compromise between minimizing the MOT temperature and maximizing the number of trapped atoms. Our MOT consists of 3 retro-reflected beams of 1" diameter, each

containing ~ 7mW of power.

When the atoms are depumped to $F_g = 3$, a repumping beam on $F_g = 3 \to F_e = 4$ repumps them efficiently to $F_g = 4$. The tuning of this beam relative to atomic resonance is far less crucial, as the atoms are only infrequently scattered to $F_g = 3$.

The atoms come from a combination of a Cs vapor cell, and Cs getters (manufactured by SAES). The benefit of this arrangement is that the bulk of the Cs is provided by the vapor cell which has an effectively unlimited supply of Cs, with quick adjustment to vapor pressure provided by the getters. The disadvantage of a vapor cell is that changes in Cs partial pressure have a $1/e$ time ≈ 1day, the time it takes for the Cs to coat the vacuum chamber walls and reach equilibrium with the ion pump. On a day-to-day basis, then, the precise amount of Cs in the chamber is adjusted with the getters, which may be controlled via a current of a few amperes.

It should also be mentioned that on the sole occasion that we accidentally opened the vapor cell valve completely we ended up with a MOT that appeared to fill our CCD camera completely (several cm rms size)! This quantity of Cs shorted the cavity piezos to the vacuum chamber walls and coated the cavity mirrors to the point that the cavity finesse dropped well below 100. All of this required only a week or two!

In the system used for previous cavity cooling experiments[6], the MOT coils were outside of the vacuum chamber. One of the primary changes made by me and James was the placement of new MOT quadrupole coils within the vacuum chamber. These square coils have 125 turns each, and inner side of 3.8cm, outer side of 7.4cm separation of 10.2cm. At a current of 2A, they produce a gradient of ~ 6.7G/cm at the center of the vacuum chamber along their axis, and 3G/cm in directions perpendicu-

lar, which is more than sufficient for a MOT. These coils require no water cooling. In contrast, the old coils required $\sim 20A$ of current and water cooling and induced huge eddy currents in the vacuum chamber[6]. The primary reason for the internal coils was in fact minimization of chamber eddy currents. Although the internal coils couple to the same eddy current modes as the external coils, the coupling is geometrically suppressed and so the amplitude of the currents (and hence the magnetic field broadening) is smaller. It should be noted that for the experiments that were sensitive to magnetic field stability we simply loaded the atoms into an optical lattice and waited 100ms for fields to ring down completely. For less sensitive tasks such as polarization gradient cooling, a few ms of wait time was sufficient to reach the requisite stabilities.

One might be concerned that having quadrupole coils inside of the vacuum chamber would introduce so much trapped volume and dirt into the system that a good vacuum could never be achieved. This was not the case. The coils were made of Kapton-dipped 1mm OD wire from Allectra. The coils were sonicated in Acetone for cleaning. During the bake, the coils were heated briefly to $400°C$, and baked continuously at $230°C$ for 24 hours by running large currents through them, to help remove any residual water. This procedure was sufficient to reach the pressures described below, although we do find that whenever the vacuum chamber is opened it is judicious to run the coils back up to 5A during the subsequent bake– the pressure always spikes briefly, indicating that the coils managed to trap some water while the chamber was open.

The magnetic fields may be shimmed with external bias coils, which can produce DC fields up to $\sim 1G$ without overheating, and may briefly be run as high as several

gauss. We use these coils to move the quadrupole zero into the mode of the optical cavity, as well as to zero the fields for Polarization Gradient Cooling and choose the appropriate bias field for our QIP experiments. They may be switched in ~ 1 ms.

4.2 Vacuum System

The actual vacuum chamber arrangement is shown in figure (4.1). It has two large $6\frac{3}{4}$-inch windows through which the horizontal MOT beams propagate. The four $2\frac{3}{4}$-inch diagonal windows are for the exclusive use of the the diagonal MOT beams. The top and bottom $4\frac{1}{2}$-inch windows are for cavity coupling, as described later. The chamber has electrical feedthroughs for cavity piezos, mirror heaters, and the quadrupole coil current. It also has a titanium sublimation pump (Varian TSP 916-0061) and an ion pump (Varian StarCell 75). The ion pump is run continuously, and the TSP is run once every few months. When operated properly we can reach pressures of order 10^{-10} Torr. More details on the vacuum chamber and vacuum system may be found in Adam Black's thesis[6].

Haruka and I discovered that ion pumps are very sturdy. When we vented the vacuum chamber to argon in preparation for the installation of the new apparatus (as described in chapter (9)) there was a really sickening crunching-crackling noise. We immediately realized that we had forgotten to turn off the Ion Pump! We frantically turned it off but whatever damage there was to be done had already (presumably!) occurred. A call to Varian revealed that the noise was a short across the the plates of the ion pump through the Argon. I still do not quite know why it was ok, but some combination of the Argon vent and the brief duration of the short meant that
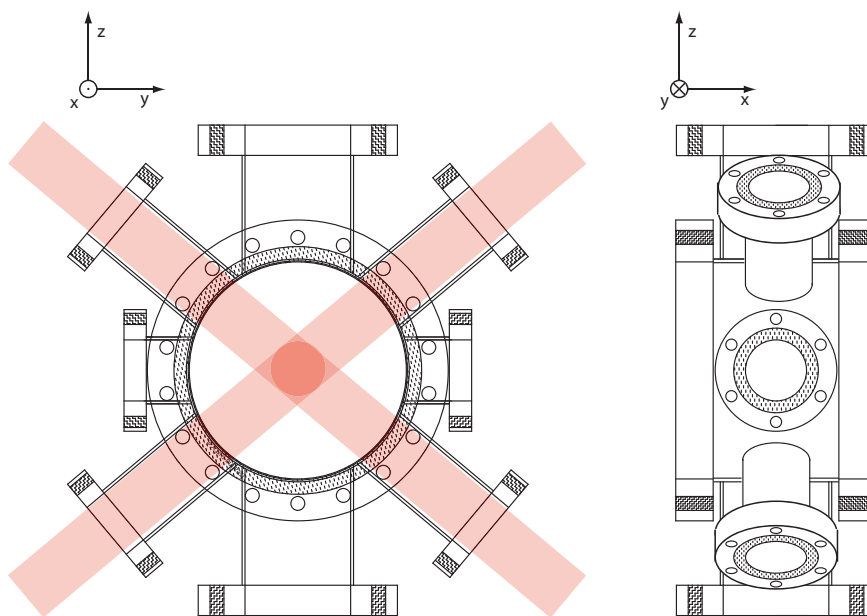
Figure 4.1: Main Vacuum Chamber, with MOT beams shown.

everything was fine when we pumped back down. The technicians at Varian suggested we might need to bake the pump to 400C to clean it, but this turned out not to be necessary in our case. I think the moral, echoed over and over during my PhD, is that you ought be as careful as you can be, but that you will often be pleasantly surprised by how over-engineered and stable commercial devices tend to be. If only our Pound-Drever-Hall locks were so robust[1]!

---

[1]They are now, thanks to Haruka and Renate.

4.3   Laser Systems

4.3.1   Laser Diode Technologies

Shortly after my arrival we began a switch to Distributed FeedBack (DFB) lasers, and have now replaced every External Cavity Diode Laser (ECDL) in the system with a DFB. The Eagleyard DFBs that we use have linewidths of $1 \sim 2\text{MHz}$, run single mode, and have similar cost to the JDS-Uniphase DBRs we used previously. They are quoted for powers up to 150mW, though we never run the diodes above half of their specified power as it seems to substantially shorten their lifetimes. At present the only remaining DBR in the system is the Repumper. Each diode comes with a built-in TEC and thermistor, and requires none of the realignment characteristic of an ECDL. While the $1 \sim 2\text{MHz}$ linewidth is greater than an ECDL, it is less than the Cs D2 atomic linewidth of 5.2MHz, so it is good enough.

For reference, the frequency tuning of a typical Eagleyard DFB laser is approximately 1GHz/mA. This means that a current source with a noise of $1\text{nA/Hz}^{\frac{1}{2}}$ for the laser will broaden a DFB to a linewidth of approximately 3MHz[2]! All of our current controllers are homemade and seem sufficient for our purposes– in situations where we need narrower linewidths the lasers may be locked to a narrow optical cavity, as described in chapter (9).

As the experiment has grown and we have needed more exotic wavelengths it has become clear that DFBs are not always as well behaved as those from Eagleyard at 852nm. We have seen Eagleyard 937nm diodes spontaneously die, or lase on two

---

[2]$\Delta\nu_{Lorentzian} = \pi S^2$, where S^2 is the laser frequency noise in Hz^2/Hz

additional wavelengths 10nm away. There is a new generation of DBR diodes which the manufacturer Photodigm claims to be intrinsically more stable (guaranteed single mode), of narrower linewidth (500KHz gaussian peak, 200KHz lorentzian tails), and more robust to current spikes. Which of these technologies will win out, only time will reveal.

4.3.2 Laser Frequency Stabilization

Our laser locking system uses a single "Reference" laser stabilized to the $F_g = 3$ to $F_e = 2$ transition of the Cs D2 line via a Doppler-Free[52] dichroic atomic vapor laser lock (DAVLL)[53] to a Cs vapor cell. The frequency offset of each of the other lasers is then measured by observing its beatnote with the reference laser, and frequency-stabilized using a frequency offset lock– allowing us each laser at an arbitrary detuning relative to the atomic resonances (up to the bandwidth of our detection electronics).

Reference Lock

The Reference lock, shown in figure (4.2) has gone through a number of iterations over the years. The final, and most stable configuration was placed in a light tight box, and run in a DAVLL configuration. Once generated, the DAVLL error signal is sent to a PID controller which adjusts the Reference laser current to stabilize the laser frequency to the ~ 1MHz. The PID controller has a bandwidth of a few KHz.

The basic operating principle of most Doppler-Free spectroscopic systems is the same. These systems are used to generate a spectroscopic signal with a linewidth unbroadened by the Doppler shifts due to the motion of the (typically room temperature)
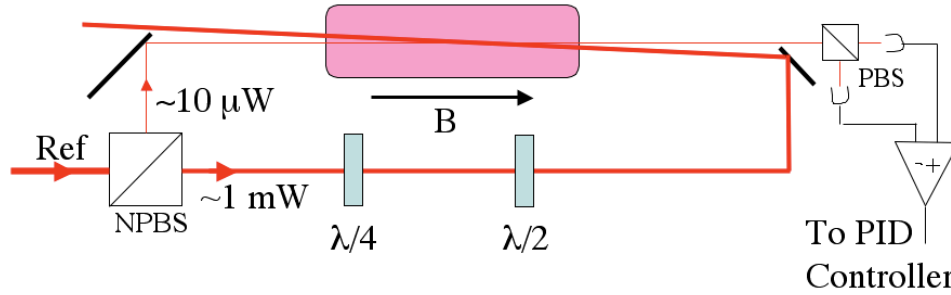
Figure 4.2: Doppler-Free DAVLL configuration.

atomic absorbers. A weak probe beam measures the absorption of the sample, which is pumped by a strong counter-propagating beam derived from the same laser. A nonlinear effect (saturation, optical pumping, etc) is observed when the pump and probe paths interact with the same velocity class. This gives rise to a Doppler-broadened error signal as well as sharp Doppler-Free features. In our case the probe beam is a few μW, and the pump a few mW.

Unlike Pound-Drever-Hall[32] and Frequency-Offset[107] locks, the DAVLL signal is measured directly at DC, and so any DC power drift (due to room lights, or stray light from laser beams switching on and off) translates directly into a frequency shift of the reference laser. This was the reason that we placed the lock in its own isolated light-tight box.

Sensitivity to DC offsets is also the reason that we chose to switch from polarization spectroscopy[125] to Doppler free DAVLL[53]. Polarization spectroscopy operates based upon absorption of a single probe beam in the presence of an optical pumping beam. Because the measurement is not differential, changes in temperature (and hence Cs density) affect the shape of the signal, and varying laser power rescales

the signal. As such, over the course of a day we have observed shifts of order 3 MHz, which substantially affect the performance of our MOT, PGC sequence, and even quantum optics experiments. In contrast, the DAVLL signal derives (largely) from differential absorption of right- and -left circularly polarized light due to a magnetic field. As the signal is differential, it is insensitive to both laser power and cesium density fluctuations. In atoms with large nuclear spin like Cesium, polarization spectroscopy provides a substantially larger signal, owing to coupling coefficient variation across m_F levels. Our experience has been that there was plenty of SNR even in the DAVLL configuration (shown in figure (4.3)), and so the decreased drift of the DAVLL made the switch worthwhile.

4.3.3   Frequency Offset Locking

All other lasers were frequency-offset locked to the reference. The working principle is that each laser is overlapped with the reference laser, and the resulting beat-note is detected on a photodiode. After amplification[3] the beatnote is sent to a frequency-to-voltage conversion circuit, and then to a PID controller which adjusts the lasers current to stabilize its frequency. These locks may have anywhere from a few kHz to a few tens of kHz of bandwidth. The frequency-to-voltage conversion takes place in one of two different ways. The first is a so called phase-locked-loop converter, and the second is a delay-line. The former has the benefit of a substantially more linear conversion, at the expense of locking range and bandwidth. We will discuss them

---

[3]For the MOT laser, which is tuned to the $F_g = 4$ to excited state transitions, the beatnote is near 9.2 Ghz, and must be down-converted via mixing with a 9.2 GHz Phase Locked Oscillator before further manipulation can take place.

Figure 4.3: Doppler-Free DAVLL signal. The reference laser is tuned across the $F_g = 3 \rightarrow$E transitions. $F_g = 3 \rightarrow F_e = 2$ is the right-most transition, and $F_g = 3 \rightarrow F_e = 4$ the left-most. In between we see $F_g = 3 \rightarrow F_e = 3$, and cross-over resonances.

separately.

Phase Locked Loop Frequency to Voltage Conversion

The MOT and Repumper beat-note frequencies are converted to voltages via a so-called PLL lock. This is a bit of a misnomer, as the MOT and Repumper lasers are still *frequency* locked, and not *phase* locked, to the Reference laser. The phase locked loop simply acts as a frequency-to-voltage converter. Our beat-notes are typically in the range of $250 - 1000$ MHz, and are divided down to $1 - 4$MHz with a high-frequency divider from RFbay (FPS-240-4). They are then further divided to $100 - 400$KHz with a TTL divider IC. Finally, this signal is fed into an LM567 tone decoder IC, which is essentially a phase locked loop on a chip. This IC locks its internal VCO to the divided-down beatnote. The control voltage to the IC is linear in the VCO (and hence beatnote) frequency, and acts as the output voltage of the frequency-to-voltage converter (see figure PLL VFC).

PLL's typically have a locking range of an octave, and this situation is no exception. We typically tune our PLL's to lock in the range from $400 - 800$MHz, which is approximately the accessible excited-state hyperfine structure from either $F_g = 3$ to excited states ($F_e = 2$ to $F_e = 4$) or $F_g = 4$ to excited state($F_e = 3$ to $F_e = 5$). The PLL has a small bandwidth due to the time required to measure the frequency of a 200kHz to a few percent. This limits the lock bandwidth to a few kilohertz.

The primary advantage of this method is that the MOT and Repumper frequencies may be adjusted in real time during a single experimental run. This allows us to *retune* the MOT and repumper from the optimal frequency for capturing atoms in a MOT

to the optimal frequencies for Polarization Gradient Cooling, in $\sim$ 1ms.

Delay Line Frequency to Voltage Conversion

For lasers whose frequencies need not be tuned so linearly, or over such a large range, we typically perform the frequency-to-voltage conversion using a delay-line and mixer, which act as a Mach-Zehnder interferometer and square-law detector. The RF beatnote is split on an RF power-splitter, with one path sent directly to one input of a mixer, and the other path sent to the other input of a mixer through a delay line (BNC cable) (see figure (4.4)) of length L. One may show that the output of the mixer, V_{IF} is given by:

$$
\begin{aligned}
V_{IF} \quad &\propto \quad V_{BN}^2 [\cos \omega_{BN} t][\cos \omega_{BN}(t - \frac{L}{c/n})] \\
&\propto \quad V_{BN}^2 \frac{1}{2}[\cos \frac{\omega_{BN} L}{c/n} + \cos \omega_{BN}(2t - \frac{L}{c/n})]
\end{aligned}
\tag{4.1}
$$

Where V_{BN} is the amplitude of the beatnote at frequency ω_{BN}. If the mixer output is low-pass filtered at a frequency far below ω_{BN}, we are left with:

$$
V_{LP} \propto \frac{V_{BN}^2}{2} \cos \frac{\omega_{BN} L}{c/n}
\tag{4.2}
$$

The output signal clearly depends upon the frequency of the beatnote, and has zero crossings every $\delta f_{BN} = \frac{c/n}{2L}$, which for a BNC (with $n = 1.5$) of length 40cm gives $\delta f_{BN} = 250$MHz. The laser can thus be frequency-stabilized at each of these zero crossings. To allow continuous tunability, we mix the beatnote with a tuneable VCO before the power splitter. This allows convenient tunability over a few hundred MHz,
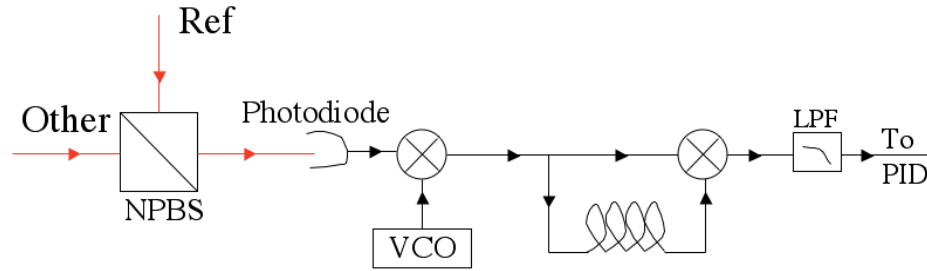
Figure 4.4: Schematic of a Delay-Line-Lock frequency to voltage converter. This figure is adapted from [6]

limited by the filters chosen to remove one of the sidebands created by mixing in the VCO.

The delay line frequency-to-voltage converter provides much larger bandwidth than the PLL converter both because the beatnote signal is not divided down before frequency discrimination, and because all of the components in the converter are fast microwave components. We have built delay-line based frequency locks with nearly a MHz of bandwidth, though this is almost never necessary.

From a practical standpoint, it is rather important that both ports of the mixer be saturated– otherwise the signal that comes out will depend upon the laser powers rather than just their frequencies. It is also important to lock to the zero crossings of the error-signal, as these have minimal sensitivity to power drifts.

Aside on Beatnotes

When generating a beatnote between two lasers, it is important that the two beams be well enough aligned that only a single (spatial) interference fringe of the two laser beams impinge on the measurement photodiode. This is because the beatnote corresponds to the spatial shifting of the interference fringes, and so having more

fringes on the photodiode decreases the amplitude of the beat signal. We find that it is thus best to couple the two beams whose beatnote we wish to form into a single-mode fiber, which is then aligned onto a Hamamatsu G4176 30ps risetime photodiode. All non mode-matched backgrounds are thus filtered out, and alignment of the beatnote is then reduced to polarization alignment and fiber-coupling.

To reach the shot-noise limit on beat-notes, one must have enough power that the laser shot noise is greater than the Johnson noise of the detection circuit, in our case the terminating impedance of $R = 50\Omega$ of the first amplifier: $R\sqrt{2\frac{\eta_{det}P}{\hbar\omega}e} > \sqrt{4K_BTR(10^{NF/10dB}-1)}$, or $P > 1$mW for $\eta_{det} \approx .7$, $NF \approx 3dB$ for a typical photodiode/amplifier combination. In this limit one expects a shot-noise limited signal to noise ratio of: $SNR = \frac{\eta_{det}\sqrt{P_1P_2}}{2\hbar\omega\Gamma_{BN}}$. For $P_1 = 1$mW, $P_2 = 10\mu$W, $\Gamma_{BN} = 2$MHz, we expect $SNR \approx 80$dB. In practice, we find that a good beatnote has ≈ 60dB of signal to noise. It is unclear if this is limited by technical (intensity) noise of the lasers, or something else. 60dB is more than enough to run the frequency-to-voltage converters stably, and so we have not investigated this further.

4.3.4 Cavity and Cavity Locking

Although the different experiments in this thesis used slightly different cavities, they all consisted of two 1-cm diameter dielectric mirrors in a near-confocal configuration 6.6cm apart. The mirrors were coated for finesses ranging from $100 \sim 400$, resulting in cavity linewidths from $22 \sim 5$MHz, respectively. In the later experiments the mirrors were also wrapped in Kapton dipped copper wire from Allectra, which was used to heat the mirrors up by $20 \sim 40\ °C$ to prevent the deposition of Cesium,

which tended to spoil the cavity finesse over a period of months.

The problem of cavity locking arises from the necessity of ensuring that the atomic ensemble interacts with a particular mode of the optical resonator, at a particular detuning from atomic resonance. The length of the cavity is controlled to bring the cavity mode of interest to the appropriate frequency relative to the atomic line. We adjust the length of the cavity with a high-voltage single-layer piezo from Channel Industries.

We measure the cavity resonance frequency using the Pound-Drever-Hall (PDH) scheme[32, 8]. In order to minimize the impact of the locking light on the atoms, we chose to lock the cavity using a mode 4 cavity free spectral ranges (9.062GHz) to the blue of the atomic line. This is a large enough detuning that at the requisite locking power of $\sim 100\mu$W, off-resonant scattering did not destroy the MOT or ruin the PGC. It is too small a detuning to filter the lock light to below the single photon rate of our quantum optics experiments, so the locking beam must be extinguished (by AOM) and the lock "held", for the $\sim$ 2ms during which the actual experiment takes place.

The actual locking scheme depends upon a laser (the *cavity* laser) frequency-offset locked to the Reference at the desired cavity resonance frequency. This laser is then sent through a resonant EOM ($3\times3\times20$mm^3 LiNbO$_3$ crystal from Castech) at 13MHz that adds FM sidebands. The resulting Pound-Drever-Hall error signal, measured in reflection off of the cavity, is used to lock the optical cavity to the cavity laser (via the piezo) with a bandwidth of a few KHz.

We chose to coat one mirror of our cavity for much higher transmission than the

other[4]. This allowed us to ensure that most ($\sim 90\%$) of photons generated by our experiments left through the cavity mirror coupled to our Single-Photon detection apparatus. By contrast, the PDH setup was coupled to the other cavity mirror, and so very little of the locking light actually entered the cavity. As a consequence we needed a lot of power for the locking beam, and became very sensitive to residual amplitude modulation (RAM)[124] and other offsets in our detection path. We ultimately compensated for the RAM by directly demodulating a portion of the beam sent *to* the cavity, and subtracting that signal from the actual PDH signal. Proper balancing of gains gave us a factor of ~ 10 RAM suppression.

4.3.5 Detection Path

Detection of the single photons leaking through the high transmission mirror of the cavity was performed using fiber-coupled single photon counting modules mode matched using a single lens and adjustable fiber collimator to the high transmission output of the cavity. The single photon counting modules (SPCM's) come from Perkin-Elmer, and the models we used have dark count rates as low as 250/sec (SPCM-AQR 13), quantum efficiency of 40% at 852nm, and dead-time of 50ns after a photon detection, for active quenching of the avalanche. This dead-time gives rise to a saturation of the detector at count rates approaching 10^6/s, with an absolute maximum rate of 10^7/s. We see up to 80% fiber-coupling efficiency of the TEM_{00} mode of the optical resonator into the detection fiber, with $1000:1$ suppression ratio between TEM_{00} and TEM_{10} fiber coupling, and $50:1$ between TEM_{00} and TEM_{20}.

---

[4]Precisely *how* much higher varies from one of the later discussed experiments, to another.

We like to operate the experiment with the room lights on, which poses something of a conundrum given that we are simultaneously attempting to detect single photons. We use 2nm wide interference filters centered around $852nm$ to filter out room lights- these filters have $60 - 80\%$ transmission. Additionally, the detection fibers are all single mode, which prevents much room light from being coupled into them anyway. Once the interference filters are in place in front of the fiber collimator, the primary remaining source of backgrounds is free-space coupled into the *cladding* of the detection fibers, through the sheath. We attenuate the cladding modes by coiling 2 or 3 loops of the fiber with 3" diameter. We wrap these loops in black electrical tape to prevent more light from being in-coupled. This seems to introduce negligible loss for the core-guided mode, and substantial losses in the cladding modes, essentially eliminating room-light-induced backgrounds.

4.3.6   Laser Power Control

We switch lasers on and off with a combination of 80MHz resonant free-space AOMs from Isomet, and 20GHz broadband fiber-coupled EOMs from Isomet. The AOMs have the advantage of actually extinguishing the beam entirely, with extinction ratio of 50dB when operated with homebuilt drivers. This extinction is limited primarily by the non-gaussian tails of the optical beam resulting from spatial aperturing. These AOMs have diffraction efficiencies near 90% when used with large (w$\sim 500\mu$m) beams. When operated with w$\sim 200\mu$m beams, the rise time may be as short as 70ns with turn-on delays as short as 200ns, limited by acoustical wave propagation within the Piezoelectric crystal.

The alternative, which we have adopted more recently, is broadband EOMs. These devices may be used to put phase modulation sidebands on a laser at an arbitrary frequency from DC to 20Ghz, with the maximal sideband fraction ($\sim 34\%$ at modulation index 1.84) requiring only a few volts. These EOMs allow a sideband to be switched on or off with in less than a nanosecond, using an appropriately fast switch (CMCS0947 from Custom Microwave Components, with total latency of 3ns). The sideband extinction is limited by the RF-switch and hence may reach 60dB, or even better when used in conjunction with an AOM. The primary downside to this approach is that the carrier remains present even once the sideband is extinguished, often necessitating an AOM in series. Until recently, it seemed that using four modulators in an I-Q configuration was the only way to direct more than 34% of the power into a particular sideband (as dictated by FM theory). A recent paper from Kasevich et. al[58] demonstrated that by using a saw-tooth generated by a nonlinear transmission line one can put up to $\sim 90\%$ of the power into a particular sideband.

4.4 Fast Pulse Sequencing

For the majority of slow applications, standard National Instruments analog (PCI-6713) and digital (NI PCI-6534) output cards are used to control the experimental sequence. Our digital and digital output cards have a maximum resolutions of 50ns and 1μs, respectively. To update at this speed our sequences a)must be quite short (we run out of memory on the card) and b)take a long time to download to the card. As such we generally run the cards at a 500KHz update rate.

For fast applications we use the PulseBlaser ESR-Pro card from SpinCore Tech-

nologies. This card has a minimum pulse width of 2.5ns, with a resolution of 2.5ns as well[5]. Unlike the NI cards, it does not update on every clock edge- instead it updates only when a channel has an edge, and so requires much less memory. In fact it only has memory for about 8000 edges, but this is deceptive because it has built in facilities for looping structures which require very little memory. As such the maximum edge count is much higher, as long as the desired sequence is periodic, as it is in our case (Write-Read-Repump).

4.5   Photon Binning and Detection

For photon correlation measurements we use industry-standard P7888 card from FAST ComTec GmbH. Given a *start* trigger, the card then provides the times when pulses come in on each of four-channels. These channels are called *stop* triggers, but this is deceptive as the card can register an arbitrarily large number of stop triggers. In fact it stops detecting pulses only after a preset *total* time.

What makes this card special is its resolution. In two-channel mode, it provides a resolution of 1ns, and in four channel mode 2ns. Either of these timescales is much faster than the dynamics of the processes which we study, $\sim \Gamma^{-1} = 30$ns. All of the correlation functions and high-resolution time traces displayed in this thesis were obtained using this card, in combination with single-photon counting modules.

---

[5]The shortest *interval* between pulses is 12.5ns.

4.6   Experimental Sequence

The experimental sequence typically consists of loading the MOT for ~ 100ms, and then extinguishing the MOT and Repumper beams briefly while the quadrupole fields are switched off, and the bias fields zeroed. The MOT and repumper are then retuned to the appropriate frequencies for the Polarization Gradient Cooling, and turned back on at new intensities. The PGC runs for approximately 10ms after which the actual experiment on the now cold ($\sim 10\mu$K) Cs atoms may begin. After the completion of the experimental sequence the MOT and repumper lasers are retuned to the appropriate resonances for cooling and trapping, and the quadrupole fields are turned back on.

Chapter 5

High Brightness Source of Fourier-Limited Photon Pairs

Our group's first effort (prior to my arrival) to implement a Single-Photon source[7] resulted in a relatively high single-photon conversion efficiency of 44(3)%. However, because the cavity used for the experiment was nearly confocal, the phase matching condition permitted the "write" and "read" photons to be emitted into different transverse resonator modes[6]. This prevented us from verifying the single photon, or even non-classical character of the scattered fields. In spite of this, there was clear experimental evidence of readout phase matching (see figure (5.1)) as per equation (3.12), so it seems clear that the DLCZ physics of collective excitations was dictating the behavior of the system.

As detailed in chapter (4), among the many changes that were made in building the "new" apparatus was to install a new, non-confocal cavity. This chapter details our first successful efforts to generate non-classical light using an atomic ensemble within
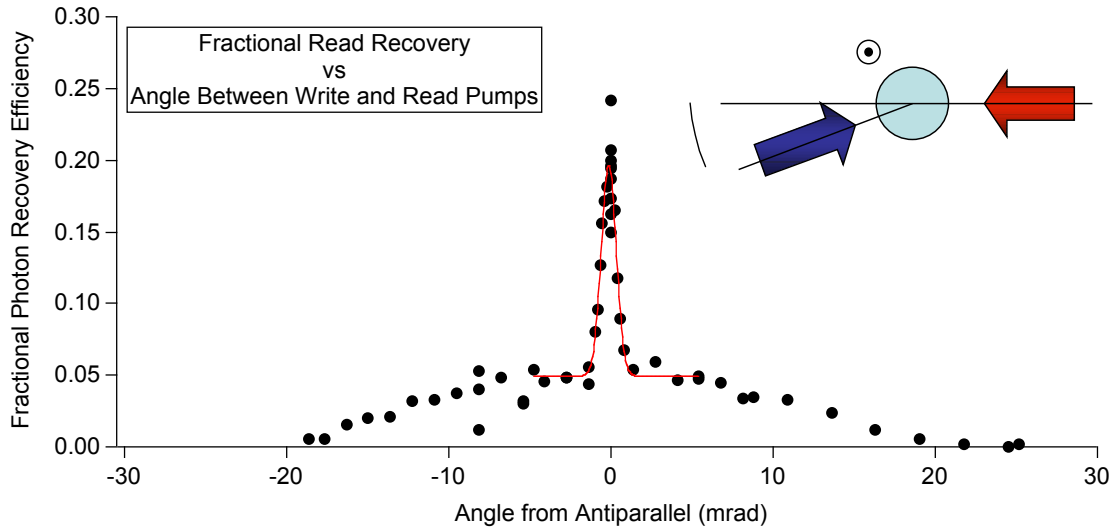
Figure 5.1: Phase matching between Write and Read pumps, for experiment in [7], with a near-confocal cavity. The observed $1/e^2$ half angle of $\phi = 0.9(1)$mrad is substantially less than the cavity TEM_{00} opening half-angle of $\lambda/\pi w_c = 2.7$mrad. This, in combination with the 10mrad pedestal, indicates emission into a superposition of higher-order cavity modes.

this cavity: A source of pairs of spectrally identical photons, of opposite polarization.

The work described here is the topic of the publication[118]:

- *J. K. Thompson, J. Simon, H. Q. Loh, and V. Vuletic, "A High-Brightness Source of Narrowband, Identical-Photon Pairs" Science 313, **74** (2006)*

5.1 Photon Pairs

Our source of photon pairs, taken as a black-box, has a lot in common with a type-II parametric downconverter: Incoming light is converted into pairs of photons which are spatially (type I/II)[109] and/or polarization (type II)[98] separated. These pairs are emitted at random (nearly) uncorrelated times, and are generated infrequently.

Parametric down-converters are solid-state, relatively simple, and stable. In contrast our source requires an atomic ensemble laser cooled to 10μK within a properly stabilized optical resonator, inside a high-vacuum chamber. What do we get for our efforts? *Spectral width of less than a MHz, and maximal spectral brightness.*

Some of the most exciting applications of single-photons and photon pairs are quantum communication and long distance entanglement generation[33, 71, 95]. For these applications it is very important that the photons be able to interact with atomic ensembles for storage and manipulation. As such, it is convenient to generate photons of bandwidth $\delta\nu_{BW} \leq \Gamma$, and for alkali atoms, $\Gamma \sim 2\pi \times 5$MHz. Without filtering, in the best case an SPDC will generate photon pairs with spectral widths of order nanometers[41]. There has been a lot of progress towards making narrower SPDC by spectral filtering and cavities[67, 106, 64]. The source in [64] produces pairs with a brightness 0.3pairs/(s MHZ mW), which at 1W of pump power is 300pairs/(s MHZ). As we will see, our source is much brighter.

Prior to our work, the Harris group at Stanford created a source very similar to ours, but in freespace [3]. Our results represent an improvement in retrieval efficiency and non-classical character of the generated light-field. Perhaps more importantly, we also characterized the spectral width of our source via heterodyne spectroscopy, and verified the indistinguishability of the photons via a Hong-ou-Mandel[54] interference experiment. A similar Hong-ou-Mandel experiment was performed by the Yamamoto group, using a quantum dot in a micro-pillar cavity[101] and since our work, has been demonstrated in freespace atomic ensemble[40, 16] and ion[79] experiments.

5.2   Photon-Pair Generation Procedure

An atomic ensemble is optically pumped such that all of the atoms are in some initial state $|G\rangle$. They are weakly driven to Raman-scatter on the $|G\rangle \to |E\rangle \to |F\rangle$ transition. There is another laser incident on the atoms in $|F\rangle$ which induce them to rapidly Raman scatter back to $|G\rangle$ through an auxiliary excited state $\left|\tilde{E}\right\rangle$.

In the case of an optically thin sample in free-space, this arrangement would have the effect of causing atoms to infrequently scatter "write" photons into freespace, and then rapidly scatter corresponding "read" photons into freespace. Already this is a source of pairs, but unfortunately it is very difficult to collect photons scattered into 4π, and so an attempt to measure correlations, except in the case of *extremely* weak drive strengths[1] would fail.

Addition of a cavity, even one with $\eta \ll 1$, may increase the optical depth of the sample to > 1. While the write photons are only emitted into the cavity with a probability $\approx \eta \ll 1$, the read photons experience a collective enhancement for scattering into the cavity mode, as long as the "write" and "read" pumps are counter-propagating. All the atoms which scattered write photons into freespace do *not* create collective excitations, and so they scatter into freespace in the read process as well. We now have a device which randomly (and infrequently) generates "write" photons scattered into the cavity detection mode, and then immediately generates corresponding "read" photons into the same spatial mode.

As mentioned previously, this process also works in freespace[3], but requires many

---

[1]In which case we would have to accumulate statistics forever, and would still find our signal ruined by detector dark counts
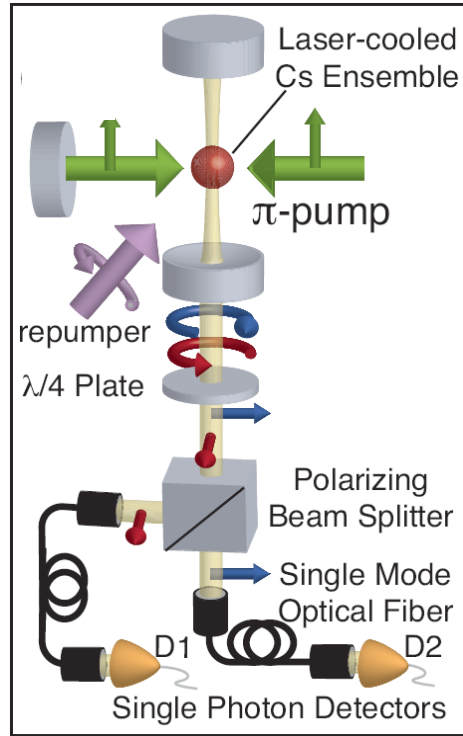
Figure 5.2: Quantum states used for photon pair generation. The π-pump frequency is chosen so that the write scattering rate is suppressed relative to the readout rate due to the large detuning from resonance. This allows the source to operate in a regime of well-separated pairs and large cross correlation. Optical pumping is realized with a combination of the π pump and a σ polarized beam on the $F_g = 4 \rightarrow F_e = 4$ transition.

more atoms and/or higher densities. As such, effects like backgrounds due to imperfect optical pumping and lensing of the read-out photon due to high optical depth impose limitations on performance which do not impact our cavity-enhanced source until a much higher quality source is required, as described in chapter (6).

5.3 The Basic Experiment

A schematic of our experimental apparatus is shown in figure (5.2). A MOT of approximately 10^6 Cesium 133 atoms (rms size $\sim 500\mu$m) is trapped across the waist of a near-confocal cavity with waist $w_c = 110\mu$m, and Finesse $\mathcal{F} = 250$. The cavity length is $L_c = 66.18$mm, resulting in an FSR $\delta\nu_{FSR} = \frac{c}{2L_c} = 2265$MHz, and a cavity linewidth $\frac{\kappa}{2\pi} = \frac{\delta\nu_{FSR}}{\mathcal{F}} = 8.6$MHz. These numbers lead to a peak cooperativity at an anti-node, on the strongest transition ($|4,4\rangle \rightarrow |5,5\rangle$) of $\eta_{peak} = \frac{24\mathcal{F}}{\pi(kw_c)^2} = 3\times10^{-3}$, and hence a maximal single-atom vacuum Rabi frequency of $\frac{g}{2\pi} = 0.36$MHz. Additionally, to increase the detection-path quantum efficiency we chose to make our cavity asymmetric, with the mirror on the detection side having ≈ 33 times more transmission than the mirror on the locking side. This had the affect of making photons scattered into the cavity 33 times more likely to leak out on the detection side rather than the locking side. The round-trip power loss of $\sim 1.4\%$ limits the cavity out-coupling efficiency through the high-transmission mirror to 45%.

Once the quadrupole fields have been turned off and the atoms are polarization gradient cooled to 10μK, we are left with approximately 10^4 *effective* atoms[2] within the waist of the cavity.

We apply a small 1mG bias field along the cavity ($\hat{z}$) direction to define a quantization axis. For 100μs, atoms are optically pumped into $|F_g = 3, m_F = -3\rangle$ with a combination of a π-polarized pump beam on $F_g = 3 \rightarrow F_e = 2'$, and a σ^--polarized pump beam on $F_g = 4 \rightarrow F_e = 4'$. This pumping scheme has dark states in

---

[2]Where the effective atom number is the number of atoms that there would be if all atoms sat at anti-nodes of the cavity field, along the axis of the cavity.

$|F_g = 4, m_F = -4\rangle$, $|F_g = 3, m_F = -3\rangle$, and $|F_g = 3, m_F = 3\rangle$. The $|F_g = 3, m_F = 3\rangle$ state is unstable in the sense that, after a few off-resonant scattering events to $F_g = 4$, the atoms will be driven to $m_f < 0$. The population ratio between the remaining $F_g = 3$ and $F_g = 4$ dark-states is determined by the relative off-resonant scattering rates (and hence beam intensities) and polarization impurities. We adjust these parameters to ensure that $\sim 80\%$ of the atoms remain in $F_g = 4$. This leaves an optical depth $N\eta \approx 1.5$ in $F_g = 3$. Shelving a majority of the atoms in $F_g = 4$ has the effect of reducing the average heating rate per atom, allowing us to run the experiment longer without re-collecting and re-cooling the sample.

We have verified and optimized the quality of the optical pumping by de-pumping the $F = 4$ fraction to $F = 3$ and driving a state-selective microwave transition at ~ 9.2GHz between $F_g = 3 \rightarrow F_g = 4$. The number of atoms transferred to $F_g = 4$ is then detected via fluorescence on the $F_g = 4 \rightarrow F_e = 5$ cycling transition. A better-than-average example, shown in figure (5.3), reveals $\sim 95\%$ of the atomic population if $|F_g = 3, m_F = -3\rangle$. This high quality optical pumping is made possible, at least in part, by the low single-pass optical depth of the sample $OD_1 \approx \frac{N\eta}{\mathcal{F}/2\pi} = .3$ for $N\eta \approx 10$. If the sample substantially absorbs and re-scatters the optical pumping beam it can become very difficult to optically pump it without detuning from resonance, which in itself degrades the quality of the optical pumping due to off-resonant scattering from other levels.

The wonderful thing about this particular setup is that the optical pumping process *produces* the photon pairs. Having pre-pumped the system, we just continue to run the optical pumping process for an additional 2ms, only now we analyze the light
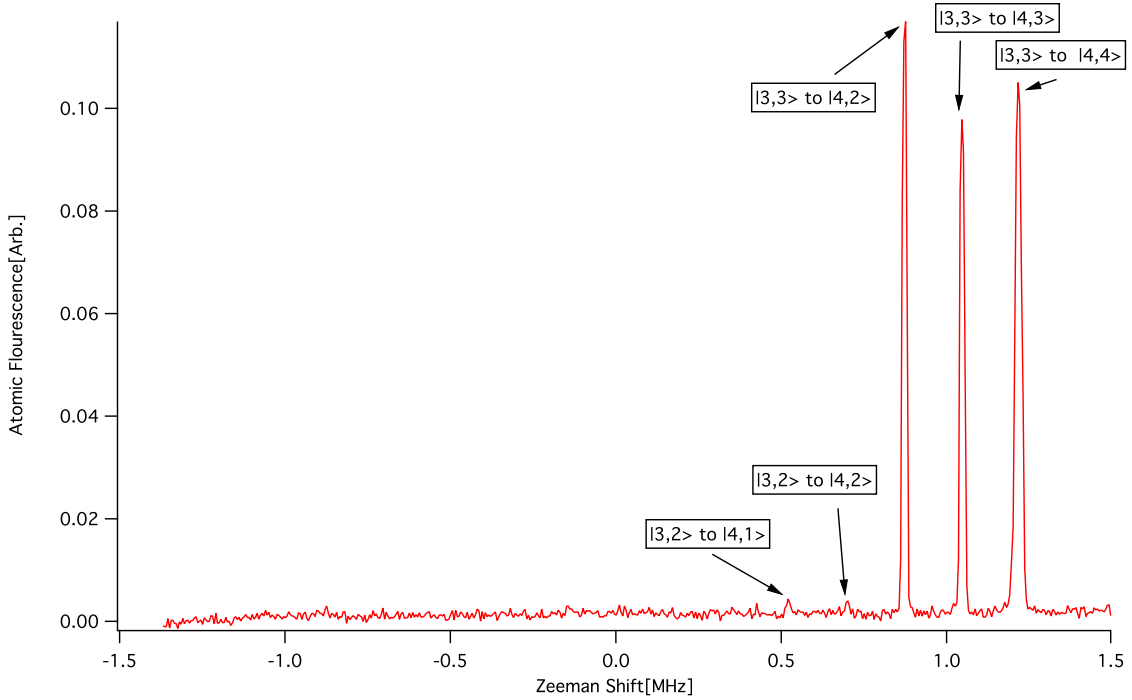
Figure 5.3: Optical Pumping Diagnostic with Microwaves. All atoms are depumped from F=4, and then Zeeman-state selective microwave transitions are driven between $F = 3$ and $F = 4$ ground state hyperfine manifolds at ~ 9.2GHz. Any transferred atoms are detected via fluorescence on the $F_g = 4 \rightarrow F_e = 5$ cycling transition. This sequence is repeated as the microwave detuning is scanned. We observe three peaks, corresponding to the three allowed transitions from $|F = 3, m_F = 3\rangle$. The lack of other peaks indicates that there are very few atoms in other states.
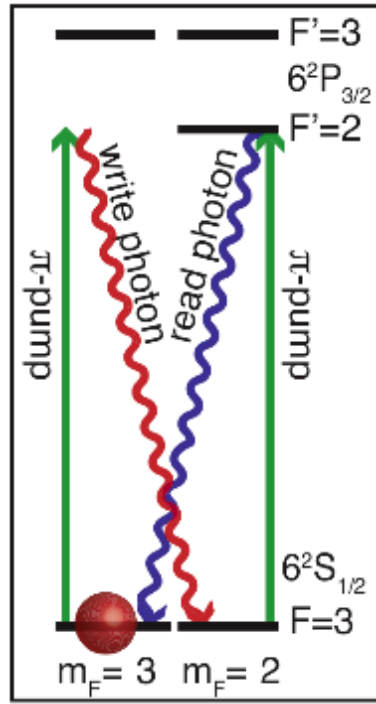
Figure 5.4: Quantum states used for photon pair generation. The π-pump frequency is chosen so that the write scattering rate is suppressed relative to the readout rate due to the large detuning from resonance. This allows the source to operate in a regime of well-separated pairs and large cross correlation. Optical pumping is realized with a combination of the π pump on $F_g = 3 \to F_e = 2'$ and a σ polarized beam on $F_g = 4 \to F_e = 4$.

scattered into the cavity. The initial state for the pair source is $|F_g = 3, m_F = -3\rangle$, and the cavity is tuned to the $F_g = 3 \leftrightarrow F_e = 2'$ resonance. Because the atoms begin in a dark state, they may only leave the state via off-resonant scattering[3] (off of $F_e = 3$). The write photons are the result of this *slow* $|3, -3\rangle \rightarrow |3', -3\rangle \rightarrow |3, -2\rangle$ Raman process. A write-photon scattered into the cavity produces a magnon, which is then immediately, collectively, and resonantly read out via cavity scattering on the $|3, -2\rangle \rightarrow |3', -2\rangle \rightarrow |3, -3\rangle$ Raman transition (see figure (5.4)). For the readout to be collective the "read" beam must counter-propagate relative to the "write" beam. This is achieved by retro-reflecting the write beam[4].

Because the "write" and "read" scattered fields have opposite circular polarizations, we separate them with a quarter wave-plate and a polarizing beam-splitter (PBS). The output of this PBS is coupled into two single mode fibers, which run to the single photon counting modules which are connected to a P7888 1ns resolution multiple-event time digitizer (from Fast Comtec GmbH), as detailed in chapter (4).

A quick check revealed that if the write- and read- pumps are not counter-propagating, the phase-matching of the process is broken, and the pairs are no-longer scattered into the cavity. In contrast to the data for the old confocal setup (figure (5.1)) which contained a narrow peak on a wide pedestal arising from the multi-mode nature of the emission process[6], with our new non-confocal cavity we observe only a single, slightly broader peak, without any pedestal to speak of (see figure (5.5)).

One might also worry that the quality of the source might be limited by imperfect

---

[3]In fact minimization of the scattering rate into the cavity is precisely the way that we fine-tune the bias field to lie along the π-pump beam.

[4]This would have been convenient anyway, as it ensures that the atoms are not pushed out of the cavity mode by the optical pumping process.
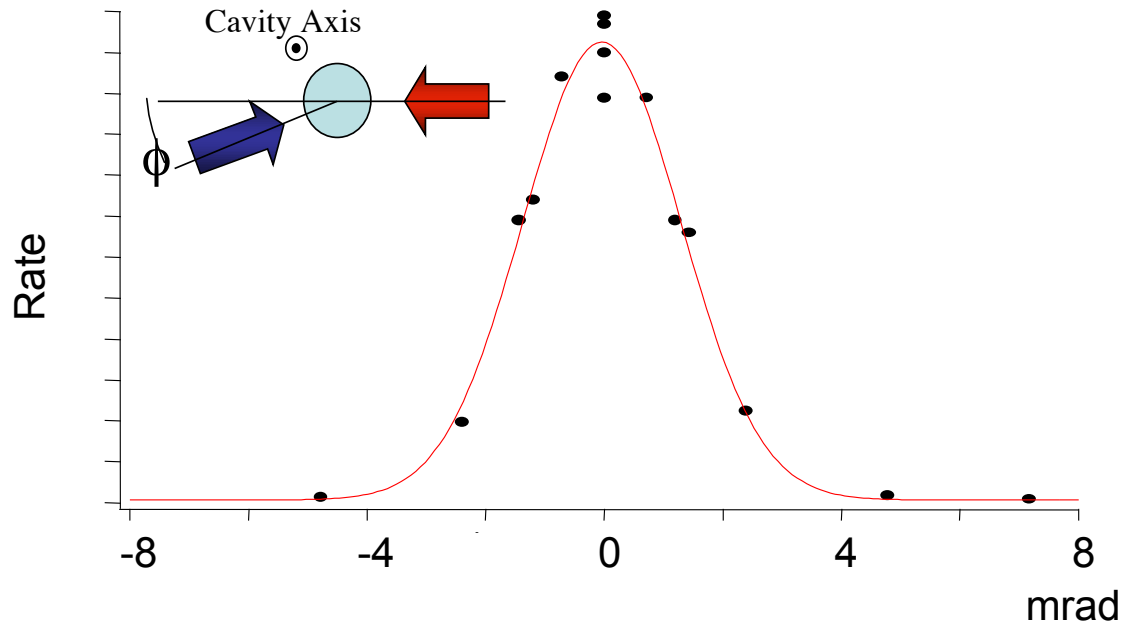
Figure 5.5: Phase matching between Write and Read pumps for our new, non-confocal cavity. The observed $1/e^2$ half angle of $\phi = 2.7$mrad, in reasonable agreement with the cavity TEM_{00} opening half-angle of 2.5mrad. The lack of a broad pedestal, in combination with the peak width corresponding to the TEM_{00} opening angle, indicates that phase matched emission proceeds into only a single mode of the cavity. It is slightly surprising that this data is clean, as it was taken for pump-powers corresponding to above-threshold four-wave mixing, where one might expect abrupt onset of the laser-like process.

optical pumping: Because the atoms on $|F_g = 3, m_F = 2\rangle$ scatter resonantly, and those in $|F_g = 3, m_F = 3\rangle$ scatter only off-resonantly (at detuning $\Delta_{32} = 150\text{MHz}$), it might seem that even $\epsilon \approx (\frac{\Gamma/2}{\Delta_{32}})^2 \approx 3 \times 10^{-4}$ imperfection in the optical pumping would result in as many write photons coming from atoms in $m_F = 2$ as from atoms in $m_F = 3$. We work at sufficiently high off-resonant write scattering rates, however, that the resonant transition is saturated, resulting in many fewer photons scattered from imperfectly pumped atoms than might be expected from the naïve low-saturation calculation.

5.4 $g_{wr}(\tau)$ and the Cauchy-Schwarz Inequality

Given that we are claiming to have built a source of photon pairs, it is interesting to look at the probability of getting a "read" photon at some particular delay τ after a "write" photon, compared to the unconditioned probability of getting a read photon. Quantum mechanically, this quantity is given by[5]:

$$g_{wr}(\tau) \equiv \frac{\langle :I_w(t)I_r(t+\tau): \rangle_t}{\langle I_w \rangle_t \langle I_r \rangle_t} \tag{5.1}$$

5.4.1 Beyond the Classical Limit

One might hope that $g_{wr} > 1$ indicates that the light is correlated beyond the classical limit, however this is not the case. Imagine a two classical light beams, both of which are off for long periods of length $T_{off} = (1 - \epsilon)T_{tot}$, and then on for brief periods of length $T_{on} = \epsilon T_{tot}$, as in figure 5.6. One may easily show that for

---

[5]We write the expressions in terms of intensities I_x rather than photon numbers n_x just to indicate the classical analog of the measured quantity.
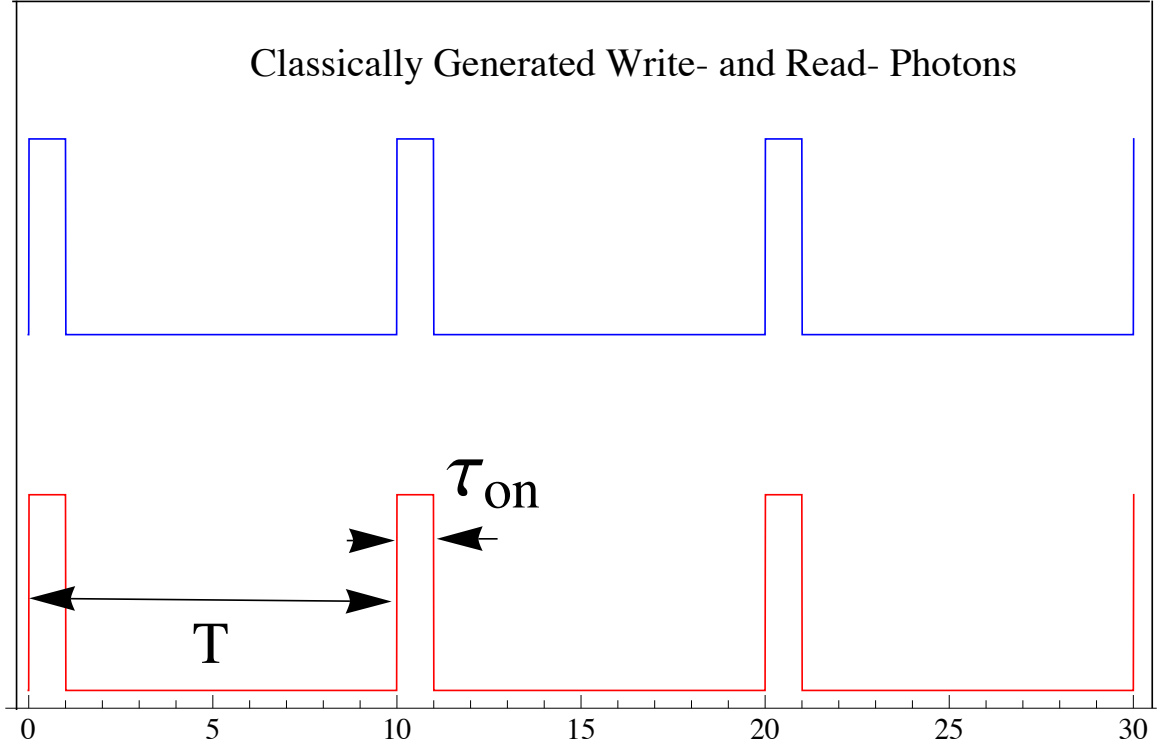
Figure 5.6: The classically controlled laser intensity wave-forms (generated for example by AOMs), one shown in orange, and the other in blue, correspond to a cross-correlation $g_{wr} \gg 1$, indicating that $g_{wr} > 1$ is *not* proof that light is non-classical.

$|\tau| < T_{tot}/2$ (and repeating with period T_{tot}):

$$g_{wr}(\tau) = \frac{1}{\epsilon} \begin{cases} 1 - |\tau/T_{on}| & \text{if } |\tau| < T_{on} \\ \\ 0 & \text{otherwise} \end{cases} \tag{5.2}$$

As such, even *classical* correlation will produce $g_{wr}(\tau) > 1$. The key point is that it will also introduce classical fluctuations into each of the two beams separately: $g_{rr}, g_{ww} > 1$. Using the Cauchy-Schwarz inequality[21] we can show that for any real valued functions of time $I_w(t)$, $I_r(t)$, we must have:

$$\langle I_w(t) I_r(t) \rangle_t^2 \leq \langle I_w(t) \rangle_t^2 \langle I_r(t) \rangle_t^2 \tag{5.3}$$

Quantum mechanically we need only add the normal ordering operators, and we are

then left with (after a bit of algebra):

$$G \equiv \frac{g_{wr}(\tau)^2}{g_{ww}(0)g_{rr}(0)} \leq 1 \tag{5.4}$$

For the example given above, $g_{ww}(0) = g_{rr}(0) = \frac{1}{\epsilon}$, so $G = 1$, and we see that, as expected, the classical fluctuations do *not* violate this inequality.

5.4.2 Extracting $g_{wr}(\tau)$ from the Measurement Record

The aforementioned expressions are idealizations of what one can hope to measure in practice, in the sense that they describe measurements made with infinite timing resolution, and ensemble averaging.

In reality, we assume that our system is ergodic and replace ensemble averages with time averages. It bears mention that the quantum-classical inequalities thus far derived are valid even when ensemble averages are replaced with time averages.

We handle the finite timing resolution by computing all correlation functions into time bins whose size is typically denoted T. The 1ns resolution of our detectors/counting card is *more* than sufficient to observe all dynamics, as we are limited our atomic excited-state lifetime $\Gamma^{-1} \approx 30$ns, and more importantly our cavity lifetime[6] of $\kappa^{-1} \approx 19$ns.

Specifically we have:

$$g_{\alpha\beta}(\tau, T) = \frac{\sum_j \left\{ N_j^\alpha N_{j+\lfloor \tau/T \rfloor}^\beta - \delta_{\alpha\beta}\delta_{\lfloor \tau/T \rfloor, 0}(N_j^\alpha)^2 \right\}}{\sum_j N_j^\alpha \sum_j N_j^\beta} \tag{5.5}$$

---

[6]It might seem that a process which inserted a photon in the cavity, and removed it faster than κ^{-1} would be visible in the field which leaks out of the cavity, but in this continuous-mode experiment, this is not the case. The reason is that the *write* photon will be stored in the cavity for a time period of order κ^{-1}, which means that the g_{wr} will, unavoidably, be smeared out by that much.

Here N_i^μ is the number of photons detected by detector μ during time bin[7] i and $\lfloor \tau/Y \rfloor$ rounds Y down to the nearest (smaller) integer. The second term fulfills the normal ordering requirement and, as it can be seen, eliminates double-counting issues. As we have seen, however, the 50ns dead-time of the SPCM's is far too large for it to be practical to measure zero-time autocorrelations with a single detector– as such the second term in equation (5.5) is basically always irrelevant.

5.4.3 Interpretation as a Source of Pairs

A high-quality cross correlation measurement from our apparatus is shown in figure 5.7. This data was collected at a write photon scattering rate of $0.01/\mu$s detected, implying $0.2/\mu$s into the cavity, due to detection path efficiency of $q = 0.053(8)$ [8]. From this data it is clear that the readout dynamics require a time of approximately (50ns) to read out the majority of the excitation, though of course full readout takes somewhat longer.

We found these first data to be particularly exciting because they show real quantum dynamics[9]! The agreement with theory is quite good. One can show that in the absence of backgrounds, the maximum g_{wr} is given by $g_{wr} \approx \frac{T_{pair}}{\tau pair}$, where T_{pair} is the average time between pairs (at the source), and τ_{pair} is the width of the bi-photon wave-packet ($\tau_{pair} \approx 50$ns, typically). For the given rate of write-photon generation,

---

[7]As determined from the measurement record stored by the P7888 counting card.

[8]This efficiency includes SPCM quantum efficiency of 0.40, cavity out-coupling of 0.45, fiber coupling efficiency of 0.75.

[9]It is true that these dynamics are the same as those predicted by the Maxwell-Bloch[121] equations. In other words, even a classical excitation would be read out in this way. As we will see shortly, however, this data definitely corresponds to a single, quantized excitation being read out.
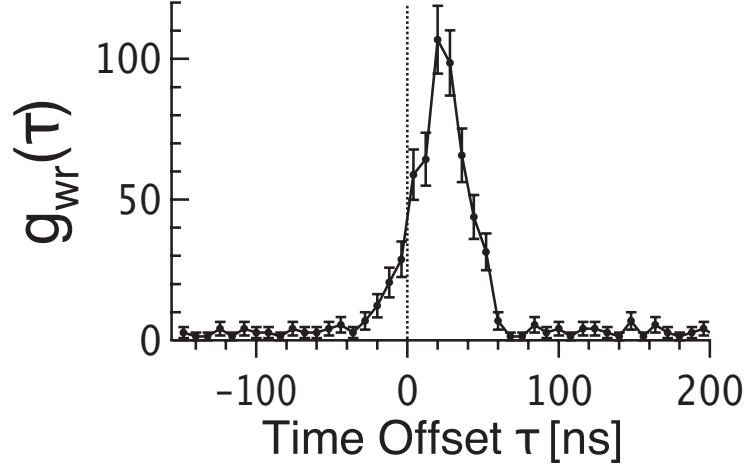
Figure 5.7: The cross correlation $g_{wr}(\tau)$ reflects the rate of detecting a read photon at a time $t + \tau$, given that a write photon was detected at time t. This rate is normalized to the unconditional rate of detecting read photons. The tail at negative time reflects the fact that the write photon may be stored in cavity for a time κ^{-1}, resulting in the read photon detection prior to the write photon detection.

$T_{pair}^{-1} \approx .2/\mu s$, we expect $g_{wr} \approx 100$. In this data set we see $g_{wr} \approx 60$, within a factor of two of the prediction.

We can analyze the data another way, noting that the ratio of the resonant, collective readout rate to the off-resonant write scattering rate ought to set an upper limit on the observable g_{wr}. The write rate is $R_w = N\eta \frac{\Omega_w^2}{4\Delta^2} \Gamma \frac{b_w^2}{b_r^2}$, and the read rate $R_r = N\eta \frac{\Omega_r^2}{\Gamma(1+N\eta)^2}$, with $b_w^2 = \frac{5}{7}$ and $b_r^2 = \frac{3}{16}$ the branching ratios for the write and read processes, respectively, and $N\eta$ the optical depth for the read process. We can now estimate $g_{wr} = \frac{R_r}{R_w} = \frac{1}{(1+N\eta)^2} \left(\frac{\Delta}{\Gamma/2}\right)^2 \frac{b_r^2 b_{rp}^2}{b_w^2 b_{wp}^2}$. For $N\eta = 7$, and $\frac{b_{rp}^2}{b_{wp}^2} = \frac{189}{80}$ is the ratio of the pump couplings, we find $g_{wr} \approx 91$. In fact the highest g_{wr} we observed in this experiment (see figure (5.7)) was ≈ 100, in good agreement with this number. To achieve a higher g_{wr} we would actually have to *reduce* the optical depth of the sample!

The high cross-correlation makes it likely that the pairs are in fact non-classical,

and not a result of classical fluctuations in the system. To be certain we must violate the Cauchy-Schwarz inequality equation (5.4). To do so we must measure the much more time consuming auto-correlations. The cross correlation $g_{wr}(\tau)$ is relatively quick to measure because the write and read photons come in pairs, and so detection of a write photon indicates a read photon is likely. In contrast the autocorrelation measures the coincidence rate for two write photons or two read photons. These are only slightly correlated, as determined either by the thermal motion of the atoms[72] which yield $g_{ww} = g_{rr} = 1 + e^{-\tau/\tau_c} \leq 2$, or classical fluctuations in atom number and beam intensity. It is for this reason that the autocorrelation SNR's are substantially worse than those of the cross correlations.

The auto-correlations and Cauchy-Schwarz inequality violation factor G are plotted in figure (5.8) versus binsize, rather than time offset, for improved statistics. It is clear that as the binsize is increased beyond the size of the bi-photon wavepacket, the g_{wr} drops, and so the G-factor drops. As it is, the peak value of the G factor, at $T = 60$ns, is $G = 760^{2100}_{320} \gg 1$, indicating a *tremendous* violation of the inequality. The enormous error-bars arise from the poor statistics in g_{ww} and g_{rr}. The method to properly compute the median value and confidence intervals of the observed quantities in the presence of very few counts is left for appendix (C). For comparison, the original pulsed source from the Kimble group[91] achieved $G = 292(57)$, while the Harris group achieved[3] $G \sim 400$.
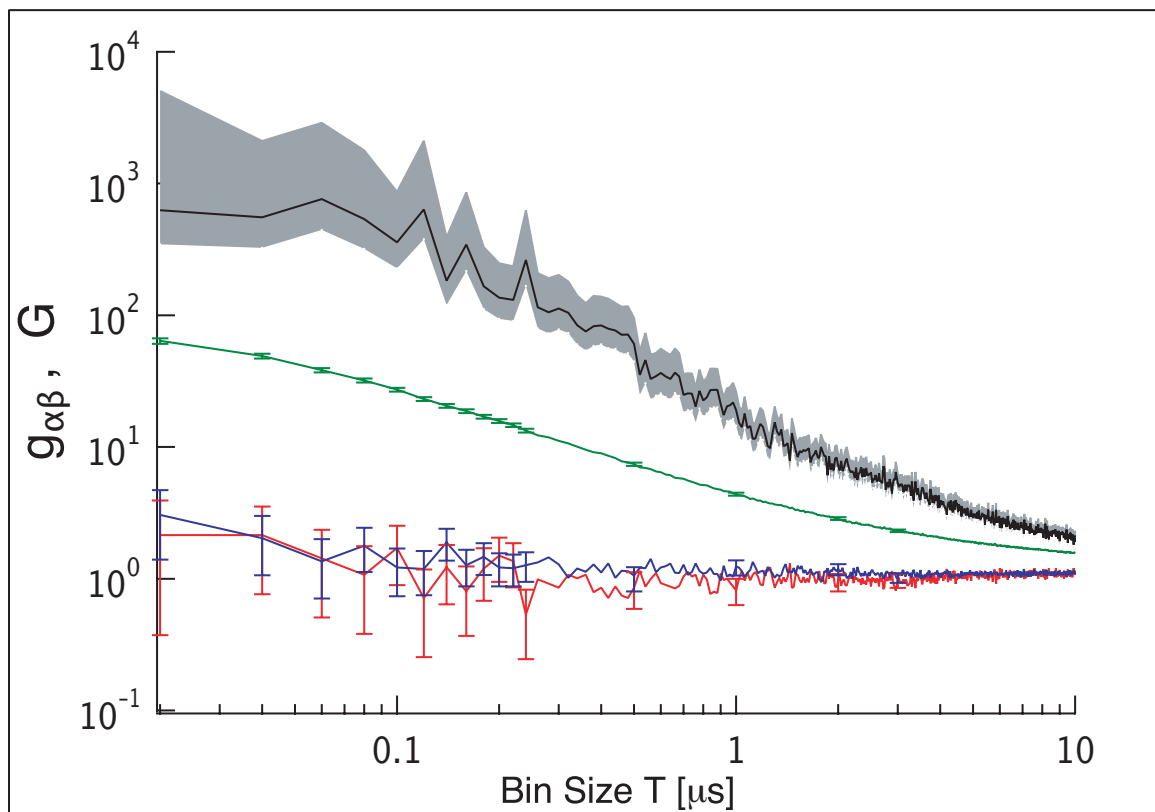
Figure 5.8: The cross and auto correlations versus binsize are plotted in green, red and blue, respectively. The ratio G is plotted in black, with grey confidence interval. $G > 1$ is the region of non-classical twin-beam squeezing, and extends beyond $10\mu s$.

5.4.4 Time-Dynamics of Readout

Included in figure (5.9) is a model curve resulting from time evolution of the three-level hamiltonian model (3.17). including additionally the effect of the storage of the write-photon in the cavity mode.

In contrast with the time-separated write-read schemes discussed in chapter (3), the read bin timing is set by the write photon arrival, and not the turn-on of the read beam. This is a fundamental difference between continuous and pulsed schemes. The general way to handle this sort of effect using Quantum Monte Carlo is to consider the full system dynamics, including write and read cavity modes, both before and after the write photon has leaked from the cavity and been detected. Because the read dynamics are entirely unaffected by the presence of the write photon within the cavity we must simply interfere all indistinguishable paths that provide write and read photons separated in time by τ:

$$P(\tau, r|w) \propto \left| \frac{2}{\kappa} \int d\tau_w e^{-\frac{\kappa}{2}\tau_w} A_r(\tau + \tau_w) \right|^2 \tag{5.6}$$

Where $A_r(\tau)$ is the time-dependent amplitude for a corresponding read process with a well-defined start time (as is the case in a pulsed scheme), according to equation (3.17).

One consequence of this expression is that $P(\tau < 0)$ is not necessarily zero, meaning that the read photon may arrive before the write photon! Since this expression embodies the storage of the write photon within the cavity mode, this is not surprising: there is a non-zero probability that the write photon will be stored so long in the cavity mode that it comes out *after* the read photon. This is borne out by the $\tau < 0$ tail in the data.
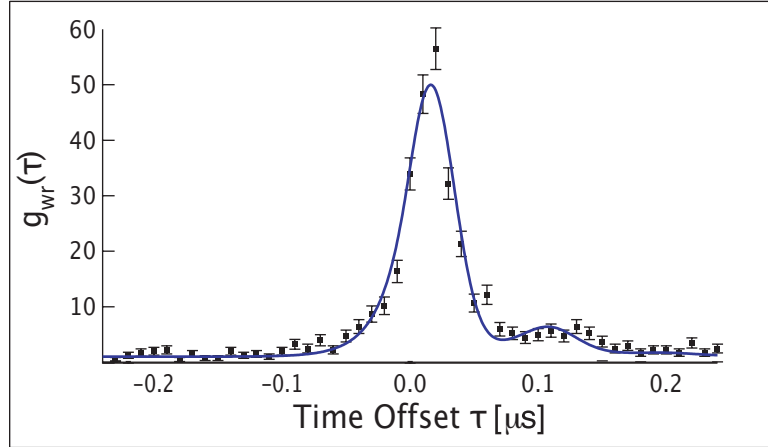
Figure 5.9: The cross correlation between write and read scattered fields g_{wr} is plotted versus delay time τ, including a curve of fit arising from a 3-level dynamical model. The Rabi-flopping, as well as $\tau < 0$ behavior, are captured by the model.

The convolution may also be understood in Fourier space, in which case it acts as a spectral filter of the bi-photon wavepacket of width κ. This has the benefit of further suppressing the bright state components of the readout, and improving the spectral purity of the source.

As can be seen from the overlap of the model curve with the data, the three-level approximation is a very good one. Even the Rabi-flopping of the read photon into and out of the cavity is evident in the data.

We are generating pairs at a rate of 5×10^4pairs/s. As will be seen shortly, the pairs have a spectral width of order $\sim$ 1MHz, yielding a spectral brightness of 5×10^4pairs/(s MHz), which is more than 2 orders of magnitude brighter than the brightest contemporary SPDC source[64], with a brightness, as mentioned previously of 3×10^2pairs/(s MHz).

5.5 Interpretation as a Single Photon Source

We have just seen that that our source produces read photons which are highly correlated in time with corresponding write photons. It would be natural to claim that *conditioned* upon the detection of a write photon, there ought to be precisely one read photon emitted, and to think of our system as a heralded source of single read photons. To determine to what extent this claim is true, we need to ask two questions:

- What is the mean number of read photons that come out, conditioned upon a write photon?

- What is the distribution of read photon numbers emitted in the read-field? Specifically, what is $g_{rr|w}$?

The first question is answered by integrating the readout probability up over time, with the integral centered near the write photon (on the peak of the cross-correlation). This integral is plotted, versus integrated bin size, as the inset to figure (5.10). The linear slope arises from uncorrelated backgrounds, and the offset is the "single photon" readout efficiency χ that we are looking for[10]. Correcting for detection-path losses, the recovery efficiency is $\chi = .57(9)$. For comparison, the Harris pair source[3] has an extracted[11] single photon retrieval efficiency of $\chi \leq 0.10$.

---

[10]Of course thus far we only know that it corresponds to the *mean* number of photons emitted in the readout process. $g_{rr|w}$ will tell us how much of this arises from the single photon component.

[11]We estimate $\chi \approx (g_{wr}^{peak} - 1)(R_s \delta T_{gwr})$, where R_s is the quoted stokes rate of $180 \times 10^3/$s, $g_{wr}^{peak} = 20$, and $\delta T_{gwr} = 20$ns is the temporal width of the biphoton peak as given in the Harris paper.
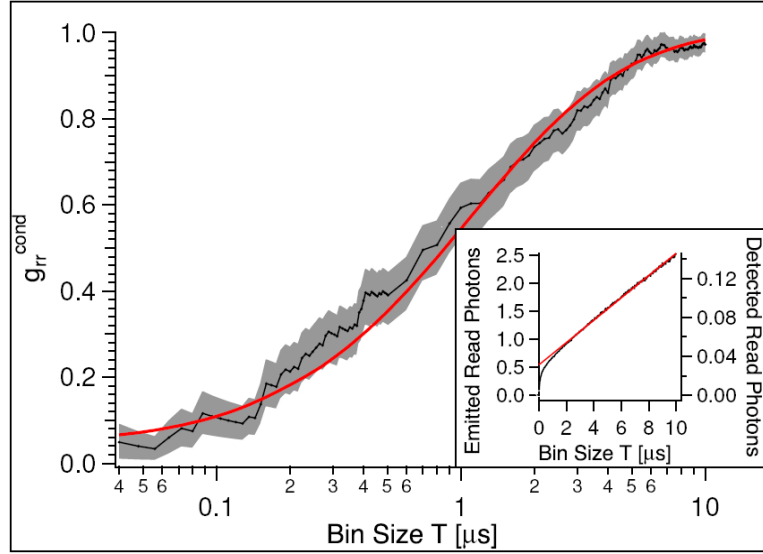
Figure 5.10: Characterization of the heralded single photon source. $g_{rr|w}$ and (**inset**) probability of generating a read photon, given the detection of a write photon. Both data-sets are plotted versus bin size T. The minimum value of $g_{rr|w} = 0.03(3 \ll 1)$ indicates a factor of ~ 30 suppression of 2 read-photon events compared with the expectation from the 1 read-photon rate, and hence highly non-classical light. The large T slope of the retrieval curve indicates the background (uncorrelated) read rate, while the extrapolated Y-intercept reflects the retrieval efficiency of $R_c = 0.57(9)$, referenced to within the cavity.

To answer the second question, the auto-correlation of the read-beam (versus bin size, with the bins centered on the peak of $g_{wr}(\tau)$, at $\tau = 20ns$), conditioned upon the detection of a write photon is plotted in figure (5.10), along with a model arising from the corresponding g_{wr}. The minimum value of this $g_{rr|w}$, for a bin of size $T = 60$ns, is $g_{ww|r} = 0.03(3)$, computed using the more accurate methods from appendix (C). In the absence of any backgrounds other than those from other write-read pairs, $g_{rr|w}$ ought to be given by $g_{rr|w} \approx 2g_{ww}n_w \approx 0.052(6)$, which agrees with the measured value[12]. Our measurement is thus consistent with nearly all backgrounds arising from other pairs!

Our 57% retrieval efficiency requires a nearly 200ns bin, as qualitatively evident from the timescale over which the recovery curve in figure (5.10) approaches the large T asymptote. In the interest of comparing apples to apples, we will analyze $g_{rr|w}$ into the same binsize, which yields $g_{ww|r}(T = 200ns) \approx 0.21(6)$. Combining these numbers we estimate $P_0 = 0.34$, $P_1 = 0.57$, $P_2 = 0.04$.

One might be tempted to claim that $g_{rr|w} \ll 1$ is evidence that the twin-beam squeezing process generates anti-bunching by *suppressing* background counts. In fact the behavior is more accurately understood as the conditional addition of a single photon with temporal wavepacket short compared to R_b^{-1}, the background rate. This means that for short times after the write photon, the added single photon dominates the statistics of the light, and we observe $g_{rr|w} \ll 1$. For longer times the (Poissonian distributed) backgrounds begin to overwhelm the single photon count, and $g_{rr|w}$ rises towards unity.

---

[12]If, as before, we take $g_{ww} = 2$, as per [72].
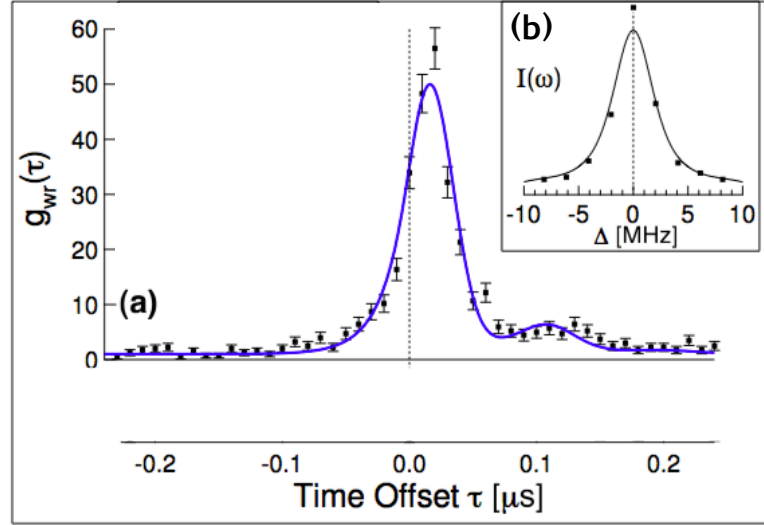
Figure 5.11: Estimate of photon linewidth from the FFT of cross correlation. In the limit that the photon pairs are Fourier limited, the biphoton linewidth may be estimated from the fourier transform of the square root of the cross correlation function. (a)A characteristic cross-correlation $g_{wr}(\tau)$ data-set, and Fourier transform $\mathcal{F}(\Delta)\{\sqrt{g_{wr}(\tau) - 1}\}$ (b). The fourier transform indicates a linewidth of ≈ 2MHz.

5.6   Bi-Photon Linewidth

For QIP applications it is very important to know how spectrally broad the photons are. There is a lower limit set by time-frequency uncertainty: Taking the Fourier transform of $\sqrt{g_{wr}(\tau) - 1}$, and squaring it, as shown in figure (5.11), gives an estimate of this limit as ≈ 2MHz.

Actual measurement of the write- or read- photon bandwidths is more involved. The idea is to beat the scattered write- or read- photons with a picked-off portion of the pump-beam, and look at the spectral properties of the resulting beat-note. We frequency shift the pump-beam with a fixed frequency AOM before beating to move the signal out of any possible $1/f$ backgrounds. This detection technique technically measures the mutual linewidth of the scattered field and the pump beam. So long as

the pump beam is well-stabilized in an absolute sense, we may interpret beat-note as a measurement of the absolute linewidth of the photons.

5.6.1 Heterodyne Detection

One might hope to measure the linewidth via a simple heterodyne setup with a standard avalanche photodiode (see figure (5.12a)). The problem with this approach is that in order to have a signal which is larger than the technical (Johnson) noise of the photodiode we will need the strong beam to be shot-noise limited, requiring at least nanowatts of strong-beam power (onto an Avalanche photodiode), to be compared with $\sim 700 attowatts$ (~ 20KHz detected rate) of signal power! The result is that we are completely buried in the technical intensity noise of the strong beam. It is really amazing how many sources of noise there are in the lab when you are looking for such a small signal. We attempted to chop between background subtraction and signal measurement on a few second timescale, but even this only won us an order of magnitude, leaving us far from being able to see our signal of interest.

5.6.2 Balanced Heterodyne Detection

An alternate approach is the so-called "balanced heterodyne detection" method[108], shown in figure (5.12b). It is a heterodyne technique to suppress the technical noise of a strong beam by measuring the difference signal between beat-notes measured on the two output ports of a beamsplitter. The intensity noise of the strong beam has the same phase on both detectors, while the beat-signal has opposite phase owing to the $\frac{\pi}{2}$ phase difference between transmission and reflection. This method requires
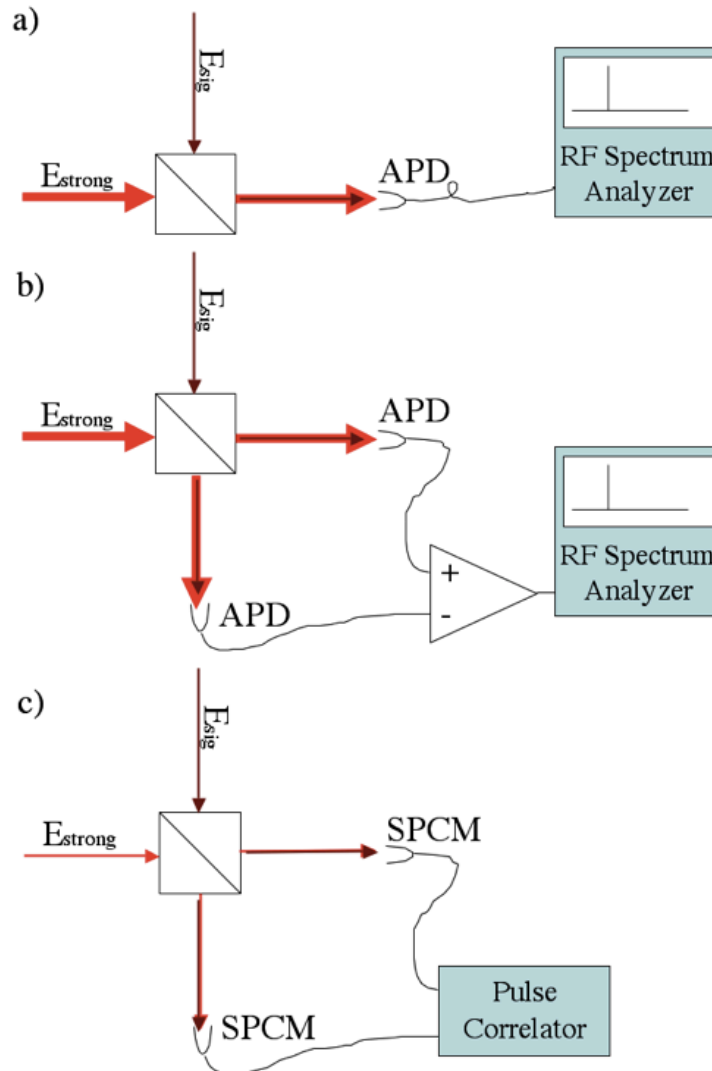
Figure 5.12: Heterodyne Spectroscopy. The spectral bandwidth of an optical signal is determined by measuring the electrical spectrum of its beat-note with a strong beam, as measured on a photodiode. The strong beam is frequency shifted to move the signal away from the 1/f noise of the detector. **(a)**Heterodyne spectroscopy performed with a single detector requires a lot of power in the strong beam to ensure that the beat signal is not buried in the detector Johnson noise. This leaves the system highly sensitive to classical intensity noise of the strong beam. **(b)** Balanced heterodyne spectroscopy may be performed by taking the difference between the two detectors, and hence canceling out the strong beam technical intensity noise while enhancing the beat signal. **(c)** Single Photon heterodyne spectroscopy is performed by replacing the two detectors with two SPCMs, whose technical noise (dark counts) is quite low, permitting much lower strong-beam intensities (on the order of the intensity of the signal beam), and hence much less sensitivity to laser technical intensity noise.

very sensitive balancing of the gains and phases of the two paths in order to achieve good suppression of technical noise at the frequency of interest.

5.6.3 SPCM-based Heterodyne Detection

It seems likely that the balanced heterodyne approach would have worked quite well, but we chose an alternate approach. By detecting the beat-signal on *both* output ports of the combining beam splitter with SPCMs, we were able to have detection noise of order 500counts/second, as determined by the SPCM dark count rates. Because the detector noise was low, we did not need to compete with it to generate the beat-note, so the so-called "strong" pump-beam could be comparable in intensity to the signal beam. By going to higher intensities there was a factor of 2 in SNR to be won, but saturation of the SPCM's and data analysis time were enough reason *not* to go to higher intensities.

The SPCM-based Heterodyne Detection setup is shown in figure (5.12c). One may show that the cross correlation function between the two detectors $g_{AB}(\tau)$ has a term which varies at the offset frequency between the two beams, and is proportional to $E_{sig}(t)E_{sig}^*(t+\tau) \propto g_1(\tau)$, which is the fourier transform of the spectrum of the light. As such the procedure is to compute the cross-correlation between the photon detection records of the two SPCM's and fourier transform it to arrive at a power spectrum. The data are shown in figure (5.13), and indicate write and read photons each with a fitted bandwidth of 1.1(2)MHz, offset from one another by approximately 1MHz. This offset likely arises from a combination of differential Zeeman- and Stark-shifts of the relevant ground states ($|3, -3\rangle$ and $|3, -2\rangle$), We have now satisfied one
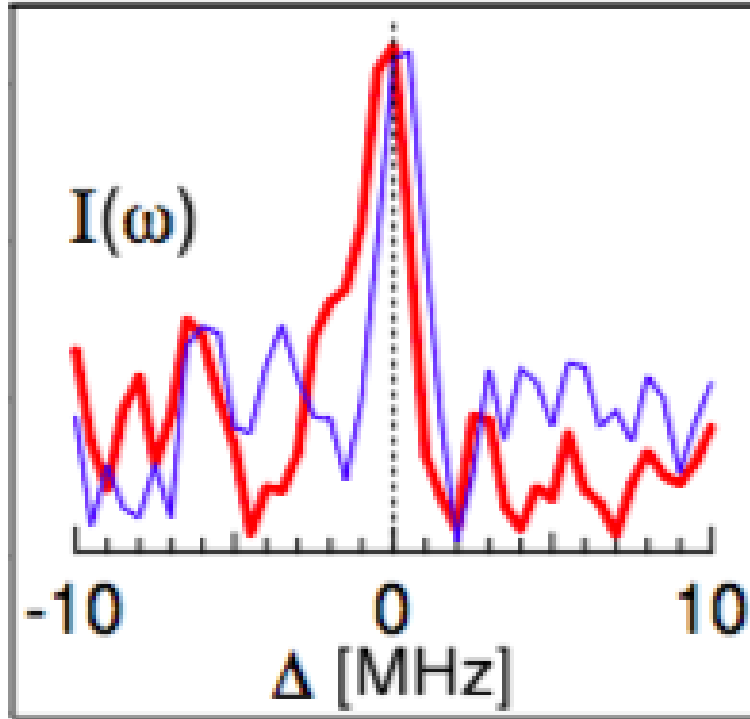
Figure 5.13: Measured spectra of write- and read- scattered fields. Each field is (separately) beat against a frequency offset pump field, and detected on a pair of SPCMs in a Hanbury-Brown Twiss[62] setup. This square root of the power spectrum of the cross correlation between the two detectors $\sqrt{|\mathcal{F}(\Delta)\{g_{wr}(\tau)\}|^2}$ reflects the frequency spectrum of the beat-note, and hence the frequency spectrum of the optical field (assuming that the pump beam is stable)

of the primary goals we set out to accomplish: a source of single photons or pairs which is sufficiently spectrally narrow to interact resonantly with the Cs atomic line of linewidth $\Gamma = 2\pi \times 5$MHz.

One might wonder why it is preferable to use two SPCM's rather than computing the autocorrelation of one SPCM. For photons with a linewidth of 1MHz, the oscillations of the auto- or cross- correlation decay with a $1/e$ time of ~ 160ns. It is clearly unwise to discard 50 of those nanoseconds because of detector dead-time. It does bear mention that the particular configuration shown here isn't *quite* a Hanbury-Brown

Twiss setup, as there is a signal coming in on what ought to be a dark part of the cube. One could in principle use a second cube, after the combining cube, to split the signal to the two detectors. This would have the effect of inverting the oscillations in the cross-correlations and decreasing the signal to noise, but would otherwise not affect the outcome.

5.7 Photon Indistinguishability and the Hong-Ou-Mandel Dip

The heterodyne measurement from the previous section revealed that the write- and read- photons have similar spectral properties, in spite of a small frequency offset. Had this measurement been taken for long enough to acquire very good statistics it would provide very clear information about how close to identical the write- and read- photons are. Here we present an alternate approach which probes distinguishability more directly.

The Hong-Ou-Mandel dip[54] is a well known phenomenon that occurs when two otherwise indistinguishable photons impinge simultaneously on the two input ports of a beam splitter (see figure (5.14)). One can easily show that in this situation *both* of the photons will leave through either one output port of the beam splitter, or the other, but that they will never leave via different ports. We now derive this effect in the single-mode approximation.

The Hong-Ou-Mandel Dip
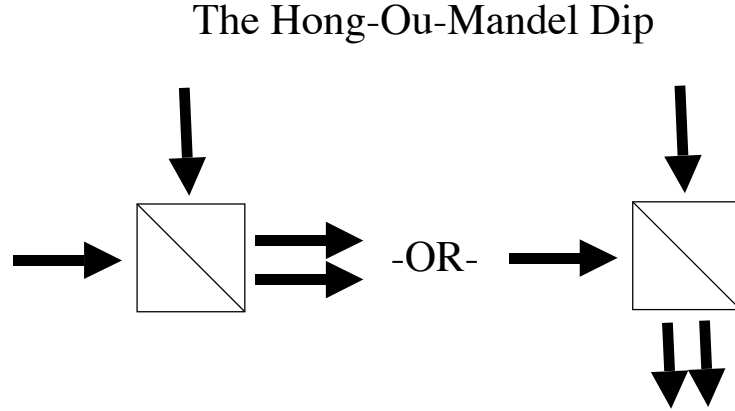
Figure 5.14: A Schematic of the Hong-Ou-Mandel effect. Identical photons are simultaneously incident on the two ports of a non-polarizing beam-splitter, and both photons will emerge from one port or the other– due to a quantum interference effect at the beamsplitter the photons never go in opposite directions.

5.7.1   HOM Dip: Single Mode Approximation

If $a^\dagger$ and $b^\dagger$ create photons in the input modes, then the initial state of the field is:

$$|\psi\rangle = a^\dagger b^\dagger |\Omega\rangle \tag{5.7}$$

That is, there are photons in each of the two input modes. Here $|\Omega\rangle$ is the vacuum state. Using the beamsplitter relations for a $50:50$ beamsplitter, equation (3.27), whose output modes are $c^\dagger$ and $d^\dagger$ reveals that $|\psi\rangle$ may be written as:

$$|\psi\rangle = \frac{1}{\sqrt{2}}(c^\dagger + d^\dagger)\frac{1}{\sqrt{2}}(c^\dagger - d^\dagger)|\Omega\rangle = \frac{1}{2}(c^{\dagger 2} - d^{\dagger 2})|\Omega\rangle \tag{5.8}$$

Which is says that either *both* photons leave through one port of the beam splitter, or *both* leave through the other port, but there is no situation in which the two photons leave through opposite ports!

5.7.2   HOM Dip: Continuous Mode Limit

Where does this derivation go wrong if the two photons are distinguishable? The answer is that if $a^\dagger$ and $b^\dagger$ create photons of different frequencies then we should really add a frequency subscript to each creation operator, and then when we apply the beam-splitter relations we will see that the terms with different frequencies commute through one another:

$$
\begin{aligned}
|\psi\rangle &= a^\dagger_{\nu 1} b^\dagger_{\nu 2} = \frac{1}{\sqrt{2}}(c^\dagger_{\nu 1} + d^\dagger_{\nu 1})\frac{1}{\sqrt{2}}(c^\dagger_{\nu 2} - d^\dagger_{\nu 2})\,|\Omega\rangle \\
&= \frac{1}{2}[(c^\dagger_{\nu 1} c^\dagger_{\nu 2} - d^\dagger_{\nu 1} d^\dagger_{\nu 2}) + (d^\dagger_{\nu 1} c^\dagger_{\nu 2} - c^\dagger_{\nu 1} d^\dagger_{\nu 2})]\,|\Omega\rangle
\end{aligned}
\tag{5.9}
$$

The interesting point is that when $\nu 1 = \nu 2$, the second pair of parenthesized terms vanishes! This is the heart of the Hong-Ou-Mandel effect: There are two different ways that we may end up with a photon in the $c^\dagger$ arm *and* a photon in the $d^\dagger$ arm, and they destructively interfere (due to phase accrued on reflection, compared to transmission) when the photons in the two input arms $a^\dagger$ and $b^\dagger$ are indistinguishable!

Now suppose that we analyze the HOM-dip for a pair-source like ours. Let us consider a bi-photon wave-packet with mean arrival time T created by the operator[13]:

$$
\alpha^\dagger = \int_{-\infty}^{\infty} d\tau\, A(\tau) a^\dagger_{T+\tau/2} b^\dagger_{T-\tau/2}
\tag{5.10}
$$

Now consider the interference of these photons on a 50:50 beamsplitter. Applying the standard beamsplitter relations and taking advantage of symmetries yields:

$$
\alpha^\dagger = \frac{1}{2}\int_0^\infty d\tau\, \Big(A(\tau)[c^\dagger_{T+\tau/2} c^\dagger_{T-\tau/2} - d^\dagger_{T+\tau/2} d^\dagger_{T-\tau/2}] + [A(\tau) - A(-\tau)]\, d^\dagger_{T+\tau/2} c^\dagger_{T-\tau/2} \Big)
\tag{5.11}
$$

---

[13]The form given here really needs to be integrated over T, weighted by the pump beam waveform, to be correct. This form is not ad-hoc– it is the most general bi-photon wave-packet which satisfies conservation of energy. If you are uncomfortable with *time* creation operators, replace them with $x = ct$ creation operators, where x is the displacement along the detection fiber at a fixed time.

This expression makes the physics clear: Coincidences between the two detectors can be suppressed by a destructive interference between the Feynman paths corresponding to the write photon arriving earlier, and the read photon arriving earlier. In other words– if no distinction can be made between the write and read photon arrivals then there will be a destructive interference in the cross-correlation even for a finite time separation. The auto-correlations will be correspondingly increased, such that the total probability $|A(\tau)|^2 + |A(-\tau)|^2$ is conserved.

To relate $A(\tau)$ to measurable quantities, it is a simple matter of considering the cross-correlation between the write- and read- paths without interference on a beam-splitter, and we see that $g_{wr}(\tau) \propto |A(\tau)|^2$. After the interfering beamsplitter we expect $g_{CD}(\tau) \propto \left| \frac{A(\tau)-A(-\tau)}{2} \right|$. Assuming that the phase of $A(\tau)$ arises primarily from a frequency difference Δ between write and read photons, we may then posit that:

$$
\begin{aligned}
g_{CD}(\tau) &= \frac{1}{4} \left| \sqrt{g_{wr}(\tau)} e^{I\Delta\tau} - \sqrt{g_{wr}(-\tau)} e^{-I\Delta\tau} \right|^2 \\
&= \frac{1}{4} \left(g_{wr}(\tau) + g_{wr}(-\tau) - 2 \cos 2\Delta\tau \sqrt{g_{wr}(\tau) g_{wr}(-\tau)} \right) \quad (5.12)
\end{aligned}
$$

Agreement of the observed HOM cross-correlation $g_{CD}(\tau)$ with this functional form would be a strong indication that any distinguishability of the two photons arises only from a fixed frequency different between them, and temporal asymmetry of the bi-photon wavepacket.

In our actual experiment, the HOM dip was most conveniently observed by analyzing the photons in the H/V basis instead of the σ^+/σ^- basis. This change is affected by rotating the analysis QWP by 45°. Upon passage through the analysis QWP, the σ^+ polarized write photon is transformed into a 45° linearly polarized pho-
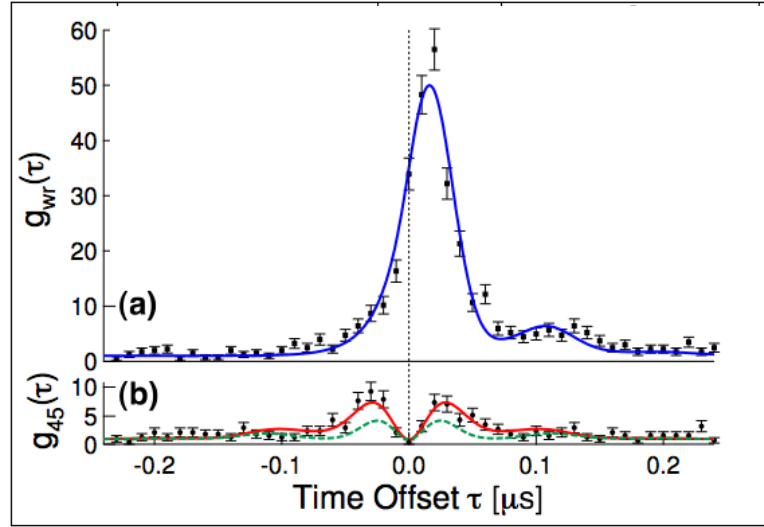
Figure 5.15: A characteristic cross-correlation data set (a), and corresponding Hong-Ou-Mandel interference of the photons (b), measured by rotating a waveplate such that the "write" and "read" photons interfere on a PBS.

ton, and the σ^- polarized read photon is transformed into a $-45°$ linearly polarized photon. The beam splitter relations transforming the $+/-45°$ linear polarizations of a single port of a PBS into the two output ports of the PBS are *identical* to the relations transforming the two (identically polarized) input ports of a non-polarizing beamsplitter to the two output ports. Thus we see that a change of basis is all that is necessary to change our apparatus from measuring $g_{wr}(\tau)$ to measuring $g_{CD}(\tau)$.

The observed cross-correlations, along with predictions coming from equation (5.12) are shown in figure (5.15). For the HOM prediction to fit the data, we need a frequency difference $\Delta = 3\text{MHz}$, in contrast to the 1MHz frequency difference measured by heterodyne spectroscopy. This discrepancy may well come from slightly different experimental parameters for the two measurements. Other than the frequency difference, the remaining coincidences arise from the asymmetry of $g_{wr}(\tau)$ with respect to $\tau = 0$. That is to say that if two two photons come separated in time

by more than the cavity write-photon storage time of $\kappa^{-}1 = 19$ns, it is fairly clear which photon is the read photon and which is the write photon- the earlier one is the write, and the later the read. As such the indistinguishability, and hence the HOM suppression, are destroyed.

Given that the mean delay between write- and read- photons is of order ~ 20ns (as is clear from figure (5.15), a fiber delay line of ~ 4m length in the write path, before an appropriate non-polarizing beam-splitter, would be make the wave-packet overlap as good as it could be, given the frequency difference. We did not try this for technical reasons: One then becomes sensitive to polarization drifts in the fibers, and beamsplitter losses, among other things.

The waterfall plot shown in figure (5.16) shows the continuous variation of cross- and -auto correlations as the detection QWP is rotated. This data shows the transition from weak write-write correlations when the write- and read- photons are polarization separated, to strong write-write bunching when the write- and read- photons are interfered. It is clear, also, that there is some pollution of the g_{ww} and g_{rr} data, arising from imperfect polarizer alignment, and hence HOM effect. This may have contributed to the larger-than-expected cross $g_{ww,rr}(\tau = 0)$ in the Cauchy-Schwarz inequality data.

For data collected at higher pump power (see figure 5.17), and hence faster read-out, the wavepacket becomes more symmetric about $\tau = 0$, and we have observed suppression of the coincidence rate below the fully distinguishable (classical) limit of $\frac{1}{2}$ by as much as 90% into a 5μs bin. We refer to this as 90% indistinguishability.
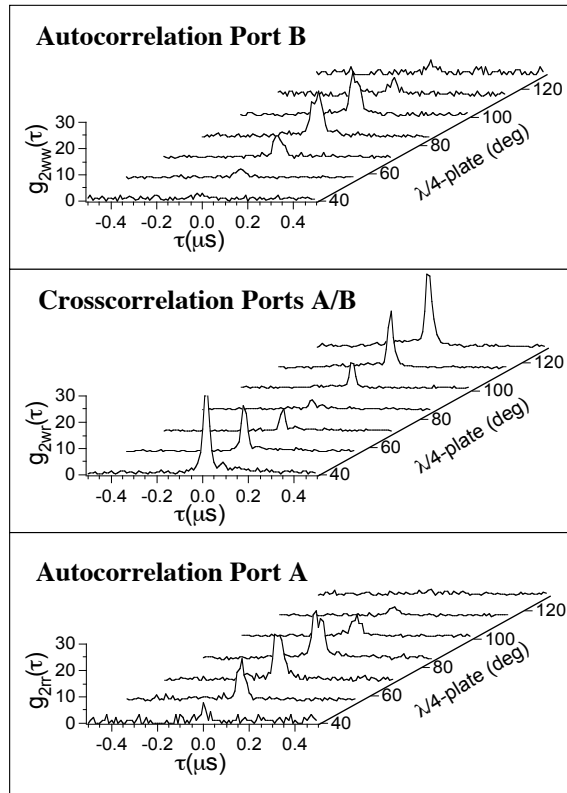
Figure 5.16: **(b)**Cross- and **(a,c)**Auto- correlations of the "write" and "read" detection paths, versus the angle of the $\lambda/4$ plate before the PBS. Rotation of this plate permits us to change continuously from a Write-Read configuration to a Hong-Ou-Mandel dip configuration. At wave plate settings where cross-correlation between the "write" and "read" paths is small, the autocorrelations of both paths are large, indicating that the photons do, indeed choose to leave the PBS in the same direction.
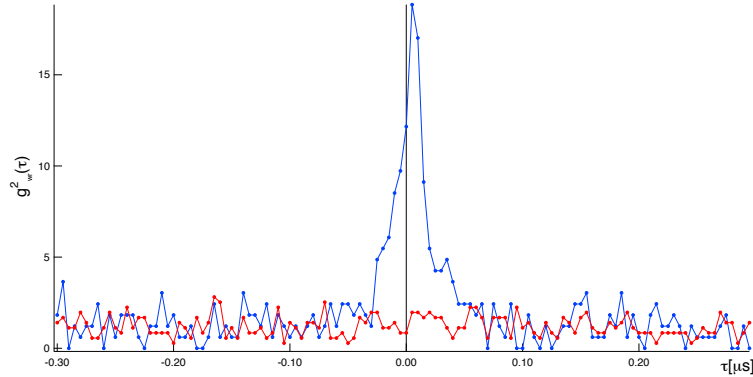
Figure 5.17: Cross correlation in polarization separating- and Hong-Ou-Mandel dip-configurations, demonstrating extremely good suppression of coincidences in the Hong-Ou-Mandel dip configuration. This results from the fast readout of the read-photon, and hence good symmetry of the $g_{wr}(\tau)$ about $\tau = 0$.

5.8   Conclusion and Outlook

This experiment was beautiful owing both to its clean results and for its relative simplicity. The same retro-reflected laser acts as write, read, and optical pumping beams! This simplicity, however, was also a curse, in that it reduced our ability to vary parameters. We would have liked to operate at lower write rate to observe a higher g_{wr}, but turning down the pump strength impacted both the read rate, as well as the quality of the optical pumping[14]. As just discussed, turning *up* the read rate was helpful for observing a better Hong-Ou-Mandel dip, but doing so also increased the write rate, and so decreased g_{wr}. Some degree of control was available in adjusting the total atom number, but even this changed a number of things at the same time (write rate, number of imperfectly pumped atoms, and readout cooperativity). It became clear to us that from here, the most sensible thing to do was to go to a

---

[14]The more fiendish effect is that when the pump beam intensity is reduced the impact of imperfectly pumped atoms *increases*: The atoms in $m_F = 3$ scatter less, while those in $m_F = 2$ are saturated and continue to scatter at the same rate.

more sophisticated system where atom number, optical pumping quality, and write and read rates could be independently tuned, which led us naturally to our next experiment.

Chapter 6

High Efficiency Single Photon Source

High quality single photons are important for linear optics quantum computing[63], quantum networking[34], and beyond. There are a large variety of single-emitter systems available which can provide highly non-classical light with $g_2 \ll 1$. However, achieving high collection efficiency, and strong, reversible coupling for narrowband photons has proven quite difficult, and for many applications it is necessary to achieve all at once.

Effective collection solid angle may be enhanced by way of an optical resonator. This technology has been demonstrated for Rydberg atoms[76], quantum dots[38], trapped ions[59], and single neutral atoms[66, 82]. In particular, McKeever et al. have successfully demonstrated strong coupling between a single atom and a single photon within a high-finesse cavity- this work required sensitive and difficult stabilization of an optical resonator to better than $\frac{\lambda}{4 \times 10^5}$, as well as localization of the trapped atom

to an antinode of the cavity field.

The natural question, then, is how strongly one can couple a collective excitation to an optical cavity. The average nature of the collective coupling means that atoms need not be so carefully localized, and the collective enhancement relaxes finesse requirements compared to single-atom systems. Contemporary free-space collective excitation experiments[20, 36, 15, 3] exhibit single photon retrieval efficiencies at or below 50%. Even feedback techniques, which enhance the *unconditional* retrieval efficiency[40, 17], cannot enhance this efficiency beyond the conditional retrieval efficiency. Given the relatively high readout efficiency of our pair source, we now turn to the question of *what* precisely limited that efficiency, and how high we can hope to push it with proper engineering.

We will discover that by using appropriately large beams nearly co-propagating with the cavity axis, carefully chosen strong transitions, and high-quality optical pumping, we can realize a source of single photons with $g_{rr|w} \ll 1$, and near-unity retrieval efficiency. The small angle between the resonator mode and the pump beams will permit us to observe magnons with long ($23\mu s$) and short (230ns) lifetimes, corresponding to long- and short- wavelength spin-waves. This lifetime measurement, in combination with studies of the read-pump frequency and sample-location dependence of magnon readout efficiency will reveal the details of the spatial structure of the stored magnon.

Many of the things that we have learned, as well as the details of the high-efficiency single photon source that we built, are described in the publication[114]:

- *J. Simon, H. Tanji, J. K. Thompson, and V. Vuletic, "Interfacing Collective*

Atomic Excitations and Single Photons" Phys. Rev. Lett. **98**,*183601 (2007)*

6.1 Overview

The work discussed thus far has treated collective excitations in one of two ways. The first is very qualitative, considering the collective scattering as arising from constructive interference of the wavelets generated by phased up dipole radiators. The second is very formal and idealized, focusing on strongly coupled manifolds of highly symmetric many-atom Hamiltonians. The reality is much messier. Among the complications investigated experimentally and theoretically are:

- Doppler Decoherence: Between the write-in and the read-out, the atoms move around both due to recoil from the write-scattering, and due to their non-zero temperature.

- MOT Location Dependence: The excitation is read out into a different longitudinal mode of the cavity than it was written into, having different spatial structure.

- Inhomogeneous Couplings: The different atoms experience different coupling coefficients to the cavity modes and pump beams, owing to the finite spatial extent of the atomic sample, pump beams, and cavity modes.

- Lensing: The cavity has higher order transverse modes to which the collective excitation may attempt to couple.

We will discover in studying these issues that in fact they are all necessary to obtaining a fundamental understanding of what a collective excitation is, and how it behaves. Proper control of these effects is crucial for reaching high retrieval efficiencies. In the process of learning to build a better source of single photons, we will also demystify the magic behind collective excitations in cavity QED.

Most of the complexity described above may be categorized as inhomogeneity of one type or another. We will address each of the preceding effects from two distinct angles. The first is a qualitative approach, wherein we understand the effect of inhomogeneity as restoring which-path information (and the corresponding failure of the quantum eraser), leading to suppression of collective enhancement. The second approach employs many-body quantum mechanics to actually compute the impacts of the various types of inhomogeneity dynamically. The former approach will typically give us the scaling of the behavior, while the latter will provide us with more precise numbers to which we can compare our data.

Finally, we will briefly address the purely technical concerns of the impact of imperfections in optical pumping, beam polarizations, and field alignments. Choice of atomic transitions for the write-in and read-out schemes determine how sensitive we are to each of these imperfections.

6.2 Experimental Setup

We came to realize that in order to investigate the behavior of our system more carefully, it would be most convenient to switch to a pulsed, hyperfine-storage, scheme. By "pulsed scheme" we mean that rather than running continuously, the "write" and

"read" lasers are pulsed on and off, one after the other. A scheme of this sort has the advantage the write- and read- pulses may have their power, frequency, and timing separately controlled. This will permit us to measure memory coherence time, as well as the frequency dependence of the write-in and readout processes. Additionally, a pulsed scheme allows for a temporally distinct optical pumping period which may also be independently controlled, hopefully permitting even higher quality optical pumping of the atomic sample. By using a scheme in which the write-in and read-out processes both change hyperfine ground-states, backgrounds due to imperfect optical pumping may be suppressed, as hyperfine pumping is *much* easier than Zeeman pumping. Zeeman pumping nonetheless remains crucial for the experiment, for reasons that will be discussed below.

The experimental setup is shown in figure (6.1). We begin with a MOT, turn off the quadrupole fields, and apply PGC, is described in chapter (4). We then apply a 1.8 G bias field perpendicular to the resonator axis, and transfer the atoms into the internal state $|G\rangle = |F = 3, m_F = 3\rangle$ via dark-state optical pumping along the $\vec{B}$-field, employing a σ^+ polarized beam on $F_g = 3 \rightarrow F_e = 3'$ and the (effectively unpolarized) MOT beam on $F_g = 4 \rightarrow F_e = 4'$. The beam on $F_g = 4 \rightarrow F_e = 4$ must be unpolarized to ensure that all atoms in $F_g = 4$ are depumped to $F_g = 3$.

The write and read beams come from separate lasers, each frequency stabilized relative to the reference through a frequency offset lock. Both have a waist $w_p = 300\mu$m, propagate at a small angle $\theta = 2°$ relative to the resonator axis (see figure (6.2)), and are linearly polarized along the bias field (ie π-polarized). The write pump, at a typical intensity of 70mW/cm^2, is applied for 60ns with a detuning of

Figure 6.1: Schematic of the setup used for this experiment. The counter-propagating write- and read- beams propagate at a small angle of $\sim 2°$ degrees relative to the cavity axis to allow for a short-wavelength, long-lifetime component of the magnon. The small B-field, perpendicular to the write- and read- pump beam propagation directions, defines a quantization axis for optical pumping.
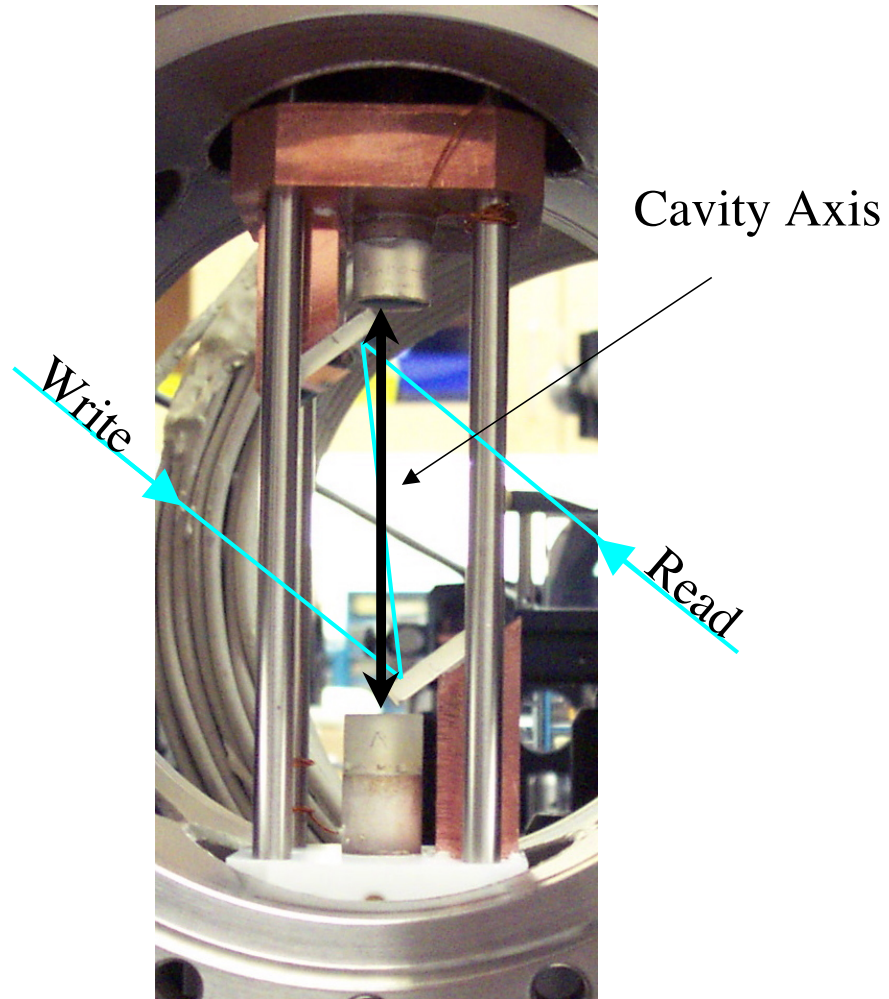
Figure 6.2: Photograph of the apparatus used for the experiment. The beam paths of the write- and read- beams are highlighted. These beams utilize the small-angle mirrors to propagate nearly along the cavity axis, at an actual angle of $\sim 2°$.

$\Delta_w = 2\pi \times -40\text{MHz}$ from the state $|E_w\rangle = |F_e = 4, m_F = 3\rangle$. With some small probability, a "write" photon is scattered into the resonator, by spontaneous Raman scattering on the $|G\rangle \to |E_w\rangle \to |F\rangle$ transition to which the resonator is tuned (here $|F\rangle = |F = 4, m_F = 3\rangle$). Detection of this "write" scattering event heralds the creation of a magnon, which may be super-radiantly read out into the resonator at a later time, via the application of a counter-propagating read pump beam on the $|F\rangle \to |E_r\rangle \to |G\rangle$ transition ($|E_r\rangle = |F_e = 3, m_F = 3\rangle$). The read pump is turned on in 100ns, with a maximum intensity of 7W/cm^2, with a detuning of $\Delta_r = 60\text{MHz}$ relative to the $|F\rangle \to |E_r\rangle$ transition (see figure (6.3)). This detuning is chosen such that the scattered read photon may be emitted into another longitudinal mode of the resonator, four free-spectral ranges of away[1]. The write, read, optical-pumping process is repeated 800 times per MOT cycle of 100ms.

For this experiment we use between 10^3 and 10^6 atoms within the optical resonator, corresponding to a variable read-process optical depth ranging from $N\eta = 0.1$ to $N\eta = 200$. Here $\eta = \frac{24\mathcal{F}}{\pi k^2 w_c^2} \times c_r^2$ is the peak single-atom cooperativity, corrected for the reduced dipole matrix element (coupling coefficient) of the read-out process.

The resonator used for this experiment is the very same one as used in the pair-source, except that in the intervening year the mirrors became coated with Cs. The resonator is 6.6cm long, with a TEM_{00} waist $w_c = 110\mu\text{m}$, finesse $\mathcal{F} = 93(2)$, and line-width $\kappa = 2\pi \times 24.4(5)\text{MHz}$. The mirror transmission M_1 and M_2, and round-trip cavity loss L for $\lambda \approx 842\text{nm}$, are $M_1 = 1.18(2)\%$, $M_2 = 0.039(2)\%$, and $L =$

---

[1]Given the detuning and power of the read beam, the effective saturation parameter of the read beam is $p = \frac{I^r/I_s}{1+(\delta_{la}^r/\frac{\Gamma}{2})^2} = 23 \gg 1$ This indicates that while the read-process takes place off-resonance, it is power-broadened onto resonance.
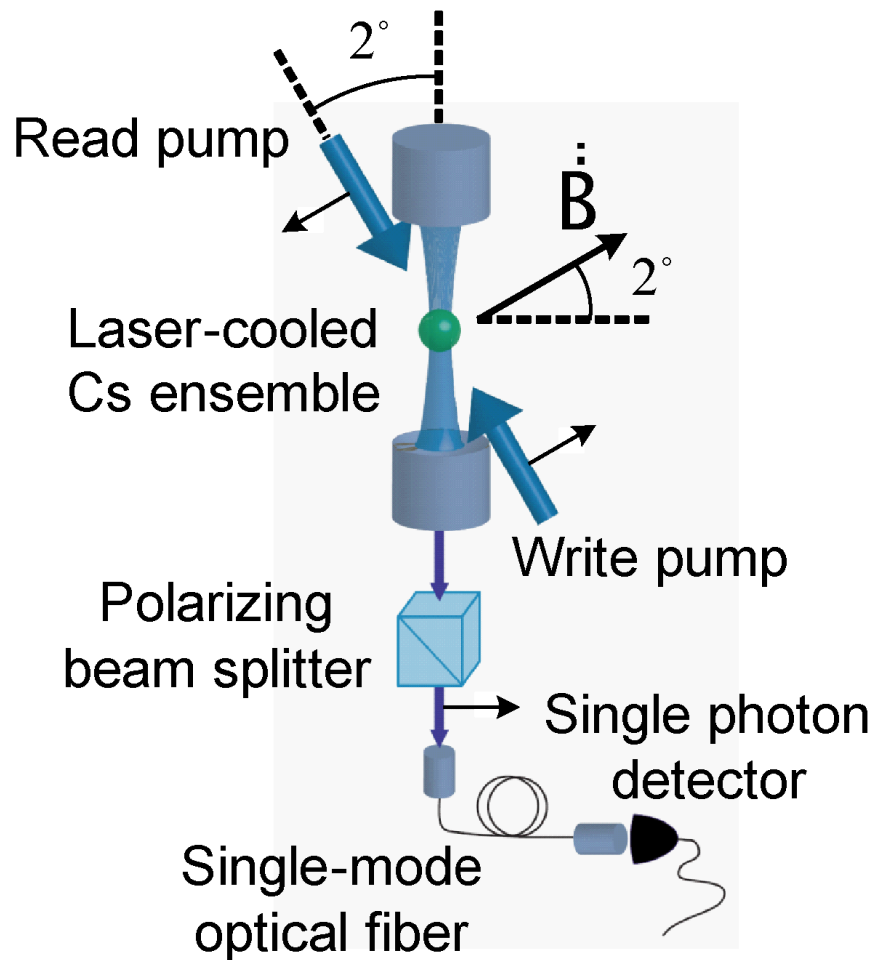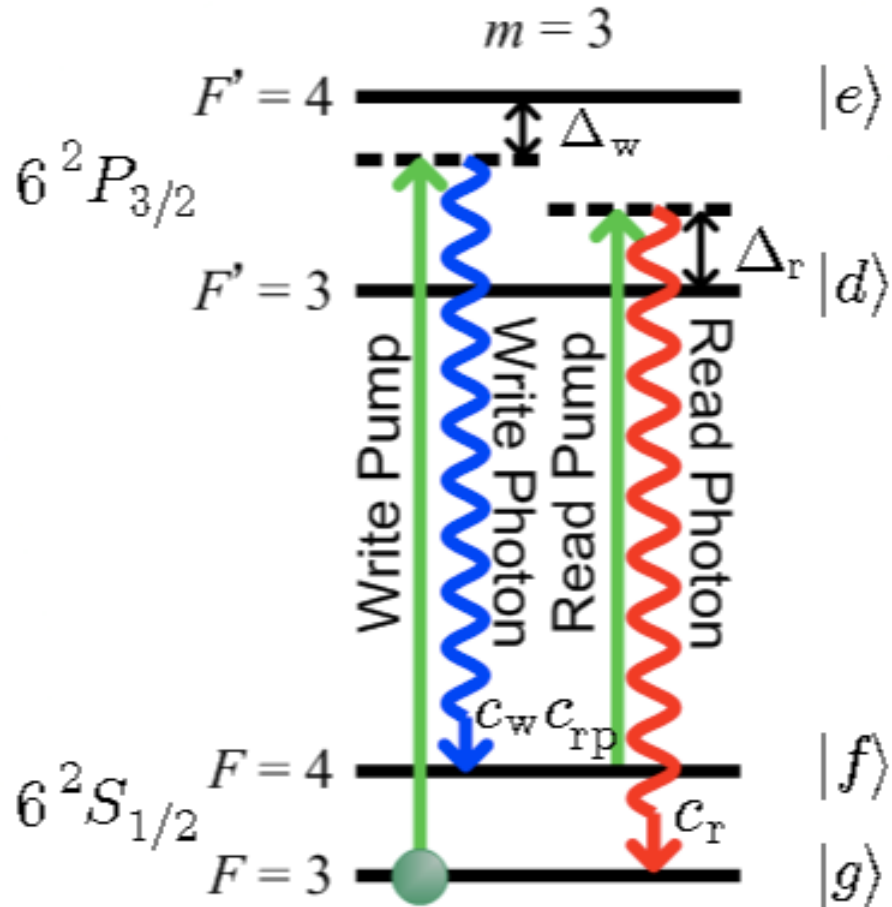
Figure 6.3: Schematic of the setup used for this experiment. The counter-propagating write- and read- beams propagate at a small angle of $\sim 2°$ degrees relative to the cavity axis to allow for a short-wavelength, long-lifetime component of the magnon. The small B-field, perpendicular to the write- and read- pump beam propagation directions, defines a quantization axis for optical pumping.

$5.5(1)\%$, such that the photon leaves the resonator through M_1, towards the detection optics with a probability $T = \frac{M_1}{M_1 + M_2 + L} \approx 0.175(4)$. The light leaving the cavity is polarization filtered, and the component which was π-polarized within the cavity is sent by way of a single-mode fiber to an SPCM. The total probability of detecting a photon emitted into the cavity is $q = Tq_1q_2q_3 = 2.7(3)\%$, which accounts for the SPCM quantum efficiency $q_1 = 0.40(4)$, interference filter transmission[2] $q_2 = 0.609(2)$, and fiber coupling and other path-losses $q_3 = 0.65(4)$.

6.3 Retrieval Efficiency

Before we can properly analyze the dependence of "Source Quality" on system parameters, it is very important to determine what quantity it is that we are interested in optimizing. In our group's earlier work[6], we chose to measure the unconditional retrieval efficiency of our source:

$$R_u \equiv \frac{P_r}{P_w} = \frac{\langle n_r \rangle}{\langle n_w \rangle} \tag{6.1}$$

This expression was known to be valid only under conditions where the signal depended upon phase matching, and hence could reasonably be considered collective. While we certainly still believe that this is a good indicator of the quality of a single photon source, measuring the phase matching at every step is quite tedious and time consuming.

If one is truly interested in using a single photon source for quantum optical applications, the sensible thing to do is measure measure $P_{read|write}$ in conjunction with

---

[2]We have since acquired filters with transmissions upwards of 80%, from Chroma Technologies.

$g_{rr|w}$, and from there extract how much of the 1-photon probability is coming from the single-photon source, and how much from backgrounds. The 3-fold coincidences necessary to measure $g_{rr|w}$ take hours to observe. We will eventually make this measurement in order to fully quantify our final device, but we do not want to do so for *every* datapoint as we optimize.

What we finally settled upon was a quantity that we call the conditional recovery efficiency:

$$R_c \equiv P_{read|write} - P_{read} = \frac{\langle n_r n_w \rangle}{\langle n_w \rangle} - \langle n_r \rangle = \langle n_r \rangle \left(g_{wr} - 1 \right) \qquad (6.2)$$

The idea here is that $P_{read|write}$ measures the probability of observing a read-photon, conditioned upon a write photon, but is still susceptible to backgrounds, and so we must subtract off our best estimate of those backgrounds- the unconditional probability of a read photon.

n_r and n_w are measured by defining "write" and "read" bins for each trial, and within these bins determining how many write (n_w) and read (n_r) photons were detected. By correlating the writes with the reads, as above, we may estimate $P_{read|write}$ and hence R_c. R_c must then be corrected for our small detection path efficiency of 2.6(3)%, as detailed above. While it is certainly true that the *measured* detection efficiency is itself a fairly important figure of merit, our primary interest is in the physics of the collective states and their interaction with the cavity, and so it is sensible to correct for all losses incurred once the photon has been emitted into the cavity. The unconditional retrieval efficiency, in contrast, is insensitive to detection path losses, as these losses are common to the write- and read- photons.

For our final source, we made detailed measurements of both R_c and R_u, versus
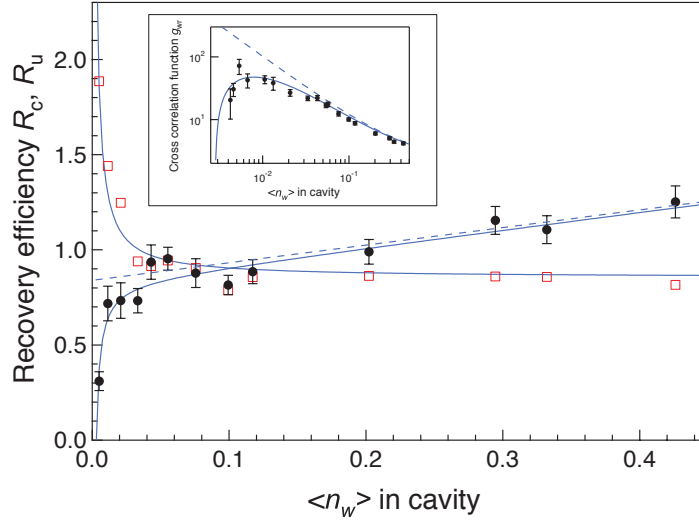
Figure 6.4: Two measures of recovery, conditional R_c and unconditional R_u versus write photon number referenced to within the cavity, n_w. The rise in R_u at low n_w is a result of read backgrounds. The rise in R_c at large n_w is a result of double-excitation. The large n_w value of R_u and the y-intercept of the asymptotic behavior of R_c both reflect the physical single magnon retrieval efficiency $\chi \approx 0.85$.

write photon number. These data are shown in figure (6.4), along with model curves. The fact that neither curve is actually flat indicates that neither R_c nor R_u is, by itself, probably a very good estimate of the retrieval efficiency. In the case of the unconditional retrieval efficiency R_u, this turns out to be because of improper accounting for read- backgrounds. In the conditional case R_c, it is because of improper accounting for write- backgrounds and write- autocorrelations.

At low write photon numbers, the read backgrounds increase R_u above the physical recovery because the write rate continues to drop, while the read rate bottoms out at the background rate. If the write backgrounds were bigger than the read backgrounds, we could never reach this regime. In our case $b_w = 0.0028(4)$ and $b_r = 0.0074(9)$ are the independently measured write and read backgrounds, referenced to within the

cavity and arising from detector dark counts and read-pump scattering, respectively. To fix R_u, we simply include an uncorrelated read background term b_r, and hence[3]:

$$R_u = \frac{\chi \langle n_w \rangle + b_r}{\langle n_w \rangle} \tag{6.3}$$

Where χ, the single-magnon retrieval efficiency, is the quantity that we are most interested in extracting.

The problems with R_c are a bit more involved. The first problem is that once n_w is decreased to $\sim b_w$, less and less frequently is an actual magnon written into the system when a "write" photon is detected, so the observed retrieval efficiency drops. This may be corrected for by simply scaling R_c up by $\frac{n_w}{n_w - b_w}$. The more complicated concern is that there is actually some correlation between write- scattering events $g_{ww} > 1$, indicating that when the atoms scatter a photon, generating a magnon, the probability of scattering another photon, and hence generating another magnon, which may be read out with efficiency χ, is enhanced. This leads to a *conditional* read background that scales with magnon number $m_w = n_w - b_w$. Our final model for R_c is thus:

$$R_c = \frac{m_w}{n_w} \chi \left[1 + (g_{ww} - 1)m_w \right] \tag{6.4}$$

Additionally, we measured that 17(4)% (referenced to within the cavity) of the write-read coincidences arise from detector after-pulsing[81]. This problem arises for two reasons: 1)Write- and read- photons have the same polarization, and hence go to the same detector, and 2)The poor detection path quantum efficiency means that

---

[3]One might wonder why it is unnecessary to include the write backgrounds in the model. This model actually has nowhere to put them! Mathematically this is because the denominator is P_w, the probability of a write photon scattered into the cavity, and not m_w, the probability of generating a magnon. Physically it is because once $n_w < b_w$, the x-coordinates of all of the data points will bunch up.

we are sensitive to even the relatively modest 0.4% *actual* after-pulsing probability. For conditional autocorrelation measurements we use multiple detectors to avoid this problem.

It is clear from figure (6.4) that this model agrees well with observation. The retrieval efficiency χ extracted from the conditional data is $\chi_c = 0.84(11)$, in good agreement with the extracted unconditional retrieval efficiency is $\chi_u = 0.85(2)$. The extracted $g_{ww} = 2.1(2)$ is in reasonable agreement with the measured $g_{ww} = 2.4(2)$.

For all later measurements, we will operate in a regime where $n_w \gg b_w$, so $m_w \approx n_w$. In this limit we will have $R_c \approx \chi(1 + (g_{ww} - 1)n_w)$. As such we can estimate the single magnon retrieval efficiency from $\chi \approx \frac{R_c}{1+(g_{ww}-1)n_w}$. We will use this expression as the benchmark throughout the remainder of this chapter (typically assuming $g_{ww} = 2$ and measuring R_c at a single value of n_w), as we analyze the dependence of our source quality on various decoherence mechanisms and system parameters.

Figure (6.4) also includes a simultaneous fit to the observed cross correlation g_{wr}, which also agrees quite well. The model curve is:

$$g_{wr} = \frac{1}{1 + \frac{c+dn_w}{\chi(n_w-b)}} \left(g_{ww} + \frac{1 - (g_{ww}-1)b + \frac{c+dn_w}{\chi}}{n_w} \right) \tag{6.5}$$

Where $g_{ww} = 2.1$ is the write-write auto-correlation, $b = 0.0067$ is the measured write background, and $c = 0.003$ is the measured read background, and $d = 0.27$ is the read background rate which scales with n_w.

Above $n_w = 0.15(3)$, g_{wr} approaches its fundamental limit of $1/n_w$. The large measured values of g_{wr} are a pre-requisite for a heralded source of single photons, but to be certain we must also measure the conditional auto-correlation function of the read photons, conditioned upon a write photon. At $n_w = 0.15(3)$ we observe

$g_{rr|w} = 0.27(21) < 1$, indicating that our source is in fact producing single photons. If the read backgrounds were simply read-photons correlated with undetected write photons (due to finite detection efficiency), we would predict $g_{rr|w} = g_{ww}n_w \approx 0.3$, which agrees with our measurement to within statistical error.

6.4 Doppler Decoherence

6.4.1 Information Leakage / Qualitative Picture

We have thus far understood the writing process as generating a collective excitation because no information leaks from the system revealing which atom scattered the write photon and was transferred $|G\rangle \to |E_w\rangle \to |F\rangle$. This allows us to write the state as a superposition state where each atom may be the scatterer, and interfere the various scattering amplitudes in the read process.

In this context, we have to wonder about the atomic recoil. This recoil manifests itself in two ways- the first is the Doppler shift of the scattered write photon, and the second is the extra distance that the atom travels due to the momentum recoil. Either of these pieces of information *could* reveal which atom underwent the scattering process, and destroy the collective state. It is just a matter of how much time we have before this happens.

The Doppler shift information is obscured by the Fourier broadening due to the finite length of the write pump beam as long as $\delta_k v_{atom} T_{pulse} \ll 1$. For Cs at 10μK, with $\delta_k \sim \approx \frac{c}{\lambda}$ (set by the angle between absorbed and emitted photons), $T_{pulse} \ll 5\mu$s. The travel distance information is obscured as long as the atom has not travelled an

added distance greater than extension of its de-Broglie wave-packet $\frac{\lambda_{DB}}{2\pi} \equiv \frac{\hbar}{p_{atom}} >$ $\frac{\hbar \delta_k}{m} T_{travel}$. Hence the maximum travel time T_{travel} between write in and readout given by $k v_{atom} T_{travel} = 1$, which is the same expression as for the pulse broadening. Thus we see that the timescale for the Doppler decoherence is given by[4] (for $\delta_k = \frac{c}{\lambda_{D2}}$):

$$\tau_{Doppler} \sim (k v_{atom})^{-1} = \frac{1}{\sqrt{2\, \omega_{rec}^{D2} \frac{k_B T}{\hbar}}} \tag{6.6}$$

An alternate picture which yields identical results is that the atoms form a phase grating, and the phase information is washed out once the atoms have travelled a distance equal to the grating wavelength. This position-space picture provides precisely the same results as the momentum space picture described in the preceding paragraphs.

6.4.2   Quantum Dynamics / Quantitative Picture

From the preceding qualitative explanation, it is clear that the Doppler coherence time scales inversely with the magnitude of the photon recoil. For this reason we chose a configuration wherein the write- and read- pump k-vectors are nearly collinear with the cavity axis. As such a photon scattered into the cavity mode heralds the creation of a magnon with a superposition of long- and short- wavelengths, corresponding to nearly forward scattering, and nearly back-scattering (see figure (6.5)). Our hope was that this would yield a recovery curve with two time constants– a short one corresponding to the large (back scattered) recoil, and a large one corresponding to the small (forward scattered) recoil. We will calculate now that it does:

---

[4]Here we have defined $\omega_{rec}^{D2} \equiv \frac{\hbar^2 k_{D2}^2}{2m_{CS}}$ is the kinetic energy that an atom acquires, on average, due to the spontaneous emission of a Cesium atom from the $6P_{3/2}$ level, due to recoil.
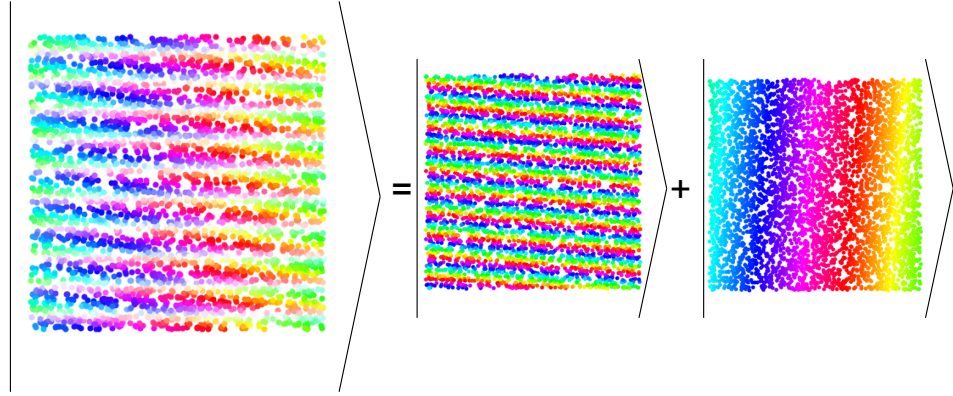
Figure 6.5: The state generated by the write scattering process may be written as a superposition of a long wavelength magnon corresponding to near-forward scattering, or a short wavelength magnon corresponding to near-back scattering.

Detection of a write photon heralds the preparation of a collective state:

$$|W\rangle = \sqrt{\frac{2}{N}} \sum_j e^{i\vec{k}_w^{pump}\cdot\vec{x}_j} \cos(\vec{k}_w^{cav} \cdot \vec{x}_j) \hat{\sigma}_{FG}^j |\Omega\rangle \qquad (6.7)$$

Where the exponential term comes from the absorption of the write-pump photon, and the cosine comes from emission into the write-cavity standing wave. This state is only approximately normalized due to the cavity amplitude modulation, but in the limit of many randomly located atoms the error becomes negligible. In this analysis we have ignored the finite transverse spatial extent of the write beam and cavity mode.

After a storage time t, atom j has moved to the location $\vec{x}_j + \vec{v}_j t$. Under the influence of a readout beam which is tuned to raman resonance with the readout cavity mode, we may compute the levels which are strongly coupled to the state $|g\rangle \equiv a_r^\dagger |\Omega\rangle$, where all of the atoms have been returned to their initial state $|G\rangle$, and one photon has been scattered into the cavity. We arrive at the standard 3-level strong-coupling Hamiltonian, equation (3.17), however the $|f\rangle$ state is now dependent

upon the states of the atom at time t:

$$|f_t\rangle = \sqrt{\frac{2}{N}} \sum_j e^{-i\vec{k}_r^{pump}\cdot(\vec{x}_j+\vec{v}_jt)} \cos\left[\vec{k}_r^{cav}\cdot(\vec{x}_j+\vec{v}_jt)\right]\hat{\sigma}_{FG}^j |\Omega\rangle \tag{6.8}$$

It is *crucial* to understand that there is no many-atom state with one atom in state $|F\rangle$, and all other atoms in $|G\rangle$, which is orthogonal to $|f\rangle$, and has *any* coupling to the cavity under the action of the atom-cavity coupling hamiltonian equation (3.15). As such, the probability that the state $|W\rangle$ may be read out after a time t to produce a photon, χ_t, is given by the magnitude squared of its overlap with $|W_t\rangle$, times the retrieval efficiency χ of the $|W_t\rangle$. Because we expect χ to be independent of t, all time dependence ought to be in the overlap:

$$\chi_t = \chi\,|\langle f_t|W\rangle|^2 \tag{6.9}$$

Equation (6.9) will be used to analyze a number of the technical features of our single photon source. At present we are interested only in decoherence due to atomic motion, so we choose $\vec{k}_w^{cav} = \vec{k}_r^{cav} \equiv \vec{k}^{cav}$, and $\vec{k}_w^{pump} = -\vec{k}_r^{pump} \equiv \vec{k}^{pump}$, $\left|\vec{k}^{pump}\right| = \left|\vec{k}^{cav}\right| \equiv k$, and $\vec{k}^{pump}\cdot\vec{k}^{cav} = k^2\cos\theta$. Computing χ_t and averaging the final expression over (uncorrelated) atomic positions and a Maxwell-Boltzmann velocity distribution at temperature T yields the expression (after a fair bit of algebra):

$$\begin{aligned}
\chi_t &= \chi\, e^{-\frac{t^2}{2\tau_D^2}} \cosh^2\left[\frac{1}{2}\frac{t^2}{2\tau_D^2}\cos\theta\right] \\
&= \chi\left[\frac{e^{-\frac{1}{2}\frac{t^2}{\tau_D^2/\sin^2\frac{\theta}{2}}} + e^{-\frac{1}{2}\frac{t^2}{\tau_D^2/\cos^2\frac{\theta}{2}}}}{2}\right]^2
\end{aligned} \tag{6.10}$$

Where $\tau_D^-1 \equiv \sqrt{8\,\omega_{rec}^{D2}\frac{k_BT}{\hbar}}$, in agreement, up to a factor of two, with the number we posited on more qualitative physical grounds in the previous section.
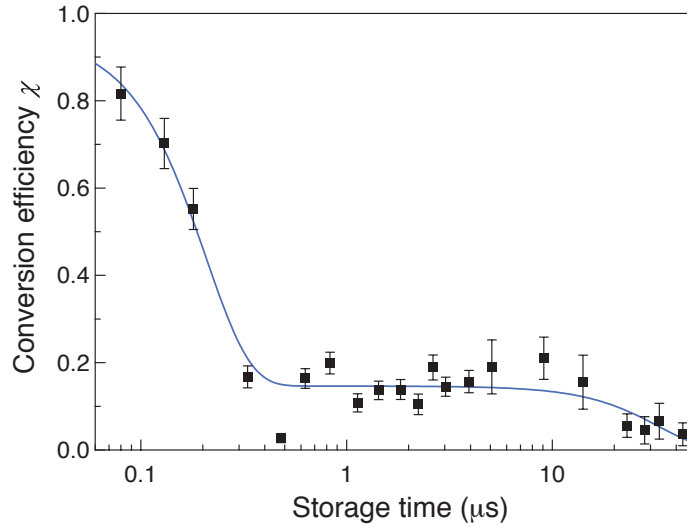
Figure 6.6: Conditional retrieval efficiency versus storage time, exhibiting both long- and short- lifetimes corresponding to long- and short- wavelength spin-waves arising from forward and backward scattering in the write process.

This functional form shows two time constants– one short $\tau_s = \tau_D / \cos \frac{\theta}{2}$, and one long $\tau_l = \tau_D / \sin \frac{\theta}{2}$, corresponding to short and long magnon wavelengths $\lambda_s = \lambda / \cos \frac{\theta}{2}$ and $\lambda_l = \lambda / \sin \frac{\theta}{2}$ respectively.

When we actually measure our retrieval efficiency as a function of storage time (see figure 6.6), we do in fact observe two time constants, as predicted by our model. The shorter one is $\tau_s \approx 240$ns, and the longer $\tau_l = 23\mu$s, corresponding to $\lambda_s \approx \lambda/2 = 400$nm and $\lambda_l = \lambda / [2 \sin (\theta/2)] \approx 23\mu$m, respectively, for $\theta \approx 2°$.

The data and theory appear to agree nicely, and have several interesting features. Perhaps the most curious is that the retrieval efficiency falls to $\frac{1}{4}$ once the short wavelength coherence has been destroyed by atomic motion, and not $\frac{1}{2}$ as one might naively expect. This is clearly evident from the second expression in equation (6.10), but we are looking for a physical *reason*.

One may understand the missing factor of two as coming from a phase mismatch between the running-wave excitation and the standing wave cavity. This picture may be formalized by treating the forward and back- scattering magnon modes separately (see figure (6.7)). This results in a 5-state hamiltonian, which may be block diagonalized into bright- and dark- hamiltonians, which couple collectively and not at all, respectively, to the cavity mode. The states which couple to the cavity are the so-called super-radiant states[30], and are distinguished from the sub-radiant states (coupled to one another under dark hamiltonian) only by the phase between the forward- and back- scattering magnon components. Detection of a write photon prepares a super-radiant state. After the short wavelength component has decohered we are left with a long wavelength magnon, which may be decomposed into a superposition super- and sub- radiant components with equal amplitudes. The super-radiant component may then be read out, while the sub-radiant component scatters into freespace. We now see the whole story: With probability $\frac{1}{2}$ the magnon has a long wavelength and persists, and then with probability $\frac{1}{2}$ it may be read out into the standing wave cavity, for a total of $\frac{1}{4}$.

We have now understood both qualitatively and quantitatively the time-dependence of the dominant decoherence process acting upon magnons composed of free thermal atoms. It is clear that if we could constrain the atomic motion to much less than the magnon wavelength, the storage time could be increased substantially, until it is limited by something else. Recently, the Kuzmich group has confined Rb atoms in a 1D optical lattice, and observed just this effect in a nearly forward-scattered configuration[35]. Similarly, the Bloch group has observed 240ms storage times using
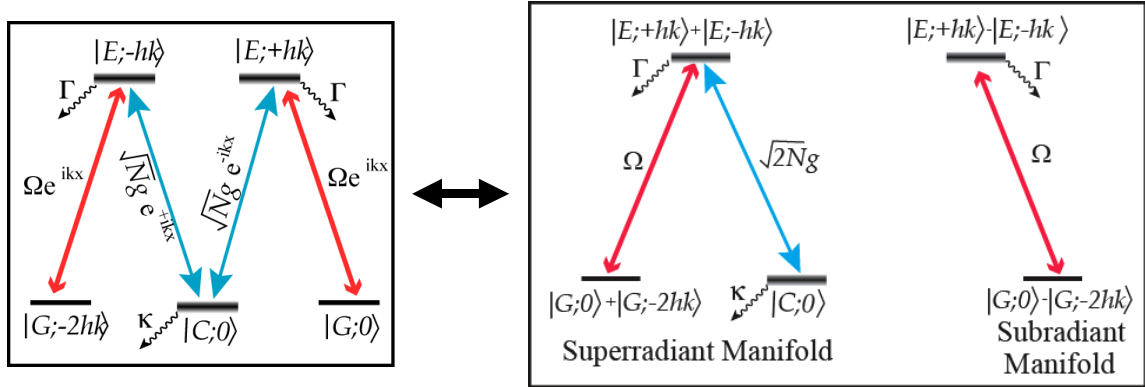
Figure 6.7: Super- and sub- radiant states in momentum space. The coupling of long- and short- wavelength gratings to the cavity standing wave may be understood in terms of super- and sub- radiant manifolds, one of which is strongly coupled to the cavity, and one of which is uncoupled.

EIT in an atomic Mott insulator in an optical lattice[105].

There remains a bit of confusion arising from the apparent violation of position-momentum uncertainty in the preceding model. It seems likely that a quantum mechanical treatment, using the lagrangian $L = T - V$, instead of H, as in atom interferometry, would yield an additional factor of two[6], or perhaps just added complexity. This merits further investigation.

6.5 MOT Location Dependence: Cavity and Pump Mode-Matching

In the preceding section, we studied the movement of the atoms, between write-in and read-out, as a time-dependent decoherence mechanism. It turns out that there is another very simple mechanism which may be understood in much the same language, arising from the difference in k-vector magnitudes between write-in and

read-out pump- and cavity- modes.

If the scattering atom absorbs different amounts of momentum during the write- and read- processes then after the full write-read process it will not have been returned to its initial momentum state. If this momentum kick is greater than the momentum uncertainty arising from the finite sample size, it will be clear which atom underwent the scattering process, and the collective enhancement of the read process will be destroyed. This means that $\Delta k^{-1} \ll l_{sample}$.

Another way to understand these effects is in the context of a Bragg-Reflector. For a wave-vector mismatch of order Δk between the reflector planes and the input beam, the reflector must have a spatial extent much less than Δk^{-1}, or the fields scattered by different parts of the reflector will begin to interfere with one another destructively in the output mode. As such we arrive at the same criterion $\Delta k^{-1} \ll l_{sample}$.

For a hyperfine changing write-in/read-out scheme, we will have an approximate frequency difference of 9.2GHz, the Cs ground-state hyperfine splitting. This corresponds to $\Delta k^{-1} \approx 3$cm. The atomic sample has dimensions of $110 \times 110 \times 500 \mu\text{m}^3$, determined by the cavity mode waist and MOT radius. All of these dimensions are much less than Δk^{-1}, so we do not expect to have to worry about spatial phase matching due to k-vector mismatch.

When we include the fact that we are employing a *standing*-wave cavity, it becomes apparent that we are not just dealing with *phase*-matching, but also *amplitude*-matching relative to a fixed reference point. More concretely, an atom which is at an anti-node of the write cavity-mode may well end up at a node of the read cavity-mode, and hence be unable to scatter a read photon at all!

All of this physics is embodied in equation (6.9). In this case we take $t = 0$, and define $\vec{\delta k}^{pump} \equiv \vec{k}_r^{pump} + \vec{k}_w^{pump}, \vec{\delta k}_c \equiv \vec{k}_r^{cav} + \vec{k}_w^{cav}$, with $\vec{\delta k}_p \cdot \vec{\delta k}^{cav} = \delta k^{pump} \delta k^{cav} \cos\theta$. Evaluating equation (6.9) dropping single-atom terms, averaging the atomic locations over 1D gaussian distributions of RMS size R, with the z-location centered on z_0, gives:

$$\chi_{Spatial} = \chi e^{-R^2(\delta k_p{}^2 + \delta k_c{}^2)} \frac{1}{2} \left[\cos 2\delta k_c z_0 + \cosh\left(2R^2 \delta k_c \delta k_p \sin\theta \right) \right] \qquad (6.11)$$

In the limit that the sample is much smaller spatially than the k-vector mismatch $(R \ll \delta k_c^{-1}, \delta k_p^{-1})$, the expression simplifies substantially:

$$\chi_{Spatial} = \chi \cos^2 \delta k_c z_0 \qquad (6.12)$$

This, now, is the equation of interest! As the MOT *moves* spatially through the cavity mode, by a distance $z_0 = \frac{\pi/2}{\delta k_c}$, the retrieval efficiency will go from a maximum, to a minimum! For our near-resonant hyperfine write-in and read-out schemes, $\delta\nu = 4\frac{c}{2L}$, and $\delta k_c = 2\pi\frac{\delta\nu}{c}$, and so $z_0 = \frac{L}{8} \approx 8mm$, and so we can actually observe this effect experimentally by moving the MOT around with bias fields.

Our experimental data[5] is shown in figure (6.8b), versus MOT (and pump beam) vertical displacement. To remove systematics arising from beam alignment, what we actually plot is the ratio of the retrieval efficiency when the write process takes place 4 FSRs from the read process, to 3 FSRs from the read process (see figure (6.8a). For this experiment the read is maintained at a fixed detuning from atomic resonance, while the write beam frequency is hopped by 1 FSR$\approx$ 2265MHz. In order to maintain a similar scattering rate for the write process in both cases, we need very high write intensities for the write-scattering process which is 3 FSRs from the read process, as

---

[5]These data were taken several months after the rest, in a slightly different level configuration and pump beam orientation, but also in a pulsed write/read/optical-pump scheme.

Spatial Phase Matching

Sour Spot

Sweet Spot

A)

4 FSRs

3 FSRs

$\log\left(\dfrac{\text{Rmode4}}{\text{Rmode3}}\right)$

B)
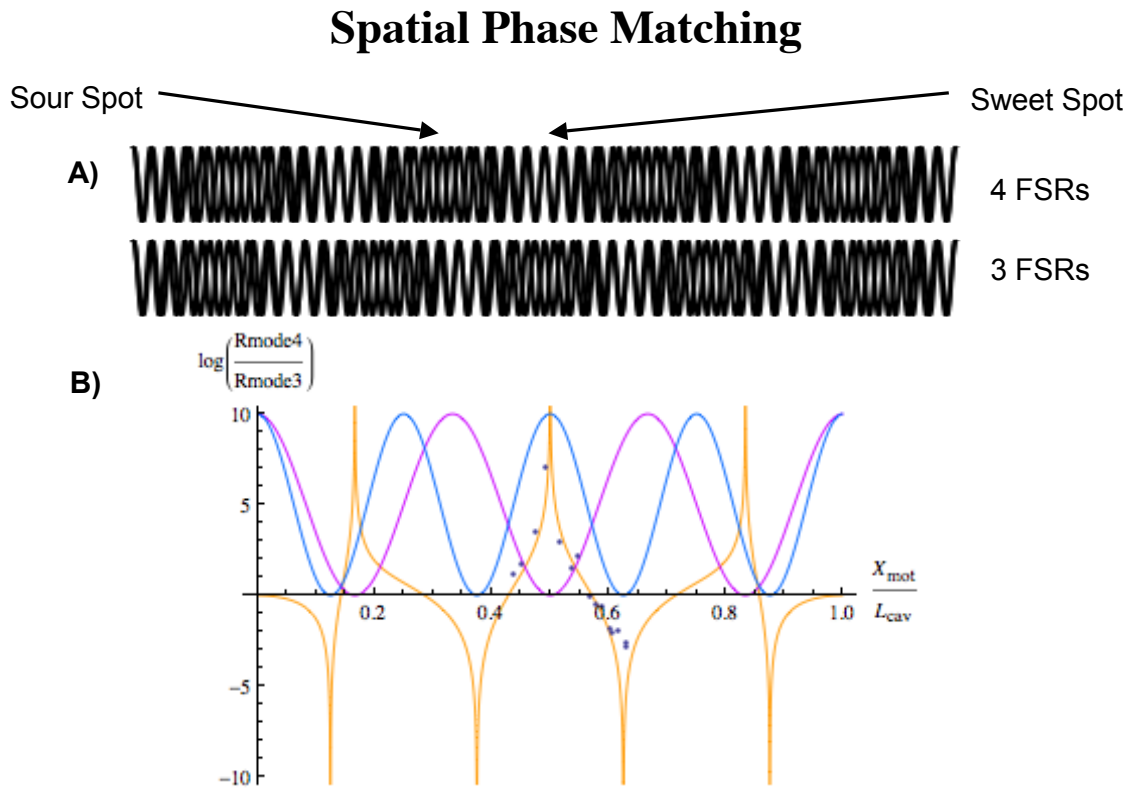
Figure 6.8: **(A)** Plot of the cavity field for modes separated by 4 (upper trace) and 3 (lower trace) cavity free spectral ranges. Modes separated by 4 FSR's overlap well in the center of the cavity, while those separated by 3 FSR's overlap well in locations slightly offset from cavity center. **(B)** Plot of recovery ratio for write-in and read-out separated by 4 and 3 FSRs, versus position along the cavity axis, with fit curve.

it is nearly 2 GHz from atomic resonance. The theory curve in the figure thus has the form (with z_0 defined here relative to the center of the cavity, rather than the end mirror):

$$\frac{\chi_4}{\chi_3} = \frac{\cos^2 \frac{cz_0}{4\nu_{FSR}}}{\sin^2 \frac{cz_0}{3\nu_{FSR}}} \tag{6.13}$$

The only free parameter for the plot is the location of $z_0 = 0$, which in many ways was the reason to collect these data. When the write-in and read-out are 4 FSR's apart, the optimal recovery occurs in the center of the cavity, and so finding this location is critical. When initially setting up the experiment, one typically estimates by eye, but by measuring this ratio, one has a consistent, stable way of finding the optimum which is insensitive to many systematics.

One of the most beautiful things about this experiment is how clean it is. A few hours spent doing quantum mechanics is worthwhile because the theory typically matches up beautifully with the experiment!

6.6   Stark Broadening: Inhomogeneous Couplings

Thus far, we have pretended that all atoms couple equally strongly to the pump beam, and to some extent, the cavity mode as well. Relaxing this constraint is complicated but very important for obtaining a complete understanding of how super-radiance works. In this section we will discuss the impact of inhomogeneous couplings on distinguishability, and then attempt to understand their impact in various limits.

One might be inclined to reason that if different atoms experience different coupling strengths, this has the potential to lead to distinguishability in the form of some atoms reading out faster than others. Distinguishability ruins the constructive

interference which we depend upon for collective readout of our magnons. Unfortunately, a similarly convincing argument can be made that as long as the write- and read- beams have the same spatial profile, the fact that an atom reads out more slowly should be offset by its reduced weight in the collective state, and hence indistinguishability should be restored. A more formal analysis will show inhomogeneous pump coupling is problematic, while inhomogeneous *cavity* coupling is not. Why there should be a difference between the pump beams and cavity mode is subtle and has to do with the structure of the many-atom Hamiltonian.

6.6.1 Terminating versus Non-Terminating Ladders

The issues with inhomogeneous couplings become glaringly obvious as soon as we attempt to employ the method of chapter (2) to the partially re-diagonalize the many-atom readout Hamiltonian H in the collective basis. Beginning in the state $|GG...GG, 1\rangle$, and repeatedly applying H generates a seemingly non-terminating[6] ladder of states! The reason for this is that repeated applications of just the many-atom read-pump operator does not even generate a terminating ladder.

The read-pump operator is given by:

$$H_{RP} = \sum_j \Omega_{rp}^j \sigma_{EF} + H.C. \tag{6.14}$$

and repeated application of this operator to the state $|W\rangle$ gives:

$$H_{RP}^{2N} |W\rangle = \sqrt{\frac{2}{N}} \sum_j \left|\Omega_{rp}^j\right|^{2N} \Omega_{wp}^j e^{i\vec{k}_w^{pump} \cdot \vec{x}_j} \cos(\vec{k}_w^{cav} \cdot \vec{x}_j) \hat{\sigma}_{FG}^j |\Omega\rangle \tag{6.15}$$

---

[6]Of course it can only generate $2N_{atom}$ orthogonal states.

where we have also included the (for now irrelevant) spatial dependence of the write pump beam. The important point is that unless all Ω_{rp} are equal, the space of states which is coupled by H_{RP} may be as large as the number of atoms! This coupling spreads the excitation from the particular collective-state which may scatter into the cavity into other states which are uncoupled from the cavity, and may only scatter into free-space. This has the effect of reducing the retrieval efficiency.

This effect has different physical interpretations in different limits. On resonance the atoms at lower (or zero!) pump couplings begin to act as absorbers during the read process. Off resonance the different light shifts experienced by the different atoms results in a slow rotation of the state away from the maximally super-radiant one, during the read-process.

This should be contrasted with the influence of the read-cavity coupling Hamiltonian H_{RC}, upon the cavity state $|c\rangle = a_r^\dagger |\Omega\rangle$. The read-cavity coupling operator is given by[7]:

$$H_{RC} = \sum_j g_r^j \sigma_{EG}^j a + H.C. \tag{6.16}$$

Repeated application of this operator to the state $|c\rangle$ yields one of two states:

$$H_{RC}^{2N} |c\rangle \quad \propto \quad |c\rangle$$

$$H_{RC}^{2N+1} |c\rangle \quad \propto \quad \sum_j g_r^j \sigma_{EG}^j |\Omega\rangle \equiv |e\rangle \tag{6.17}$$

This behavior is *distinctly* different! In spite of the inhomogeneity of the coupling of the various atoms to the cavity mode, the manifold of coupled states terminates at

---

[7]Notice that, as always, we are ignoring higher-order transverse modes of the cavity- in the non-confocal case they are non-degenerate, so any imperfect orthogonality is suppressed substantially. For more details read the section on lensing!

two states: $|c\rangle$, with one photon in the cavity and all of the atoms returned to their initial state, and $|e\rangle$, where that photon has been collectively absorbed by the atomic sample. As such the inhomogeneity does *not* adversely effect the recovery, except to slightly adjust the effective optical depth $N\eta$.

If we had analyzed the write process rather than the read process, we would have found that the *pump* coupling, and not the cavity coupling, is the one whose inhomogeneities do not complicate things. This is because it is not an intrinsic property of the pump or cavity mode which determines the impact of inhomogeneities, but rather the dimensions of the manifolds under consideration! Inhomogeneous couplings have a simple effect upon the dynamics if one of the manifolds of interest has dimension 1 (contains only a single state state). In the read-out process this manifold is the one containing only the state $|c\rangle$. The excited state (E), and intermediate state (F) manifolds each contain N_{atoms} states, corresponding to each of the atoms being excited. It bears mention that because the write process takes place entirely in the weak-coupling limit, we are not so concerned about these inhomogeneous coupling effects.

What we have learned, then, is that during the read-process, the inhomogeneous couplings of the atoms to the cavity mode do not limit the retrieval, while inhomogeneous couplings to the pump beams do.

6.6.2 Experiment and Analysis

In light of the fact that read-cavity inhomogeneity does not adversely impact the retrieval efficiency, one route (and the one that we took), is to align the pump-beams
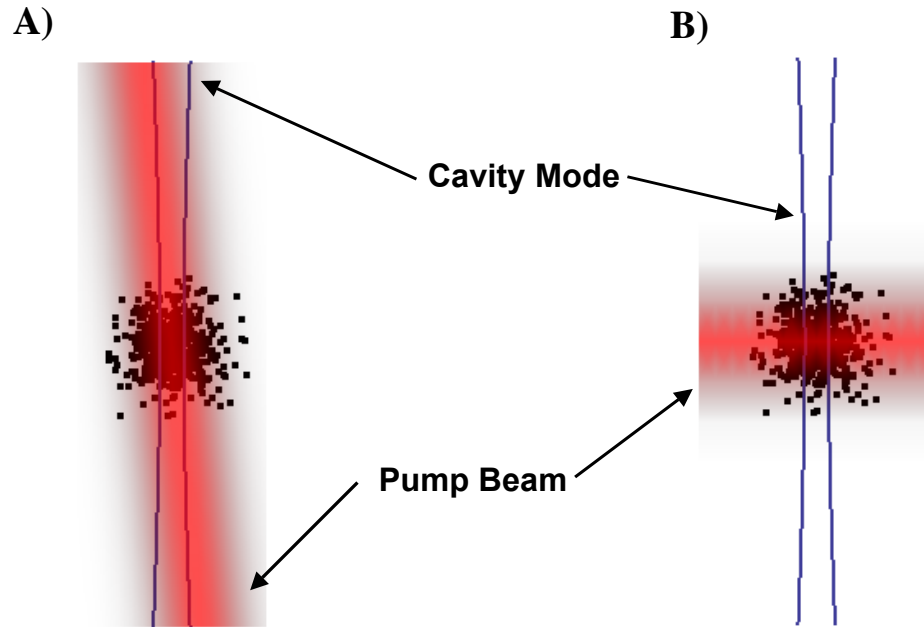
Figure 6.9: **(A)** In our current configuration, the cavity mode selects out atoms well within the waist of the pump beam. **(B)** In the configuration we typically use, the atoms in the wings of the pump beam participate in the readout process, reducing its efficiency.

to be nearly co-propagating with, and somewhat larger than, the cavity mode (see figure (6.9a)). Because only atoms within the cavity mode can scatter write-photons into the cavity, the collective state produced via the write-process will not contain any atoms in the wings of the pump-beams, and the inhomogeneous coupling to the read-beam should be suppressed. In our more standard crossed-beam configuration (see figure (6.9b)), the pump beams would have to be several millimeters across to have any hope of attaining the same homogeneity factor.

We found a maximum in retrieval efficiency when the cavity was detuned to the blue of the $F_g = 3 \rightarrow F_e = 3$ resonance by 60MHz. At this detuning we believe that the dominant consequence of the read beam inhomogeneity is the position dependent
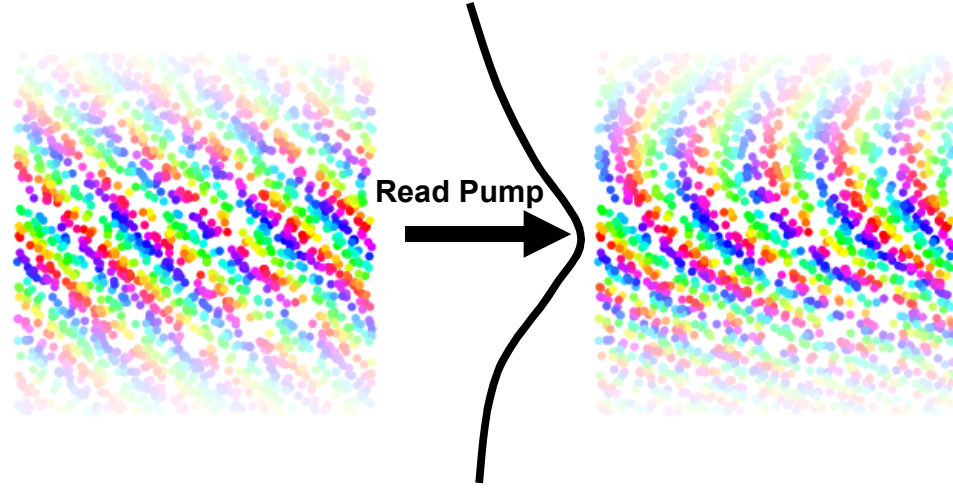
Figure 6.10: Effect of stark decoherence during readout. A magnon written in with a finite-size pump beam generates a spin-grating (magnon) which will deflect a single photon by 90°. As the magnon is read out, the read-pump generates a spatially varying stark shift which distorts the grating and prevents it from scattering efficiently at 90°.

stark-shifts due to the $F_e = 4$ excited state. These stark-shifts distort the shape of the phase grating and hence reduces the retrieval efficiency of the source. An exaggerated example of such an effect is shown in figure (6.10).

To understand this process more quantitatively we note that in the low inhomogeneity limit, the state which reads out collectively into the cavity is given by (dropping irrelevant spatial phase factors):

$$|f\rangle = \sqrt{\frac{1}{N}} \sum_j \hat{\sigma}_{FG}^j |\Omega\rangle \tag{6.18}$$

Under the influence of the spatially inhomogeneous stark effect, the this state evolves during the readout process into the state (with Ω_r' and δ_{la}' the Rabi-coupling and detuning, respectively to the dephasing level):

$$|f_t\rangle = \sqrt{\frac{1}{N}} \sum_j e^{i\frac{\Omega_r'^{j\,2}}{\delta_{la}'}t} \hat{\sigma}_{FG}^j |\Omega\rangle \tag{6.19}$$

If the readout process takes on average a time t_r, the fraction of the excitation which can be super-radiantly read out after this time is given by:

$$\chi_{stark}(t) = |\langle f_t | f \rangle|^2 \tag{6.20}$$

Computing this expectation value by averaging over a 2D normal distribution of atoms of e^{-2}-waist size w_{sample} (which will be w_c for our actual experiment, as the write beam co-propagates with the cavity), within a readout beam of waist $w_{beam} \gg w_{sample}$, yields:

$$\chi_{stark}(t) \approx \frac{1}{1 + (4\Delta_s t(\frac{w_c}{w_s}))^2} \tag{6.21}$$

Where $\Delta_s(t) = \frac{\Omega_r'^2}{4\delta_{la}'}$ is the ground-state stark-shift induced phase experienced by an on-axis (maximally coupled) atom due to the next excited state after a time t. This expression means that, if the excitation has not been read out or scattered into free space after a time t, the probability that it remains in the super-radiant state is given by $\chi_{stark}(t)$. From here we may compute the total probability that the collective excitation scatters into the cavity:

$$\chi_{TOT} = \int_0^\infty dt \chi_{stark}(t) \Gamma_{cav} e^{-(\Gamma_{cav} + \Gamma_{fs})t} \tag{6.22}$$

We can compute this integral in closed form. In the on-resonant case, $\Gamma_{cav} = \Gamma_{sc} \frac{N\eta}{(1+N\eta)^2}, \Gamma_{fs} = \Gamma_{sc} \frac{1}{(1+N\eta)^2}$:

$$
\begin{aligned}
\chi_{TOT} &= \frac{N\eta}{1 + N\eta} \left\{ \nu \left[\text{Ci}\,\nu \sin \nu + \frac{1}{2}(\cos \nu)(\pi - 2\,\text{Si}\,\nu) \right] \right\} \\
&\approx \frac{N\eta}{1 + N\eta} \left(1 - 2\nu^{-2} + 24\nu^{-4} + \ldots \right) \\
\nu^{-1} &\equiv (\frac{w_c}{w_{beam}})^2 (1 + N\eta) \frac{\Delta_s}{\Gamma_{sc}}
\end{aligned}
\tag{6.23}
$$

A measurement of retrieval efficiency versus optical depth is shown in figure (6.11). Initially, as expected, the retrieval grows according to $\chi = \frac{N\eta}{1+N\eta}$. As the optical depth grows, the readout slows (in the on-resonant dark state rotation limit), and stark decoherence begins to destroy the excitation. The curve shown corresponds to a slightly different fit form[8] which is less accurate than the one given here, but also includes a small contribution from dephasing of the magnon due to the write stark shift, which should go away as the write beam induces less stark shift per atom, either due to smaller n_w or higher $N\eta$ (and hence less stark shift per atom for the same n_w). The fit curve has $(\frac{w_c}{w_{beam}})^{-1} = 3$, in agreement with the measured 3.0(4).

It bears mention that our analysis assumes resonant readout, while the reality is that we were detuned by ~ 60MHz on the readout process. Because of the high read-intensity used, however, this was likely not a problem. In fact off-resonant readout is typically slower than resonant readout, and so we expect that the detuning from $F_e = 3$ may have made things *worse*.

In the limit of pump beam which is much larger than the atomic sample, we have succeeded in understanding the dynamics. I wish there were a closed form expression or simple perturbative expansion that I could provide which could be used to reach a general conclusions for any geometry at any detuning, but alas if such an expansion exists I have not been able to derive it[9]. Lacking an absolute scaling law or expression,

---

[8]The actually used fit form is: $\chi = \frac{N\eta}{1+N\eta} \frac{1}{\sqrt{1+(\frac{A_w}{N\eta} - A_r(N\eta+\alpha))^2}}$. Here A_w parameterizes the write stark decoherence as compared with the write scattering rate and n_w, as well as the difference between coupling coefficients for the write process. A_r parameterizes the stark shift/scattering event for the read process.

[9]The issue seems to be that the read pump, whose strength is typically the small parameter, couples to other states which are *degenerate* with our initial state $|f\rangle$, and so our perturbation series diverges. A more careful application of the resolvent method might solve this problem.
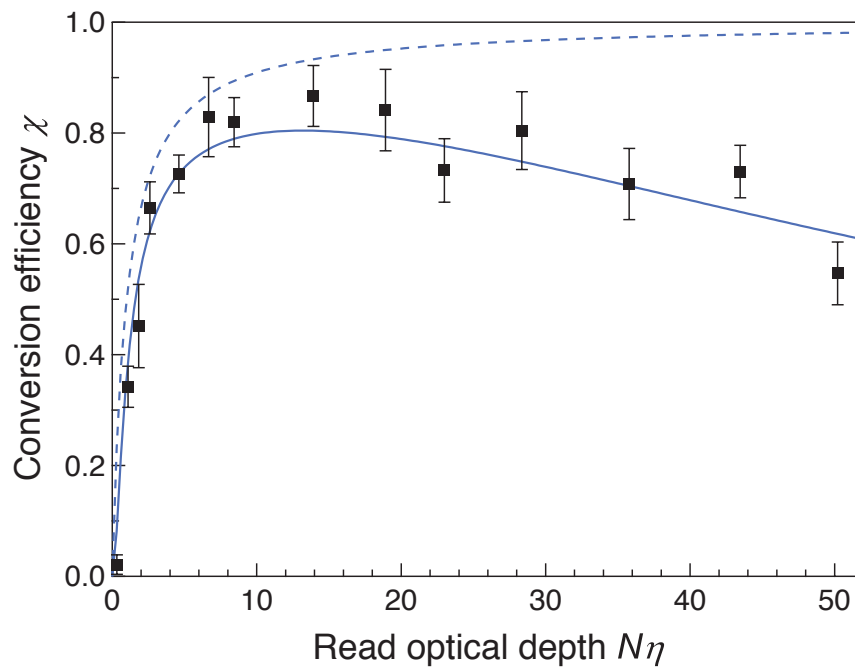
Figure 6.11: Experimentally observed retrieval efficiency versus optical depth. Initial rise with increasing optical depth results from collective suppression of the free-space loss process. The eventual decay at large optical depth results from inhomogeneous stark shifts decohering the magnon. The dotted curve is theory including only the competition between free-space and cavity scattering, while the solid curve also incorporates the stark decoherence.

the message seems to be:

Inhomogeneous pump couplings definitely make the 3-level model a bad approxima-

tion, and reduce the retrieval efficiency, while inhomogeneous cavity couplings cause

no such problems. Inhomogeneities may be suppressed in any number of ways, but

must be taken seriously in the design phase in order to achieve much better than 50%

retrieval efficiency.

6.6.3 Inhomogeneous Cavity Couplings

Although, as we have just seen, the cavity ladder *does* terminate almost immedi-

ately, we still must worry about how good the overlap is between the state which is

maximally coupled to the readout cavity mode, and the state produced by the write

process followed by the application of a read pump beam. These are:

$$
\begin{aligned}
|\psi_{super}\rangle &\propto \sum_j g(x_j)\sigma_{EG}^j |\Omega\rangle \\
|\psi_{readpump}\rangle &\propto \sum_j g(x_j)\Omega_p^w(x_j)\Omega_p^r(x_j)\sigma_{EG}^j |\Omega\rangle
\end{aligned}
$$

$$(6.24)$$

Inserting the proper normalization constants, we compute the overlap of these two

states in the limit that $\epsilon = \frac{w_c}{w_p} \ll 1$:

$$
\chi_{cavinhomog} \equiv |\langle\psi_{super}|\psi_{readpump}\rangle|^2 \approx 1 - \epsilon^4 \tag{6.25}
$$

This means that a fraction ϵ^4 of the read pump beam scatters non-collectively into

free-space. In the off-resonant limit of the retrieval process, this amounts to a renor-

malization of the optical depth $\tilde{N}\eta \approx \frac{N\eta}{1+2\epsilon^4}$, which is quite ignorable. In the on-

resonant case, however, the collective readout is *slower* than the unsuppressed free

space readout rate by a factor $\frac{N\eta}{(1+N\eta)^2}$, and so the situation is quite different. An analogous computation is performed in section (6.8.1), with the result being a maximal achievable recovery of $\chi^{max} = 1 - 2\varepsilon^2$.

For $\epsilon^{-1} = 3$, this expression predicts $\chi_{max} = 0.78$, which is inconsistent with our observation of ~ 0.85 (especially once stark broadening is included as well). Given that the detuning from atomic resonance was ~ 60MHz, the off-resonant analysis is more appropriate, and so we do not expect to be limited by this effect.

6.7 Distortion of the Cavity Mode by the Atoms

One might be inclined to wonder what impact the spatially varying index of refraction of the atomic sample has on the cavity mode shape. Might not the atoms cause some lensing of the beam going past them, especially in the limit of many passes that one experiences within a resonator?

It turns out that for samples which are large compared to the cavity waist, this is not a particular concern, as the orthogonality of the cavity modes an prohibits collective couplings of the magnons to higher order modes. This is equivalent to saying that if the lens (atoms) has little curvature across the beam (cavity mode), there will be little lensing. We operate in the limit of a MOT larger than the cavity mode waist, and so we need not worry.

In the opposite limit of a sample well-localized within the cavity waist, there may be cause for concern, as the collective couplings can be substantial. For a non-confocal cavity, these couplings are off-resonant, and numerical calculations reveal that they do not impact recovery.

The concerning situation, then, is a confocal cavity coupled to an atomic ensemble well localized within the cavity waist. In this limit the atom distribution breaks the orthogonality between the transverse modes, and their degeneracy permits the atoms to emit resonantly into higher order modes. I have often wondered if this mechanism imposes limits on the performance of free-space sources, which are necessarily confocal.

6.8 Alignment Imperfections and Misalignments

Imperfect optical pumping and beam polarizations give rise to a number of different, though all bad, effects. We cannot hope to list them all, but go through a number of the most important or interesting ones which informed our experimental setup decisions.

6.8.1 Extraneous Read Pump Beam Couplings

This situation most often arises due to poor choice of pump beam polarization, or imperfect polarization alignment. If our read-pump beam does not couple only to the read-out transition, as in figure (6.12), the retrieval efficiency becomes sensitive to the detuning of the cavity from atomic resonance.

Far from atomic resonance the collective enhancement speeds up the cavity scattering (by a factor $N\eta$), leaving free space scattering unaffected. In this limit we expect the retrieval to have the form:

$$\chi = \frac{N\eta}{1 + \epsilon + N\eta} \tag{6.26}$$
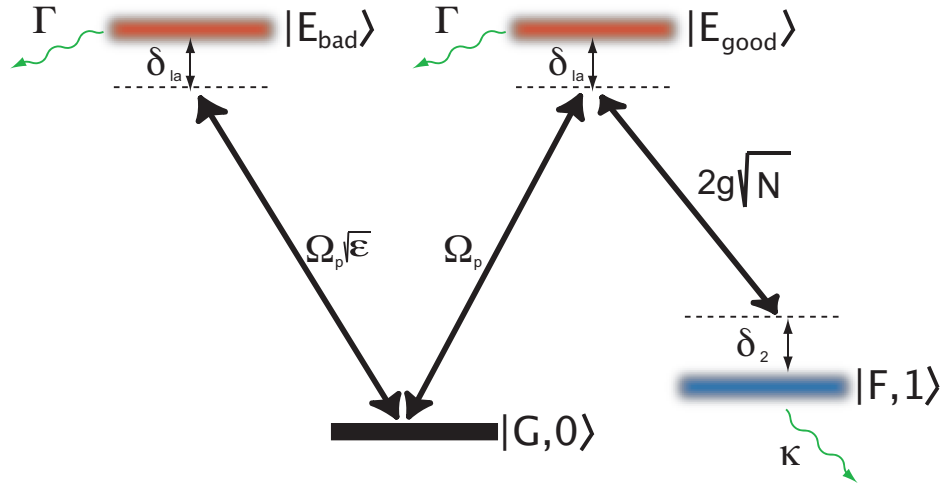
Figure 6.12: Impact of imperfect read-pump polarization. If a small fraction ϵ of the read pump power couples to a different excited state $|E_{bad}\rangle$, we are left with the hamiltonian shown. Far from atomic resonance this bad coupling slightly suppresses the effective cooperativity. Near atomic resonance it limits the maximum achievable retrieval efficiency.

Where ϵ is the fraction of read-pump power which has the wrong polarization (corrected for coupling constant differences. It is clear that in this limit $N\eta$ has simply been renormalized to $\tilde{N}\eta = \frac{N\eta}{1+\epsilon}$, and so more atoms compensates for the extraneous couplings.

In contrast, on atomic resonance the collective enhancement suppresses *both* cavity and free-space scattering, but suppresses the free space process more (by the same factor of $N\eta$). The improperly polarized component, on the other hand, always scatters at the unaffected free-space rate. In this limit we find the retrieval efficiency has the form (on EIT resonance):

$$\chi = \frac{N\eta}{1 + \epsilon(1 + N\eta)^2 + N\eta} \tag{6.27}$$

This curve eventually gets *worse* with increasing optical depth, as the readout is

slowed by the collective process. It has a maximum at $N\eta = \sqrt{1 + 1/\epsilon}$ of $\chi = 1 - 2\epsilon(\sqrt{1 + 1/\epsilon} - 1)$, which in the low loss limit is:

$$\chi^{max} \approx 1 - 2\sqrt{\epsilon} \tag{6.28}$$

This means that near resonance, even 5% of the read-power in the wrong polarization results in a maximum retrieval efficiency of 65%! This requires only a $\sim 7°$ misalignment of a half-wave plate.

This phenomenon would be observable directly by scanning the readout beam across the cavity resonance, while monitoring the retrieval efficiency. As the beam is tuned away from the EIT resonance and through the dressed states the recovery occurs more quickly (though less efficiently due to increased free-space scattering), and hence we become less sensitive to the (fixed rate) free-space scattering.

Before we understood this effect we would often make a poor choice of quantization axis and read pump polarization (typically out of geometrical convenience): If the read pump is $\hat{x}$-polarized when the polarization needed is $\sigma^+ = \frac{1}{\sqrt{2}}(\hat{x} + i\hat{y})$. This results in fully *half* the power having the wrong (σ^-) polarization. The reasoning that the improperly polarized component ought not matter, as component coupling to the collective process ought to "dominate," is only valid in the large detuning limit.

6.8.2 Extraneous Cavity Coupling

Because of imperfect alignment between the cavity mode and the bias fields, or poor choice of geometry, an extraneous atom-cavity coupling may exist on the read process, which can re-scatter the emitted single photon into free-space, or shift the location of the cavity resonance (see figure (6.13)). Atoms which do not participate
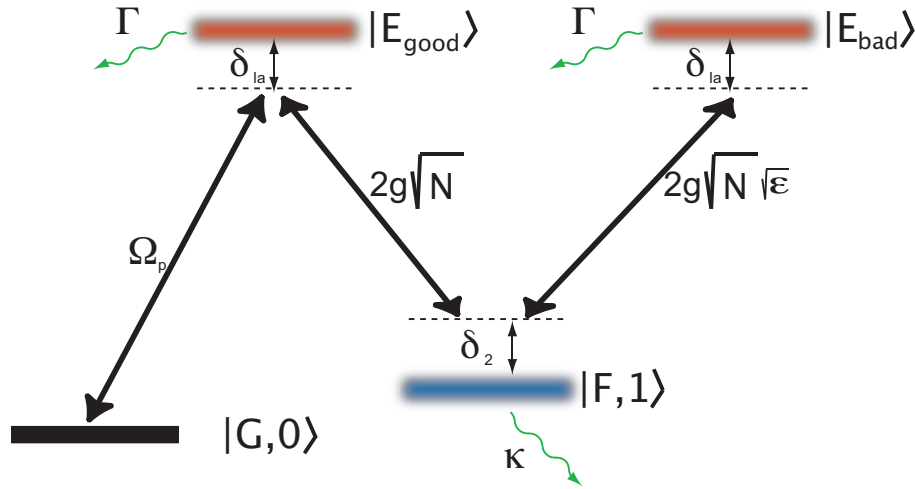
Figure 6.13: Impact of extraneous cavity coupling. If a small fraction ϵ of the atom-cavity coupling is to a different excited state $|E_{bad}\rangle$, we are left with the hamiltonian shown. The physics of this imperfection turns out to be precisely the same as that for a pump coupling to another (frequency degenerate) excited state: Far from atomic resonance this bad coupling slightly suppresses the effective cooperativity. Near atomic resonance it limits the maximum achievable retrieval efficiency.

in the write process (for example because they are not within the pump beams), but that are within the cavity, may also be analyzed this way.

It turns out that we can block-diagonalize this Hamiltonian to contain bright- and dark- states, coupled-to and uncoupled-from the cavity. The read pump beam couples our initial state to both of them, leaving us with precisely the same hamiltonian that we dealt with in the preceding section. The same conclusions about detuning dependence may thus be reached.

It is for this reason, among a variety of others, that working near atomic resonance is dangerous– our sensitivity to all sorts of misalignments is enhanced.

6.8.3   Atoms in the Wrong Initial State- Optical Pumping

An imperfectly optically pumped sample results in different atoms having different coupling strengths to the various pump beams, and cavity modes. This may be understood as destroying the complete indistinguishability of the various atoms within the magnon, or more simply as a sort of inhomogeneous broadening. As an extreme example, imagine atoms in an initial state which couples strongly to the write pump and write cavity, and only very weakly to the read pump and read cavity. These atoms will generate write photons, but almost never the corresponding read photons, and hence will reduce the retrieval efficiency.

6.8.4   Atoms in the Wrong Intermediate State- Write Polarization

If the write pump or write detection path polarization is misaligned, some write photons will correspond to atoms in the wrong intermediate state. In order to achieve collective coupling to the cavity during the read process, these atoms must undergo a transition which returns them to their initial state- this transition has the wrong polarization, and so the corresponding read photons will have the wrong polarization. In the best case this will have the effect of rotating the polarization of the read out photon, since the read-photon is now a superposition of both polarizations. More likely the dipole matrix elements will not be as favorable, and the retrieval efficiency will be reduced.

6.8.5 Non-Participating Atoms in the Intermediate State: Backgrounds and Reabsorption of Write Photons

At a write rate of n_w scattered into the cavity per trial, a total of $n_t = \frac{n_w}{\eta_w}$ atoms scatter into 4π, where $\eta_w \ll 1$ is the single atom cooperativity for the write transition. Of these n_t atoms $n_j = n_t \times b_j^w$ atoms make the j transition where $j \in \{\sigma^-, \pi, \sigma^+\}$, and b_j^w is the branching ratio of transition j.

Backgrounds read out slower than signal by a factor $N\eta_r$, independent of the detuning of the cavity from atomic resonance. As such we can estimate that the peak value of the cross-correlation will be:

$$
\begin{aligned}
g_{wr} &\approx \frac{n_w N \eta_r}{n_w (n_w N \eta_r + \sum_j n_j \eta_r b_j^r / b^r)} \\
&= \frac{1}{n_w (1 + \frac{\eta_w / \eta_r \sum_j b_j^w b_j^r / b^r}{N \eta_r})}
\end{aligned}
\tag{6.29}
$$

So we see that in fact the g_{wr} approaches the fundamental limit of $\frac{1}{n_w}$ only in the limit that $N\eta_r \gg \eta_w/\eta_r \sum_j b_j^w b_j^r / b^r$, so that the second term within equation (6.29) is suppressed. It is clear that having $\eta_w \gg \eta_r$ would be a poor decision, as it would increase our sensitivity to backgrounds, decreasing the g_{wr} and increasing $g_{rr|w}$. Ensuring that $\eta_r \gg \eta_w$ is simply a matter of geometry and atomic level choices– all cavity parameters drop out of the expression.

It also bears mention that the optical depth of absorbing atoms in the intermediate state is of order $\sum_j n_j \eta_w \approx n_w$, indicating that as n_w approaches unity the write photons begin to experience re-scattering into free-space by atoms in the intermediate state. This will degrade the observed cross-correlation and conditional autocorrelations g_{wr} and $g_{rr|w}$.

6.8.6   Choice of Level Scheme

For many of the preceding imperfections, choice of level scheme has the potential to make a big difference. If, for example, the dipole matrix element for the pump and cavity coupling transitions of interest are stronger than the matrix elements corresponding to beams of other polarizations or atoms in other states, our sensitivity to the pump polarizations, and optical pumping quality are suppressed. In contrast, if the matrix elements for the desired transition are quite weak, we can become tremendously sensitive to alignment errors!

6.8.7   Multiple-Excited-State Effects

There is an additional effect, not considered thus far, arising from scattering off of multiple excited-state hyperfine manifolds. At substantial detunings from atomic resonance the interference of multiple scattering pathways becomes important for both the collective readout and the free space scattering. Depending upon the signs and amplitudes of the various detunings and coupling coefficients, constructive and destructive interferences result. These interference effects may also shift the retrieval efficiency maximum around, so simply plotting versus optical depth at fixed detuning can be quite deceptive.

While the perturbative methods used throughout this thesis may be used to compute the impact of these effects on retrieval efficiency in closed form, the resulting expression is very complicated and provide little insight. To give a taste of the complexity, we have plotted the impact of the $F_e = 3$ and $F_e = 4$ excited states, at fixed cavity detuning of 60MHz from $F_g = 3 \rightarrow F_e = 3$, versus pump detuning from the
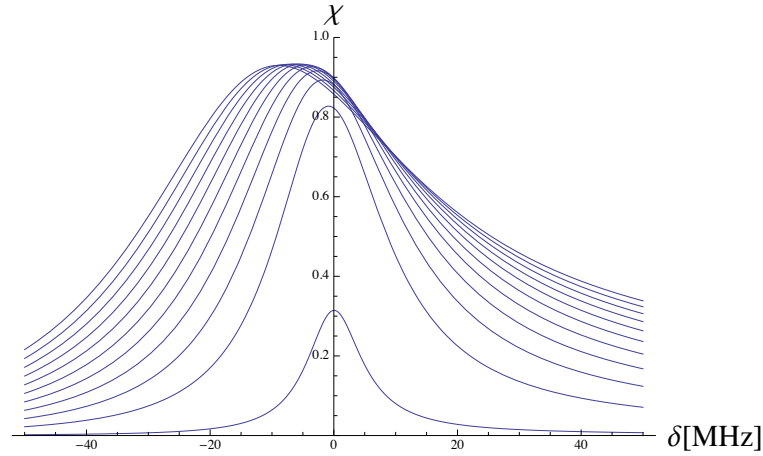
Figure 6.14: Impact of scattering off of multiple excited states. Each curve shows the retrieval efficiency at a different optical depth $N\eta$, ranging from 1 to 101 in steps of 10. The readout is performed at a cavity-detuning of 60MHz from the $F_g = 3 \to F_e = 3$ atomic resonance, where it is clear that the $F_g = 3 \to F_e = 4$ transition plays a role in the readout-process. There is an atom-induced cavity shift arising from the second transition, but more importantly the recovery efficiency does not continue to rise with $N\eta$, reaching a peak value of $\sim 93\%$.

expected EIT resonance, for a perfectly optically pumped sample, at various optical depths (referenced to the $|F_g = 3, m_F = 3\rangle \leftrightarrow |F_e = 3, m_F = 3\rangle$ transition). These curves are shown in figure (6.14).

It seems likely that without very careful choice of levels, this effect could set the ultimate limit on performance for an atomic-ensemble single photon source.

6.8.8 A Remaining Puzzle^{Printed by Mathematica for Students}

Figure (6.15) shows a scan of retrieval efficiency versus read-pump detuning from atomic resonance under near-optimal conditions, revealing high retrieval efficiency on the peak, and little structure in the wings. In contrast, figure (6.16) shows retrieval efficiency versus read-pump detuning under highly non-optimal conditions- we are
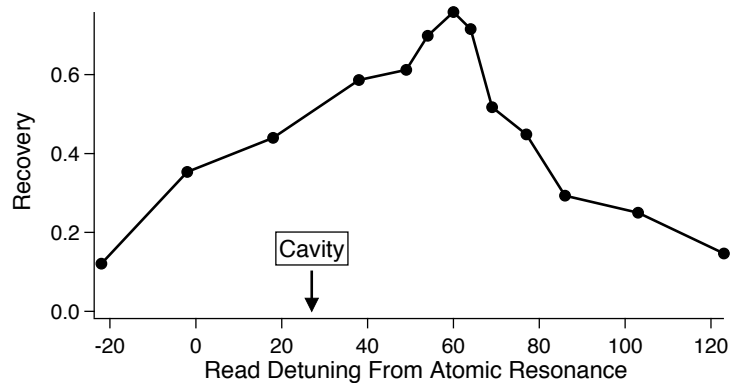
Figure 6.15: Retrieval efficiency versus read-pump detuning from atomic resonance under near-optimal conditions, with the location of the readout EIT resonance depicted with an arrow. Aside from the small shift resulting from read-beam induced stark effects and cavity couplings, the recovery peak has little structure and a single maximum.

using a different level scheme, and the read-pump beam is incident from the side. It does not seem that any one of the above mechanisms correctly predicts the detuning dependence of all four curves in figure (6.16) at once. Either the dip in the middle is too deep for the near-resonance case, or the efficiency is not higher for the off-resonance cases than the on resonance cases, or the relative peak heights are wrong. The two-excited state models were not included in this analysis, nor were the inhomogeneous pump coupling models, as it seemed unlikely that they would produce split spectra like this.

If one were interested in really optimizing this system for the maximum possible retrieval efficiency, spectra like (6.15) and (6.16) would be a good starting point. They contain a real wealth of information, and fitting them to comprehensive models of *all* of the above effects at once could prove to be a valuable diagnostic tool.
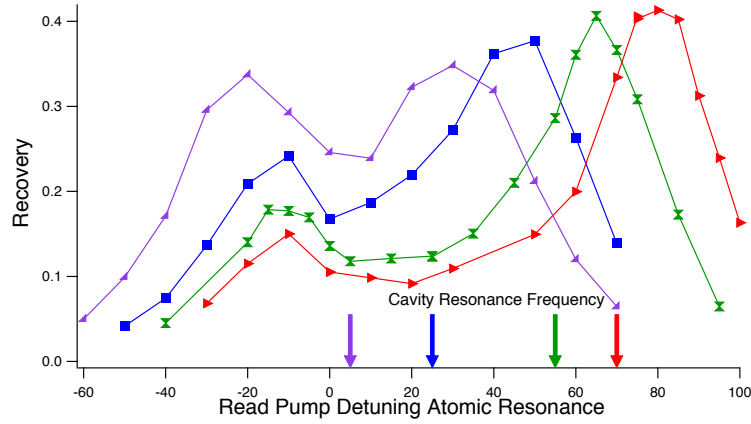
Figure 6.16: Retrieval efficiency versus read-pump detuning from atomic under non-optimal conditions. These data were taken at atom-cavity detunings of 5,25, 55, and 70 MHz, with the read-pump propagating orthogonal to the cavity mode. The peaks are split, and the retrieval efficiency is low.

6.9 Conclusion

Through a relatively systematic study of the decoherence mechanisms which limit the performance of of a single photon source, we have realized a single-magnon retrieval efficiency of 84(11)%, with proven single photon character arising from $g_{rr|w} = 0.27(21)$. We have understood the readout-time dependence of the decoherence as arising from thermal motion by observing two distinct timescales in agreement with our chosen beam geometry. If we use this Doppler curve to *extrapolate* our single-magnon retrieval efficiency to zero time, we anticipate a peak magnon-photon conversion efficiency of 90%. Larger pump-beam waists, more careful level selections, and very careful optimization of polarizations would likely allow us to push this even higher. To improve the coherence time we could add an optical lattice to confine the atoms in the Lamb-Dicke regime.

Having understood a number of fundamental properties of single photon sources

in atomic ensembles, we chose not to pursue high retrieval efficiency further. This was in part because this study was very difficult and tedious, and in part because we wanted to use our acquired knowledge to build interesting quantum devices.

In spite of the fact that our later experiments all operated at substantially lower retrieval efficiencies near 60%, the lessons we learned here were critically important. Our later work used samples optically pumped in a rotating frame, and samples defined by beams smaller than the spatial extent of the sample within the cavity. Design of these experiments depended critically upon knowledge of what imperfections we could tolerate, and which we could not- knowledge that we obtained through this study.

Chapter 7

Quantum Bus Connecting Magnon Memories

In the last chapter we discussed work towards understanding the fundamental limits on the performance of collective excitations for making single-photon sources. What we learned was essentially that the more indistinguishable the atoms can be made, the more they behave as a single super-atom, all acting in unison to release a single photon into the cavity mode. The natural question to ask, then, is how far can we extend this super-atom analogy? Can we induce a second "super-atom" to absorb a photon emitted by the first "super-atom"? Can we generate entanglement this way? What about a quantum gate?

In this chapter we will show that, with the exception of the quantum gate, all of the above is possible! We will first demonstrate the deterministic conversion of a magnon in ensemble A into a cavity photon, and into a collective excitation of ensemble B. We will then verify that the process is phase coherent, in the sense that

a partial conversion generates entanglement-on-demand between the two ensembles. The work described herein is summarized in the paper:

- *J. Simon, H. Tanji, S. Ghosh, and V. Vuletic, "Interfacing Collective Atomic Excitations and Single Photons" Nature Physics* **3**, *765 (2007).*

The groups of Kuzmich and Lukin have performed similar pitch-and-catch experiments between free-space ensembles, connected by an optical fiber[15, 78, 36]. Using EIT, they induce a B atomic ensemble to adiabatically stop a photon emitted by the A ensemble. In a seminal (and contemporary) experiment, the Kimble group demonstrated measurement-induced entanglement between two ensembles[19]. Later, in an experiment quite similar in spirit to the work described here, the Kimble group demonstrated deterministic entanglement [18].

Our experiment differs in a number of ways from the aforementioned works, most significantly in that both the A and B ensembles of our experiment are contained within a single optical resonator, whereas in all of the above works, the two ensembles are in free-space. Placing the two samples in the same cavity removes fiber coupling losses, and greatly relaxes the phase-stability requirements for entanglement generation. Additionally, our system admits a very simple physical picture based upon two-atom strong-coupling cavity QED. In this language it is evident that the emission/re-absorption experiment may be performed as a Rabi-flopping induced transfer of a magnon from one ensemble, into the cavity (in the form of a photon), and then into a magnon in the other ensemble. It may also be performed as an adiabatic transfer[88] between ensembles. It is now clear that a partial transfer will generate entanglement between the ensembles.

While the works of the Kimble, Kuzmich, and Lukin groups are most relevant to applications in quantum communication and repeaters, this work may be regarded as a step towards connecting quantum memories connected via a bus, for example for quantum computing or simulation. Such a bus needs to be phase stable, as coherence between the two memories will otherwise be destroyed as the path-length between them drifts. Generating entanglement between the ensembles via adiabatic transfer has the advantage that the phase coherence is sensitive only to the relative path length jitter between the two transfer beams, between the write-in and read-out. The apparatus is thus insensitive to DC path length drifts, and requires sub-wavelength spatial stability for timescales $\sim T_{storage}$, which in our case is $\sim \mu$s. There is little acoustical noise on these timescales, and hence the apparatus need not be actively stabilized by interferometer, as in [19].

Before we proceed to the experimental details, we shall take a brief detour to investigate how efficiently one can hope to transfer a collective excitation between two ensembles within an optical resonator.

7.1   The Transfer Process: Formalism

Our previous work with single-photon sources leads us to believe that the only important parameters ought to be $N_A \eta$ and $N_B \eta$, independent of detuning from atomic resonance, as these quantify the absorption cross sections of the two samples. One might suspect that since the one-photon cross-section decreases off-resonance, so too should the transfer efficiency. In fact the *two-photon* absorption cross section is independent of detuning from atomic resonance[13], and so we expect no excited-state

detuning dependence.

One might also expect the transfer to have an efficiency of $\frac{N_A\eta}{1+N_A\eta}\frac{N_B\eta}{1+N_B\eta}$, in analogy with a single-photon source, and its time reversal. This is not the case, however, as a single-photon source need not keep the whole photon *within* the cavity mode at one time– cavity leakage is permissible. In contrast, coherence transfer depends upon small cavity leakage, and hence, as we will see, requires larger optical depth.

A formal understanding of the adiabatic transfer process may be reached using the methods of chapter (2) to generate the collective states participating in the transfer process, and their couplings under the influence of the Hamiltonian. We ignore all inhomogeneous coupling effects, as they do not impact the fundamental physics:

Having prepared a collective excitation in the A sample via the write process, the transfer process between the two samples may be understood in terms of a five-level system (see figure (7.1)). converting a collective excitation in the A sample into a cavity photon, into a collective excitation in the B sample. The collective excitation prepared by the write process is:

$$|f_A\rangle \equiv \sqrt{\frac{2}{N}} \sum_{j \in S_A} e^{i\vec{k}_w^p \cdot \vec{x_j}} \cos(\vec{k}_w^c \cdot \vec{x_j}) \sigma_{FG}^j |\Omega\rangle \tag{7.1}$$

where $S_A(S_B)$ is the set of atoms addressed by the A(B)-sample pump beams. The A-sample read-pump beam (with Rabi frequency Ω_p^A) converts the ground-state magnon into a polariton:

$$|e_A\rangle \equiv \sqrt{\frac{2}{N}} \sum_{j \in S_A} \cos(\vec{k}_w^c \cdot \vec{x_j}) \sigma_{EG}^j |\Omega\rangle \tag{7.2}$$

The atom-cavity coupling converts the state $|e_A\rangle$ into a state with a single photon in the cavity:

$$|c\rangle \equiv a^\dagger |\Omega\rangle \tag{7.3}$$
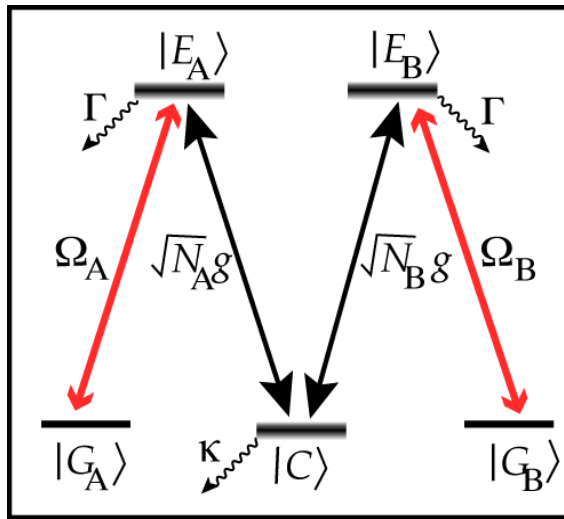
Figure 7.1: Hamiltonian for magnon transfer between two atomic ensembles A and B. The magnon in the A ensemble $|G_A\rangle$ is converted into a polariton ($|E_A\rangle$) via the A-pump beam with Rabi frequency Ω_A. The polariton in ensemble A collectively emits into the cavity, generating a cavity photon ($|C\rangle$) with Rabi frequency $\sqrt{N_A}g$. This cavity photon is then absorbed by the B ensemble, generating a polariton ($|E_B\rangle$) with a Rabi frequency $\sqrt{N_B}g$. Finally the polariton in the B ensemble is converted into a magnon in the B ensemble with Rabi frequency Ω_B, by the B-pump beam. This Hamiltonian applies regardless of whether the transfer is adiabatic, or a four-photon Rabi-flop, or something in-between.

with a collective Rabi-frequency $\sqrt{N_A}g$. Before the photon can leak out of the cavity, it is collectively absorbed by the B-sample, with collective Rabi-frequency $\sqrt{N_B}g$, generating the state:

$$|e_B\rangle \equiv \sqrt{\frac{2}{N}} \sum_{j \in S_B} \cos(\vec{k}_r^c \cdot \vec{x}_j) \sigma_{EG}^j |\Omega\rangle \tag{7.4}$$

The atoms are then de-excited the B pump-beam with Rabi-frequency Ω_p^B, into the state:

$$|f_B\rangle \equiv \sqrt{\frac{2}{N}} \sum_{j \in S_B} e^{-i\vec{k}_r^p \cdot \vec{x}_j} \cos(\vec{k}_r^c \cdot \vec{x}_j) \sigma_{FG}^j |\Omega\rangle \tag{7.5}$$

In this notation, the Hamiltonian (depicted in figure (7.1)) is then:

$$
\begin{aligned}
H &= (\Delta + I\frac{\Gamma}{2})(|e_A\rangle \langle e_A| + |e_B\rangle \langle e_B|) + I\frac{\kappa}{2} |c\rangle \langle c| \\
&+ (\frac{\Omega_p^A}{2} |e_A\rangle \langle f_A| + \frac{\Omega_p^B}{2} |e_B\rangle \langle f_B| + H.C.) \\
&+ (\sqrt{N_A}g |c\rangle \langle e_A| + \sqrt{N_B}g |c\rangle \langle e_B| + H.C.)
\end{aligned} \tag{7.6}
$$

Having ascertained the levels which are coupled during the transfer process, the question becomes: *How efficiently can we transfer an excitation from $|f_A\rangle$ to $|f_B\rangle$, without losing it due to free-space scattering from the excited states $|e_A\rangle$ and $|e_B\rangle$ or cavity leakage from the state $|c\rangle$?*

We will show that the transfer efficiency is a function only of $N\eta$ whether we are far off resonance, in which case we may consider the transfer process as multi-photon Rabi flopping, or on resonance, where we may consider the transfer as an adiabatic dark-state transfer.
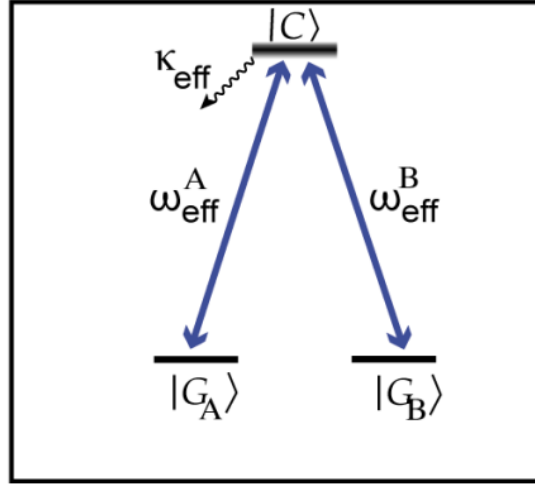
Figure 7.2: 3-Level Hamiltonian for off-resonant transfer of a single magnon between ensembles A and B. The couplings ω_A and ω_B are effective, two-photon Rabi couplings. In this limit the levels $|G_A\rangle$ and $|G_B\rangle$ have acquired linewidths(not shown) arising from their couplings to $|E_A\rangle$ and $|E_B\rangle$.

7.1.1 Off-Resonant Case: Four-Photon Rabi Flopping

In the case that we are detuned from the excited state by Δ, and the cavity by δ, we may adiabatically eliminate the cavity and excited states, leaving the three-level Hamiltonian shown in figure (7.2). We may then compute the loss during a $\frac{\pi}{2}$ pulse from $|f_A\rangle$ to $|f_B\rangle$:

For computational simplicity we will set $N_A = N_B = N_S$, with $\Omega_p^A = \Omega_p^B = \Omega_p^s$. We will work below saturation, in the large detuning limit, such that $\Omega_p, \sqrt{N}g < \Delta$, $\Omega_p \sqrt{N}g < \delta\Delta, \delta > \kappa$, and $\Delta > \Gamma$. This gives us a loss rate from each of our two remaining states of $\Gamma_t = \frac{\Omega_p^{s\,2}}{4\Delta^2}\Gamma + \frac{(\frac{\Omega_p^{s\,2}\sqrt{N_S}g}{2\Delta})^2}{4\delta^2}\kappa$, and a four-photon Rabi frequency of

$$\Omega_4 = \frac{(\frac{\Omega_p^s \sqrt{N_S} g}{2\Delta})^2}{2\delta}.$$

In the limit that $\Omega_4 > \Gamma_t$, the transfer Rabi-flopping process requires at time $T \approx \frac{\pi}{\Omega_4}$. The transfer efficiency $Q_{transfer}$ is then given by the flopped population:

$$Q_{transfer} = e^{-\Gamma_t T} = e^{-\frac{\pi \Gamma_t}{\Omega_4}} \tag{7.7}$$

We optimize this efficiency over δ, the detuning from the cavity resonance, and find a maximum at a detuning of $\delta = \sqrt{N_S \eta} \frac{\kappa}{2}$ of:

$$Q_{transfer}^{max} = e^{-\frac{2\pi}{\sqrt{N_S \eta}}} \tag{7.8}$$

This maximum may be understood as a tradeoff between losses due to cavity leakage and losses due to free-space scattering. If the detuning from the cavity state $|c\rangle$ is small then the $\frac{\pi}{2}$ pulse takes places very quickly, and there is little free space scattering, but the cavity leakage rate is high. If the detuning from the cavity state is large then there is very little cavity leakage, but the $\frac{\pi}{2}$ pulse is quite slow, so there is a lot of free-space scattering. It is interesting that the performance is not actually dependent upon the pump strengths, or detuning from the excited states, as long as they have appropriate values for adiabatic elimination of the excited state (ie we are in the detuned limit).

Considering instead the (slightly more accurate) expression:

$$Q_{transfer} = e^{-\Gamma_t T} \sin^2 \frac{\Omega_4}{2} t \tag{7.9}$$

and optimizing over both T and δ, we find:

$$Q_{transfer}^{max} = \frac{N_S \eta}{4 + N_S \eta} \left(\sqrt{-1 + \frac{4}{2 - i\sqrt{N_S \eta}}} \right)^{\frac{4i}{\sqrt{N_S \eta}}} \tag{7.10}$$

This expression is somewhat more accurate at small $N_S \eta$.

Using an analysis similar to the simpler of the above two, and allowing for different pump strengths Ω_p^A and Ω_p^B, as well as different atom numbers N_A and N_B reveals an optimum for $\frac{\Omega_p^B}{\Omega_p^A} = \sqrt[4]{\frac{N_A}{N_B}}$, of:

$$Q_{transfer}^{max} = \exp\left(-\frac{2\pi}{\sqrt{\eta \frac{2N_A N_B}{N_A + N_B + 2\sqrt{N_A N_B}}}}\right) \quad (7.11)$$

If $N_A = N_B$ this expression reduces to equation (7.8), as expected. If either N_A or N_B is substantially larger, the transfer efficiency is then limited by the smaller of the two. What this means is that we cannot efficiently transfer from an ensemble to a single atom if the system is in the ensemble strong-coupling limit, but the single-atom weak coupling limit.

7.1.2 Resonant Case: Dark State Rotation

When atomic and excited state detunings are small ($\delta, \Delta = 0$), the transfer process must be performed using the so-called counter-intuitive pulse sequence, or STImulated Raman Adiabatic Passage (STIRAP[87]). In this process, the system is constantly maintained in a dark state of the control laser beams, such that the atom is never placed in an excited state, and hence may never scatter into free-space. By adjusting in time the relative intensities of the pump beams, the excitation is transferred from the A-sample to the B-sample. The more slowly the process takes place, the less diabatic excitation of the atoms occurs, and hence the less freespace scattering. When the excitation is shared equally between the two samples, however, there is a substantial cavity population. As such, if the transfer process takes place too slowly,

much of the excitation will be lost into free-space. We will now estimate the optimal

transfer rate.

For computational simplicity we will choose equal atom numbers for the two samples, $N_A = N_B = N_S$, and a pulse sequence $\Omega_p^{A,B} = \Omega_s(\sin \alpha t, \cos \alpha t)$. $\frac{\pi/2}{\alpha}$ is now the time required for the transfer process. Under these conditions the dark state of equation (7.6) at time t is given by:

$$|\psi_D\rangle = \frac{\cos \alpha t \, |f_A\rangle - \frac{1}{2} \frac{\Omega_p^s}{2\sqrt{N_S}g} \sin 2\alpha t \, |c\rangle + \sin \alpha t \, |f_B\rangle}{\sqrt{1 + \frac{1}{2}(\frac{\Omega_p^s}{2\sqrt{N_S}g})^2 \sin^2 2\alpha t}} \tag{7.12}$$

The cavity loss during the transfer process is given by (where for simplicity we assume $\Omega_p^s \ll \sqrt{N_S}g$):

$$\begin{aligned} \mathcal{L}_{cav} &= \int_0^{\frac{\pi}{2\alpha}} dt \, |\langle c \, |\psi_D \rangle|^2 \, \kappa \\ &= \frac{\pi \Omega_p^{s2}}{64 N_S g^2 \alpha} \end{aligned} \tag{7.13}$$

The loss due to diabatic transitions may be computed by realizing that in the basis of instantaneous eigenstates $\{|j\rangle\}$, there is an additional coupling between amplitudes of the form[75]: $-\sum_j \left(\frac{d}{dt} |j\rangle\right) \langle j|$. From this we see that(again for $\Omega_p^s \ll \sqrt{N_s}g$):

$$\frac{d}{dt} |\psi_D\rangle \approx -\alpha \sin \alpha t \, |f_A\rangle - \frac{\alpha \Omega_p^s}{s\sqrt{N_S}g} \cos 2\alpha t \, |c\rangle + \alpha \cos \alpha t \, |f_B\rangle \tag{7.14}$$

So we see that non-adiabaticity drives Rabi-couplings to bright components of the atomic ground state, with Rabi-frequencies given by $\Omega_D^{A,B} = 2\alpha\{\sin \alpha t, \cos \alpha t\}$. These bright components of the atomic ground state have linewidths of order $\Gamma_{Bright}^{A,B} = \frac{\Omega_p^{s2}}{\Gamma} \times \{\sin^2 \alpha t, \cos^2 \alpha t\}$ set by their coupling to the excited state. As such the rate of population leaving the dark state due to the diabatic couplings is $\Gamma_{Diabatic}^{A,B} = \frac{\Omega_D^{A,B\,2}}{\Gamma_{Bright}^{A,B}} =$

$\frac{\alpha^2}{\Omega_p^{s2}/\Gamma}$, and so the total loss due to diabatic couplings is:

$$
\begin{aligned}
\mathcal{L}_{Diabatic} &= (\Gamma_{Diabatic}^A + \Gamma_{Diabatic}^B)\frac{\pi}{2\alpha} \\
&\approx \frac{8\alpha^2}{\Omega_p^{s2}/\Gamma}\frac{\pi}{2\alpha}
\end{aligned}
\tag{7.15}
$$

Combining this expression with the cavity loss terms gives for the total loss:

$$
\begin{aligned}
\mathcal{L}_{Tot} &= \mathcal{L}_{cav} + \mathcal{L}_{Diabatic} \\
&= \frac{\pi\Omega_p^{s2}}{64N_S g^2\alpha} + \frac{8\alpha^2}{\Omega_p^{s2}/\Gamma}\frac{\pi}{2\alpha}
\end{aligned}
\tag{7.16}
$$

Minimizing this quantity over α yields a maximum for $\alpha = \frac{\Omega_p^{s2}/\Gamma}{8\sqrt{2}\sqrt{N_S\eta}}$ of:

$$
\mathcal{L}_{Tot} = \frac{\pi}{\sqrt{N_S\eta}}
\tag{7.17}
$$

In the small loss limit where this expression is valid, it is identical to the expression for the off-resonant case, up to a factor of 2. Because the on-resonant case was computed only approximately, owing to the complicated dark-state rotation angle dependence, this small discrepancy in numerical factors is not so surprising.

7.1.3 Interpretation

In the large optical-depth limit, the failure rate of a triggered single-photon source is $\mathcal{L}_{source} \approx \frac{1}{N_S\eta}$. Our initial expectation was that the dark-state transfer could be understood as emission and then absorption of a single photon, and hence would have an error rate $\mathcal{L}_{transfer} \approx \frac{2}{N_S\eta}$. Our calculation reveals that because the transfer will only be successful if the excitation does not leak out of the cavity, it has a loss rate $\mathcal{L}_{transfer} \approx \frac{2\pi}{\sqrt{N_S\eta}}$. This is not so surprising, as it indicates that the (coherent) transfer

process, which is essentially a Rabi-flopping process, has an efficiency which scales as $\frac{1}{\sqrt{\eta}} \propto \frac{1}{g}$, and not $\frac{1}{\eta} \propto \frac{1}{g^2}$

This square-root scaling of the transfer with optical depth means that we need a *much* higher optical depth than we would need to achieve similar efficiencies for a single-photon source. This is very interesting because there are schemes to make quantum gates using single atoms within an optical cavity, and adiabatic transfer[88]. In order to attain a gate fidelity of 99% a single-atom cooperativity of $\eta = 400000$ would be required. The highest realized cooperativity in cold-atom cavity QED experiments is ~ 400 for Fabry-Perot resonators[96], with an anticipated maximum[55] of approximately ~ 6000, for a cavity of length $\frac{\lambda}{2}$! This is still a far cry from $\eta = 400000$, indicating that quantum computing will be very difficult to realize with a Fabry-Perot cavity. By contrast, the toroidal resonators[115, 25] have the potential to reach single atom cooperativities of order 5×10^6, making them a much more realistic candidate for fault tolerant quantum computing.

More to the point for our experiment, we see that with a modest optical depth $N_S \eta \approx 10$ we expect to be able to achieve a transfer efficiency $e^{-\frac{2\pi}{\sqrt{N_S \eta}}} \approx 0.14$. In fact, the above adiabatic models become inaccurate in the large-loss limit, and numerical modeling reveals that in fact an optical depth of 10 will allow admit a substantially higher transfer efficiency of 40%. We have also shown in this section that we are free to work at whatever detuning from atomic resonance is most technically beneficial, without sacrificing transfer efficiency.

7.2 Experimental Setup

In qualitative terms, our experiment is quite simple: We prepare two atomic ensembles A and B within an optical resonator, and drive the write-process in sample A. Detection of a write-photon prepares a magnon in ensemble A. Reading out this magnon generates a read-photon within the cavity, which may then be absorbed by ensemble B. By applying a laser beam to the B ensemble we may cause it to convert the absorbed photon into a magnon in ensemble B, rather than scattering it into free-space. Depending upon whether we want to demonstrate a transfer or entanglement, we either read out the magnon directly from sample B into the cavity mode, or make more sophisticated joint measurements of the two ensembles.

Our experimental setup is shown in figure (7.3). Instead of preparing two spatially distinct samples within two optical dipole traps/lattices, we work with one large polarization gradient cooled MOT at temperature $T \approx 20\mu$K of rms size 1mm. From this MOT we simply select out two samples with spatially non-overlapping beams. The A sample is defined by a write-beam and a phase matched read-beam. The B sample is defined by only one pump beam. This is because the transfer process writes a magnon into the B sample via stimulated emission *into* the pump beam, and so read-out from the B sample will be phased matched with a single photon *absorbed* from the same beam.

Because the pump-beams define the samples there are a quite a number of atoms within the cavity mode which are part of neither sample A nor sample B. This means that the transfer and read-out processes must take place at finite detuning from atomic resonance to avoid re-absorption by the non-participating atoms. With
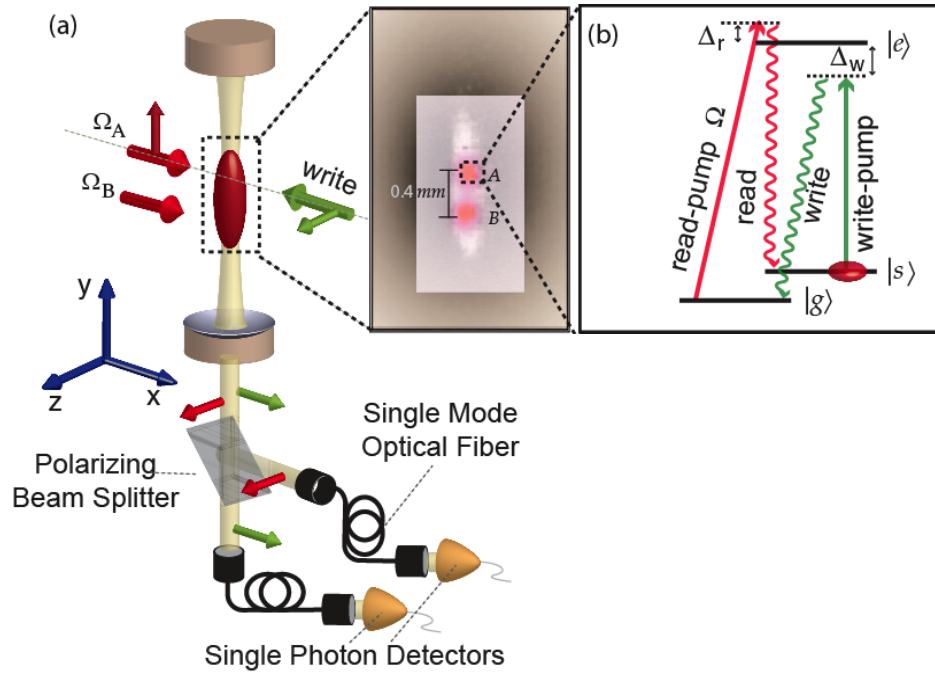
Figure 7.3: **(A)** Schematic of experimental setup to demonstrate adiabatic transfer of a magnon from one sample (A) to another (B). The two samples subsets of the atoms within a single MOT, defined by the pump beams. All inferences about atomic states are made via measurement of the cavity leakage detected on two SPCMs which are coupled to the two polarizations of the TEM_{00} mode of the cavity. The inset shows the MOT with the pump-beam defined sub-samples overlaid. **(B)** The level scheme chosen for the write-in and read-out/transfer. Because the intermediate state $|G\rangle$ is in a different hyperfine groundstate from the initial state $|S\rangle$, the write-in and read-out took place four cavity FSRs apart and hence had different detunings from the excited state. A read detuning of 20MHz was experimentally found to limit re-absorption of read-photons by non-participating atoms while minimizing other sources of decoherence which could reduce the transfer and retrieval efficiencies.
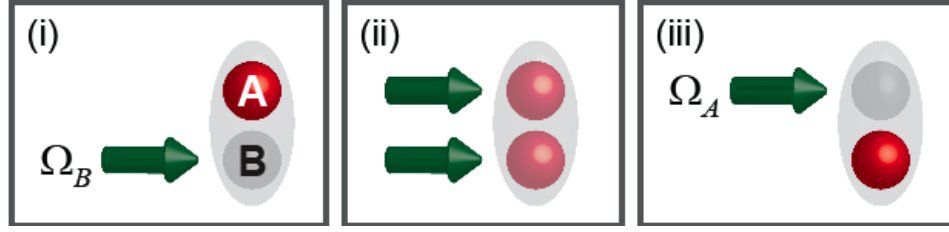
Figure 7.4: Schematic of the STIRAP sequence to transfer a magnon from a sample A and to a sample B. **(i)** The B pump is applied to the B-sample, ensuring that the system dark-state is exclusively $|G_A\rangle$. **(ii**) The A-pump is turned on adiabatically so that the system remains in the "dark"-state, with the magnon is shared between the two samples. **(iii)** the B-pump is adiabatically turned off, (ideally) leaving the entire magnon in the B sample.

this consideration in mind we chose to read out (and transfer) $\Delta = 20$MHz off of atomic resonance. At this detuning, the non-participating atoms only broaden out the cavity resonance by $\kappa \times \frac{N_{nonpart}\eta}{1+(\frac{\delta}{\Gamma/2})^2} \approx \kappa \times 0.02 \times N_{nonpart}\eta$. As such, even a non participating optical depth $N_{nonpart}\eta = 10$ only increases the cavity linewidth by 15%, reducing the transfer efficiency by a similar amount. By the same token, at an optical depth $N_S\eta = 1$, $\frac{2\sqrt{N_S}g}{\Delta} \approx \frac{1}{3}$, and so the transfer process is nearly on-resonance. As such we can treat the transfer process as a dark-state rotation and use the counter-intuitive STIRAP pulse sequence, shown in figure (7.4).

The experiment was performed in a cavity with finesse $\mathcal{F} \approx 240$, and a waist size of $w_c \approx 110\mu$m. This yields a maximum cooperativity of $\eta \approx \frac{\mathcal{F}}{"5"} \frac{\lambda^2}{w_c^2} \approx 3 \times 10^{-3}$. The cavity length of 6.6cm gives a cavity linewidth $\kappa = 2\pi \times 9.5$MHz. The pump beams have waist of $w_p = 210\mu$m, defining samples of r.m.s. dimensions[1] 55μm$\times55\mu$m$\times105\mu$m, separated by 390μm, as shown in figure (7.3a, inset). The read-pump beams have typical Rabi frequencies $\Omega_{A,B} \approx 2\pi \times 50$MHz.

---

[1]The other two sample dimensions are determined by the cavity waist w_c.

7.3   Polarization Sensitive Cavity Transmission Spectroscopy: Optical Pumping

As we learned previously, high quality optical pumping is critically important to achieving strong coupling and high readout efficiency of stored magnons. In this experiment we moved away from microwave spectroscopy for optimizing our optical pumping, and instead used a polarization sensitive cavity transmission spectroscopy. This was achieved by temporarily tuning the cavity to an atomic resonance wherein, once the sample was properly pumped, one polarization would couple strongly to the atoms and experience a large vacuum Rabi splitting, and the other would be entirely uncoupled from the atoms and hence have no vacuum Rabi splitting.

Because we have many atoms in our system, we could scan across the full Rabi-resonance in a single run, compared to the *hundreds* of runs necessary to achieve a full microwave spectrum.[2] Achieving good optical pumping is subtle and time consuming, as one must simultaneously optimize the polarization of the pump beam, the direction of the bias field, and the orientation of polarizing optics in the detection path. We must ensure not only that the sample is well polarized along the quantization axis defined by the bias field, but also that this field is aligned relative to the cavity axis. Cavity spectroscopy is sensitive to *all* of these misalignments, while microwave spectroscopy is insensitive to the alignment of the bias field to the detection axis.

---

[2]While there were tricks to make microwave spectroscopy based optical pumping optimization faster, I did not find them to be as robust as the cavity transmission spectroscopy technique. For initial alignments and magnetic field zeroing in particular, the microwaves are quite helpful, as they provide more detailed information about the atomic population distribution and the magnitude of the magnetic field via the Zeeman splittings.

As our experiments have grown in complexity and good optical pumping has become more crucial, we have found real-time diagnostics for optical pumping to be invaluable.

7.4 Experimental Transfer Sequence

At the beginning of each trial, all atoms are optically pumped into the state $|G\rangle = |F = 4, m_F = 4\rangle$ by two circularly polarized laser beams propagating along the 900 mG bias field which defines the quantization axis. This bias field is oriented in the $\hat{z}$ direction, perpendicular to the cavity axis. The write beam, which propagates in the plane of the quantization axis, and is polarized along it, is applied to the A sample for 90ns, tuned 110MHz to the red[3] of the $|G\rangle \to |E\rangle \equiv |F = 4', m_F = 4\rangle$ transition, at a typical peak intensity of $100\mathrm{mW}/cm^2$. The cavity is tuned to the write-beam Raman resonance on the hyperfine changing $|G\rangle \to |E\rangle \to |F\rangle \equiv |F = 3, m_3\rangle$ transition. Detection (via SPCM) of a "write" photon leaking from the cavity heralds the creation of a magnon in the A sample, projecting the system into the state $|f_A\rangle$[4].

Subsequent to the detection of the write photon from ensemble A, application of a phase-matched read pump beam was used to convert the magnon into a single photon. This beam was linearly polarized[5] along the cavity $(\hat{y})$ axis, and tuned 20MHz to the

---

[3]The write detuning was chosen so that the read process could take place at a detuning of 20 MHz from atomic resonance.

[4]Our level selection means that the atom may only scatter σ^+-polarized photons when it undergoes the hyperfine changing transition. Only the $\hat{x}$ polarized component may be scattered into the cavity, and so we polarization analyze with a PBS and condition upon only $\hat{x}$-polarized detection events.

[5]One might worry that the read beam would also drive $|F\rangle \to |E'\rangle \equiv |F = 4', m_F = 2\rangle$ free-space scattering, destroying the magnon rather than reading it out. It turns out that the coupling matrix element for this process is smaller by a factor of $\sim \sqrt{40}$, and so the rate is suppressed by a factor of ~ 40. Even in the on-resonance limit, where collective effects slow down the transfer and readout,

blue of the $|F\rangle \rightarrow |E\rangle$ transition, such that another cavity mode, 4 FSR's from that used from the write process, was in resonance with the field scattered on the $|F\rangle \rightarrow |E\rangle \rightarrow |G\rangle$ transition. The beam used for this readout process has a typical Rabi frequency of $\Omega_p^A = 2\pi \times 40\text{MHz}$, at a waist size of 210μm. With this setup we observe retrieval efficiencies nearing 40%, limited by the sample optical depth $N_A\eta \approx 1$[6] The total detection efficiency for a photon generated within the cavity was $q_e = 0.11(2)$, due to the quantum efficiency of the photon counter ($q_{spcm} = 0.40(5)$), cavity output coupling ($q_{cav} = 0.43(1)$), and fiber coupling and other losses ($q_{misc} = 0.66(4)$).

The transfer was realized by application of a second pump beam, Ω_p^B, defining the B ensemble, which was phase-locked to Ω_p^A, with parallel propagation direction and polarization.. The B-pump had a Rabi frequency of $2\pi \times 70\text{MHz}$, and was turned on in accordance with the counter-intuitive STIRAP pulse sequence described previously. The lasers need to be phase locked because any phase jitter between them destroys the coherence of the transfer process- this would both reduce the transfer efficiency, and ruin any entanglement generated by a partial transfer. This phase lock is achieved by deriving both Ω_p^A and Ω_p^B from the same laser, switched with AOMs driven with the same RF signal. For entanglement verification it will be important to adjust the optical phase between write-in and read-out, which we achieve by jumping the RF-phase sent to one of the AOMs (see figure (7.5)).

The pump waveforms $\Omega_p^A(t)$, $\Omega_p^B(t)$ used for the STIRAP transfer process are

---

this free space scattering rate is not enough to limit our experiment, owing to its small OD.

[6]Increasing the optical depth would have been difficult, and we would quickly have run into limits arising from inhomogeneous broadening due to the pump waist being substantially smaller than the MOT size. Dipole traps to increase the density and create two spatially separated samples would have solved these problems.
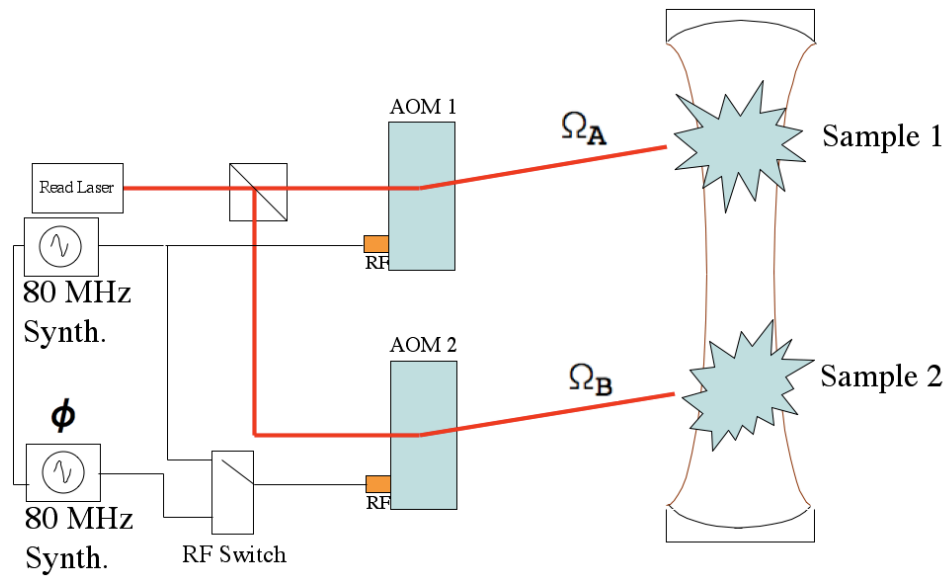
Figure 7.5: Setup for fast (100ns) jumping of Ω_b phase between transfer and readout. Ω_A and Ω_B are derived from the same laser. For the transfer process the two pump beams Ω_A and Ω_B are driven by the same synthesized source. For the readout the Ω_B is switched to a second, phase-locked source which is phase-shifted by ϕ. The delay of 100ns arises from the latency of the RF switch and propagation delays in cables and in the acousto-optic crystal.
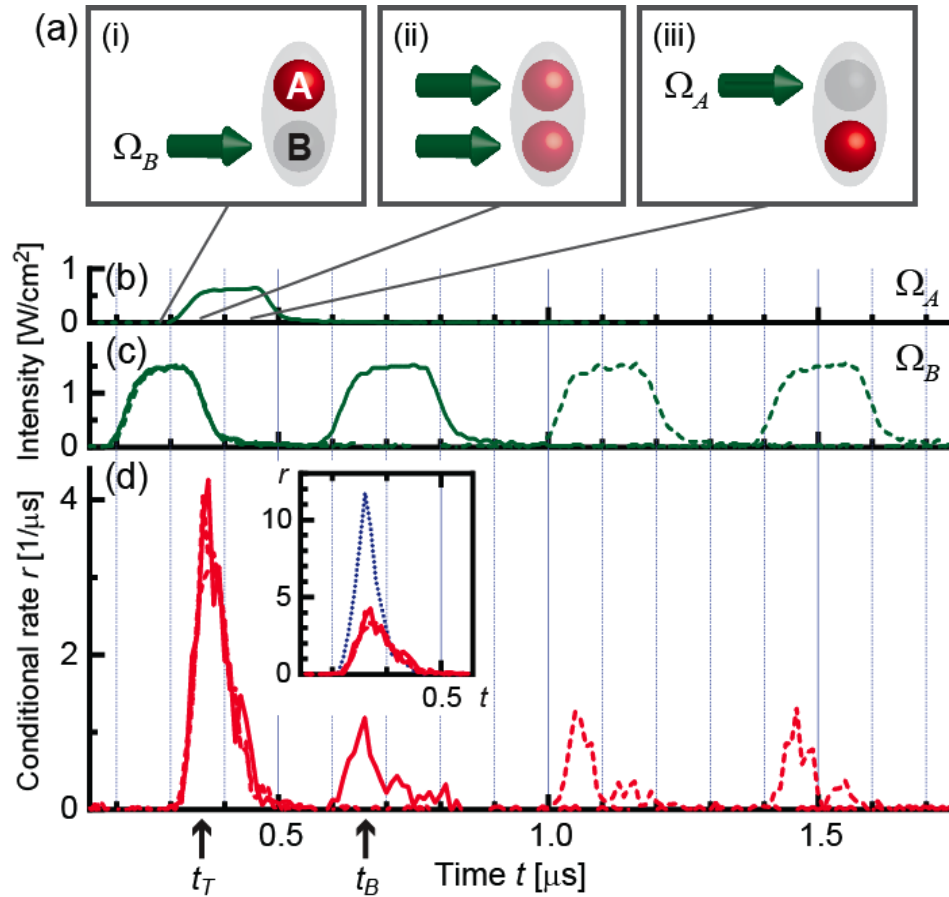
Figure 7.6: **(A)** Schematic of adiabatic transfer process. **(B,C)** Measured pump waveforms for cavity mediated adiabatic transfer of a magnon between atomic ensembles. The B pump is turned back on in order to read the transferred excitation back into the cavity, for verification purposes. **(D)** Observed cavity leakage during transfer and readout. Inset: Blue is cavity leakage in the absence of a pump beam on the B sample, and red is with the pump beam on the B sample present. The suppression of cavity leakage in the presence of the B pump is a signature of the dark-state suppression of cavity population.

shown in figure (7.6b,c), with the corresponding cavity leakage in figure (7.6d). As is visible in the cavity leakage waveform, the B-pump is turned back on to read the excitation back into the cavity at a later time, as a means of measuring the transfer efficiency. Assuming that sample B has a readout efficiency similar to sample A, we observe transfer efficiencies between 10% and 25% for optical depths $N_{A,B}\eta$ between $.4 \sim 1$. These efficiencies are substantially better than what we would expect from equation (7.8), indicating that the adiabatic elimination used to derive this equation is invalid in the large-loss limit. Direct numerical integration of the differential equations yields a maximum transfer efficiency of 6% for $N_S\eta = 1$, and 24% for $N_S\eta = 4$ (see figure (7.7)), indicating that we have most likely under-estimated our atom number.

Figure (7.6d, inset) shows the cavity leakage during the transfer both with, and without, the B-pump beam. In the absence of the B-pump, there is substantially more cavity leakage- this is direct evidence that our understanding of the transfer as a dark state rotation with suppressed cavity population is valid.

7.4.1 Aside: Excitation Lifetimes and Transfer-Induced Enhancement

The recovery versus storage time from each of the A and B samples are shown in figure (7.8). These curves have the gaussian shape typical of doppler decoherence, as described in chapter (6). The lifetimes of 1.3μs and 1.7μs in the A and B samples, correspond to temperatures of 50μK and 20μK, respectively. To compute these temperatures we utilize our knowledge of the $90°$ angle between pump-beams and cavity axis. It is not so surprising that the A sample is at a higher temperature, as we scatter
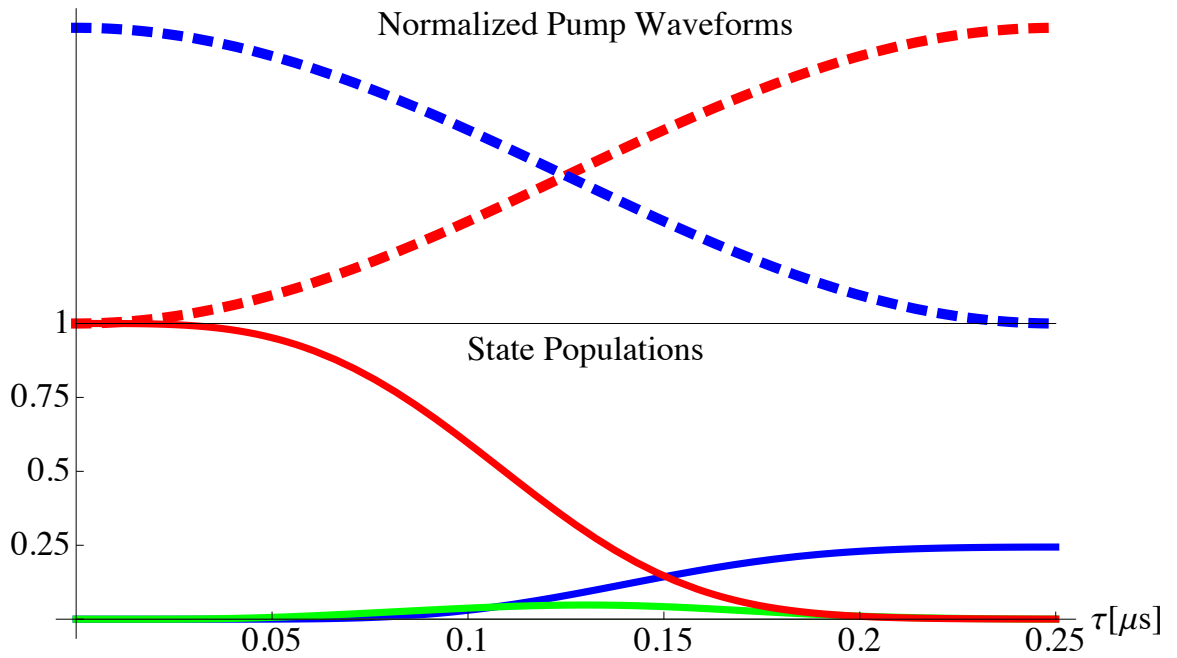
Figure 7.7: Simulation of the 5-level dynamics of the transfer process. The dashed curves show the normalized A and B pump intensities in red and blue, respectively. The solid curves show the populations of $|f_A\rangle$, $|c\rangle$, and $|f_B\rangle$ in red, green, and blue respectively. The simulation takes place at $N\eta_{A,B} = 4$, with peak pump intensities $\Omega_{A,B}^{max} = 2\pi \times 10\text{MHz}$, on atomic resonance. The transfer efficiency is 24%.
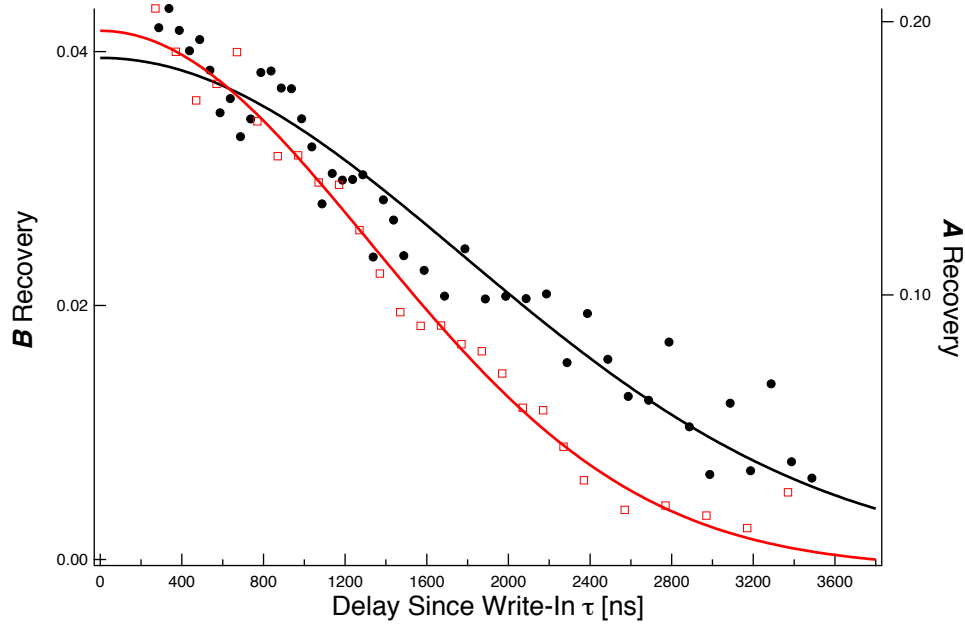
Figure 7.8: Coherence time of original and transferred magnons. The open red squares correspond to the retrieval efficiency of the magnon written into the A sample, while the filled black circles correspond to the retrieval efficiency of the magnon transferred to the B sample. The solid red curve is a gaussian fit to the A data, with a doppler lifetime of 1.3μs corresponding to 50μK. The solid black curve is a gaussian fit to the B data, with a doppler lifetime of 1.7μs, corresponding to a temperature of 20μK. The temperature difference arises from recoil heating of the A sample.

many more photons off of it during the write process, leading to recoil heating.

The gaussian decay of the recovery for the transferred excitation is consistent with a curve centered on the *transfer* time, indicating that coherence is reset upon transfer. It is thus conceivable that given sufficiently high transfer efficiency, one could increase the storage time of a magnon by transferring it between samples before the doppler decoherence destroys it. This is more a curiosity than a useful tool, since long storage times can also be achieved via the Lamb-Dicke regime[29] in an optical lattice[35].

As an example (see figure (7.9): At $\tau = 10\tau_D$, we expect a retrieval efficiency of $e^{-100} \approx 10^{-44}$. At a transfer efficiency of 90%, the optimal retrieval of 14% is
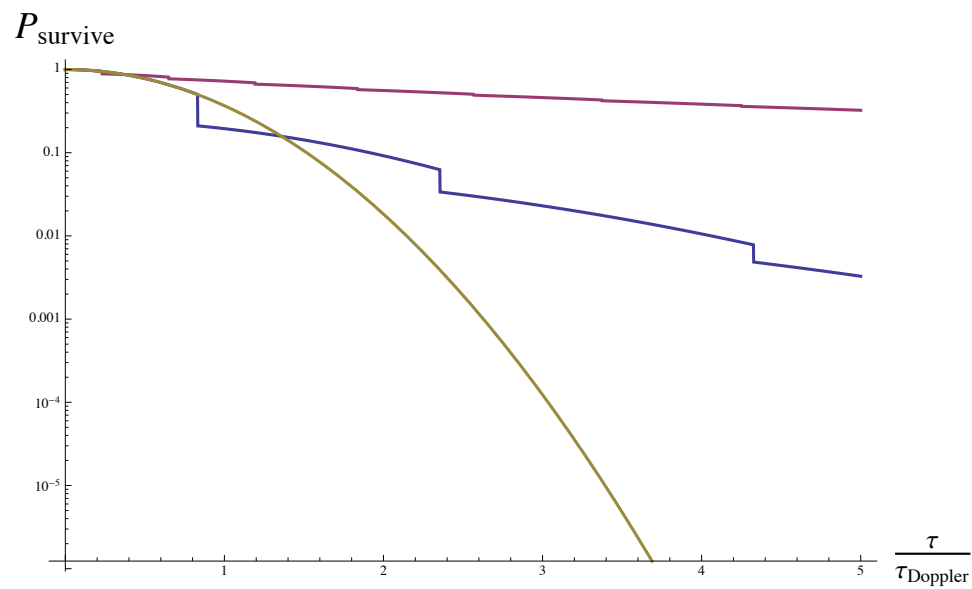
Figure 7.9: Enhancement of magnon lifetime via repeated adiabatic transfer. *Gold Curve:* No adiabatic transfers, and hence a simple gaussian decay of excitation as the storage time is increased. *Blue Curve:* Transfer efficiency of 25%, and *Red Curve:* Transfer efficiency of 90%. We see that within 3 doppler times the transferred magnon has a larger survival probability than the untransferred magnon by ~ 2 orders of magnitude, even for a transfer efficiency of only $\sim 25\%$.

achieved with 12 transfers. Even at a transfer efficiency of 25%, 5 transfers increase the retrieval efficiency to 10^{-5}, an improvement by 39 orders of magnitude!

7.5   Entanglement Generation and Verification

We begin by rewriting the expression for the dark state of the system during the transfer process, including an additional spatial phase arising from the differing path lengths for the A and B pumps, φ

$$|\psi_D\rangle = \frac{\cos \alpha t \, |f_A\rangle - \frac{1}{2} \frac{\Omega_p^s}{2\sqrt{N_S}g} \sin 2\alpha t \, |c\rangle + e^{i\varphi} \sin \alpha t \, |f_B\rangle}{\sqrt{1 + \frac{1}{r}(\frac{\Omega_p^s}{2\sqrt{N_S}g})^2 \sin^2 2\alpha t}} \tag{7.18}$$

we see that for $\alpha t \sim \frac{\pi}{4}$, the excitation is shared between the A and B samples, with only a small cavity population in the limit that $\Omega_s < \sqrt{N_S}g$ (ie $\Gamma_{sc} < N_S \eta \kappa$). If we were to simultaneously turn off both A and B pumps while maintaining the intensity ratio (or turning them off non-adiabatically to prevent further population transfer), we ought to end up in the entangled state:

$$|\psi_D\rangle = \cos\theta \, |f_A\rangle + e^{i\varphi} \sin\theta t \, |f_B\rangle \tag{7.19}$$

The remainder of this chapter is concerned with performing this experiment, and characterizing the state so generated!

Before we concern ourselves with *proving* that we have generate entanglement, it is worthwhile to first think about what sorts of *indications* of entanglement we might expect, and then combine them to prove entanglement.

Entanglement requires both *correlation* and *coherence*. As such, the first thing to check is that, after this partial transfer, we have an excitation in either sample A,

p_{00}	p_A	p_B	$p_{A\&B}$
0.88	0.08(1)	0.030(4)	0.0005(2)

Table 7.1: Magnon Occupation Numbers after Partial Adiabatic Transfer. Magnon Probabilities in two samples A and B measured by independent and joint readouts of the two samples. The magnon statistics are extracted from the photon statistics by assuming equal retrieval efficiencies given by magnon retrieval efficiency from sample A in the absence of a transfer, and using the known detection path quantum efficiency.

or sample B, but not both. To do this, we sequentially read the excitations out of the two samples, and measured the cross correlation between the extracted photons. As shown in table (7.1), we measured magnon read-out probabilities (referenced to within the cavity) of $p_A = 0.08(1)$, $p_B = 0.030(4)$, corresponding to $\theta = 32°$. The measured coincidence probability $p_{A\&B} = 0.0005(1)$ corresponds to $g_{AB} = 0.21(8)$, and implies a five-fold suppression of magnon coincidences between the A and B samples, compared with what we would expect if the samples were independently prepared in coherent states with mean p_A and p_B magnons, respectively. We have also made measurements at $\theta = 45°$, but our largest dataset was measured at $\theta = 32°$. In a separate measurement, we found that $g_{AA} = 0.13(8) \ll 1$, indicating that before the transfer we had only one magnon in the A sample.

To show coherence, we must verify that the phase between $|f_A\rangle$ and $|f_B\rangle$ in equation (7.18) is a well-defined and controllable quantity. We follow a method akin to that of Chou et. al[19], and read out the two samples A and B at the same time, and jump the phase of the B pump by ϕ . When $\phi = 0$, the cavity amplitudes from the two samples will destructively interfere, resulting in very little cavity readout. When $\phi = \pi$, the amplitudes will constructively interfere, resulting in maximal cavity readout.
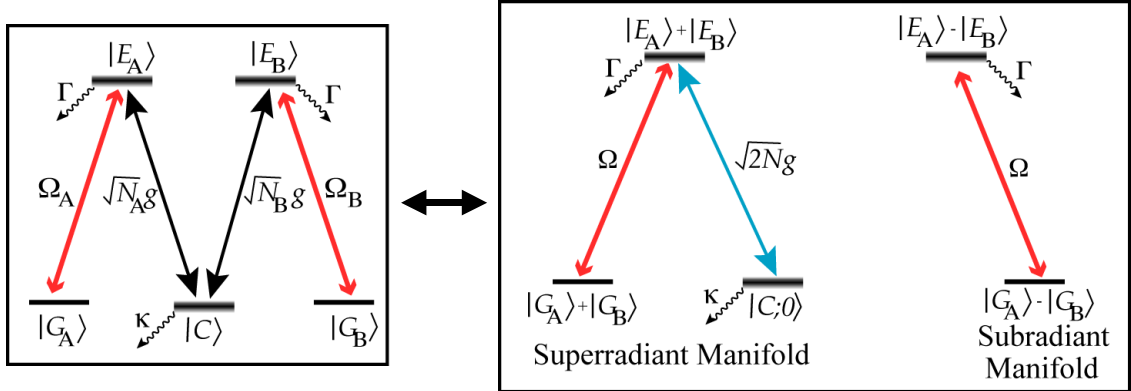
Figure 7.10: Coherence verification in the Super/Sub Radiant Basis: The readout Hamiltonian, depicted schematically on the left, may be block diagonalized into super- and sub- radiant hamiltonians. The super-radiant component reads out into the cavity with some probability, while the sub-radiant component is uncoupled from the cavity. The phase between $|G_A\rangle$ and $|G_B\rangle$ that forms a super-radiant state is offset by π from the phase used to generate the state. As such we can continuously tune from sub- to super- radiant readout by varying the phase of the readout beams.

This constructive/destructive interference may be understood as preparing a superposition of super- and sub- radiant states of the cavity. Even in the presence of dissipation, the 5-level Hamiltonian may be block-diagonalized into $H_{transfer} = H_{bright} \oplus H_{dark}$, where H_{bright} is the 3-level hamiltonian of a magnon of $2N_S$ atoms, collectively coupled to the cavity, and H_{dark} is the 2-level hamiltonian of a magnon of $2N_S$ entirely uncoupled from the cavity (see figure (7.10)). The transfer process prepares the sub-radiant state, and so it is necessary to adjust the relative phase of the pump beams ϕ to rotate this state into the super-radiant state. We expect the retrieval efficiency to be proportional to the overlap between super-radiant state, and

the rotated state: $\chi \propto |\langle \psi_{super} | \psi \rangle|^2$. In the simple case that $\theta = \frac{\pi}{4}$, we have:

$$
\begin{aligned}
|\psi_{super}\rangle &= \frac{1}{\sqrt{2}}(|f_A\rangle - e^{i\varphi} |f_B\rangle) \\
|\psi\rangle &= \frac{1}{\sqrt{2}}(|f_A\rangle + e^{i(\varphi-\phi)} |f_B\rangle) \\
\rightarrow \chi &\propto \sin^2 \frac{\phi}{2}
\end{aligned}
\tag{7.20}
$$

So we expect to observe a fringe which varies sinusoidally with ϕ. The more general analysis for unbalanced amplitudes, with backgrounds, is treated in appendix. (A).

Our experimentally measured fringe is shown in figure (7.11). We observe a fringe visibility of $V^{photonic} = 0.88(4)$, which is consistent with a contrast limited by population imbalance ($\theta \neq \frac{\pi}{4}$): $V_{max}^{photonic} = \frac{2}{\tan\theta + 1/\tan\theta} = 0.90(1)$. Optical backgrounds arising from non-collective excitations or non-transferred (inhomogeneously broadened) magnons could also limit our contrast. Double (collective) excitations should generally be coherently transferred, and hence should not impact the fringe contrast.

One might also be concerned that adjusting ϕ might somehow impact beam intensities, and directly affect the individual magnons rather than simply impacting their phases. The worry would then be that the contrast fringe might be a result of this, rather than interference between read-out from the two samples. The inset to figure (7.11) shows the separate read-outs of the A and B samples, versus ϕ, verifying that the retrieval efficiencies from the two samples are individually independent of ϕ, so adjusting the phase most likely does *not* otherwise impact the magnons.

In figure (7.12) we show the time dependence of readout waveforms for as we vary the phase $\varphi - \phi$. While the amplitude of the readout waveform varies sinusoidally with ϕ, the *shape* is otherwise unaffected, indicating that the super-/sub- radiant picture is the right one: When the excitation is in the bright state, it always reads out according
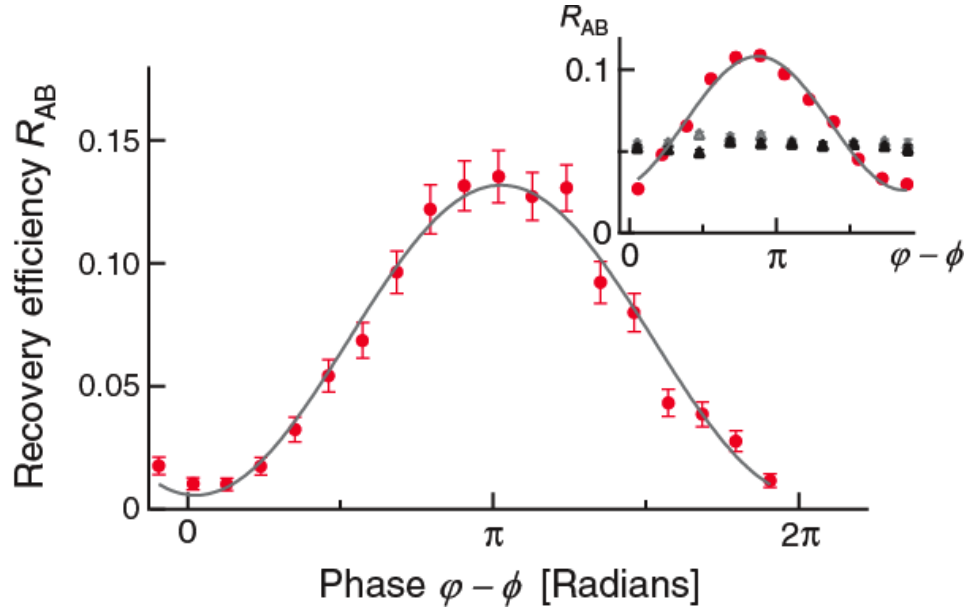
Figure 7.11: Coherence Verification between A and B Ensembles. Retrieval Efficiency versus readout phase $\varphi - \phi$ as both samples A, and B are read out simultaneously, at a write rate $n_w = 0.02(1)$ per trial. The observed fringe has a contrast $V^{photonic} = 0.88(4)$, limited by the observed population imbalance between the two ensembles. This large fringe contrast is indicative of the coherence between the two ensembles. **Inset:** Another interference fringe taken at higher n_w and $\theta \approx 45°$, along wit separate measurements of the readout efficiencies of the two sample independently. The lack of variation of the independent readouts with $\varphi - \phi$ is an indication that adjusting the readout phase is not somehow impacting the beam intensities.
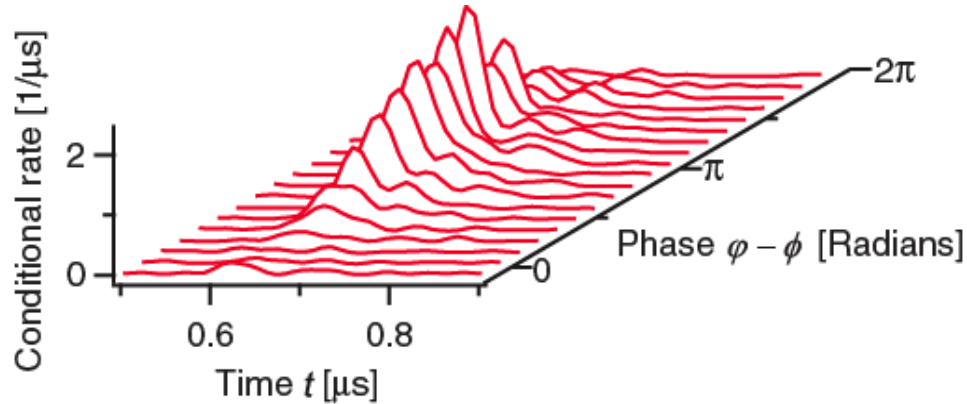
Figure 7.12: Readout Waveform versus phase angle $\varphi - \phi$. The sinusoidal variation in retrieval efficiency is evidence of the coherence between the samples. The fact that the waveform simply scales, without a change in shape, is evidence of the super/sub radiant dynamics.

to the super-radiant dynamics! All that changes with ϕ is the probability that it is in the bright state.

7.5.1   Aside on Phase Stability

The astute reader may worry that φ is uncontrolled and fluctuating, and will wash out the fringe. As long as we read out along the same beam paths (as required by phase matching), with the same beams used for transfer, the phase factor φ will be precisely cancelled[7], and we will be left with a fringe whose phase is determined solely by ϕ. Because Chou et. al. generated heralded entanglement, phase-matching precluded readout with the same write beams, and so φ could only be controlled by actively stabilizing the total optical path. This is not a critique of that experiment so much as a comment that, save in exceptional situations like ours, coherence con-

_____

[7]Up to path length fluctuations between the transfer and readout, which are quite small over the intervening 100's of ns, in our experiment.

tained in photon number is much more delicate than coherence carried in photon polarization- this is because the former is sensitive to path length variation, while the latter is sensitive to only birefringence variation (differential path length variation between polarizations). It is true, however, that converting number entanglement to polarization entanglement is non-trivial.

7.5.2 Concurrence and Entanglement of Formation

Having verified that we have both correlation and coherence, we would like to *prove* that we have entanglement. We follow the method of Chou et al.[19], and combine these pieces of information to compute the entanglement of formation[4] $\mathcal{E}_f$.

In general, computation of the entanglement of formation is a very complicated task. It requires a complete reconstruction of the density matrix of interest via tomography, and then a time-consuming numerical minimization. It happens, however, that for a bi-partite, two-state system there is a closed form expression for the entanglement of formation[126]:

$$
\begin{aligned}
\mathcal{E}_f &= h\left(\frac{1}{2}[1 + \sqrt{1 - \mathcal{C}_{full}^2}]\right) \\
h(x) &\equiv -x \log_2 x - (1-x)\log_2(1-x) \\
\mathcal{C}_{full} &\equiv \max(0, \sqrt{\lambda_1} - \sqrt{\lambda_2} - \sqrt{\lambda_3} - \sqrt{\lambda_4})
\end{aligned}
\tag{7.21}
$$

and $\lambda_1 \ldots \lambda_4$ are the eigenvalues, in decreasing order, of the (rank 4) operator:

$$
\rho(\sigma_y \otimes \sigma_y)\rho^*(\sigma_y \otimes \sigma_y)
\tag{7.22}
$$

Where ρ is the system density operator. $\mathcal{E}_f > 0$ is equivalent to $\mathcal{C}_{full} > 0$.

It still seems that we need to measure the full 4×4 density matrix for the bi-partite

two-level system, however, following logic similar to Chou et al.[19], and appendix (A),

one can show that ignoring coherences between different numbers of excitations will

only *reduce* $\mathcal{C}_{full}$. Since we are interested in putting a *lower* bound on the concurrence,

we will assume these elements are zero. In the subspace $H_1 = 0, 1_A \otimes 0, 1_B$ of up to

1 magnon in each of the two ensembles, one can then show:

$$\mathcal{C}_{full} \geq \mathcal{C} = \max \left[2m(V^{magnon} - \sqrt{G_{AB}}), 0 \right] \tag{7.23}$$

Here we have defined $m \equiv \sqrt{m_{10}m_{01}}$, $G_{AB} \equiv m_{00}m_{11}/(m_{10}m_{01})$, and m_{ij} is the

probability to find i and j magnons in ensembles A and B respectively. V^{magnon} is

the normalized magnon coherence within H_1, as described in the appendix.

As a sanity check, one can consider the case a product state, in which we have

Poissonian magnon distributions in both samples A and B. Such a situation has no

entanglement, and so we would expect $\mathcal{C}_{full} = 0$. One can show (see appendix A)

that in this situation $G_{AB} = 1$, and $V^{magnon} \leq 1$, as it is a fringe visibility. As such

$\mathcal{C} \leq 0$, so $\mathcal{C}_{full} = 0$, as we expect.

We can only directly measure photonic quantities, and not atomic ones, and so

we must place bounds on the magnonic quantities accordingly. In appendix (A) we

show that $G_{AB} \leq g_{AB}$, $V^{magnon} \geq V^{photonic}$. What this means is that measurements

that we have already made are sufficient to put a lower bound on the amount of

entanglement present in our system!

Using $m \geq \sqrt{p_A p_B} = 0.049(6)$, we find that $\mathcal{C} \geq 0.041(11)$ (or $\mathcal{C} \geq 0.0046(11)$

without correcting for detection path losses). In either case, we have verified that our

concurrence is greater than zero at the 4σ level, which means that we almost certainly

have entanglement[8]. Correspondingly, $\mathcal{E}_f \geq 0.0053(25)$, also indicating entanglement.

Our concurrence $\mathcal{C}$ is primarily limited by finite transfer and readout efficiencies. These efficiencies could be increased by using an a dipole trap to increase the optical depth and decrease the pump-beam induced inhomogeneous broadening.

---

[8]1 in every 32000 graduate students to make a claim like this is wrong! How many PhD's are there each year in physics? ☺

Chapter 8

Heralded Polarization Preserving Quantum Memory

Our final work with the old apparatus was a heralded quantum memory which could preserve the polarization of a stored photon. Our scheme required optical pumping in a Larmor precessing frame, which necessitated the development of rotating frame optical pumping characterization techniques. To achieve a stable Larmor frequency we needed to suppress chamber eddy-currents, and so our sample was loaded into a 1D optical lattice at 1064nm, to increase our hold time and allow the eddy-currents to ring down. These improvements, as well as a detailed description and characterization of the work, will be discussed in detail in the thesis of Haruka Tanji. The work is also described in the paper[117] (which follows):

- *H. Tanji, S. Ghosh, J. Simon, B. Bloom, and V. Vuletic, "Heralded Single-Magnon Quantum Memory for Photon Polarization States" Phys. Rev. Lett.* ***103***, *043601 (2009).*

Heralded Single-Magnon Quantum Memory for Photon Polarization States

Haruka Tanji,[1,2] Saikat Ghosh,[2] Jonathan Simon,[1,2] Benjamin Bloom,[2] and Vladan Vuletić[2]

[1]*Department of Physics, Harvard University, Cambridge, Massachusetts 02138, USA*
[2]*Department of Physics, MIT-Harvard Center for Ultracold Atoms, and Research Laboratory of Electronics,
Massachusetts Institute of Technology, Cambridge, Massachusetts 02139, USA*
(Received 26 August 2008; published 20 July 2009)

We demonstrate a heralded quantum memory where a photon announces the mapping of a light polarization state onto a single collective-spin excitation (magnon) shared between two atomic ensembles. The magnon can be converted at a later time into a single polarized photon with polarization fidelity over 90(2)% for all fiducial input states, well above the classical limit of $\frac{2}{3}$. The process can be viewed as a nondestructive quantum probe where a photon is detected, stored, and regenerated without touching its—potentially undetermined—polarization.

Among systems for the storage of light, one can distinguish between a device that can retain an initially prepared, and thus known, state [1,2], a quantum receiver that can receive and retain any (unknown) incoming state [3], and a quantum memory that can receive, retain, and recreate any (unknown) incoming state for further processing [4–7]. The attribute "quantum" indicates that the device outperforms any "classical" device (that attempts to measure and recreate the state) when averaged randomly over the Hilbert space of operation [3]. For instance, a classical polarization memory for single photons has a fidelity limit of $\frac{2}{3}$ since a single measurement allows only incomplete characterization of an unknown input state.

Quantum communication can benefit from quantum receivers and memories [8–10]. Moreover, the detrimental effects of photon loss can be largely remedied by a heralding ("state purification" [8]) feature that announces photon arrival and storage without destroying or revealing the stored quantum state. Heralded quantum memories may thus advance long-distance quantum communication [8–10], linear-optics quantum computing [11], and schemes aimed at breaking quantum encryption [12], or convert probabilistic [2,13,14] into heralded entanglement.

A continuous-variable quantum receiver has been realized by Julsgaard *et al.* [3] who mapped a weak coherent electromagnetic field containing up to eight photons onto the collective spin of an atomic ensemble with a fidelity of $\mathcal{F} = 0.67$ after 0.7 ms of storage. Recently, squeezed vacuum has been stored in and retrieved from an atomic ensemble [15], and a weak coherent state has been stored in a single atom [5].

Work with quantized excitations demonstrated capture and release of a single photon of fixed polarization [16,17] and coherent adiabatic transfer of a single photon between two ensembles via an optical resonator [18]. Matsukevich and Kuzmich [1] first introduced two ensembles, each capable of storing a single photon of fixed polarization, as a two-state system that can be mapped onto a single photon of variable polarization [19]. The two states can

also be implemented as momentum states of the stored spin wave [2] or, as in the present work, using atoms in two different magnetic sublevels. The latter allows the direct mapping of the spin polarization onto a single spatial mode of an optical resonator.

The first system capable of functioning as a quantum memory was realized by Choi *et al.*, who mapped the polarization state of an incoming photon onto two ensembles, and later retrieved the photon [6]. This (unheralded) device was tested for a single input polarization, for which it achieved a fringe visibility of 0.91 at a photon retrieval probability of 0.17 and a lifetime of 8 μs. A recent teleportation experiment by Chen *et al.* can also be viewed as a quantum memory, where the polarization state of an incoming photon is erased in a two-photon measurement, and teleported with probability between 17% and 95% onto two atomic ensembles [7] at polarization fidelities $\mathcal{F}$ between 0.74 and 0.87. If this experiment were performed with a single input photon, heralded storage would occur with a probability of $\sim 10^{-4}$.

In this Letter, we demonstrate a heralded quantum memory where a single photon announces polarization storage in the form of a single collective-spin excitation (magnon) that is shared between two spatially overlapped atomic ensembles. The heralded storage occurs rarely ($h \approx 10^{-6}$ per photon in our nonoptimized setup), but when it does, the stored photon can later be recreated with good efficiency ($\varepsilon \approx 0.5$) and sub-Poissonian statistics ($g_2 = 0.24$), while its polarization state is restored with very high fidelity ($\mathcal{F} > 0.9$). In the absence of a second setup for the production of narrowband single photons [13,17,20], we test the quantum memory with coherent states of arbitrary polarization (containing typically 500 photons per pulse to improve the data collection rate). The scheme, however, is designed for single-quantum storage and stores only one photon even for coherent input beams [8,21].

Heralded storage is achieved by means of a spontaneous Raman process that simultaneously creates the herald and the magnon. To store an arbitrary polarization state

$$|\psi\rangle = \cos\theta|R\rangle + e^{i\phi}\sin\theta|L\rangle, \quad (1)$$

written as a superpositions of right (left) circularly polarized states $|R\rangle$ ($|L\rangle$) with two arbitrary angles θ, ϕ, we use two spatially overlapped atomic ensembles A, B inside an optical resonator. The atomic levels are chosen such that ensemble A (B) absorbs only $|R\rangle$ ($|L\rangle$) polarized light, while both can emit a photon of the same polarization (π) into the resonator on the Raman transition of interest [Fig. 1]. The detection of the emitted π photon heralds the mapping of the input polarization state onto a magnon, but does not provide "which-path" information to distinguish between A and B. The "write" process thus maps a polarization state $|\psi\rangle$ onto a magnon superposition state

$$|\psi\rangle \rightarrow |\Psi\rangle = \cos\theta|1\rangle_A|0\rangle_B + e^{i\phi}\sin\theta|0\rangle_A|1\rangle_B, \quad (2)$$

where $|n\rangle_k$ denotes n magnons in ensemble k ($k = A, B$). At a later time, the stored state can be retrieved on demand as a single photon by utilizing the strong coupling of the magnon to the resonator [8,21] ("read" process).

The heralding serves to enhance the fidelity of the write process by announcing successful events. In our present nonoptimized setup, the heralding probability per incoming photon is $h = \alpha\eta q \approx 10^{-6}$, where $\alpha = 0.01$ is the absorption probability, $\eta = 10^{-3}$ is the single atom cooperativity (the emission probability into the resonator in this case), and $q = 0.1$ is the photon detection efficiency. Whenever there is a heralding event, however, a single magnon corresponding to the input-field polarization is stored with high fidelity and can be retrieved with good efficiency. The single-photon nature of the retrieved field is confirmed by a conditional autocorrelation measurement indicating sub-Poissonian statistics [$g_2 = 0.24(5) < 1$]. The heralding process may thus be viewed as a quantum nondemolition measurement where a single photon is detected and stored while preserving its polarization.

The quantum memory uses precessing spins [22] in order to take advantage of resonator emission in both heralding and read processes, and of atomic symmetries; the former provides mode selection and high photon collection efficiency and the latter good polarization fidelity. We choose a π transition for heralding, while any input state is expressed as a superposition of $\sigma^{\pm}$ polarizations [Fig. 1(b)]. Given the corresponding atomic angular emission patterns, we then need to rotate the atomic-spin direction by 90° between the heralding and the readout. This is achieved with a magnetic field of $\sim$1.4 G that induces Larmor spin precession with a period of $\tau_L = 2$ μs [Fig. 1(a) and 1(c)], enabling us to access the same magnon with different light polarizations at different times. Note that a spatially homogeneous magnetic field maintains the interatomic coherence and does not affect the magnon momentum, or equivalently, the phase matching condition for the read process [23].

We load cesium atoms from a magneto-optical trap into a far-detuned (trap wavelength $\lambda_t = 1064$ nm) one-dimensional optical lattice overlapped with
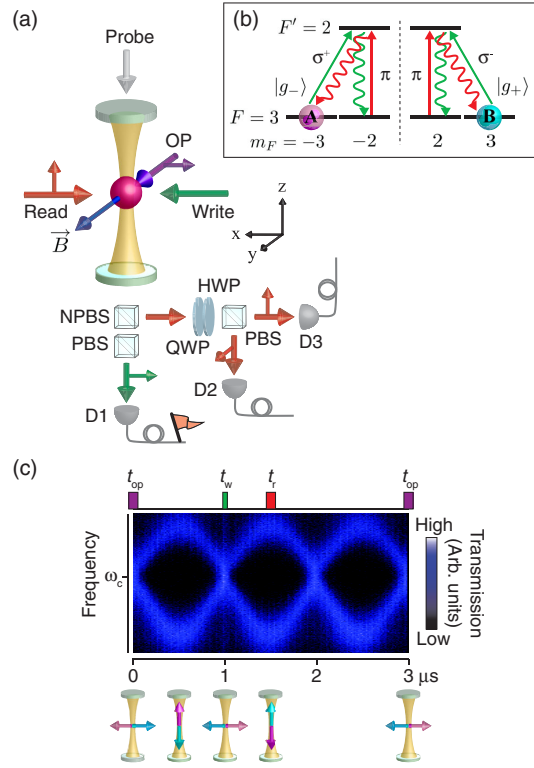
FIG. 1 (color online). (a) Setup. The small arrows indicate beam polarizations. OP is the optical pumping beam. NPBS, PBS, QWP, and HWP denote a nonpolarizing beam splitter, a polarizing beam splitter, a quarter wave plate, and a half wave plate, respectively. D1, D2, D3 are single-photon counting modules for herald detection and polarization analysis. A static magnetic field induces magnon precession. (b) Energy levels. Ensembles A and B are initially prepared in $|g_{\mp}\rangle \equiv |F = 3, m_F = \mp 3\rangle$. The write (green) and the read (red) processes are $\sigma^{\pm}$-π and π-$\sigma^{\pm}$ spontaneous Raman transitions, respectively. (c) Precession of the two macroscopic spins, as measured via cavity transmission, and timing of the optical-pumping (t_{op}), write (t_w), and read (t_r) processes.

the mode of a medium-finesse ($f = 140$) optical resonator [21]. Ensembles A and B consist of approximately 8000 atoms each at a temperature of 30 μK, optically pumped into hyperfine and magnetic sublevels $|g_{\pm}\rangle \equiv |6S_{1/2}, F = 3, m_F = \pm 3\rangle$, respectively, in the rotating frame. (The quantization axis is defined to rotate with the atomic spins and coincide with the propagation direction of the write beam at the optical-pumping time $t_{op} = 0$.) Optical pumping is achieved by periodic application of a short (100 ns $\ll \tau_L$), linearly ($\hat{x}$-) polarized optical-pumping pulse, resonant with the $6S_{1/2}$, $F = 3 \rightarrow 6P_{3/2}$, $F' = 2$ transition. The ensembles A, B thus form macroscopic spins in opposite directions that Larmor precess in

the x-z plane with a period τ_L [Fig. 1(c)]. We choose a pumping period of $\tau_{op} = 3\tau_L/2 = 3$ μs, such that the ensembles are interchanged at every trial, which reduces population imbalance between $|g_\pm\rangle$.

The atomic-spin precession and the efficiency of the optical pumping are monitored via resonator transmission of a weak, linearly ($\hat{\mathbf{x}}$-) polarized beam. In the frame rotating with the atomic spin, the probe beam polarization, and thus the coupling to the polarized atoms, change periodically with time. Since the states $|g_\pm\rangle$ do not couple to π-polarized light on the chosen transition $F = 3 \rightarrow F' = 2$ [see Fig. 1(c)], the otherwise observable atom-induced splitting of the cavity resonance [24] disappears. By optimizing the sinusoidal variation of the splitting [Fig. 1(c)], we prepare more than 99% of the $F = 3$ population in either of the $|g_\pm\rangle$ sublevels.

The photon storage and readout processes are timed to match the sample precession [Fig. 1(c)]. A sequence of optical-pump, write, and read pulses is applied once every τ_{op} for 30 ms, corresponding to a total of 10^4 trials before the sample is recooled.

The light whose polarization state is to be stored (write beam) is tuned to the $F = 3 \rightarrow F' = 2$ atomic transition, propagates along the $\hat{\mathbf{x}}$ direction, and is pulsed on for 50 ns $\ll \tau_L$ at $t_w = \tau_L/2 = 1$ μs, when the macroscopic spins are aligned along $\mp\hat{\mathbf{x}}$. At this time, ensembles A and B can absorb only $|R\rangle(\sigma^+)$ and $|L\rangle(\sigma^-)$ photons, respectively [Fig. 1(b)]. For equal populations in A and B, a π-polarized photon originating from a spontaneous $\sigma^\pm$-π (absorbing a $\sigma^\pm$ photon and emitting a π photon) Raman process has the same probability for having been emitted by either ensemble. Thus, it does not provide any "which-path" information, and, if detected by detector D1 [Fig. 1(a)], serves as a herald that announces the storage of a (not revealed) polarization state $|\psi\rangle$ as a magnon $|\Psi\rangle$.

At $t_r = t_w + \tau_L/4 = 1.5$ μs, when the atomic spins point along the resonator axis $\pm\hat{\mathbf{z}}$, the $\hat{\mathbf{z}}$-polarized read beam, tuned to the $F = 3 \rightarrow F' = 2$ transition, is applied for 100 ns $\ll \tau_L$. The read beam addresses a π transition, such that collectively enhanced [8] π-$\sigma^\pm$ Raman scattering maps the magnon state onto a single-photon polarization state. If the populations, $|\cos\theta|^2$, $|\sin\theta|^2$, and the relative phase ϕ of the magnons in ensembles A, B are preserved between the write and read processes [Eq. (2)], the polarization of the regenerated single photon is a faithful copy of the write beam polarization.

To quantify the performance of the heralded memory, we determine the density matrix ρ_{meas} of the output polarization [examples are shown in Fig. 2(a)] by measurements in three polarization bases [25]: $\frac{1}{\sqrt{2}}(|L\rangle \pm |R\rangle)$ (H-V), $|L\rangle$ and $|R\rangle$ (L-R), and $\frac{1}{\sqrt{2}}(|L\rangle \pm i|R\rangle)$ (S-T). The polarization fidelities $\mathcal{F}$ of the retrieved single photons for ten states of varying angle θ [Fig. 3] as well as for the six fiducial input states, H, V, L, R, S, and T [Fig. 2], are evaluated as $\mathcal{F} = \mathrm{Tr}(\rho_{meas}|\psi\rangle\langle\psi|)$, where $|\psi\rangle$ is the input state in Eq. (1). Figure 3 shows that $\mathcal{F}$ is close to unity with no systematic
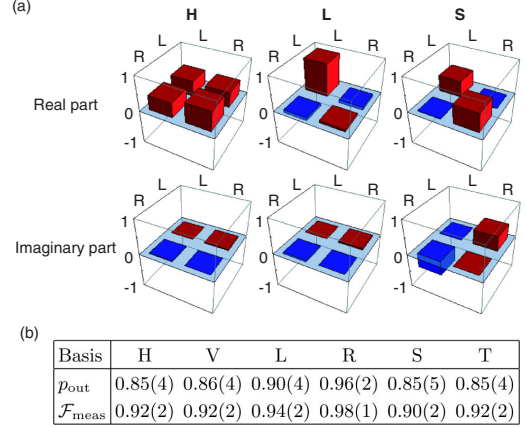
FIG. 2 (color online). (a) Density matrices ρ_{meas} of the retrieved single photons for fiducial input states H, L, and S. (b) The measured degrees of polarization (p_{out}) and fidelities ($\mathcal{F}$) of the retrieved single photons.

Basis	H	V	L	R	S	T
p_{out}	0.85(4)	0.86(4)	0.90(4)	0.96(2)	0.85(5)	0.85(4)
$\mathcal{F}_{meas}$	0.92(2)	0.92(2)	0.94(2)	0.98(1)	0.90(2)	0.92(2)

dependence on the zenith angle θ, and we have verified separately that the same is true for the azimuth angle ϕ. For any of the six fiducial states, the measured fidelity $\mathcal{F}$ without any background subtraction is significantly above the classical limit of $2/3$ for state-independent storage [Fig. 2(b)]. [The larger fluctuation of the fidelities in Fig. 3 (measured over ~8 hours) relative to Fig. 2(b) (measured over ~1 hour) is due to a slow uncompensated magnetic field drift.] If we correct the fidelities presented in Fig. 2(b) for the effect of the independently measured photon backgrounds, all fidelities are unity within statistical errors of a few percent.

The major source of photon backgrounds is the finite Larmor precession of 0.3 rad during the 100-ns read process. The read pump beam acquires a small admixture of $\sigma^\pm$ components in the frame precessing with the atomic
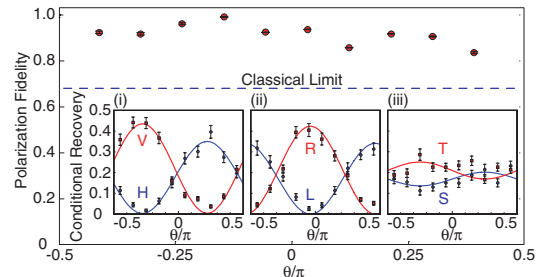
FIG. 3 (color online). Polarization fidelity of the stored photon as a function of θ for $\phi = 0$ [Eq. (1)]. Insets (i)–(iii): The results of projection measurements of the output field in three mutually orthogonal bases, H-V, L-R, and S-T. The solid curves are a simultaneous fit for all 60 data points. No backgrounds have been subtracted.

PHYSICAL REVIEW LETTERS

spin [Fig. 1(b)], which results in strong resonator emission by atoms in $|g_\pm\rangle$. These backgrounds deteriorate not only the stored polarization, but also the single-photon character of the retrieved field. The predicted autocorrelation due to this effect is $g_2 \approx 0.2$, in good agreement with the measured value of $g_2 = 0.24(5)$. These backgrounds can be reduced by slowing down the Larmor precession, which requires an increase in the memory lifetime which is currently $\sim 3~\mu$s. With a lifetime of a few milliseconds as demonstrated recently [26], the autocorrelation will then be $g_2 \sim 0.02$, limited only by the rare storage of two photons. The current lifetime is set by the magnon Doppler decoherence [21] that is presently faster than polarization (spin) decoherence. The one-dimensional optical lattice in the setup does not confine the atoms along the direction of momentum transfer in the write process [21], and thus an additional lattice is required for long lifetime.

Finally, we discuss the performance limits for the heralded quantum memory scheme investigated here. The success probability may be improved upon by adding a second resonator to increase the absorption probability of the incident photon. The fundamental limit for the heralding probability h for $N \gg 1$ would then be given by $h = \frac{\eta}{1+\eta} q$. Under realistic conditions ($N = 100$, $\eta = 10$, $q = 0.6$), one could thus achieve $h \sim 0.5$ for an incident single photon with retrieval efficiencies near 90% [21]. With a lifetime of ~ 6 ms [26], Larmor precession and spin decoherence would limit the polarization fidelity only at the 10^{-3} level.

By applying this scheme to photons of undetermined polarization from a probabilistic source of entangled photon-magnon pairs [2,13,14], it should be possible to realize a *heralded* source of entangled-photon pairs for various tasks in quantum information processing. If loaded by a photon from a high-purity Bell pair, the estimated Bell parameter for the heralded source employing our current quantum memory would be $2.5(1) > 2$, exceeding the classical limit. For the above improved parameters, such a source would then produce heralded Bell pairs at a rate of ~ 500 s^{-1}.

[1] D. Matsukevich and A. Kuzmich, Science **306**, 663 (2004).
[2] S. Chen, Y.-A. Chen, B. Zhao, Z.-S. Yuan, J. Schmiedmayer, and J.-W. Pan, Phys. Rev. Lett. **99**, 180505 (2007).
[3] B. Julsgaard, J. Sherson, J. I. Cirac, J. Fiurášek, and E. S. Polzik, Nature (London) **432**, 482 (2004).
[4] A. A. Kiselev, K. W. Kim, and E. Yablonovitch, Appl. Phys. Lett. **80**, 2857 (2002).
[5] A. D. Boozer, A. Boca, R. Miller, T. E. Northup, and H. J. Kimble, Phys. Rev. Lett. **98**, 193601 (2007).
[6] K. Choi, H. Deng, J. Laurat, and H. Kimble, Nature (London) **452**, 67 (2008).
[7] Y.-A. Chen, S. Chen, Z.-S. Yuan, B. Zhao, C.-S. Chuuand, J. Schmiedmayer, and J.-W. Pan, Nature Phys. **4**, 103 (2008).
[8] L.-M. Duan, M. D. Lukin, J. I. Cirac, and P. Zoller, Nature (London) **414**, 413 (2001).
[9] L. Jiang, J. M. Taylor, and M. D. Lukin, Phys. Rev. A **76**, 012301 (2007).
[10] Z.-B. Chen, B. Zhao, Y.-A. Chen, J. Schmiedmayer, and J.-W. Pan, Phys. Rev. A **76**, 022329 (2007).
[11] E. Knill, R. Laflamme, and G. Milburn, Nature (London) **409**, 46 (2001).
[12] G. Brassard, N. Lütkenhaus, T. Mor, and B. C. Sanders, Phys. Rev. Lett. **85**, 1330 (2000).
[13] D. N. Matsukevich, T. Chanelière, M. Bhattacharya, S.-Y. Lan, S. D. Jenkins, T. A. B. Kennedy, and A. Kuzmich, Phys. Rev. Lett. **95**, 040405 (2005).
[14] H. de Riedmatten, J. Laurat, C. W. Chou, E. W. Schomburg, D. Felinto, and H. J. Kimble, Phys. Rev. Lett. **97**, 113603 (2006).
[15] K. Honda, D. Akamatsu, M. Arikawa, Y. Yokoi, K. Akiba, S. Nagatsuka, T. Tanimura, A. Furusawa, and M. Kozuma, Phys. Rev. Lett. **100**, 093601 (2008); J. Appel, E. Figueroa, D. Korystov, M. Lobino, and A. I. Lvovsky, Phys. Rev. Lett. **100**, 093602 (2008).
[16] T. Chaneliere, D. N. Matsukevich, S. D. Jenkins, S. Y. Lan, T. A. B. Kennedy, and A. Kuzmich, Nature (London) **438**, 833 (2005).
[17] M. D. Eisaman, A. André, F. Massou, M. Fleischhauer, A. S. Zibrov, and M. D. Lukin, Nature (London) **438**, 837 (2005).
[18] J. Simon, H. Tanji, S. Ghosh, and V. Vuletić, Nature Phys. **3**, 765 (2007).
[19] C. W. Chou, H. de Riedmatten, D. Felinto, S. V. Polyakov, S. J. van Enk, and H. J. Kimble, Nature (London) **438**, 828 (2005).
[20] J. K. Thompson, J. Simon, H. Loh, and V. Vuletić, Science **313**, 74 (2006).
[21] J. Simon, H. Tanji, J. K. Thompson, and V. Vuletić, Phys. Rev. Lett. **98**, 183601 (2007).
[22] D. N. Matsukevich, T. Chanelière, S. D. Jenkins, S.-Y. Lan, T. A. B. Kennedy, and A. Kuzmich, Phys. Rev. Lett. **96**, 033601 (2006).
[23] A. T. Black, J. K. Thompson, and V. Vuletić, Phys. Rev. Lett. **95**, 133601 (2005).
[24] Y. Zhu, D. J. Gauthier, S. E. Morin, Q. Wu, H. J. Carmichael, and T. W. Mossberg, Phys. Rev. Lett. **64**, 2499 (1990).
[25] D. F. V. James, P. G. Kwiat, W. J. Munro, and A. G. White, Phys. Rev. A **64**, 052312 (2001).
[26] B. Zhao, Y.-A. Chen, X.-H. Bao, T. Strassel, C.-S. Chuu, X.-M. Jin, J. Schmiedmayer, Z.-S. Yuan, S. Chen, and J.-W. Pan, Nature Phys. **5**, 95 (2009); R. Zhao, Y. O. Dudin, S. D. Jenkins, C. J. Campbell, D. N. Matsukevich, T. A. B. Kennedy, and A. Kuzmich, Nature Phys. **5**, 100 (2009).

Chapter 9

Hybrid EIT/Cavity QED

Apparatus

9.1 Motivation

All of the work described thus far has made use of the collective coupling of an atomic ensemble to an optical resonator to reach the strong-coupling regime. The primary limitation of such an approach is that devices so created are inherently *linear*[127], insofar as they cannot distinguish between one photon (or magnon) and two. All of our experiments have used a projective measurement with an SPCM (which is *not* a linear device) to prepare the system in the single excitation manifold, after which the linear evolution provided by ensemble-cavity coupling is enough to generate the interactions we desire.

In light of our growing desire to observe quantum nonlinear effects, we decided to implement a cavity appropriate for entering the single-atom strong-coupling limit.

The apparatus we have built was designed for one objective, and finds itself ideally suited to attack an even more exciting secondary problem. The former was to generate controlled coupling between *at least two* atoms in a single high-finesse cavity. We have since discovered that using EIT and CQED together, there is hope to create very high efficiency QND single photon detectors, and at a minimum an efficient single photon detector and a single-photon gated transistor.

9.1.1 Two Atoms in a Cavity

Previous work with single optical cavity QED has found great success in fields from single atom detection[9] to single non-linearities[5, 82], to cavity cooling[80, 65] and beyond. The cost of this work has been the remarkable effort required to transport, load, and manipulate single atoms. Cavity systems sufficiently sensitive to distinguish between 1 and 2 atoms have been realized [43, 60, 61, 96], and single atom positioning of up to 6 atoms has even been realized outside of a cavity[84]. Recently, the Rempe group has succeeded in resolving (via imaging) two atoms within a cavity[122]. To date, however, no one has succeeded in deterministically loading, individually addressing and coherently manipulating two atoms *within* a cavity. From the prospective of QIP, this is a very important objective[88, 131].

The groups of Grangier and Weinfurter have had impressive success localizing single atoms at the waist of tightly focused dipole traps[123, 103] The volume of these traps is so small that two atoms held in the trap are likely to collide and be ejected on a time-scale short compared with the one-body loss. This results in strongly squeezed trapped number atom distribution, with an achievable mean atom

number of 0.5 and undetectable 2-atom probability. These traps thus provide single atoms with less technical complexity, at rates comparable to standard techniques for loading single atoms within an optical resonator. Rydberg blockade in the excitation of two such atoms has begun to show promise as a route to quantum gates[45].

Our objective is to combine the efficient readout and control of a high-finesse cavity with the deterministic loading and addressing of a pair of very small waist dipole traps. This will allow us to deterministically load two atoms in very controlled locations within the cavity field, and induce cavity mediated interactions.

9.1.2 Single Photon Transistors and Detectors

There are numerous applications for high-efficiency single photon detectors from linear optics quantum computing [63], to loophole-free tests of Bell inequalities[102], to increased range between quantum repeaters[34], and beyond.

There exist proposals for very high efficiency detectors, from James et al.[57] and Imamoglu[56]. These detectors use an atomic ensemble optically pumped to a state $|G\rangle$ to adiabatically stop an incident photon by transferring a single atom to an intermediate ground state $|F\rangle$, and then fluorescence scattering on a closed transition to detect the atom in $|F\rangle$. If such a detector could be built, single photon detection efficiencies up of 99% within a time interval of a few $\Gamma^{-1} \approx 100$ns, would be within reach. The problem is that such schemes depend upon large detection solid angle (for efficient detection of a single transferred atom) over a large atomic sample (to achieve efficient stopping of the incident photon).

Our new apparatus has the potential to solve the above limitations by using an

atomic ensemble trapped within a high-finesse resonator to detect a single transferred atom by its effect on cavity transmission. Adiabatic capture of a single photon will be performed by addressing the atomic ensemble from the side of the optical cavity, using the high-NA lens to focus the incident single photon down into a 2μm waist, thus minimizing the necessary number of atoms.

Because cavity-based atom detection is in principle non-destructive (in the $\eta \gg 1$ limit where free-space scattering may be ignored), and does not distinguish between the various atoms, the stopped photon can be restarted by re-application of the stopping laser! This is because the stopping process[89] essentially writes a free-space magnon into the atomic ensemble, and so as long as the atoms do not scatter any photons into free-space during the cavity probing, the detection of the transferred atom will not destroy the magnon.

The ability to detect a photon without destroying it, known as a quantum non-destructive or QND measurement, has both fundamental and practical implications. An optical QND photon detector could be used to implement a quantum gate[112].

Additionally, the switching of cavity transmission by a single photon may be viewed as a single-photon transistor. In the absence of impedance matching issues, this switch would have the potential to act as a quantum non-destructive single-photon transistor, which is a quantum gate.

9.2   A Long, High Finesse Cavity?

The primary limitation that we face is technical in nature. Over the long history of optical Fabry-Perot cavity QED, there has been a continuous push to resonators with

smaller volumes and higher finesses. This push arose from the conventional wisdom that while a single atom switch requires only $g^2 > \kappa\Gamma$, single photon nonlinearities require $g > \Gamma$. To reach this latter limit requires a high finesse, a small waist, and a short cavity! The problem, then, was that we needed *a lot* of optical access to generate a 2μm dipole-trap focal spot within the cavity, and get in MOT beams of 2mm diameter. Typical cavity lengths of $10 - 50\mu$m[5] would not provide nearly the necessary optical access. We then had to face the question: *Could we get away with moving to a longer cavity design from the short design which seemed to be preferred for most Cavity QED experiments, or, put another way, do we need $g > \kappa, \Gamma$, or simply $g^2 > \kappa\Gamma$?*

Our first hint that we might be alright was that for each of the schemes described in this thesis, the efficiency scaled with a power of $\eta \equiv \frac{4g^2}{\kappa\gamma}$, and not $\frac{g}{\kappa}$ or $\frac{g}{\gamma}$ independently[1]. Noting that $\eta = \frac{4g^2}{\kappa\Gamma} = \frac{24\mathcal{F}}{\pi}\frac{1}{(kw_c)^2}$, it is clear that as long as the finesse and cavity waist remain fixed, the cavity length may be varied arbitrarily without affecting η. A longer cavity would leave space for a MOT within the cavity, as well as the small waist dipole trap.

There are, admittedly, a number of other applications for which one might like to use a cavity, other than those that we know scale with η. Among them are single atom detection, photon blockade, vacuum Rabi spectroscopy, etc... Some of these processes obviously scale with η, and some do not. We will see in (9.7) that single atom detection has a rate which scales with η and Γ, otherwise independent of the cavity length. I will show, in the next section, that given a 3-level Λ atom, the third

---

[1]Of course all of our work made use of atomic ensembles, and so $g \to \sqrt{N}g$, but our analyses applied equally well to single atom effects.

level may be used to engineer an appropriately narrow excited state such that *any* scheme which would normally utilize a two-level atom in a cavity will scale with a power of η, as long as $\Gamma > \kappa$. In the opposite limit of ultrashort cavities $\kappa > \Gamma$, this method fails, and the fundamental scaling is less clear.

Thereafter, I will describe a new apparatus, built during the final year and a half of my PhD, which reaches the strong-coupling limit between single atoms and a long, high-finesse Fabry-Perot cavity. I will discuss difficulties faced and surmounted arising from the narrow linewidth of the long cavity, and finally, I will describe a number of interesting applications of this new apparatus, with some preliminary data.

9.3   The η Limit

In the preceding chapters we have discussed in excruciating detail why it is that η sets the limit for single photon sources, quantum memories, and quantum buses. The qualitative explanation, backed up by math in a number of limiting cases, is that η is essentially the single pass absorption probability of a single atom, times the mean number of passes through the cavity mode.

This is a convincing argument, and for all of the things we have tried to do, it holds water. Problems begin to appear when we analyze the vacuum Rabi spectrum of a single atom (or ensemble!) coupled to a single cavity mode [130, 9]. Without even doing much calculating, it is easy to show that the doublet splitting in the first excited manifold of the Jaynes-Cumming Hamiltonian is $2g$[9], and each dressed level has a linewidth of $\frac{\kappa + \Gamma}{2}$. This means that our spectroscopic resolution (where larger is

better) is:

$$R = \frac{4g}{\kappa + \Gamma} = \frac{2\sqrt{\eta}}{\sqrt{\frac{\kappa}{\Gamma}} + \sqrt{\frac{\kappa}{\Gamma}}^{-1}} \tag{9.1}$$

which depends upon the ratio of $\frac{\kappa}{\Gamma}$, and not just η!

Similarly, an analysis of the the photon blockade[5] shows that the zero-time autocorrelation function (which parameterizes the degree of blockading of the cavity by a single atom) is given by[11]:

$$g_2(\tau = 0) \approx \frac{9(\kappa + \Gamma)^2}{4g^2} = 9\frac{(\sqrt{\frac{\kappa}{\Gamma}} + \sqrt{\frac{\kappa}{\Gamma}}^{-1})^2}{\eta} \tag{9.2}$$

and again we see explicit dependence on $\frac{\kappa}{\Gamma}$.

How do we reconcile this with our intuition? The answer is that, for a two-level atom, we cannot: There seem to be a class of problems in which the mismatch between the cavity and atomic linewidths substantially degrades the performance of the system!

For a *three*-level atom, however, the situation is quite different. Using a detuned dressing laser, a narrow excited state may be custom-built with an arbitrary linewidth $\tilde{\Gamma}$ arising from an controllable admixture of the excited state induced by the dressing beam.

9.3.1 Engineering an Arbitrarily Narrow Excited State

Suppose our cavity is tuned near the $|G\rangle \leftrightarrow |E\rangle$ transition, with the $|F\rangle \leftrightarrow |E\rangle$ transition dressed with a laser of Rabi frequency Ω at a detuning δ from the excited state, as shown in figure (9.1). If $\Omega \ll \delta$, this laser builds two new states, $\left|\tilde{E}\right\rangle$ and $\left|\tilde{F}\right\rangle$, where the important state $\left|\tilde{F}\right\rangle \approx |F\rangle + \frac{\Omega}{2\delta}|E\rangle$ This state is stark shifted
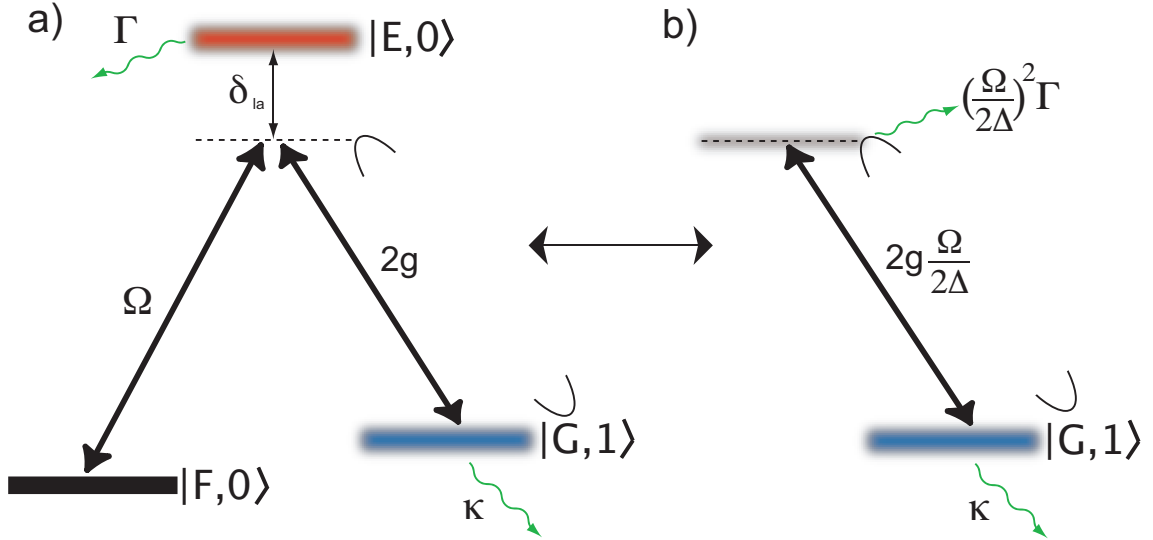
Figure 9.1: Engineering a narrow excited state using EIT in a 3-level atom. **(a)** The 3-level scheme, using the pump beam Ω to dress the state $|F\rangle$, thus introducing a small admixture of the state $|E\rangle$. **(b)** Effective two-level scheme, showing a narrowed excited state and a reduced atom cavity coupling, such that $\tilde{\eta} = \eta$, but $\tilde{\Gamma} \ll \Gamma$.

downwards by $\Delta_s = \frac{\Omega^2}{4\delta}$, and has a linewidth of $\tilde{\Gamma} = \frac{\Omega^2}{4\delta^2}\Gamma$. Because the excited state component is only $\frac{\Omega}{2\delta}$, the effective vacuum Rabi coupling between this state and the cavity is $2\tilde{g} = 2g\frac{\Omega}{2\delta}$. As such we see that when the cavity is tuned to $\left|\tilde{F}\right\rangle$, the effective η is $\tilde{\eta} = \frac{4\tilde{g}^2}{\kappa\tilde{\Gamma}} = \frac{4\tilde{g}^2}{\kappa\tilde{\Gamma}} = \eta$, that is, η is unaffected by the dressing process. Quantities like $\frac{\tilde{\Gamma}}{\kappa}$, however, may now be adjusted freely between 0, and $\frac{\Gamma}{\kappa}$, simply by tuning $\frac{\Omega}{2\delta}$!

What this means is that vacuum Rabi splitting resolution can be tuned to its optimal value $R_{max} = \sqrt{\eta}$, and similarly the photon blockade autocorrelation may be optimized to $g_2^{opt}(\tau = 0) \approx \frac{36}{\eta}$. We have saved the day– everything scales with η only!

While we are mostly interested in situations where this explicit construction of a narrow level is unnecessary, it certainly good to know that this exists as a possibility for our apparatus, and the many other apparatuses that have $\eta \gg 1$ but $\kappa \ll \Gamma$ and

would like to be able to access the full range of quantum mechanical phenomena!

9.4   Design of the New Apparatus

The new apparatus is shown in figure (9.2). Our top priorities was to squeeze a MOT, strong-coupling cavity, and two optical dipole traps with 2μm waist into the same volume. We wanted as large a cavity linewidth as possible, which meant making the cavity as short as we could without compromising the MOT beams. Two of the MOT beams entered along the diagonals, between cavity mirrors and dipole trap lenses, while the third entered through a hole in the baseplate.

For simplicity it was decided that the new cavity setup ought to be affixed to the same stainless steel rods as the old one. The old setup had serious vibration problems, which were suppressed to an extent in the new apparatus by mounting the full apparatus on a single Macor[2] block which slid onto the steel rods and was fixed in place with steel rings locked in place with set-screws.

9.4.1   Mechanical Design and Assembly of the Cavity

The cavity mirrors were each mounted to a tube piezo from Channel Industries, made of Navy II (5500), with OD 0.314", length 0.500", and thickness 0.03", making it slightly smaller in OD than the mirrors themselves. This made the task of centering the mirrors on the piezos quite tedious, and in the end one of the mirrors was aligned

---

[2]Macor is a vacuum compatible, "machinable" ceramic. Machining it cleanly is apparently quite difficult as it is prone to crumble. Even the external shop we used had serious trouble threading holes into the Macor, and so in the end none of the threaded holes in the Macor were even used.
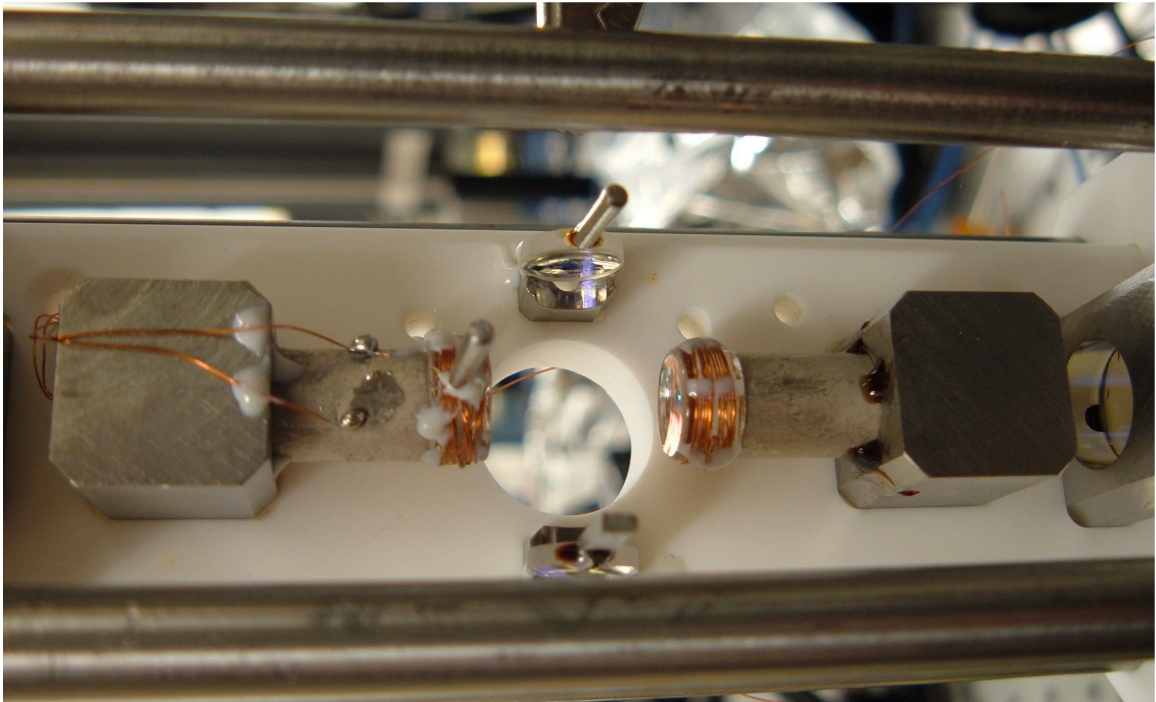
Figure 9.2: Photograph of the new apparatus. The hole in the Macor plate is for the horizontal MOT beams. The diagonal MOT beams pass between the cavity mirrors and the dipole trap lenses. Each cavity mirror is wrapped in 34AWG Kapton-coated heating wire, to prevent Cs deposition on the mirror surfaces. One of the 40mm mode-matching lenses is visible at the far-right of the image.

by insisting that the TEM_{00} mode be centered upon it, and that the incident beam be retro-reflected by the mirror-surface.

The piezo tubes were glued with ND-353 to (non-magnetic) steel mounting blocks, which were then affixed to the Macor block from below with slot-vented, silver plated 4-40 screws from UC components. One of the mounting blocks was elevated by $\sim$ 11mils to compensate for off-centered mounting of mirror on the Piezo. The elevation was generate with a carefully flattened and cleaned copper wire placed between the steel mounting block and the Macor block.

The piezo wires were 34AWG, Kapton-dipped copper wires from Allectra, and we had substantial difficulty soldering them to the piezos. This seemed to be because the piezos were quite old, and so there was a substantial oxidation layer built up on their surfaces. Once the piezo wires were soldered to the piezo's they were secured with ND-353 to the steel blocks for strain relief. Unfortunately the inner piezo wire for one of the piezos came loose in this process[3]- everything was already aligned, however, so we proceeded onwards, leaving one of the piezos floating.

The piezos were chosen to have approximately 800nm throw with 250V applied, corresponding to approximately two cavity FSRs at 852nm. We have found nearly 1.6μm throw, possibly resulting from the exposure of the piezos high-temperatures during glue curing and chamber bake-out.

---

[3]We attempted to attach the piezo wires more firmly to one of the piezos with ND353. The large quantity of ND353 necessary actually shattered the piezo: Curing ND-353 requires heating it past its glass transition, near 100°C. When it cools, the differential contraction between the *extremely* stiff ND353 and the piezo was enough to shatter the piezo. In the end we just soldered the wires to the piezos and took our chances.

9.4.2 Cavity Characteristics

The mirrors used were 0.3" diameter, 4mm thick substrates with radius of curvature 1cm, from REO. These mirrors have an intrinsic power loss of $\mathcal{L} = 26$ ppm, and using the method described below were found to have a finesse of approximately $63(5) \times 10^3$ at 852nm. This corresponds to a power transmission of $\mathcal{T} = 26$ppm. This would mean that we expect an intra-cavity photon to be out-coupled with a probability $P = \frac{\mathcal{T}}{\mathcal{T}+\mathcal{L}} \approx 0.5$, or 0.25 through each mirror assuming equal transmissions.

In general we have found it to be easier to align the input beam to the TEM_{00} mode and perform the initial mode matching using 780nm light, because the cavity finesse at this wavelength was only~ 5000, as compared with 852 or 817nm, where the finesse was ~ 60000. Working at 937nm, where the finesse was ~ 300 would have been even easier- at the time we did not yet have an available laser at 937nm.

The cavity length was chosen to be 13.7 mm. If the cavity had been made shorter, we expected the MOT beams to be clipped by the cavity mirrors– as it was the edges of the vacuum chamber windows, and the edges of the dipole lenses, were expected to limit their size. Increasing the cavity length further would have made the mode larger on the mirrors, and increased the likelihood that dust-particle would land in the mode and spoil the cavity finesse[4].

The cavity length of 13.7mm corresponds to a free-spectral range of 10909MHz,

---

[4]We initially investigated the possibility of going to a near-concentric cavity, but found ourselves limited to a finesse of 6000 at a waist size of 5μm. We would then have been loss dominated, making cavity out-coupling very difficult. Additionally, concentric cavities are notoriously difficult to keep aligned, typically require in-vacuum adjustment[51], and so we chose to forgo this possibility for now. It was tantalizing, however, as $\mathcal{F} \approx 6000$ and $w_c \approx 5\mu$m correspond to a peak cooperativity $\eta \approx 55$. In retrospect it is good that we did not go in this direction, as we are now trying to pack as many atoms as possible into the cavity waist in an effort to increase our absorption probability from the side.

which, in fact, is how we measured the cavity length. At 852nm we can measure the cavity length to better than 50KHz, corresponding to an uncertainty in *absolute* cavity length of only 62nm! Our most precise measurement of the cavity length puts it at 13742592(25)nm, for the longitudinal mode which we like to use for our experiments!

At this cavity length and for the known mirror curvatures of 1cm, we anticipate a transverse mode spacing(to the TEM_{10} mode) of 4123MHz$\gg \kappa$, and a waist size of a cavity waist size of 35.2μm. Using these numbers we performed mode matching calculations using ABCD matrices , and concluded that a 40mm EFL plano-convex singlet lens at a distance of 31.55mm from the cavity mirror back surface would collimate the TEM_{00} mode out-coupled from the cavity to a beam with a waist size of 420μm. This beam was mode matched to an OZ-Optics single mode fiber via a C-340TMB 4mm EFL aspherical collimating lens from Thorlabs. The 40mm EFL mode matching lenses were glued in stainless steel mounting blocks, which were then affixed to the Macor block with screws.

9.4.3 Cavity Linewidth Characterization

One of the challenging aspects of working with a cavity with such a narrow linewidth is characterizing it. At a linewidth of $\kappa = 2\pi \times 173(13)$KHz, the cavity was substantially narrower than any of the lasers available in lab[5] In our old setup with $\kappa \approx 2\pi \times 10 - 15$MHz, the cavity linewidth was most easily characterized by putting $\sim$ 30MHz sidebands on a laser and sweeping it across the cavity resonance

---

[5]This obviously eventually changed with active laser frequency stabilization, but that took time.

while monitoring the cavity transmission. The sidebands act as a calibrated ruler for a measurement of the observed cavity line of $\kappa + \gamma_{laser}$. As long as $\gamma_{laser} \ll \kappa$, the observed linewidth reflects κ. Clearly, in the limit $\kappa \ll \gamma_{laser}$, this technique fails.

Once the cavity is locked, the simplest (and likely most accurate way) to measure the cavity linewidth is via the "ringdown" method: We inject a small amount of power into the cavity and allow it to reach steady state, and then turn off the incident beam and monitor the cavity leakage on a fast photodiode. The intracavity power will decay with an envelope $e^{-\kappa t}$, giving a direct indicator of κ, independent of probing laser linewidth. While we ultimately measured our cavity linewidth this way, it is not a terribly useful technique until the cavity is stably locked.

The technique described by Poirson et al.[90] proved to be quite useful. By sweeping the cavity resonance (via the cavity piezo) rapidly across the laser line and monitoring the cavity transmission, we acquired curves akin to figure (9.3). From a fit to this data, both the cavity sweep rate and cavity finesse may be extracted. This method works quite similarly to the "Ringdown" method, in that it is not biased by laser linewidth. Use of a 1MHz bandwidth high transimpedance gain ($\sim 100\text{k}\Omega$) avalanche photodiode($M \sim 30$) was helpful for observing the signal. We found that the full fit form from [90] was not really necessary, and that the approximate expression provided was sufficient:

$$\frac{\kappa}{2\pi} = \frac{1}{2\pi} \frac{R + 2 - e}{2\Delta t} \tag{9.3}$$

Where R is the ratio of the height of the first peak to the second, and Δt is the time between the first peak, and the second.

The mirrors were cleaned with a combination of Opti-Clean and then acetone on
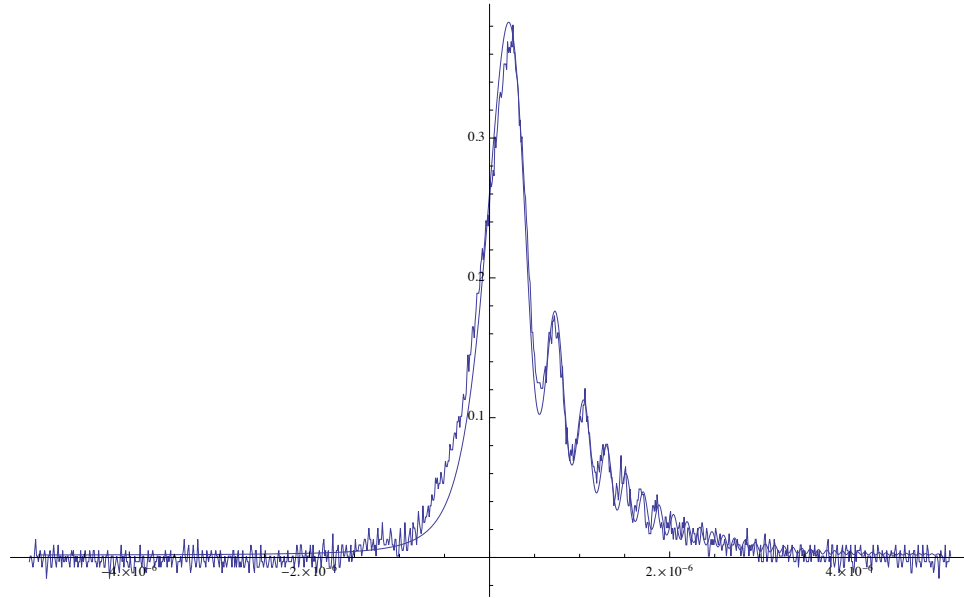
Figure 9.3: Sample swept cavity ringdown curve measured at 852nm, corresponding to a finesse of 50000.

tightly folded sheets of lens paper. Following the bake, we measured the following finesses:

λ	$\mathcal{F}$
937nm	330(10)
852nm	$63(4) \times 10^3$
817nm	50×10^3
780nm	5×10^3

Combining the finesse at $\lambda = 852$nm of 63000, and a waist of $w_c = 35\mu$m, we anticipate a peak single atom cooperativity of $\eta = 7.2 > 1$, so we are in regime of single-atom strong coupling!

9.4.4 Mirror Heating Coils

To avoid Cs deposition on the mirror surfaces, each mirror is heated with 10 turns of 34AWG Kapton-dipped wire from Accu-Glass, with approximately .4Amps of current running through it, providing an anticipated 30°C heating, assuming good thermal grounding of the heating-wire to the mirror surface.

10 turns of wire, all in the same direction, wrapped around the mirror, would generate a field of 3.6Gauss/Amp at the location of the atoms. To avoid this, each heating element consists of 5 clock-wise turns, and 5 counter-clockwise turns. We nonetheless observe a residual field of 0.4G/A, and as such whenever the heating coil current is adjusted the MOT bias coils must be accordingly compensated to recenter the MOT.

9.4.5 Mechanical Design of the Dipole Traps

The 2μm dipole traps were generated from 11mm EFL A397-B unmounted aspheric collimator lenses from THORLABS, mounted in stainless steel blocks on either side of the cavity mode. We were very concerned about having enough optical access to get MOT beams through the cavity, so we chose the longest focal length asphere that fit into a 7.2mm diameter package, with which we could consistently produce a $w_{trap} = 2\mu$m focal spot.

Alignment of the aspheric lens focal spot to the cavity waist proved to be a very difficult task, largely because locating the center of the cavity mode was quite difficult. Any object placed within approximately 60μm of the cavity axis spoils the cavity finesse at 852nm and extinguishes cavity transmission. The field of view of the asphere

for a nearly collimated gaussian beam seems to be ~ 60 microns in each of $\hat{x}, \hat{y}$, and $\hat{z}$, before spherical aberration increased the size of the beam waist. In addition, once the vacuum chamber was closed we were concerned that it could be quite difficult to move the focus of the small-waist dipole trap into the cavity mode.

Using a combination of razor blades and small $(100 - 150\mu\text{m})$ apertures, and working at 780nm, Haruka managed to align the focus of each of the two aspheres onto the cavity axis to within $\pm 5\mu\text{m}$. The foci are separated along the cavity axis by approximately $80\mu\text{m}$. This procedure was quite involved, and will be explained in greater detail in the thesis of Haruka Tanji.

9.5   Locking the Cavity

9.5.1   Motivation

We have, to an extent, laid to rest concerns that long cavities with $g < \Gamma$ cannot not induce single-photon nonlinearities. That, however, is not the sole argument against the use of long cavities. The other big concern is that such cavities are very difficult to stabilize- both absolutely, and relative to lasers.

A cavity of finesse $\mathcal{F}$ must have length fluctuations suppressed to better than $\frac{\lambda}{\mathcal{F}}$ for its linewidth can be resolved by a stable laser. This would seem to indicate that longer cavities are no more difficult to work with than shorter ones, but there are several reasons why this is not the case. The first is that the displacement induced by given noise source is likely to be proportionately larger for a longer cavity, and so more gain is required to achieve the requisite stability. The second is that a longer cavity is

likely to be less stiff and couple to more mechanical resonances at lower frequencies, making the control loop more complicated. The third is that longer cavities have proportionately smaller linewidths, so standard diode lasers are too broad to address the cavity resonance.

For our old experiment we locked our cavity on a longitudinal mode separated from the Cs D2 line by several cavity FSRs, up to about 9GHz. During the experimental sequence we held the lock, extinguishing the locking light, to avoid saturating the detectors or perturbing the atoms. For this to be alright we depended upon the mechanical stability of the cavity (to better than $\frac{\lambda}{\mathcal{F}}$) over the few milliseconds of data collection. In practice this worked fine for the finesses we used, up to ~ 400. While the new apparatus is somewhat more rigid and the cavity shorter, the finesse of ~ 60000 is a factor of at least 150 larger, and so we do not expect to be able to hold the cavity very long at all before it drifts off of resonance.

Equally importantly, our cavity linewidth of $\kappa \approx 2\pi \times 160\text{kHz}$ is substantially smaller than the linewidth of our DFB lasers $\gamma_{dfb} \approx 2\pi \times 1\text{MHz}$. The simplest way to deal with this is to actively narrow the laser against the experimental cavity, but even this would not work since any near-resonant locking light must be extinguished the experimental cycle. We considered optically narrowing the laser, and then locking the cavity to it, hoping all the while that during the experiment neither the narrowed laser, nor the cavity, would drift too far. While this seemed a marginal solution, we hoped for something better.

9.5.2   A Transfer Cavity: Overview

The more robust and unfortunately more complicated solution upon which we finally settled was a transfer cavity, which allows us to lock the experimental cavity at one frequency, and probe it at another, transferring the frequency stability across a very large frequency range otherwise accessible only by frequency comb. As shown in figure (9.4), we built a transfer cavity whose length and finesse were quite similar to the one installed in the chamber, but whose mechanical stability and noise immunity were much improved via geometry and teflon isolation rods[73]. The transfer cavity has a free-spectral range of 11257MHz.

Two lasers were narrowed and locked to this cavity, one at 852nm (henceforth the η laser), and one at the edge of the wavelength-region where the cavity finesse remained high, at 817nm (the *transfer* laser). We actively stabilized (via a piezo) the length of the transfer cavity at *very* low frequencies $\omega < 2\pi \times 100$Hz by monitoring the beat signal between the η laser and the reference laser. The experimental cavity was then locked (via piezo) to the transfer laser, which was far enough detuned from any atomic resonance that its intracavity power hardly impacted the atoms at all. The wavelength difference of ~ 35nm allowed for efficient filtering using interference filters from Omega Optical, such that the transmitted locking power did not disturb the photodetectors monitoring the cavity transmission.

The η laser could then be used to probe the cavity. Because the transfer laser does not perturb the atoms or the detectors, it could be left on during the experimental sequence. The narrowing of the lasers to the transfer cavity ensured that their linewidths were smaller than the linewidth of the experimental cavity. The full

a)   b)
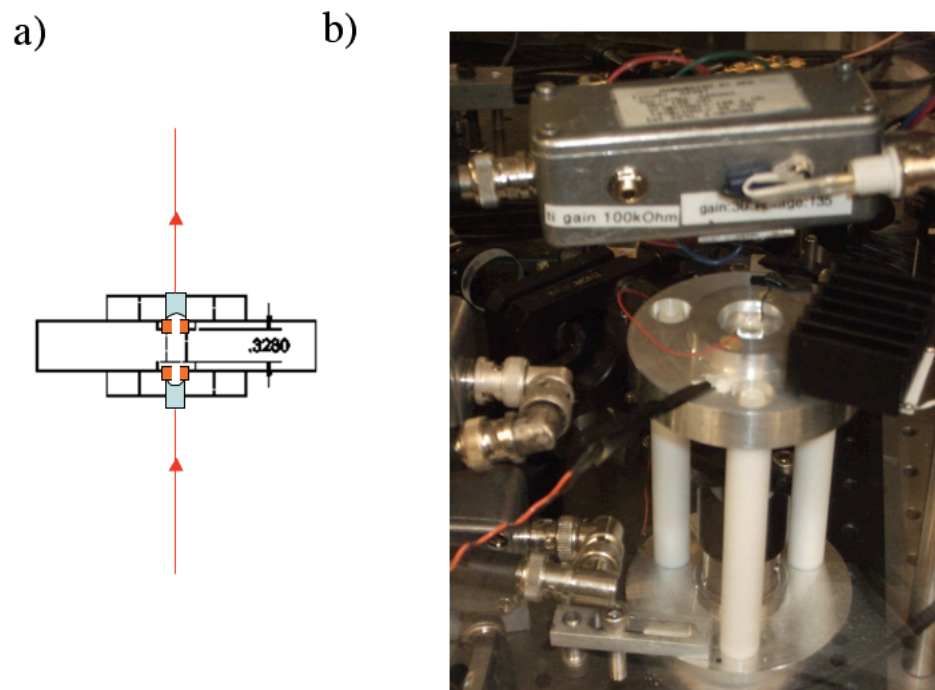
Figure 9.4: Transfer Cavity. **(a)** Schematic of the transfer cavity setup. The mirrors are the same high-finesse super-mirrors used in the experimental cavity, but with radius of curvature is R= 2.5cm. They are shown in blue, the piezo (and symmetrical standoff) in orange, and the high-symmetry aluminum mounting block in black. **(b)** Photograph of the transfer cavity. The cavity is isolated from mechanical vibrations with teflon mounting rods. Temperature stability is achieved with the shown thermistor and TEC (with fins), in conjunction with a digital PI loop.

scheme, then:

The experimental cavity was locked to the transfer laser, which was locked to the transfer cavity which was locked to the η laser which was locked to the reference laser.

Among the subtleties ignored in the above description is that the transfer cavity cannot be more absolutely stable than the reference laser to which it is locked at low frequencies. Since the reference laser has a Lorentzian line of width ~ 1MHz, the experimental and transfer cavity frequencies drift around by a substantial fraction of this width. It turns out, however, that the *absolute* experimental cavity frequency matters only on the scale of Γ, which is 5.2MHz. In contrast, the drift of the cavity *relative* to any probing laser must be stabilized to better than κ.

With the exception of the reference laser step, the fluctuations in all of the locking steps listed above add up to give the final cavity-laser linewidth. As such, *all* locks must be good to substantially better than a κ. In what follows, we will describe how the various challenges implementing these locks were surmounted, such that in the end, we could sweep the η laser across the experimental cavity resonance and resolve a peak of width $\kappa_{eff} = 2\pi \times 158(7)kHz\approx \kappa$, as shown in figure (9.5). Because κ_{eff} is indistinguishable from κ, the full transfer sequence can be said to stabilize η relative to the experimental cavity to much better than κ.

9.5.3 Narrowing and Locking the η and Transfer Lasers

The η and Transfer lasers were locked to the transfer cavity via high-bandwidth Pound-Drever-Hall Locks. The locks to the transfer cavity used EOM-generated sidebands at 25MHz and 30MHz for 852 and 817nm, respectively. The 5MHz frequency

a)

b)
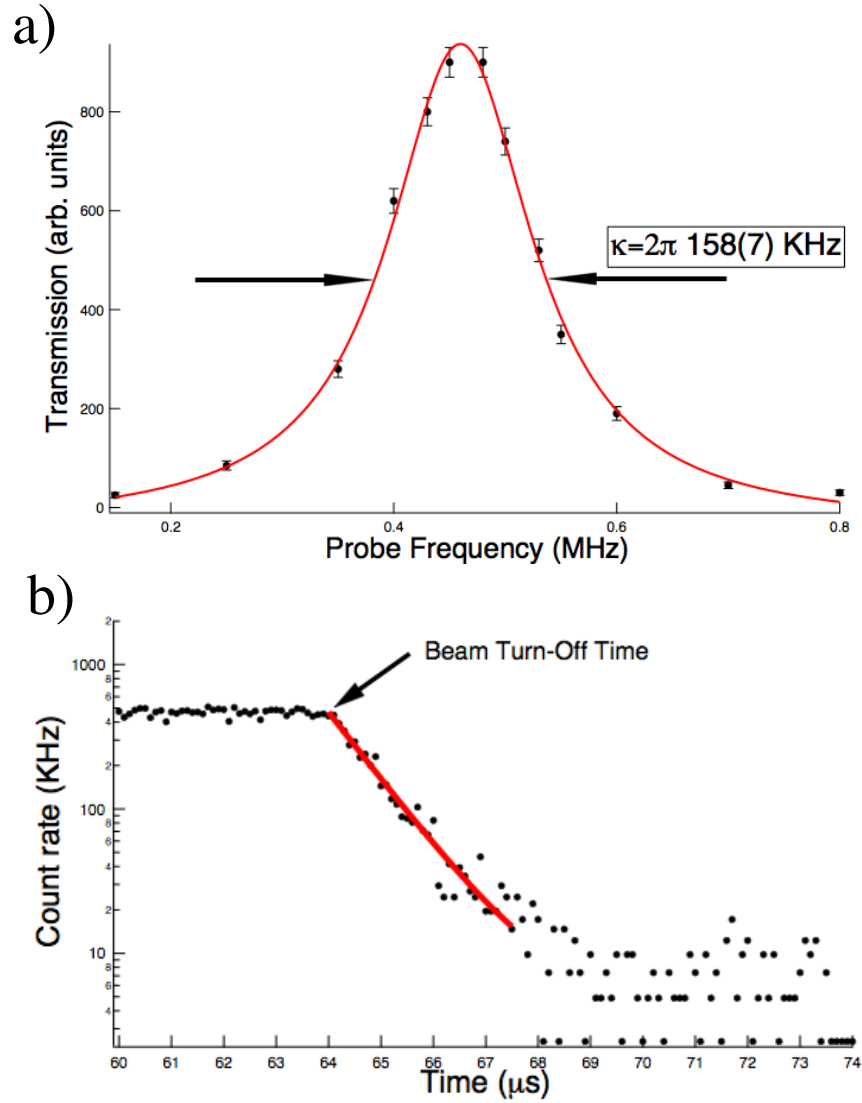
Figure 9.5: **(a)**Cavity transmission spectrum taken with cavity in lock, by sweeping the η laser across the cavity resonance. The observed laser-cavity mutual linewidth is $\kappa = 2\pi \times 158(7)$KHz. **(b)** An independent cavity ringdown measurement yields $\kappa = 2\pi \times 173(12)$KHz. The agreement between the two measurements indicates that the laser has a linewidth $\gamma_{laser} \ll \kappa$.

difference was chosen to minimize crosstalk between lock paths. A typical DFB laser has an instantaneous linewidth of 1MHz, and so a unity-gain locking bandwidth of nearly a 1MHz is necessary to narrow such a laser- otherwise we will succeed only in removing low-frequency noise without placing a substantial fraction of the power in a narrow carrier.

At low frequencies (up to ~ 50KHz), the feedback from the PDH error signal goes into a Proportional-Integral (PI) lockbox and then to the laser current-controller. Above 50KHz the phase lag of the current controller and PI-box limit performance, and and so a direct, high-frequency feedback path is sent to the diode through a bias-tee and lead-lag filter to compensate for the shift from temperature to carrier density tuning. The high-frequency loop is shaped via a OPA 657 high GBWP (1.6GHz) op-amp from Texas instruments. The transfer function rolled back to proportional at around 100KHz because the finite cavity lifetime rolls the gain off above this frequency, and a $1/f^2$ rolloff at unity gain is unstable (see figure (9.6)).

As with all of our cavity locks in the new apparatus (save the 937nm dipole trap), we lock the cavity to a PDH sideband, rather than the carrier. This is because we reach the same technical noise performance at substantially lower intra-cavity power when locked to the sideband. Additionally, it can be quite difficult (without a lock-detection scheme) to sweep to resonance and lock the cavity to the carrier, while a small error offset will induce the cavity to sweep and lock to a sideband.

Once the η laser is stabilized to the transfer cavity, the transfer cavity is locked via the beatnote between the η laser and the Reference laser, with a small unity-gain bandwidth of < 100Hz. This can be achieved with very little bandwidth because the
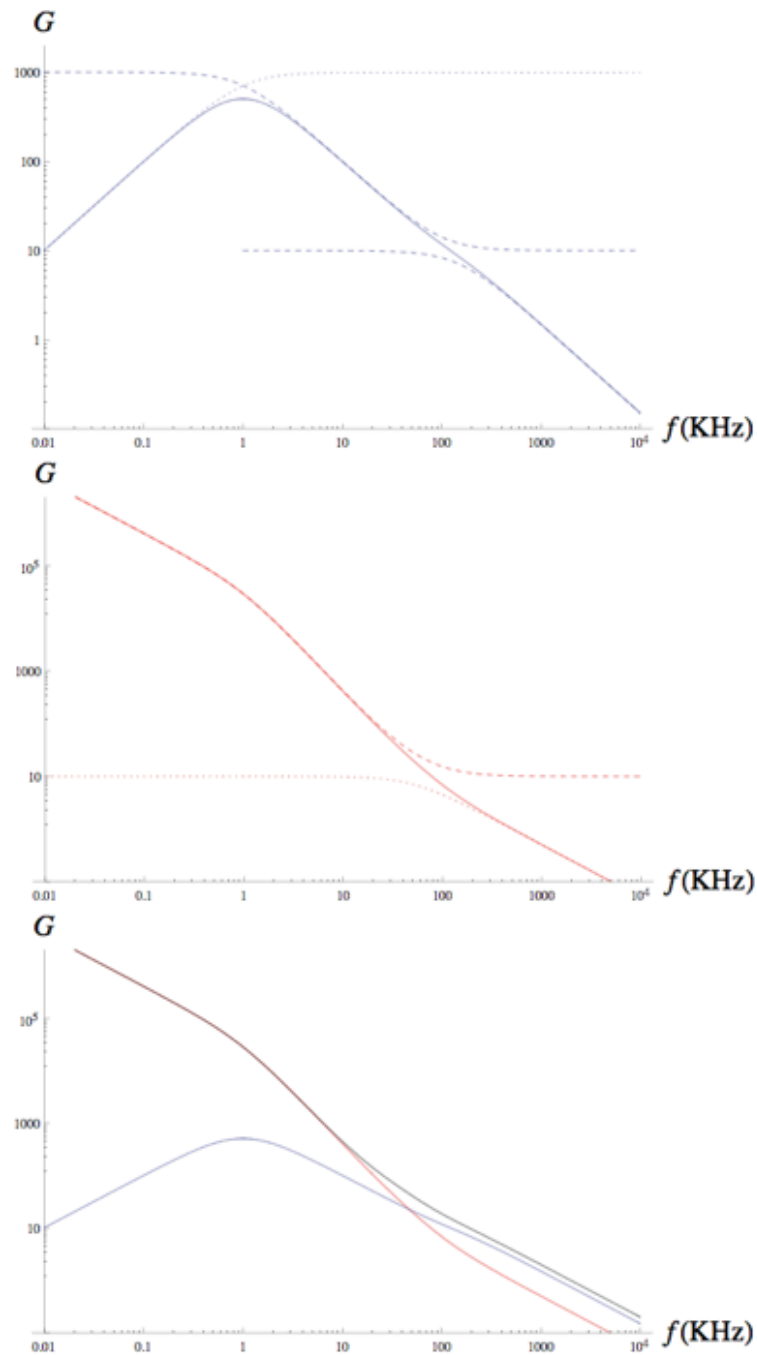
Figure 9.6: Transfer Lock Open Loop Behavior (qualitative). **Top** Fast Path: Solid curve is full response, from (dotted) bias-tee roll on, (upper dashed) Op-amp loop filter, and (lower dashed) cavity roll-off. **Middle** Slow Path: Solid curve is full response, from (dashed) lockbox, and (dotted) current controller rolloff.

transfer cavity is *very* mechanically stable, on the scale of our experiments.

9.5.4 Pre-Narrowing the 817nm Transfer Laser

The transfer laser, purchased from Sarnoff Corporation, is a DFB laser running single-mode at 817nm. The diode unfortunately has a linewidth of ~ 10MHz, meaning that we have very poor SNR for our PDH lock. Additionally, we would need substantially more bandwidth to narrow a laser with an instantaneous linewidth of 10MHz than 2MHz wide laser.

We solved this problem by adding adding feedback in the form of a glass-plate (AR coated on one side) on a piezo at a distance of 14cm from the laser. This glass plate provides so much optical feedback that it becomes the primary frequency determining element in the system. Feed-forward to the current is adjusted to maximize the mod-hop free tuning range, in our case to a value of 1GHz.

9.5.5 Experimental Cavity Stabilization

A PDH lock at 28.6MHz was used to lock the experimental cavity to the 817nm laser. We hit a serious hitch here, as the cavity exhibited mechanical resonances as low as 5KHz (see figure (9.7)). The system was liable to oscillate at either the low-frequency mount resonances, or the higher frequency piezo resonances, depending upon where we chose to put the unity gain frequency of the loop. We added high-Q (Q$\sim$ 20) active notch filters using gyrators as low loss inductors to suppress the various resonances and make the system more stable, and achieved a unity gain bandwidth of 1.5KHz.
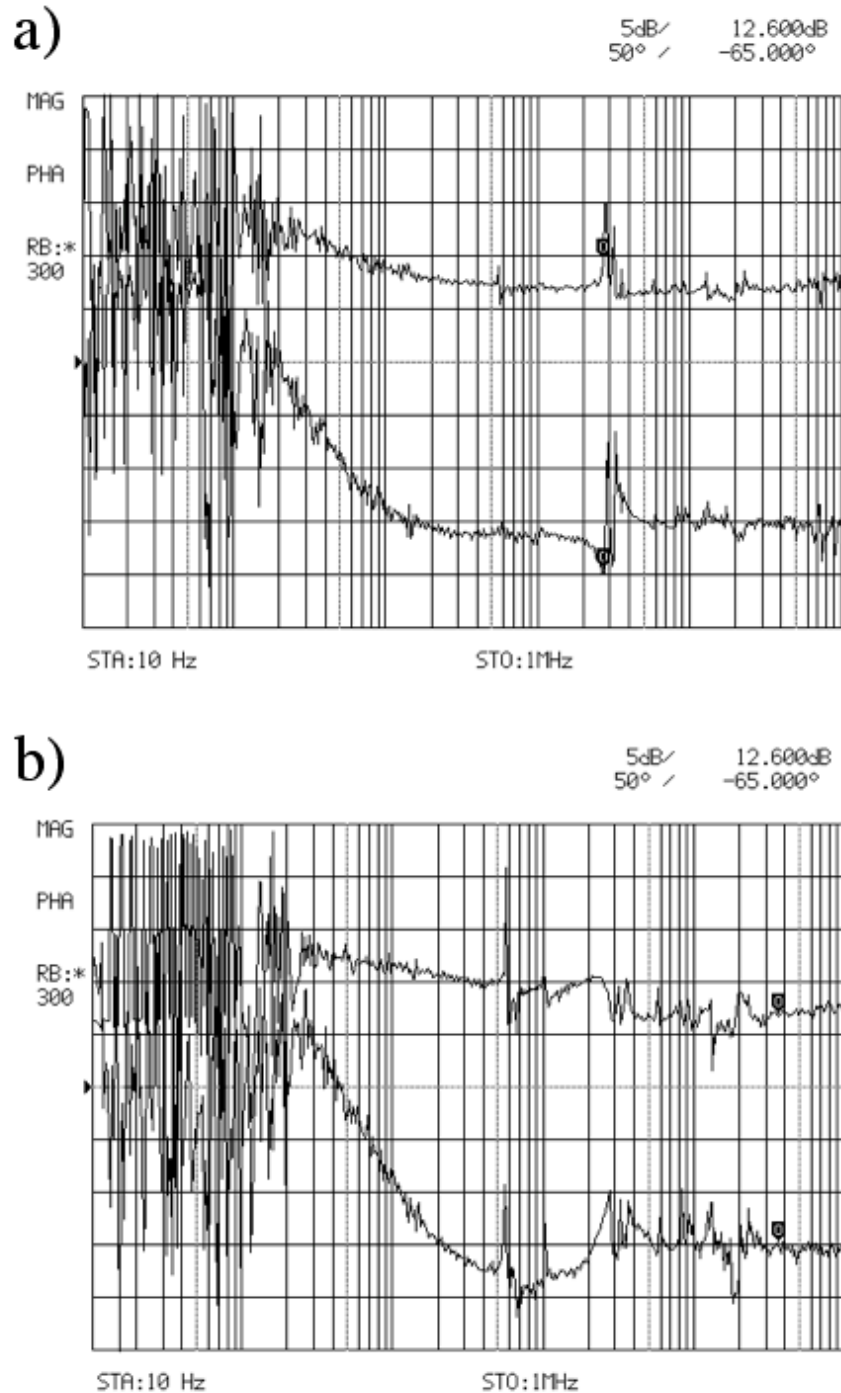
Figure 9.7: **(a)** Mechanical response of the experimental cavity versus drive frequency, with low frequency resonances at $5 \sim 10$KHz notched out. The dominant remaining resonances are at 30KHz. **(b)** Similar to (a), but with the low high frequency resonances notched out, leaving only the low frequency resonances. When running the experiment we employ both sets of notches to suppress all resonances. In each plot the *upper* trace is the magnitude, and the *lower* trace the phase, of the response. Noise at frequencies ≤ 1KHz is an artifact of the network analyzer.

When we attempted to observe the cavity linewidth by scanning the η laser across a cavity resonance, we observed the line broadened out to more than a Megahertz. This is less than the atomic linewidth of 5MHz, so the absolute stability requirements are thus fulfilled. The laser cavity stability can now be improved with a high bandwidth feedback to the transfer laser itself.[6]. To do this, we added afrequency shifter in the path of the transfer-laser to the experimental cavity, and fed back on the transfer laser accordingly. The frequency shifter we chose was composed of a double-passed AOM (see figure (9.8)) driven by a VCO. By feeding back on the control voltage to the VCO, we acquired a fast-feedback path with a bandwidth of $\sim$ 200kHz, limited primarily by the propagation delays of the acoustical wave in the AOM crystal ($\tau_{AOM} \approx$ 250ns), as well as optical and electrical path lengths ($\tau_{prop} \approx$ 90ns).

It is important to note that while this fast feedback path does suppress *relative* noise between the transfer-laser and the cavity resonance, the absolute stability of the cavity resonance is probably not improved. The gain in the fast path allows us to increase the gain in the slow (piezo) path, so one might expect increased noise suppression. The reality, however, is that it is a comparison of the slow path gain to the fast path gain, and not the slow-path gain to unity, which determines the absolute noise suppression. This is because any correction made by the fast path actually *reduces* our absolute stability, since the transfer-laser is stably locked to the transfer-cavity, and fast-path corrections actually adjust its frequency! Since

---

[6]If we were to start again, I think it would be wise to mount the experimental cavity on teflon blocks to suppress vibrational coupling, and drive one cavity mirror with a substantially shorter piezo with correspondingly higher-frequency mechanical resonances. The reality, however, is that designing, assembling, testing, cleaning, and installing a new apparatus is *very* time-consuming, so we wanted to work with what we had.
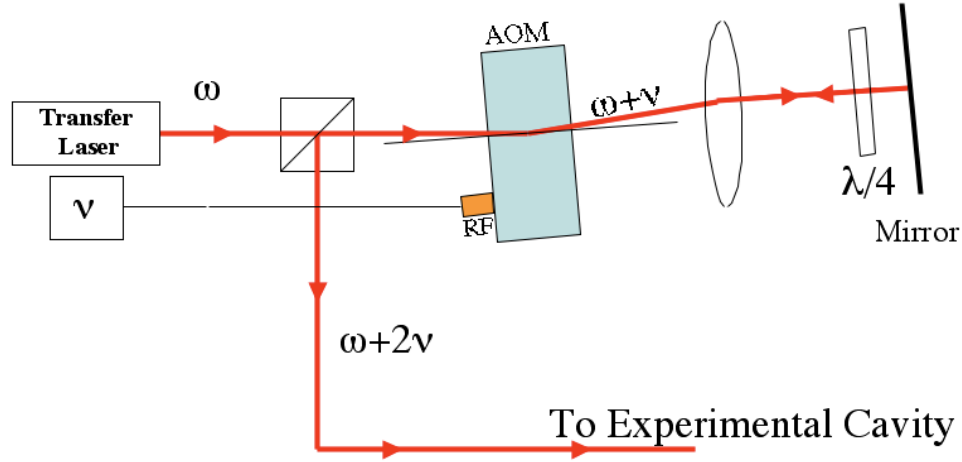
Figure 9.8: Double-passed AOM used as a high-bandwidth frequency shifter for the transfer laser. The frequency ν is derived from the fractional divider setup described in the feedforward section.

$G_{fast} \geq G_{slow}$ at the frequency that was previously the unity gain of the slow loop[7], the noise suppression unity-gain bandwidth of the slow loop is not enhanced by the addition of the fast loop.

9.5.6 η Feedforward

Because we were forced to feedback not only on the experimental cavity frequency but also the transfer laser frequency, we also had to feed these corrections forward to the η laser frequency. The subtlety is that we could not *directly* feed the frequency corrections forward with an AOM or EOM, only to the substantial wavelength difference between 817 and 852nm:

If, in closed loop, the fast past of the experimental cavity lock has a frequency excursion of Δ_{817}, this indicates that the length of the experimental cavity must have

---

[7]This is usually necessary because the slow loop would otherwise be likely to oscillate at its new unity gain frequency.

increased by an amount $\delta_L = -L_{cav}\frac{\Delta_{817}}{\nu_{817}}$. The corresponding correction required for

the 852nm laser to remain on the cavity resonance is $\Delta_{852} = -\nu_{852}\frac{\delta_L}{L_{cav}}$. Combining

these relations yields:

$$\Delta_{852} = \Delta_{817} \times \frac{\lambda_{817}}{\lambda_{852}} \tag{9.4}$$

This crucial relation indicates that if we just directly feed the 817nm frequency

correction forward to the 852nm laser, we will be making a 4% error. What this

means is that any gain of the fast path above 25 is wasted, as the compensation on

the 852 path will be incorrect. Put another way, the fast feedback to the 817nm laser

was used to suppress the $\sim$ 2MHz jitter of the cavity. This 4% error introduces a

frequency error of 2MHz$\times$0.04 = 80KHz, which is a nearly half of a cavity linewidth.

Our actual configuration, shown in figure (9.9), uses a $\sim$ 1840MHz VCO, in com-

bination with two frequency dividers, $\div23$ and $\div12$. The $\div23$ is routed to the 817nm

double-passed AOM, while the $\div12$ is used to drive the feed-forward to the 852nm

EOM. The ratio of these dividers[8] is $\frac{23/2}{12} = 0.9583$, while $\frac{\lambda_{817}}{\lambda_{852}} = 0.9589$, indicating

that we now have only a 0.06% error in feedforward, corresponding to a maximum

useful gain of 1700.

9.5.7 A Few Technical Details to Remember in Building such a System

- All lasers need at least 60dB of optical isolation or they become unstable at the

  100s of KHz level due to optical feedback from the high-finesse cavities.

---

[8]the factor of two numerator comes from the double-pass
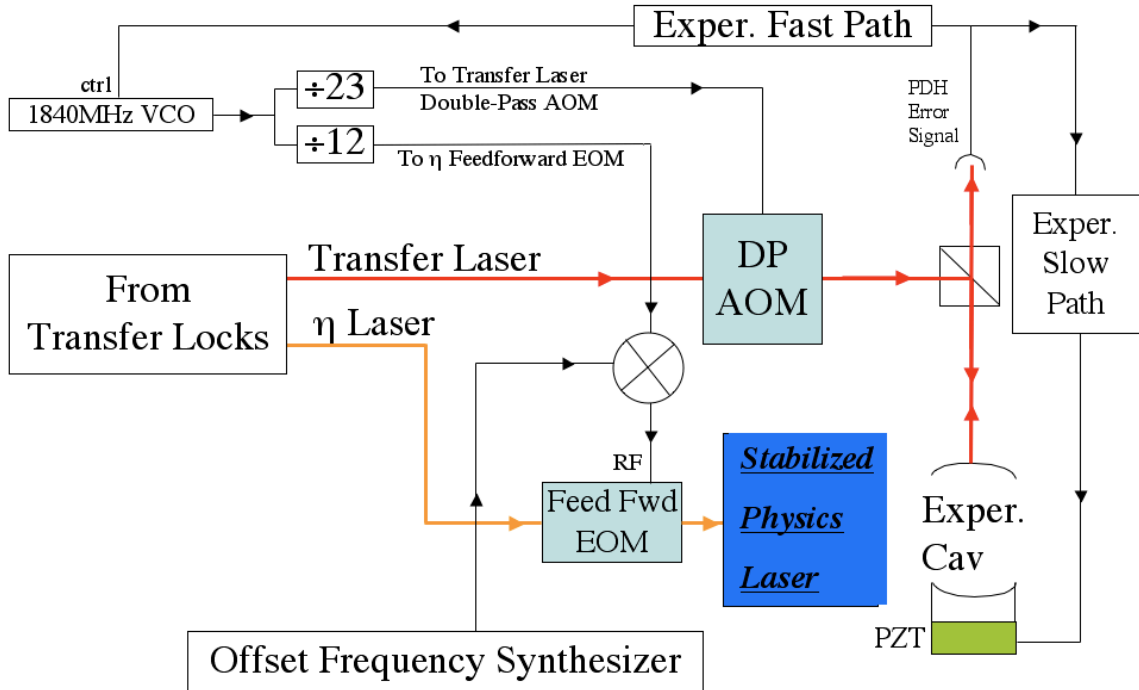
Figure 9.9: Schematic of Experimental Cavity Locking Scheme. Once stabilized to the transfer cavity, the transfer laser is reflected off of the main cavity in a Pound-Drever-Hall configuration. The derived error signal has is fed first to the experimental cavity piezo through a low-frequency feedback box. This locks the cavity to the transfer laser at low frequencies. At high frequencies the transfer laser is locked to the experimental cavity via a double-passed AOM. This high-frequency correction must then be fed forward to the η laser, through an appropriate frequency multiplication network. To place the η laser on the cavity resonance we also need a fixed frequency offset determined by the relative mode numbers of the η and transfer cavities.

- All lasers need to be placed as close to the transfer cavity as possible, to minimize the phase lag arising from path length, and thus maximize the useable feedback bandwidth.

9.5.8 Putting it all Together: Lock-Points

Once the experimental and transfer cavities are stably locked, the remaining task is to tune the experimental cavity relative to atomic resonance. The difficulty is that even if the transfer cavity is stabilized such that one of its modes coincides with η laser, the (locked) experimental cavity will *not* have a mode which is resonant with the η laser. This results from the small length difference between experimental and transfer cavities, and the fact that we are performing the experimental cavity lock using the transfer laser, which is at a substantially different linewidth from the η laser.

In order to span the gap, an EOM is used in the η beam path which goes to the experimental cavity, to offset the laser such that it will be resonant with the experimental cavity mode. Then, as the length of the transfer cavity is adjusted (via the beatnote lock of η to the Reference laser), the experimental cavity follows (via the transfer-laser locks), and we can tune the experimental cavity to atomic resonance.

The necessary offset-frequency for the η EOM can vary from DC to the free spectral range of about 11GHz. In practice, it is most convenient for us to work at around 8GHz (determined by available synthesizers), and so we tune which mode of the transfer and experimental cavities we lock to to adjust the necessary offset frequency. The transfer cavity is temperature stabilized and may thus be temperature

X	T_-	T_0	T_+
E_-	15	-460	-934
E_0	475	0	-475
E_+	934	460	-15

Table 9.1: Amount of frequency shift, in MHz, necessary for the η EOM sideband to remain resonant with the experimental cavity as the transfer and experimental cavity lengths are jumped by a wavelength of the 817 and 852nm lasers, respectively.

tuned by many FSRs, while the experimental cavity can only be tuned by the ~ 4FSRs accessible via the piezo.

It is straightforward to show that when the transfer and experimental cavity lengths are adjusted by m and n FSRs, respectively, the requisite shift of the η offset frequency is: $\delta\nu_{Offset} = (m\Delta\nu_{FSR}^{852} - n\Delta\nu_{FSR}^{817})(1 - \frac{\lambda_{852}}{\lambda_{817}})$. This expression is tabulated for increase $(+)$ and decreasing $(-)$ each of the Transfer(T) and η lasers by a free spectral range. The numbers given here are good only to approximately 1MHz.

9.6   Optical Lattice

The atoms are loaded into a 937nm intra-cavity optical lattice with a trap depth of $U_{trap} \approx 50\mu$K, estimated from a measured (via parametric heating[46]) trap frequency $\omega_{trap} = 2\pi \times 90$KHz, arising from a power of ≈ 1.5mW transmitted through the cavity[9].

---

[9]We would actually expect a trap frequency of 160KHz and a trap depth of 190μK for 1.4mW transmitted through the cavity. We typically find a factor of two discrepancy in trap frequency, when we measure it by modulating the trap depth at a frequency ω_{mod}, and looking for a loss resonance at $\omega_{mod} = 2\omega_{trap}$. Since the lattice potential is anharmonic, this method will only yield the *maximum* trap frequency if heating the coldest atoms causes hotter atoms to rethermalize and leave the trap. If the rethermalization times are too long then we will observe a trap frequency corresponding to atoms near the top of the trap, which experience a much smaller trap frequency.

This trapping has the effect of allowing us to store and manipulate atoms for hundreds of milliseconds before parametric heating[46] boils the atoms out of the trap. The radial confinement afforded by the trapping ensures that all of the trapped atoms experience the (maximal) on-axis atom-field coupling, though the incommensurate nature of the 937 and 852nm standing waves that the axial averaging remains. Any atom which is trapped is confined to less than an optical wavelength, and is thus in the Lamb-Dicke limit of recoil-free scattering[29]. This is crucially important because the cavity lifetime of nearly a μs is on the order of the doppler time for an atom at 10μK, so atoms not in the Lamb-Dicke limit would experience doppler broadening of the cavity line, and hence a reduction of η.

For Cesium, 937nm is a so-called "magic wavelength"[129, 128]. At this wavelength, coupling between $\left|6^2 P_{3/2}\right\rangle$ and higher excited states ensures that the $\left|6^2 P_{3/2}\right\rangle$ state experiences the *same* stark shift as the $\left|6^2 S_{1/2}\right\rangle$ state. The atomic transition is thus unbroadened by the trapping potential, to lowest order.

We have observed intra-cavity optical depths as high as 30000 for atomic ensembles loaded into the lattice, as observed by cavity shift.

9.7   Single Atom Detection

As a first step towards a high-efficiency single-photon detector, we have demonstrated the efficient detection of single atoms within the waist of the optical resonator. A sample of atoms is loaded into the intra-cavity optical lattice, and optically pumped into $F_g = 3$. We then shine a weak laser beam on the sample, resonant with the $F_g = 3 \rightarrow F_e = 4$ transition, which sometimes causes an atom to be transferred from

$F_g = 3$ to $F_g = 4$. To detect these transitions we tune our optical resonator to the $F_g = 4 \to F_e = 5$ cycling transition, and probe its transmission with a resonant laser. When then repump all atoms to $F_g = 3$, and repeat the process.

In the absence of an atom the transmission will be unity, and in the presence of an atom it will be suppressed by a factor $\frac{1}{(1+\eta)^2}$. In order to not saturate the atom, the maximum rate at which information (photons) may leak out of a single-sided cavity is $R_{out}^{max} = \frac{S_{max}\Gamma}{4}\frac{(1+\eta)^2}{\eta}$ in the absence of an atom, where $S_{max} \approx \frac{1}{2}$ is the maximum allowable saturation parameter before the transmission begins to increase. For our average $\eta \approx 2$ (averaged over the cavity standing wave and different Zeeman levels), we expect $R_{out}^{max} = 17\mu s^{-1}$.

We expect a shot-to-shot variation in the observed transmission arising from both photon shot-noise, and the η variation caused by the distribution of atoms over the cavity standing wave. Taking both of these effects into account, we expect to observe transmission similar to that shown in figure (9.10). Our total detection path efficiency[10] of $q = 4\%$ indicates that to detect an average of $N_{det} = 10$ photons in the absence of an atom, we will need a time $T_{meas} = \frac{N_{det}}{qR_{out}^{max}} = 15\mu s$.

We have verified that our setup is shot-noise limited over several minutes for ~ 30 photons transmitted, as shown in figure (9.11)- this means that our laser-cavity detuning, and laser power, are stable to $\approx \frac{1}{\sqrt{30}} \approx 3\%$, into the measured bin size of approximately $100\mu s$, over the several minute measuring time.

The remaining question, then, is whether we can detect the effect of an atom on

---

[10]This efficiency arises from: Chroma filters to remove 937 and 817nm light, each with $\sim 85\%$ transmission at 852nm, SPCM efficiency of 40% at 852nm, 60% fiber coupling efficiency, and 25% cavity out-coupling due to from losses and transmission out of the wrong cavity mirror.
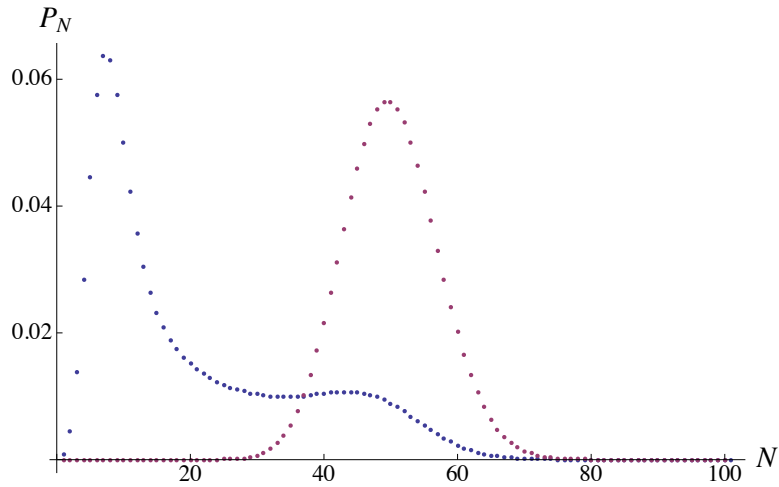
Figure 9.10: Expected photon number histogram for 1 and 0 atoms intracavity, with the 1-atom curve averaged over the cavity standing-wave. For this calculation we choose $\eta_{peak} = 2$.
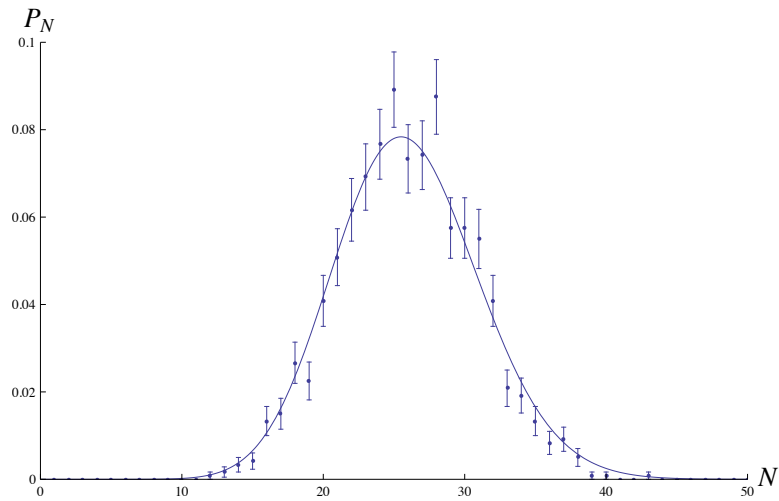
Figure 9.11: Photon Shot-Noise Limited Detection. The shown data is a histogram of the detected photon number transmitted through the optical cavity, in the absence of atoms, into $\sim 100\mu s$ bins, averaged over a few minutes. The model curve is a poisson-distributed model, and the agreement between data and model indicates that, over a few minutes, the cavity transmission is stable to 3% into a $100\mu s$ bin.

cavity transmission before it is either heated out of the trap due to recoil heating from the intra-cavity light, off-resonantly pumped back to $F = 3$, or its signal overrun by optical pumping backgrounds arising from other atoms.

Figure (9.12) shows the observed histogram into binsizes of 15μs and 70μs. For the 15μs bin, this data indicates that an atom detection efficiency of approximately 50% can be achieved, with a dark-count rate of 0.008/trial. For the 70μs bin, the 0 and 1 atom peaks are much better resolved. The small tail between them is likely a result of background atoms which are pumped to $F_g = 4$ in the middle of the detection interval, or the atoms sitting at nodes of the cavity field. The single-atom detection efficiency and dark count rates are clearly much improved, but a quantitative estimate would require a careful study of how far the bridge between zero- and one- atom peaks goes.

The contribution of atoms at cavity antinodes by using the 2μm dipole lens to address the atoms, and only addressing those at anti-nodes of the cavity field. 2μm is sufficient resolution because the beat-period between the intra-cavity lattice at 937nm and the cavity standing wave at 852nm is 4.7μm.
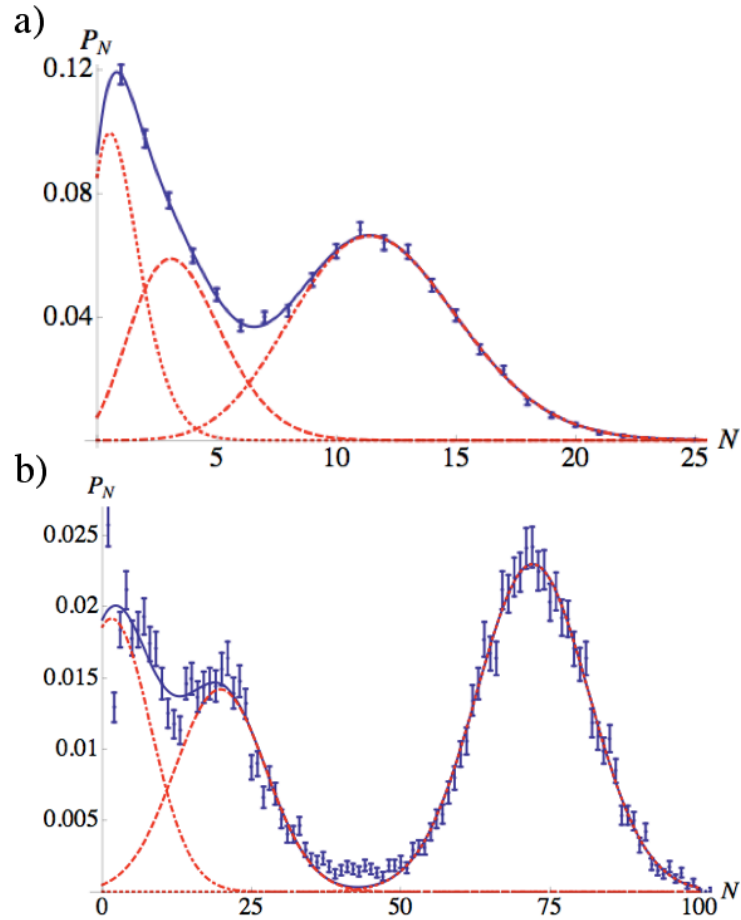
Figure 9.12: Single Atom detection. **(a)** Histogram of detected photon number into 15μs, bins. The fit curve is the weighted sum of three Poisson distributions, presumably indicating 0, 1, and 2 atoms. **(a)** Histogram of detected photon number into 70μs bins. The broadening due variation in η across the standing wave is now greater than the photon number shot noise, visible from the added structure in the curves. This broadening means that arbitrary normal- rather than poisson- distributions must be used to fit the data.

Chapter 10

Conclusions

The work in this thesis began with gaining a deep understanding of the behavior of magnons and transitioned into implementations of interesting quantum devices using magnons. Recent work has focused on the construction and characterization of a new apparatus in the single-atom strong-coupling limit.

It seems fitting, then, that the most promising next step is to combine collective effects and single atom strong-coupling to build a single-photon transistor or single photon detector. By loading enough atoms into the intra-cavity lattice to achieve many-atom strong coupling from the side, the ensemble can be used to efficiently stop a single photon[49], and detect the correspondingly generated collective excitations via the cavity. It is not altogether unreasonable to hope to non-destructively detect the magnons with some small, but finite probability. The magnons could then be read back out, realizing a single-photon QND detector.

An alternative, though no less interesting project would be to attempt to de-terministically load *two* atoms into the 2μm dipole traps via a collisional blockade

interaction. This would permit high-efficiency readout of the atomic states, as well as cavity mediated interactions.

Bibliography

[1] A. V. Akimov, A. Mukherjee, C. L. Yu, D. E. Chang, A. S. Zibrov, P. R. Hemmer, H. Park, and M. D. Lukin. Generation of single optical plasmons in metallic nanowires coupled to quantum dots. *Nature*, 450:402–406, November 2007.

[2] M. H. Anderson, J. R. Ensher, M. R. Matthews, C. E. Wieman, and E. A. Cornell. Observation of bose-einstein condensation in a dilute atomic vapor. *Science*, 269(5221):198–201, July 1995.

[3] V. Balić, D.A. Braje, P. Kolchin, G.Y. Yin, and S.E. Harris. Generation of paired photons with controllable waveforms. *Phys. Rev. Lett.*, 94:183601, 2005.

[4] Charles H. Bennett, David P. DiVincenzo, John A. Smolin, and William K. Wootters. Mixed-state entanglement and quantum error correction. *Phys. Rev. A*, 54(5):3824–3851, Nov 1996.

[5] K. M. Birnbaum, A. Boca, R. Miller, A. D. Boozer, T. E. Northup, and H. J. Kimble. Photon blockade in an optical cavity with one trapped atom. *Nature*, 436(7047):87–90, July 2005.

[6] A. T. Black. *Collective Atom-Light Interactions Applied to Laser Cooling and Quantum Communication*. PhD thesis, Stanford University, 2005.

[7] Adam T. Black, James K. Thompson, and Vladan Vuletić. On-demand superradiant conversion of atomic spin gratings into single photons with high efficiency. *Phys. Rev. Lett.*, 95(13):133601, Sep 2005.

[8] E. D. Black. An introduction to Pound-Drever-Hall laser frequency stabilization. *American Journal of Physics*, 69:79–87, January 2001.

[9] A. Boca, R. Miller, K. M. Birnbaum, A. D. Boozer, J. McKeever, and H. J. Kimble. Observation of the vacuum rabi spectrum for one trapped atom. *Phys. Rev. Lett.*, 93(23):233603, Dec 2004.

[10] Torsten Bondo, Markus Hennrich, Thomas Legero, Gerhard Rempe, and Axel Kuhn. Time-resolved and state-selective detection of single freely falling atoms. *Optics Communications*, 264(2):271 – 277, 2006. Quantum Control of Light and Matter - In honor of the 70th birthday of Bruce Shore.

[11] R. J. Brecha, P. R. Rice, and M. Xiao. n two-level atoms in a driven optical cavity: Quantum dynamics of forward photon scattering for weak incident fields. *Phys. Rev. A*, 59(3):2392–2417, Mar 1999.

[12] Dmitry Budker, Derek Kimball, and David Demille. *Atomic physics: An exploration through problems and solutions*. OUP Oxford, November 2003.

[13] Y. Castin, J. I. Cirac, and M. Lewenstein. Reabsorption of light by trapped atoms. *Phys. Rev. Lett.*, 80(24):5305–5308, Jun 1998.

[14] Carlton M. Caves and David D. Crouch. Quantum wideband traveling-wave analysis of a degenerate parametric amplifier: erratum. *J. Opt. Soc. Am. B*, 5(6):1343–1343, 1988.

[15] T. Chaneliere, D. N. Matsukevich, S. D. Jenkins, S. Y. Lan, T. A. B. Kennedy, and A. Kuzmich. Storage and retrieval of single photons transmitted between remote quantum memories. *Nature*, 438:833, 2005.

[16] T. Chanelière, D. N. Matsukevich, S. D. Jenkins, S.-Y. Lan, R. Zhao, T. A. B. Kennedy, and A. Kuzmich. Quantum interference of electromagnetic fields from remote quantum memories. *Phys. Rev. Lett.*, 98(11):113602, Mar 2007.

[17] S. Chen, Y.-A. Chen, T. Strassel, Z.-S. Yuan, B. Zhao, J. Schmiedmayer, and J.-W. Pan. A deterministic and storable single-photon source based on quantum memory. *Phys. Rev. Lett.*, 97:173004, 2006.

[18] K. S. Choi, H. Deng, J. Laurat, and H. J. Kimble. Mapping photonic entanglement into and out of a quantum memory. *Nature*, 452(7183):67–71, March 2008.

[19] C. W. Chou, H. de Riedmatten, D. Felinto, S. V. Polyakov, S. J. van Enk, and H. J. Kimble. Measurement-induced entanglement for excitation stored in remote atomic ensembles. *Nature*, 438:828–832, 2005.

[20] C. W. Chou, S. V. Polyakov, A. Kuzmich, and H. J. Kimble. Single-photon generation from stored excitation in an atomic ensemble. *Phys. Rev. Lett.*, 92:213601, 2004.

[21] John F. Clauser. Experimental distinction between the quantum and classical field-theoretic predictions for the photoelectric effect. *Phys. Rev. D*, 9(4):853–860, Feb 1974.

[22] Claude Cohen-Tannoudji, Jacques Dupont-Roc, and Gilbert Grynberg. *Atom-Photon Interactions: Basic Processes and Applications.* Wiley-Interscience, March 1992.

[23] Guoqiang Cui and M. Raymer. Quantum efficiency of single-photon sources in the cavity-qed strong-coupling regime. *Opt. Express*, 13(24):9660–9665, 2005.

[24] K. B. Davis, M. O. Mewes, M. R. Andrews, N. J. van Druten, D. S. Durfee, D. M. Kurn, and W. Ketterle. Bose-einstein condensation in a gas of sodium atoms. *Phys. Rev. Lett.*, 75(22):3969–3973, Nov 1995.

[25] Barak Dayan, A. S. Parkins, Takao Aoki, E. P. Ostby, K. J. Vahala, and H. J. Kimble. A Photon Turnstile Dynamically Regulated by One Atom. *Science*, 319(5866):1062–1065, 2008.

[26] H. de Riedmatten, J. Laurat, C. W. Chou, E. W. Schomburg, D. Felinto, and H. J. Kimble. Direct measurement of decoherence for entanglement between a photon and stored atomic excitation. *quant/ph0606249*, 2006.

[27] Samuel Deleglise, Igor Dotsenko, Clement Sayrin, Julien Bernu, Michel Brune, Jean-Michel Raimond, and Serge Haroche. Reconstruction of non-classical cavity field states with snapshots of their decoherence. *Nature*, 455(7212):510–514, September 2008.

[28] B. DeMarco and D. S. Jin. Onset of Fermi Degeneracy in a Trapped Atomic Gas. *Science*, 285(5434):1703–1706, 1999.

[29] R. H. Dicke. The effect of collisions upon the doppler width of spectral lines. *Phys. Rev.*, 89(2):472–473, Jan 1953.

[30] R. H. Dicke. Coherence in spontaneous radiation processes. *Phys. Rev.*, 93:99, 1954.

[31] R. H. Dicke. The Coherence Brightened Laser. In P. Grivet & N. Bloembergen, editor, *Quantum Electronics*, page 35, 1964.

[32] R. W. P. Drever, J. L. Hall, F. V. Kowalski, J. Hough, G. M. Ford, A. J. Munley, and H. Ward. Laser phase and frequency stabilization using an optical resonator. *Appl. Phys. B*, 31:97, 1983.

[33] L.-M. Duan and H. J. Kimble. Efficient engineering of multiatom entanglement through single-photon detections. *Phys. Rev. Lett.*, 90:253601, 2003.

[34] L.-M. Duan, M. D. Lukin, J. I. Cirac, and P. Zoller. Generation of nonclassical photon pairs for scalable quantum communication with atomic ensembles. *Nature*, 414:413, 2001.

[35] Y. O. Dudin, S. D. Jenkins, R. Zhao, D. N. Matsukevich, A. Kuzmich, and T. A. B. Kennedy. Entanglement of a photon and an optical lattice spin wave. *Phys. Rev. Lett.*, 103(2):020505+, 2009.

[36] M. D. Eisaman, A. André, F. Massou, M. Fleischhauer, A. S. Zibrov, and M. D. Lukin. Electromagnetically induced transparency with tunable single-photon pulses. *Nature*, 438:837, 2005.

[37] John Ellis. Physics at lhc. Nov 2006.

[38] Dirk Englund, Andrei Faraon, Bingyang Zhang, Yoshihisa Yamamoto, and Jelena Vučković. Generation and transfer of single photons on a photonic crystal chip. *Opt. Express*, 15(9):5550–5558, 2007.

[39] Eric D. Feigelson and Gutti Jogesh Babu. *Statistical Challenges in Modern Astronomy.* Springer-Verlag, 1992.

[40] D. Felinto, C. W. Chou, J. Laurat, E. W. Schomburg, H. de Riedmatten, and H. J. Kimble. Conditional control of the quantum states of remote atomic memories for quantum networking. *Nature Physics*, 2:844–848, 2006.

[41] Marco Fiorentino, Sean M. Spillane, Raymond G. Beausoleil, Tony D. Roberts, Philip Battle, and Mark W. Munro. Spontaneous parametric down-conversion in periodically poled ktp waveguides and bulk crystals. *Opt. Express*, 15(12):7479–7488, 2007.

[42] M. Fleischhauer, S. F. Yelin, and M. D. Lukin. How to trap photons? storing single-photon quantum states in collective atomic excitations. *Optics Communications*, 179(1-6):395 – 410, 2000.

[43] Kevin M. Fortier, Soo Y. Kim, Michael J. Gibbons, Peyman Ahmadi, and Michael S. Chapman. Deterministic loading of individual atoms to a high-finesse optical cavity. *Phys. Rev. Lett.*, 98(23):233601, Jun 2007.

[44] Stuart J. Freedman and John F. Clauser. Experimental test of local hidden-variable theories. *Phys. Rev. Lett.*, 28:938–941, 1972.

[45] Alpha Gaetan, Yevhen Miroshnychenko, Tatjana Wilk, Amodsen Chotia, Matthieu Viteau, Daniel Comparat, Pierre Pillet, Antoine Browaeys, and Philippe Grangier. Observation of collective excitation of two individual atoms in the rydberg blockade regime. *Nature Physics*, 5(2):115–118, January 2009.

[46] M. E. Gehm, K. M.OHara, T. A. Savard, and J. E. Thomas. Dynamics of noise-induced heating in atom traps. *Phys. Rev. A*, 58:3914, 1998.

[47] Sebastien Gleyzes, Stefan Kuhr, Christine Guerlin, Julien Bernu, Samuel Deleglise, Ulrich Busk Hoff, Michel Brune, Jean-Michel Raimond, and Serge Haroche. Quantum jumps of light recording the birth and death of a photon in a cavity. *Nature*, 446(7133):297–300, March 2007.

[48] Alexey V. Gorshkov, Axel André, Mikhail D. Lukin, and Anders S. Sørensen. Photon storage in λ -type optically dense atomic media. i. cavity model. *Phys. Rev. A*, 76(3):033804, Sep 2007.

[49] Alexey V. Gorshkov, Axel André, Mikhail D. Lukin, and Anders S. Sørensen. Photon storage in λ -type optically dense atomic media. ii. free-space model. *Phys. Rev. A*, 76(3):033805, Sep 2007.

[50] M. Greiner, O. Mandel, T. W. Hänsch, and I. Bloch. Quantum phase transition from a superfluid to a mott insulator in a gas of ultracold atoms. *Nature (London)*, 419:6901, 2002.

[51] Albrecht Haase, Björn Hessmo, and Jörg Schmiedmayer. Detecting magnetically guided atoms with an optical cavity. *Opt. Lett.*, 31(2):268–270, 2006.

[52] T. W. Hänsch, I. S. Shahin, and A. L. Schawlow. High-resolution saturation spectroscopy of the sodium d lines with a pulsed tunable dye laser. *Phys. Rev. Lett.*, 27(11):707–710, Sep 1971.

[53] A. Hecker, M. Havenith, C. Braxmaier, U. Strner, and A. Peters. High resolution doppler-free spectroscopy of molecular iodine using a continuous wave optical parametric oscillator. *Optics Communications*, 218(1-3):131 – 134, 2003.

[54] C. K. Hong, Z. Y. Ou, and L. Mandel. Measurement of subpicosecond time intervals between two photons by interference. *Phys. Rev. Lett.*, 59:2044–2046, 1987.

[55] Christina J. Hood, H. J. Kimble, and Jun Ye. Characterization of high-finesse mirrors: Loss, phase shifts, and mode structure in an optical cavity. *Phys. Rev. A*, 64(3):033804, Aug 2001.

[56] A. Imamoglu. High efficiency photon counting using stored light. *Phys. Rev. Lett.*, 89:163602, 2002.

[57] Daniel F. V. James and Paul G. Kwiat. Atomic-vapor-based high efficiency optical detectors with photon number resolution. *Phys. Rev. Lett.*, 89(18):183601, Oct 2002.

[58] D. M. S. Johnson, J. M. Hogan, S. w. Chiow, and M. A. Kasevich. Broadband optical serrodyne frequency shifting. *Opt. Lett.*, 35(5):745–747, 2010.

[59] Matthias Keller, Birgit Lange, Kazuhiro Hayasaka, Wolfgang Lange, and Herbert Walther. Continuous generation of single photons with controlled waveform in an ion-trap cavity system. *Nature*, 431:1075, 2004.

[60] M. Khudaverdyan, W. Alt, I. Dotsenko, T. Kampschulte, K. Lenhard, A. Rauschenbeutel, S. Reick, K. Schörner, A. Widera, and D. Meschede. Controlled insertion and retrieval of atoms coupled to a high-finesse optical resonator. *New J. Phys.*, 10(7):073023+, July 2008.

[61] M. Khudaverdyan, W. Alt, T. Kampschulte, S. Reick, A. Thobe, A. Widera, and D. Meschede. Quantum jumps and spin dynamics of interacting atoms in a strongly coupled atom-cavity system. *Phys. Rev. Lett.*, 103(12):123006, Sep 2009.

[62] H. J. Kimble, M. Dagenais, and L. Mandel. Photon antibunching in resonance fluorescence. *Phys. Rev. Lett.*, 39(11):691–695, Sep 1977.

[63] E. Knill, R. Laflamme, and G. Milburn. A scheme for efficient quantum computation with linear optics. *Nature*, 409:46, 2001.

[64] Friedrich König, Elliott J. Mason, Franco N. C. Wong, and Marius A. Albota. Efficient and spectrally bright source of polarization-entangled photons. *Phys. Rev. A*, 71(3):033805, Mar 2005.

[65] A. Kubanek, A. Ourjoumtsev, I. Schuster, M. Koch, P. W. H. Pinkse, K. Murr, and G. Rempe. Two-photon gateway in one-atom cavity quantum electrodynamics. *Phys. Rev. Lett.*, 101(20):203602, Nov 2008.

[66] Axel Kuhn, Markus Hennrich, and Gerhard Rempe. Deterministic single-photon source for distributed quantum networking. *Phys. Rev. Lett.*, 89:067901, 2002.

[67] Christopher E. Kuklewicz, Franco N. C. Wong, and Jeffrey H. Shapiro. Time-bin-modulated biphotons from cavity-enhanced down-conversion. *Phys. Rev. Lett.*, 97(22):223601, Nov 2006.

[68] A. Kuzmich, W. P. Bowen, A. D. Boozer, A. Boca, C. W. Chou, L.-M. Duan, and H. J. Kimble. Generation of nonclassical photon pairs for scalable quantum communication with atomic ensembles. *Nature*, 423:731, 2003.

[69] J. Laurat, H. Riedmatten, D. Felinto, C. W. Chou, E. W. Schomburg, and H. J. Kimble. Efficient retrieval of a single excitation stored in an atomic ensemble. *Optics Express*, 14:6912, 2006.

[70] D. Leibfried, E. Knill, S. Seidelin, J. Britton, R. B. Blakestad, J. Chiaverini, D. B. Hume, W. M. Itano, J. D. Jost, C. Langer, R. Ozeri, R. Reichle, and D. J. Wineland. Creation of a six-atom schrodinger cat state. *Nature*, 438:639–643, 2005.

[71] Han Chuen Lim, Akio Yoshizawa, Hidemi Tsuchida, and Kazuro Kikuchi. Distribution of polarization-entangled photonpairsproduced via spontaneous parametricdown-conversion within a local-area fibernetwork: Theoretical model and experiment. *Opt. Express*, 16(19):14512–14523, 2008.

[72] Rodney Loudon. *The Quantum Theory of Light*. Oxford University Press, Oxford, third edition, 2000.

[73] A. D. Ludlow, X. Huang, M. Notcutt, T. Zanon-Willette, S. M. Foreman, M. M. Boyd, S. Blatt, and J. Ye. Compact, thermal-noise-limited optical cavity for diode laser stabilization at 1×10^{-15}. *Opt. Lett.*, 32(6):641–643, 2007.

[74] M. D. Lukin. Colloquium: Trapping and manipulating photon states in atomic ensembles. *Rev. Mod. Phys.*, 75(2):457–472, Apr 2003.

[75] M. D. Lukin and L. Childress. Course notes for physics 285b: Amo physics.

[76] X. Maitre, E. Hagley, G. Nogues, C. Wunderlich, P. Goy, M. Brune, J. M. Raimond, and S. Haroche. Quantum memory with a single photon in a cavity. *Phys. Rev. Lett.*, 79:769, 1997.

[77] D. N. Matsukevich, T. Chaneliere, S. D. Jenkins, S. Y. Lan, T. A. B. Kennedy, and A. Kuzmich. Deterministic single photons via conditional quantum evolution. *Phys. Rev. Lett.*, 97:013601, 2006.

[78] D. N. Matsukevich, T. Chaneliere, S. D. Jenkins, S.-Y. Lan, T. A. B. Kennedy, and A. Kuzmich. Entanglement of remote atomic qubits. *Phys. Rev. Lett.*, 96:030405, 2006.

[79] P. Maunz, D. L. Moehring, S. Olmschenk, K. C. Younge, D. N. Matsukevich, and C. Monroe. Quantum interference of photon pairs from two remote trapped atomic ions. *Nature Physics*, 3(8):538–541, June 2007.

[80] P. Maunz, T. Puppe, I. Schuster, N. Syassen, P. W. H. Pinkse, and G. Rempe. Cavity cooling of a single atom. *Nature*, 428(6978):50–52, March 2004.

[81] J. McKeever. *Trapped Atoms in Cavity QED for Quantum Optics and Quantum Information*. PhD thesis, Caltech, 2004.

[82] J. McKeever, A. Boca, A.D. Boozer, R. Miller, J.R. Buck, A. Kuzmich, and H.J. Kimble. Deterministic generation of single photons from one atom trapped in a cavity. *Science*, 303:1992, 2004.

[83] S. L. Mielke, G. T. Foster, and L. A. Orozco. Nonclassical intensity correlations in cavity qed. *Phys. Rev. Lett.*, 80(18):3948–3951, May 1998.

[84] Y Miroshnychenko, W Alt, I Dotsenko, L Forster, M Khudaverdyan, A Rauschenbeutel, and D Meschede. Precision preparation of strings of trapped neutral atoms. *New Journal of Physics*, 8(9):191, 2006.

[85] Klaus Mlmer and Yvan Castin. Monte carlo wavefunctions in quantum optics. *Quantum and Semiclassical Optics: Journal of the European Optical Society Part B*, 8(1):49, 1996.

[86] B. Odom, D. Hanneke, B. D'Urso, and G. Gabrielse. New measurement of the electron magnetic moment using a one-electron quantum cyclotron. *Physical Review Letters*, 97(3), 2006.

[87] J. Oreg, F. T. Hioe, and J. H. Eberly. Adiabatic following in multilevel systems. *Phys. Rev. A*, 29(2):690–697, Feb 1984.

[88] T. Pellizzari, S. A. Gardiner, J. I. Cirac, and P. Zoller. Decoherence, continuous observation, and quantum computing: A cavity qed model. *Phys. Rev. Lett.*, 75:3788, 1995.

[89] D. F. Phillips, A. Fleischhauer, A. Mair, R. L. Walsworth, and M. D. Lukin. Storage of light in atomic vapor. *Phys. Rev. Lett.*, 86:783, 2001.

[90] Jérôme Poirson, Fabien Bretenaker, Marc Vallet, and Albert Le Floch. Analytical and experimental study of ringing effects in a fabry–perot cavity. application to the measurement of high finesses. *J. Opt. Soc. Am. B*, 14(11):2811–2817, 1997.

[91] S.V. Polyakov, C.W. Chou, D. Felinto, and H.J. Kimble. Temporal dynamics of photon pairs generated by an atomic ensemble. *Phys. Rev. Lett.*, 93:263601, 2004.

[92] E. M. Purcell. Spontaneous emission probabilities at radio frequencies. *Phys. Rev.*, 69:681, 1946.

[93] E. L. Raab, M. Prentiss, A. Cable, S. Chu, and D. E. Pritchard. "trapping of neutral sodium atoms with radiation pressure". *Phys. Rev. Lett.*, 59:26312634, 1987.

[94] J. M. Raimond, P. Goy, M. Gross, C. Fabre, and S. Haroche. Statistics of millimeter-wave photons emitted by a rydberg-atom maser: An experimental study of fluctuations in single-mode superradiance. *Phys. Rev. Lett.*, 49(26):1924–1927, Dec 1982.

[95] Mohsen Razavi and Jeffrey H. Shapiro. Long-distance quantum communication with neutral atoms. *Phys. Rev. A*, 73(4):042303, Apr 2006.

[96] S. Reick, K. Mølmer, W. Alt, M. Eckstein, T. Kampschulte, L. Kong, R. Reimann, A. Thobe, A. Widera, and D. Meschede. Analyzing quantum jumps of one and two atoms strongly coupled to an optical cavity. *ArXiv e-prints*, February 2010.

[97] P. R. Rice and H. J. Carmichael. Single-atom cavity-enhanced absorption. I - Photon statistics in the bad-cavity limit. *IEEE Journal of Quantum Electronics*, 24:1351–1366, July 1988.

[98] Morton H. Rubin, David N. Klyshko, Y. H. Shih, and A. V. Sergienko. Theory of two-photon entanglement in type-ii optical parametric down-conversion. *Phys. Rev. A*, 50(6):5122–5133, Dec 1994.

[99] C. A. Sackett, D. Kielpinski, B. E. King, C. Langer, V. Meyer, C. J. Myatt, M. Rowe, Q. A. Turchette, W. M. Itano, D. J. Wineland, and C. Monroe. Experimental entanglement of four particles. *Nature (London)*, 404:256, 2000.

[100] J. J. Sakurai. *Modern Quantum Mechanics (Revised Edition)*. Addison Wesley, rev sub edition, September 1993.

[101] C. Santori, D. Fattal, J. Vuckovic, G. S. Solomon, and Y. Yamamoto. Indistinguishable photons from a single-photon device. *Nature*, 419:594, 2002.

[102] Emilio Santos. Unreliability of performed tests of bell's inequality using parametric down-converted photons. *Physics Letters A*, 212(1-2):10 – 14, 1996.

[103] N. Schlosser, G. Reymond, I. Protsenko, and P. Grangier. Sub-poissonian loading of single atoms in a microscopic dipole trap. *Nature*, 411:1024–1027, June 2001.

[104] Dominik Schneble, Yoshio Torii, Micah Boyd, Erik W. Streed, David E. Pritchard, and Wolfgang Ketterle. The Onset of Matter-Wave Amplification in a Superradiant Bose-Einstein Condensate. *Science*, 300(5618):475–478, 2003.

[105] U. Schnorrberger, J. D. Thompson, S. Trotzky, R. Pugatch, N. Davidson, S. Kuhr, and I. Bloch. Electromagnetically induced transparency and light storage in an atomic mott insulator. *Phys. Rev. Lett.*, 103(3):033003, Jul 2009.

[106] Matthias Scholz, Lars Koch, and Oliver Benson. Statistics of narrow-band single photons for quantum memories generated by ultrabright cavity-enhanced parametric down-conversion. *Physical Review Letters*, 102(6):063603+, 2009.

[107] U. Schünemann, H. Engler, R. Grimm, M Weidemüller, and M. Zielonkowski. Simple scheme for tunable frequency locking of two lasers. *Rev. Sci. Instrum.*, 70:242, 1999.

[108] M. Scully and M. Suhail Zubairy. *Quantum Optics*. Cambridge University Press, third edition, 2001.

[109] Y. H. Shih and C. O. Alley. New type of einstein-podolsky-rosen-bohm experiment using pairs of light quanta produced by optical parametric down conversion. *Phys. Rev. Lett.*, 61(26):2921–2924, Dec 1988.

[110] P. W. Shor. Algorithms for quantum computation: discrete logarithms and factoring. *Foundations of Computer Science, 1994 Proceedings., 35th Annual Symposium on*, pages 124–134, 1994.

[111] A. E. Siegman. *Lasers*. University Science Books, Sausalito, 1986.

[112] Joo Batista Rosa Silva and Rubens Viana Ramos. Implementations of quantum and classical gates with linear optical devices and photon number quantum non-demolition measurement for polarization encoded qubits. *Physics Letters A*, 359(6):592 – 596, 2006.

[113] Jonathan Simon, Haruka Tanji, Saikat Ghosh, and Vladan Vuletić. Single-photon bus connecting spin-wave quantum memories. *Nature Physics*, 3:765, 2007.

[114] Jonathan Simon, Haruka Tanji, James K. Thompson, and Vladan Vuletić. Interfacing collective atomic excitations and single photons. *Phys. Rev. Lett.*, 98:183601, 2007.

[115] S. M. Spillane, T. J. Kippenberg, K. J. Vahala, K. W. Goh, E. Wilcut, and H. J. Kimble. Ultrahigh- q toroidal microresonators for cavity quantum electrodynamics. *Phys. Rev. A*, 71(1):013817, Jan 2005.

[116] D. A. Steck. Cesium d line data. 1998.

[117] Haruka Tanji, Saikat Ghosh, Jonathan Simon, Benjamin Bloom, and Vladan Vuletić. Heralded single-magnon quantum memory for photon polarization states. *Phys. Rev. Lett.*, 103(4):043601, Jul 2009.

[118] James K. Thompson, Jonathan Simon, Huanqian Loh, and Vladan Vuletic. A High-Brightness Source of Narrowband, Identical-Photon Pairs. *Science*, 313(5783):74–77, 2006.

[119] Q. A. Turchette, C. S. Wood, B. E. King, C. J. Myatt, D. Leibfried, W. M. Itano, C. Monroe, and D. J. Wineland. Deterministic entanglement of two trapped ions. *Phys. Rev. Lett.*, 81:3631–3634, 1998.

[120] B Ueberholz, S Kuhr, D Frese, V Gomer, and D Meschede. Cold collisions in a high-gradient magneto-optical trap. *Journal of Physics B: Atomic, Molecular and Optical Physics*, 35(23):4899, 2002.

[121] Changxin Wang and Reeta Vyas. Cavity-modified maxwell-bloch equations for the vacuum rabi splitting. *Phys. Rev. A*, 55(1):823–826, Jan 1997.

[122] B. Weber, H. P. Specht, T. Müller, J. Bochmann, M. Mücke, D. L. Moehring, and G. Rempe. Photon-photon entanglement with a single trapped atom. *Phys. Rev. Lett.*, 102(3):030501, Jan 2009.

[123] Markus Weber, Jürgen Volz, Karen Saucke, Christian Kurtsiefer, and Harald Weinfurter. Analysis of a single-atom dipole trap. *Phys. Rev. A*, 73(4):043406, Apr 2006.

[124] Edward A. Whittaker, Manfred Gehrtz, and Gary C. Bjorklund. Residual amplitude modulation in laser electro-optic phase modulation. *J. Opt. Soc. Am. B*, 2(8):1320–1326, 1985.

[125] C. Wieman and T. W. Hänsch. Doppler-free laser polarization spectroscopy. *Phys. Rev. Lett.*, 36(20):1170–1173, May 1976.

[126] William K. Wootters. Entanglement of formation of an arbitrary state of two qubits. *Phys. Rev. Lett.*, 80:2245–2248, 1998.

[127] Y. Yamamoto and Atac Imamoglu. *Mesoscopic Quantum Optics*. Wiley, 1999.

[128] Jun Ye, H. J. Kimble, and Hidetoshi Katori. Quantum State Engineering and Precision Metrology Using State-Insensitive Light Traps. *Science*, 320(5884):1734–1738, 2008.

[129] Zheng Yu-Nan, Zhou Xiao-Ji, Chen Jing-Biao, and Chen Xu-Zong. Magic wavelength for caesium transition line 6s1/2 – 6p3/2. *Chinese Physics Letters*, 23(7):1687–1690, 2006.

[130] Yifu Zhu, Daniel J. Gauthier, S. E. Morin, Qilin Wu, H. J. Carmichael, and T. W. Mossberg. Vacuum rabi splitting as a feature of linear-dispersion theory: Analysis and experimental observations. *Phys. Rev. Lett.*, 64(21):2499–2502, May 1990.

[131] P. Zoller, Th. Beth, D. Binosi, R. Blatt, H. Briegel, D. Bruss, T. Calarco, I. Cirac, Deutsch, J. Eisert, A. Ekert, C. Fabre, N. Gisin, P. Grangiere, M. Grassl, S. Haroche, A. Imamoglu, A. Karlson, J. Kempe, L. Kouwenhoven, S. Krll, G. Leuchs, M. Lewenstein, D. Loss24, N. Ltkenhaus, S. Massar, J. E. Mooij, M. B. Plenio, E. Polzik, S. Popescu, G. Rempe, A. Sergienko, D. Suter, Twamley, G. Wendin, R. Werner, A. Winter, J. Wrachtrup, and A. Zeilinger. Quantum information processing and communication. *Eur. Phys. J. D*, 36:204–228, 2005.

Appendix A

Supplementary Information from Quantum Bus Paper

Supplemental Information for "Single-photon bus connecting spin-wave quantum memories"

Jonathan Simon,[1,2] Haruka Tanji,[1,2] Saikat Ghosh,[2] and Vladan Vuletić[2]

[1]*Department of Physics, Harvard University, Cambridge, Massachusetts 02138, USA*
[2]*Department of Physics, MIT-Harvard Center for Ultracold Atoms, and Research Laboratory of Electronics,*
Massachusetts Institute of Technology, Cambridge, Massachusetts 02139, USA
(Dated: August 6, 2007)

I. EXPERIMENTAL METHODS

A sample of laser cooled caesium atoms at a typical temperature of 20 μK is optically pumped into the state $|s\rangle = |6S_{1/2}; F = 4, m_F = 4\rangle$ by two circularly polarized laser beams propagating along a 900 mG magnetic field, defining a quantization axis. The magnetic field is perpendicular to the vertically oriented optical resonator of finesse $\mathcal{F} = 240$ and TEM_{00} waist $w_c = 110$ μm.

In order to prepare a single spin excitation, the atoms are driven for 90 ns by a weak "write" laser beam propagating in the horizontal plane orthogonal to, and polarized along, the quantization axis. The beam frequency is tuned 110 MHz to the red of the $|s\rangle \rightarrow |e\rangle = |6P_{3/2}; 4, 4\rangle$ transition. This beam has a waist of 210 μm, a typical peak intensity of 100 mW/cm^2, and is directed towards the upper half of the atomic cloud with a typical root-mean-square size of 1 mm. The atoms in the overlap region of the write laser beam and the cavity TEM_{00} mode are henceforth referred to as ensemble A.

The resonator TEM_{00} mode is tuned to be resonant with spontaneous Raman scattering on the $|s\rangle \rightarrow |e\rangle \rightarrow |g\rangle = |6S_{1/2}; 3, 3\rangle$ hyperfine-ground-state changing transition. Detection of an $|e\rangle \rightarrow |g\rangle$ "write" photon exiting the resonator projects the atomic ensemble into a state with a collective spin excitation:

$$|G\rangle = \sum_{i=1}^{N_A} |s_1 \ldots g_i \ldots s_N\rangle \, e^{i\vec{k}_{write} \cdot \vec{r}_i} \cos{(\vec{k}_{cav} \cdot \vec{r}_i)}. \tag{1}$$

Here s_j or g_j indicates the internal state of the j-th atom, r_j its position, and $\vec{k}_{write}$ and $\vec{k}_{cav}$ are the write beam and cavity wavevectors. Photon detection is performed with single photon counting modules coupled by single mode fibers to the optical resonator.

The collective spin excitation can then be converted into a single photon in the cavity mode by application of a phase-matched[1] "read" beam counter-propagating relative to the write beam, tuned 20 MHz to the blue of the $|g\rangle \rightarrow |e\rangle$ transition, with a Rabi frequency of $2\pi \times 40$ MHz. This beam also has a waist of 210 μm, is phase-matched to the write beam, addresses only sample A, and will henceforth be referred to as Ω_A. When the excitation is simply read out, we routinely achieve a conditional photon retrieval efficiency R_A near 40%, referenced to within the cavity. R_A is limited by the optical depth $N_A \eta \sim 1$ of the sample to $R_A = \frac{N_A \eta}{1 + N_A \eta}$. The total detection efficiency for a photon generated inside the cavity is $q_e = 0.11(2)$, due to the quantum efficiency of the single photon counting module ($q_{spcm} = 0.40(5)$), cavity output coupling ($q_{cav} = 0.43(1)$), and fiber coupling and other losses ($q_{misc} = 0.66(4)$).

The excitation can be transferred to a second ensemble B by concurrent application of a secondary read beam, termed Ω_B, during the read process. Ω_B has a Rabi frequency of $2\pi \times 70$ MHz, the same 210 μm waist size as Ω_A, and the distance between the two beams is 390 μm. By turning Ω_B on first, then turning Ω_A on, and Ω_B off, according to the so-called counter-intuitive pulse sequence[2], the excitation can be transferred from sample A to sample B.

We believe that the efficiency of the transfer process is limited by two factors: The first is the variation of write- and read- beam intensities across the samples, resulting in imperfect phase matching, and hence re-absorption and free-space scattering of the generated single photon. The second limiting factor is our small optical depth $N_A \eta \sim N_B \eta \sim 1$. In the ideal case of perfect phase matching, the transfer efficiency T_{AB} is limited to $T_{AB} = \frac{N_A \eta \cdot N_B \eta}{(1 + N_A \eta)(1 + N_B \eta)} \approx 0.25$. We observe that the transfer efficiency improves with larger optical depth of the sample. We anticipate that by trapping the ensembles in two far detuned dipole traps, both of the above limitations may be circumvented.

In demonstrating entanglement between the two samples, the phase of Ω_A needs to be jumped between the adiabatic transfer process, and the interferometric read-out[2]. This is achieved by jumping the phase of the radio-frequency drive of the acousto-optic modulator which controls Ω_A.

In order to maximize our data collection rate, and also to minimize magnon-loss due to decoherence, we operate at a separation of $200 \sim 300$ ns between write, transfer, and read-out. In principle, we could separate the write, transfer, and read-out by as much as the magnon lifetimes in ensembles A and B. Measurements of these lifetimes are displayed in Supplementary Fig. 1, with the storage times $\tau_d = 1.3$, 1.7 μs for samples A and B, respectively,

2
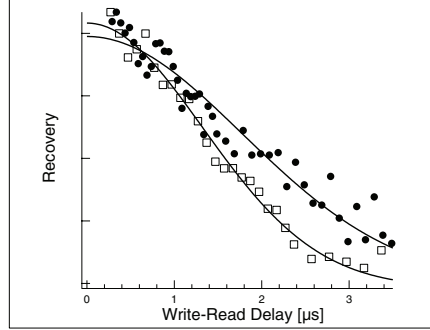
Supplementary Figure 1: **Magnon lifetime for collective spin excitations in ensembles** A **(open squares) and** B **(solid circles).** A spin excitation is written into sample A, and read out after a variable delay τ. The gaussian decay is a result of the random thermal motion of the atoms destroying the magnon, with a time constant $\tau_A = 1.3$ μs for ensemble A. After transfer of the excitation to ensemble B, the gaussian decay has a time constant $\tau_B = 1.7$ $\mu s > \tau_A$, indicating that sample B is at a lower temperature than sample A. The vertical axis has been rescaled by a factor of 5 for the two curves, to allow for a more direct comparison of timescales.

indicating temperatures of 50 and 20 μK. The difference is likely due to the recoil heating of ensemble A during the write process.

II. VERIFICATION OF ENTANGLEMENT BETWEEN ATOMIC ENSEMBLES

We wish to verify the presence of entanglement between the A and B ensembles, as generated by the adiabatic partial transfer of the spin excitation. Ideally, this entanglement takes the form[2] (for $\theta \neq 0, \frac{\pi}{2}$): $|\theta, \phi\rangle = \cos\theta \, |1\rangle_A \, |0\rangle_B - \sin\theta e^{i\phi} \, |0\rangle_A \, |1\rangle_B$, where $|j\rangle_k$ denotes j magnons stored in sample k. In reality, a density matrix is used to parameterize the joint state of the two ensembles after detection of the write photon.

The phase ϕ is determined by the relative phase ϕ_T of the two read beams Ω_A, Ω_B during the transfer process, relative to an arbitrarily chosen (classical) phase reference ϕ_0 shared between ensembles A and B. We have verified that ϕ_T is stable to better than $7°$ over a time scale of 30 ms (limited by optical path length jitter). We could easily stabilize or record the classical phase ϕ_T during the measurement. However, it would not change any of our results since the optical path length is stable over the microsecond magnon storage time, and the joint readout depends only on the phase difference $\phi_T - \varphi_R$, where φ_R is the relative phase of beams Ω_A, Ω_B during readout relative to the chosen phase reference ϕ_0. To measure the coherence of the two components of the state $|\theta, \phi\rangle$, we vary φ_R relative to ϕ_T.

Our method of probing the magnon statistics is to convert the magnons into photons, and measure photon correlations. To this end, we define a density matrix for the magnons in a reduced Hilbert space, compute the concurrence, and then determine the relevant terms (or appropriate bounds thereupon) from measured photon correlation data. In several situations we need to set lower bounds on the concurrence because the measured photon statistics do not completely determine the magnon state.

Calculation of concurrence in terms of reduced density matrix for the magnons

The reduced density matrix conditioned upon detection of a write photon, and truncated into the subspace $H_1 = \{0, 1\}_A \otimes \{0, 1\}_B$ with at most one magnon in each ensemble A and B, can be written in the form:

$$\rho^{at}(t=0) = \begin{pmatrix} m_{00} & 0 & 0 & 0 \\ 0 & m_{10} & k^* & 0 \\ 0 & k & m_{01} & 0 \\ 0 & 0 & 0 & m_{11} \end{pmatrix}. \tag{2}$$

3

States with two or more photons in each ensemble have been ignored (see also the supplemental information for Ref.[3]), as these states can be selected out, in principle, by local non-destructive measurements of each sample, and such measurements cannot increase the entanglement[4]. In addition, all coherences with different magnon numbers in A and B are set to zero. This is because the phase of a non-local state must be defined relative to a reference, such as provided by the read beams. The phases of these read pump beams can be randomly varied for both samples together(requiring only classical communication), thus removing the coherences, and at worst reducing the entanglement of the two ensembles[3].

Conditioned upon being in the subspace of the reduced density operator given above, the concurrence is defined as[5]: $\mathcal{C}_1 = \frac{1}{M} \max[0, \ \sqrt{\lambda_1} - \sqrt{\lambda_2} - \sqrt{\lambda_3} - \sqrt{\lambda_4} \ ]$, with the λ's defined as the eigenvalues (in decreasing order) of the matrix $\rho \sigma_y^A \sigma_y^B \rho^* \sigma_y^A \sigma_y^B$. For $\rho = \rho^{at}(0)$, this gives $\mathcal{C}_1 = \frac{1}{M} \max[0, 2(|k| - \sqrt{m_{00}m_{11}})]$. Unconditionally, the concurrence C_{full} is bounded from below by[3] $M \cdot \mathcal{C}_1 = \max[0, \mathcal{C} = 2(|k| - \sqrt{m_{00}m_{11}})]$, with $M = m_{00} + m_{10} + m_{01} + m_{11}$ the probability of being in said subspace. To demonstrate entanglement, we need to have $\mathcal{C} = 2(|k| - \sqrt{m_{00}m_{11}}) > 0$.

Mapping of photon statistics onto magnon statistics, and calculation of concurrence bounds

Because we cannot directly measure the elements of the magnon density operator, we proceed by decomposing the concurrence into a combination of quantities which we can easily bound with measurements of photon correlations.

It turns out that two different photon correlation experiments need to be performed in order to determine the concurrence of the density operator. The simplest way to see this is to rewrite the concurrence bound as:

$$\mathcal{C} = 2 \cdot \sqrt{m_{10}m_{01}} \left(\frac{|k|}{\sqrt{m_{10}m_{01}}} - \sqrt{\frac{m_{00}m_{11}}{m_{10}m_{01}}} \right) = 2m(V - \sqrt{G_{AB}}), \tag{3}$$

where $V = \frac{|k|}{\sqrt{m_{10}m_{01}}}$, $G_{AB} = \frac{m_{00}m_{11}}{m_{10}m_{01}}$, $m = \sqrt{m_{10}m_{01}}$.

In what follows, we first address G_{AB} and demonstrate that it may be bounded by a loss-insensitive correlation function of the optical field. We then address V, and show that it can be appropriately bounded by an optically measured fringe contrast of the jointly-read-out excitation, in spite of the fact that the read-out efficiencies may be different for the two samples.

Conditional cross correlation term

G_{AB} appears similar to the magnon-magnon cross correlation function $g_{AB} = \frac{<m_A m_B>}{<m_A><m_B>} = \frac{m_{11}}{(m_{10}+m_{11})(m_{01}+m_{11})}$ for ensembles A and B, conditioned upon the detection of a write photon. It should be noted that strictly speaking, g_{AB} has higher order terms like m_{20}, but in our experiment this amounts to a 1% correction to g_{AB}, which is much smaller than the error-bars on g_{AB} from finite statistics.

In this section we first show that for $g_{AB} \leq 1$, $G_{AB} \leq g_{AB}$ (Theorem 1), using the fact that $g_{AB} \leq 1$ implies $G_{AB} \leq 1$ (Lemma 1). Next we argue that $g_{AB} \leq g_{AB}^{photonic}$ (Argument 1), where $g_{AB}^{photonic}$ is the quantity which we can actually measure using photon correlations. At the end, this leaves us with $G_{AB} \leq g_{AB}^{photonic}$.

In order to show $G_{AB} \leq g_{AB}$ for $g_{AB} \leq 1$, we first show $G_{AB} \leq 1$ for $g_{AB} \leq 1$.

Lemma 1. $g_{AB} \leq 1$ *implies* $G_{AB} \leq 1$.

Proof. $g_{AB} \leq 1$ is equivalent to $\frac{m_{11}}{(m_{10}+m_{11})(m_{01}+m_{11})} \leq 1$.
A bit of algebra yields $m_{11}(m_{10} + m_{01} + m_{11} - 1) + m_{10}m_{01} \geq 0$.
Identifying $m_{00} \leq 1 - m_{11} - m_{10} - m_{01}$, we arrive at $m_{10}m_{01} - m_{00}m_{11} \geq 0$, or $G_{AB} \leq 1$.

Theorem 1. $g_{AB} \leq 1$ *implies* $G_{AB} \leq g_{AB}$.

Proof. We begin with the result of Lemma 1, namely that $G_{AB} \leq 1$ for $g_{AB} \leq 1$.
$G_{AB} \leq 1$ is equivalent to $m_{10}m_{01} \geq m_{00}m_{11}$.
Multiplying through by $m_{11}(1 - m_{00})$, and noting that $1 - m_{00} = m_{10} + m_{01} + m_{11} + (1 - M)$, we find:

$$m_{11}m_{10}m_{01}(1 - m_{00}) \geq m_{00}m_{11}^2(m_{11} + m_{10} + m_{01} + (1 - M)) \tag{4}$$

and after some algebra this becomes:

$$m_{11}m_{10}m_{01} \geq m_{11}m_{00}[(m_{10} + m_{11})(m_{01} + m_{11}) + m_{11}(1 - M)] \tag{5}$$

or

$$\frac{m_{11}}{(m_{10}+m_{11})(m_{01}+m_{11})} \geq \frac{m_{00}m_{11}}{m_{10}m_{01}}[1+(1-M)\frac{m_{11}}{(m_{10}+m_{11})(m_{01}+m_{11})}] \tag{6}$$

or finally $g_{AB} \geq G_{AB}[1+(1-M)g_{AB}]$, which gives (using $0 \leq M \leq 1$) $G_{AB} \leq g_{AB}$.

Argument 1. $g_{AB} \leq g_{AB}^{photonic}$.

We sequentially read out the (possibly) stored magnon from each of the two samples, and compute the cross correlation of the emitted photons, conditioned upon the detection of a write photon. It is well known[6] that in the absence of backgrounds, losses do not affect the cross correlation function. This argument can be applied to the finite and different magnon-photon conversion efficiencies for samples A and B as well. The relevant backgrounds in our experiment are either poissonian, or super-poissonian, and thus $g_{AB}^{photonic} \geq g_{AB}$.

Hence for $g_{AB}^{photonic} \leq 1$, $G_{AB} \leq g_{AB}^{photonic}$, and:

$$\mathcal{C} \geq 2\sqrt{m_{10}m_{01}}[\frac{|k|}{\sqrt{m_{10}m_{01}}} - \sqrt{g_{AB}^{photonic}}]. \tag{7}$$

One might worry that the sequential read-out of the two excitations could artificially produce anti-correlation between the detection of a photon from sample A, and sample B. While this is in principle possible, it would require a substantial single-photon non-linearity which is inconsistent with our (maximum) single atom cooperativity[7] of $\eta_0 = g^2/\kappa\Gamma = \frac{24F/\pi}{(k_{cav}w_c)^2} \approx 3 \times 10^{-3} \ll 1$.

For the parameters of Fig. 3 of Ref. 2 we measure $g_{AB}^{photonic} = \frac{p_{11}}{(p_{10}+p_{11})(p_{01}+p_{11})} = 0.21(8)$.

Visibility term

The first term within the parentheses in Eqn. 3 can be interpreted as a normalized fringe visibility for magnons within H_1. We will demonstrate that a bound on this visibility can be extracted from a measurement of the recovery efficiency during a joint readout of the two samples, varying only the relative phases of the two readout beams. We first argue that varying the relative phases serves only to rotate the phase of the state written in. We then use this fact to place a bound on V from the measured optical fringe visibility $V^{photonic}$. Lastly, we bound the error on $V^{photonic}$ from the experimental inclusion of trials with two- or more magnons in each sample.

Because the pumps are spatially separated and address disjoint collections of atoms, a change in pump beam phase may actually be re-interpreted as a change in the phase of magnon modes interacting with said beam (via a corresponding phase change in the magnon annihilation and creation operators[8]). The important point is that changing the relative phases of the pumps should have no other impact upon the dynamics of the system.

One might worry that a small spatial overlap of Ω_A and Ω_B could generate a coupling term which depends upon the phase φ_R during readout. For our experiment this overlap is far too small to explain the observed fringe contrast. Furthermore, φ_R is not controlled (only $\phi_T - \varphi_R$ is fixed), and thus must be averaged over, washing out effects which would otherwise depend upon it.

To extract a bound on V from the observed visibility of the photonic system (Fig. 3 of Ref. 2), we can analyze the time evolution of an arbitrary initial state of the combined atom-cavity system, and compute the expected photonic fringe visibility in the one excitation subspace (including higher order terms contributes errors smaller by a factor $\sim g_{AA}p_{10} = 10^{-2}$, which is smaller than our statistical error on $V^{photonic}$, as explained below):

$$\rho(t=0,\varphi) = \begin{pmatrix} m_{00} & 0 & 0 & 0 \\ 0 & m_{10} & k^*e^{i\varphi} & 0 \\ 0 & ke^{-i\varphi} & m_{01} & 0 \\ 0 & 0 & 0 & m_{11} \end{pmatrix} \otimes |0\rangle_C {}_C\langle 0| = \rho^{at}(t=0,\varphi) \otimes |0\rangle_C {}_C\langle 0|, \tag{8}$$

where $|j\rangle_C$ denotes a state with j cavity photons.

The rate of photons leaving the cavity during the readout may be obtained by time evolving $\rho(t=0,\varphi)$ and computing the expectation value of $\frac{\kappa}{2}a_c^\dagger a_c$, where κ is the cavity linewidth and $a_c^\dagger(a_c)$ is the operator which creates (destroys) a photon in the caivty mode:

$$R(t,\varphi) = \frac{\kappa}{2}Tr[\rho(t,\varphi)a_c^\dagger a_c] = m_{10}|A_{10}(t)|^2 + m_{01}|A_{01}(t)|^2 + 2|k||C(t)|^2\cos(\varphi+\beta(t)+\phi_k) + m_{00}\alpha(t) + m_{11}\epsilon(t), \tag{9}$$

where $k = |k| e^{i\phi_k}$, and the time dependent terms ($A_{10}(t)$, $A_{01}(t)$, $C(t)$, $\alpha(t)$, $\beta(t)$, $\epsilon(t)$) are sums of matrix elements of an arbitrary time-evolution super-operator, and are independent of $\rho(t = 0, \varphi)$, and φ. It can easily be shown that $|C(t)|^2 \leq |A_{10}(\tau)| |A_{01}(\tau)|$, with equality indicating that the system is not polluted by phase jitter and statistical variations which reduce fringe visibility. The terms $\alpha(\tau)$ and $\epsilon(\tau)$ must be real and non-negative, because in principle one could prepare zero magnons, or one magnon in each sample, and in each case expect to observe a non-negative cavity emission rate. As such, these two terms can only decrease the photon fringe visibility $V^{photonic} = (R_{max} - R_{min})/(R_{max} + R_{min})$ at fixed magnon visibility V. It should be noted that photon backgrounds contribute primarily to the $\alpha(\tau)$ term. In the presence of such backgrounds, the photon fringe visibility will be less than the actual magnon visibility.

All that remains is to compute the photonic fringe visibility $V^{photonic}$, and maximize it with respect to the matrix elements of time-evolution super-operator:

$$V^{photonic} = \frac{\max_\varphi \int_0^T R(t)dt - \min_\varphi \int_0^T R(t)dt}{\max_\varphi \int_0^T R(t)dt + \min_\varphi \int_0^T R(t)dt} \leq \frac{2|k| \int_0^T |A_{10}(t)| |A_{01}(t)| \, dt}{m_{10} \int_0^T |A_{10}(t)|^2 \, dt + m_{01} \int_0^T |A_{01}(t)|^2 \, dt} \tag{10}$$

$$\leq \frac{2|k| \sqrt{\int_0^T |A_{10}(t)|^2 \, dt \int_0^T |A_{01}(t)|^2 \, dt}}{m_{10} \int_0^T |A_{10}(t)|^2 \, dt + m_{01} \int_0^T |A_{01}(t)|^2 \, dt} \leq \frac{|k|}{\sqrt{m_{10}m_{01}}} = V. \tag{11}$$

The first inequality results from dropping $\alpha(t)$ and $\epsilon(t)$, and setting $|C(t)|^2 = |A_{10}(t)| |A_{01}(t)|$, $\beta(t) = 0$, the worst case allowed by the positivity of $R(t)$. The second inequality results from application of the Cauchy-Schwartz inequality[9]. The third inequality arises from maximizing the photon visibility with respect to $\int_0^T |A_{10}(t)|^2 \, dt / \int_0^T |A_{01}(t)|^2 \, dt$, i.e., adjusting the photon retrieval efficiencies to compensate for an imbalance in magnon populations to maximize the observed photon fringe contrast.

Finally we show that inclusion in the density matrix of terms outside of H_1 introduces errors in V which are substantially smaller than the existing error-bar for $V^{photonic}$.

Under the assumption of linearity in the magnon-photon conversion process, one can show that including terms to next order in photon number results in the following $R(t, \varphi)$ (to lowest order in retrieval efficiency):

$$R(t, \varphi) = m_{00}\alpha(t) \;+\; (m_{10} + m_{11} + 2m_{20}) |A_{10}(t)|^2 + (m_{01} + m_{11} + 2m_{20}) |A_{01}(t)|^2$$
$$+ \; 2(|k| + \sqrt{2} |k_{11}^{20}| + \sqrt{2} |k_{11}^{02}|) |C(t)|^2 \cos(\varphi + \beta(t) + \phi_k), \tag{12}$$

where $k_{\alpha\beta}^{\gamma\delta}$ is the coherence between the states $|\alpha\rangle_A |\beta\rangle_B$ and $|\gamma\rangle_A |\delta\rangle_B$. Here we have already assumed that the higher order coherence terms are in phase with the lowest order coherence term, which maximizes the observed photonic coherence, hence placing a lower bound on V. We can next solve for a bound on $V^{photonic}$ following the procedure of the preceding section:

$$V^{photonic} \leq \frac{|k| + \sqrt{2} |k_{11}^{20}| + \sqrt{2} |k_{11}^{02}|}{\sqrt{(m_{10} + m_{11} + 2m_{20})(m_{01} + m_{11} + 2m_{20})}} \tag{13}$$

Assuming maximal coherence for the higher order terms also places a lower bound on V, so we impose $k_{11}^{20} = \sqrt{m_{11}m_{20}}$, $k_{11}^{02} = \sqrt{m_{11}m_{02}}$. We then identify $V = \frac{k}{\sqrt{m_{10}m_{01}}}$, and using $m_{11} \simeq m_{10}m_{01}g_{AB}$, $m_{20} \simeq \frac{m_{10}^2 g_{AA}}{2}$, $m_{02} \simeq \frac{m_{01}^2 g_{BB}}{2}$, to set a bound on V:

$$V \geq V^{photonic} \sqrt{(1 + g_{AB}m_{01} + g_{BB}m_{10})(1 + g_{AB}m_{10} + g_{AA}m_{01})} - \sqrt{g_{AB}}(\sqrt{g_{AA}}m_{01} + \sqrt{g_{BB}}m_{10}) \tag{14}$$

Using the known recovery efficiency $R_A, R_B \simeq 0.40$ to map $(p_{10}, p_{01}) \to (m_{10}, m_{01})$, and minimizing the above bound with respect to g_{BB} (which we did not measure), we find (for $g_{BB} = 0.28$), $V \geq 0.87$, well within the statistical error of $V \geq V^{photonic} = 0.88(4)$ given by the simpler analysis presented above.

Conclusion

Given that $V^{photonic} \leq V$, it is clear that $\mathcal{C} \geq 2\sqrt{m_{10}m_{01}}[V^{photonic} - \sqrt{g_{AB}^{photonic}}]$. A lower bound on each of m_{10} and m_{01} is set from the measured photon number inside the cavity: $\mathcal{C} \geq 2\sqrt{p_{10}p_{01}}[V^{photonic} - \sqrt{g_{AB}^{photonic}}]$. This justifies Eq. (2) and the subsequent paragraph of Ref. 2, used to establish a lower bound on the concurrence between the atomic ensembles A and B.

6

III.   CONCURRENCE FOR POISSONIAN MAGNON DISTRIBUTIONS

The (truncated to the single-excitation subspace in each sample) density matrix for macro-atoms A and B, each with a coherent state written into it (with means p_A and p_B respectively), and a well defined phase between them, is given by:

$$\rho_{coh} = e^{-p_A} e^{-p_B} \begin{pmatrix} 1 & 0 & 0 & 0 \\ 0 & p_A & \sqrt{p_A p_B} & 0 \\ 0 & \sqrt{p_A p_B} & p_B & 0 \\ 0 & 0 & 0 & p_A p_B \end{pmatrix}. \tag{15}$$

Noting that $\mathcal{C} = 2(|k| - \sqrt{m_{00} m_{11}})$, it is immediately clear that for ρ_{coh}, $\mathcal{C} = 0$. One can also use this density matrix to show that $G_{AB} = 1$, $V = 1$. Any phase jitter will decrease V, thus making $\mathcal{C} < 0$, while the concurrence $\mathcal{C}_{full}$ remains zero.

---

[1] J. K. Thompson, J. Simon, H.-Q. Loh, and V. Vuletic, "A High-Brightness Source of Narrowband, Identical-Photon Pairs," Science **313**, 74 (2006).

[2] J. Simon, H. Tanji, S. Ghosh, and V. Vuletic, "A Single-photon bus connecting spin-wave quantum memories," Nature Physics (2007).

[3] C. W. Chou, H. de Riedmatten, D. Felinto, S. V. Polyakov, S. J. van Enk, and H. J. Kimble, "Measurement-induced entanglement for excitation stored in remote atomic ensembles," Nature **438**, 828–832 (2005).

[4] C. H. Bennett, H. J. Bernstein, S. Popescu, and B. Schumacher, "Concentrating partial entanglement by local operations," Phys. Rev. A **53**, 2046–2052 (1996).

[5] W. K. Wootters, "Entanglement of Formation of an Arbitrary State of Two Qubits," Phys. Rev. Lett. **80**, 2245–2248 (1998).

[6] R. Loudon, *The Quantum Theory of Light* (Oxford University Press, Oxford, 2000), third edn.

[7] R. J. Thompson, Q. A. Turchette, O. Carnal, and H. J. Kimble, "Nonlinear spectroscopy in the strong-coupling regime of cavity QED," Phys. Rev. A **57**, 3084–3104 (1998).

[8] L.-M. Duan, M. D. Lukin, J. I. Cirac, and P. Zoller, "Long distance quantum communication with atomic ensembles and linear optics," Nature **414**, 413 (2001).

[9] L. Mandel and E. Wolf, *Optical coherence and quantum optics* (Cambridge University Press, New York, 1995).

Appendix B

Perturbation Theory with

Non-Hermetian Hamiltonians

Suppose we are interested in understanding how a state $|\psi_0\rangle$ of energy ϵ_0, initially uncoupled from all other states and the environment, is affected by a very weak perturbation $\hat{V}$. Suppose also that the only eigenvector of the system hamiltonian H_0 that is known is $|\psi_0\rangle$, and that H_0 incorporates loss, and is thus non-hermitian.

We would typically attack this problem by using normal first (or second) order perturbation theory, but the prescription in standard quantum mechanics textbooks does not quite apply to non-hermitian Hamiltonians, and in its standard form requires knowledge of the spectrum of eigenvectors and eigenvalues of H_0. For large-dimensional hilbert spaces calculation of the eigenvectors and eigenvalues requires solving a high-order characteristic equation, and cannot generally be accomplished in closed form.

We will follow the standard prescription the perturbative expansion as far as it

goes, and then make the necessary corrections for a non-hermetian hamiltonian. The expression that we end up with will be quite familiar. Following a line of reasoning similar to the resolvent method[22], we will reinterpret it, arriving at a perturbative expansion in $\hat{V}$ which does not require knowledge of the spectrum of H_0, and in fact may be computed in closed form (via a matrix inversion) for any finite dimensional system. We will require only that H_0 be diagonalizable and invertible.

Let us rewrite $\hat{V} \equiv \tilde{V}\Omega$, where Ω is our small parameter. We can now write out $|\psi_t\rangle$, the exact eigenstate of $H_t \equiv H_0 + \hat{V}$ as a perturbative expansion in powers of Ω:

$$|\psi_t\rangle = \sum_n \Omega^n |\psi_n\rangle \tag{B.1}$$

The corresponding energy ϵ_t may be written in a similar perturbative expansion:

$$\epsilon_t = \sum_n \Omega^n \epsilon_n \tag{B.2}$$

Our eigenvalue equation is then:

$$H_t |\psi_t\rangle = \epsilon_t |\psi_t\rangle \tag{B.3}$$

We may now substitute into (B.3) the perturbative expansions in powers of Ω, and match the powers of Ω. We arrive at equations of the form:

$$\Omega^m : H_0 |\psi_m\rangle + \tilde{V} |\psi_{m-1}\rangle = \sum_{n=0}^{m} \epsilon_n |\psi_{m-n}\rangle \tag{B.4}$$

Thus far everything we have done follows the standard prescription for perturbation theory. The standard perturbative techniques now make use of the bras $\langle n|$, which are eigenvectors of H_0, and satisfy $\langle n|m\rangle = \delta_{n,m}$. We do not have this luxury, because the (unknown) bra $\langle n|$ corresponding to the (unknown) ket $|n\rangle$ does *not*

necessarily satisfy $\langle n | m \rangle = \delta_{n,m}$. We can only be sure that this is the case if H_0 is hermitian, and it need not be!

Instead let us specify a *single* bra $\langle \psi_0^c |$ such that:

$$\langle \psi_0^c | \psi_0 \rangle = 1$$

$$\langle \psi_0^c | n \rangle = 0 \tag{B.5}$$

Where $|n\rangle$ are the (unknown) eigenvectors of H_0, excluding $|\psi_0\rangle$. Such a $\langle \psi_0^c |$ must exist, as H_0 is invertible and diagonalizable. We apply it to (B.4) and after simplification arrive at:

$$\epsilon_n = \left\langle \psi_0^c \left| \tilde{V} \right| \psi_{n-1} \right\rangle - \sum_{m=1}^{n-1} \epsilon_m \langle \psi_0^c | \psi_{n-m} \rangle \tag{B.6}$$

Solving (B.3) for $|\psi_n\rangle$, we find:

$$|\psi_n\rangle = \frac{1}{H_0 - \varepsilon_0 \mathbf{1}} \left(\sum_{m=0}^{n-1} \epsilon_{n-m} |\psi_m\rangle - \tilde{V} |\psi_{n-1}\rangle \right) \tag{B.7}$$

Together, (B.6) and (B.7) form recurrence relations which may be used to compute $|\psi_t\rangle$ and ϵ_t to all orders. The important point is that once H_0 has been written in matrix form (in any orthonormal basis), then $\frac{1}{H_0 - \varepsilon_0 \mathbf{1}} \equiv (H_0 - \varepsilon_0 \mathbf{1})^{-1}$, where X^{-1} is the matrix-inverse of X.

Without loss of generality, we put any component of $\hat{V}$ into H_0 which makes $\left\langle \psi_0^c \left| \tilde{V} \right| \psi_0 \right\rangle$ non-zero. We may now compute the first two orders of the energy and

wavefunction correction:

$$
\begin{aligned}
\epsilon_1 &= \left\langle \psi_0^c \left| \tilde{V} \right| \psi_0 \right\rangle = 0 \\
\epsilon_2 &= \left\langle \psi_0^c \left| \tilde{V}\tilde{Q}\frac{1}{H_0 - \epsilon_0 \mathbf{1}}\tilde{Q}\tilde{V} \right| \psi_0 \right\rangle \\
|\psi_1\rangle &= \frac{1}{H_0 - \epsilon_0 \mathbf{1}}\tilde{Q}\tilde{V}|\psi_0\rangle \\
|\psi_2\rangle &= \frac{1}{H_0 - \epsilon_0 \mathbf{1}}\tilde{Q}\tilde{V}\frac{1}{H_0 - \epsilon_0 \mathbf{1}}\tilde{Q}\tilde{V}|\psi_0\rangle
\end{aligned}
\tag{B.8}
$$

Where $\tilde{Q} \equiv \mathbf{1} - |\psi_0\rangle \langle \psi_0^c|$ projects onto the subspace orthogonal to $|\psi_0\rangle$.

(B.8) is the central result of this appendix. As an example of its application, we now use it to compute the transmission spectrum of a cavity containing an atom.

Transmission Spectrum of a Cavity Coupled to a Single Atom

In the limit of 0 or 1 excitations in the system, we have three accessible levels. $|0\rangle$ is a ground state atom with no photons in the cavity, $|E\rangle$ is an excited atom and no cavity photons, and $|C\rangle$ is a ground state atom and one cavity photon. The probe beam constitutes a weak perturbation to $|\psi_0\rangle \equiv |0\rangle$, coupling it to $|C\rangle$, so $\hat{V}$ and H_0 are given by:

$$
\begin{aligned}
H_0 &= \delta_{lc}|0\rangle\langle 0| + |E\rangle\langle E|\left(i\frac{\Gamma}{2} + \Delta_{ac}\right) + |C\rangle\langle C| i\frac{\kappa}{2} + g(|E\rangle\langle C| + \langle C||E\rangle) \\
\hat{V} &= \Omega(|C\rangle\langle 0| + |0\rangle\langle C|)
\end{aligned}
\tag{B.9}
$$

Where the energy offset δ_{lc} is the detuning of the probe beam from cavity-resonance (which has been defined as our zero of energy). Because H_0 does not couple $|0\rangle$ to the other states, we may now write out the 2×2 matrix describing H_0 in the strongly coupled manifold of $|E\rangle$ and $|G\rangle$. We note that $\hat{V} = \Omega\tilde{V}$ where $\tilde{V} = (|C\rangle\langle 0| + \langle 0||C\rangle)$. The cavity transmitted field is proportional to $\langle a^\dagger\rangle = \langle C|\psi_t\rangle$, which we may now

compute to first order in Ω using (B.8):

$$\langle E \rangle \propto \langle a^\dagger \rangle \approx \langle C \,|\psi_t\rangle \approx \frac{-i\frac{2\Omega}{\kappa}}{\left(1 - i\frac{\Delta_{la}}{\kappa/2}\right) + \frac{\eta}{1 - i\frac{\Delta_{ac} + \Delta_{la}}{\Gamma/2}}} \tag{B.10}$$

This expression accurately reproduces vacuum rabi splittings, cavity shifts, and so forth, so long as the atom/cavity system is probed well below saturation. This method may be used to model a variety of experiments with a discrete set of levels coupled by a (possibly) non-hermitian hamiltonian H_0. We have found it to be terrifically useful for understanding the magnon-light coupling in the presence of multiple excited states, improper beam and atom polarizations, and multiple samples- we can diagonalize an arbitrarily large matrix, though we quite likely *cannot* compute its eigenvectors!

The second order corrections may be used to compute autocorrelations of transmitted/scattered fields. Care must be taken, however, to ensure that the expressions are not used to a higher order than they are valid. In the preceding example, for instance, the second order correction should not be used as we have not included couplings to the two excitation manifold in either H_0 or $\hat{V}$.

Appendix C

Bayesian Estimates of Rates from Counting Statistics

Suppose we are attempting to estimate the rate r of a poisson process, given the detection of N events in a time T. Naively, we would expect $\langle r \rangle = \frac{N}{T}$, and in the large N limit this is a good estimate. For N small we much be more careful, as the distributions are not at all normal!

For our model we will follow closely the reasoning of reference [39]. We take a Bayesian approach to our statistical analysis, and treat r as a random variable sampled from a distribution- our detection of N photons should be an indication of r, as described by Baye's rule:

$$P(r|N) = P(N|r)\frac{P(r)}{P(N)} \tag{C.1}$$

Where for a poisson process $P(N|r) = e^{-rT}\frac{(rT)^N}{N!}$. If we assume no prior knowledge of the rate r, we can take a flat prior $P(r) = \frac{1}{r_{max}}$, $P(N) = \frac{1}{r_{max}T}$, and ultimately let $r_{max} \to \infty$. From here we can compute the maximum likelihood estimate of the rate

$r_{MLE} = \frac{N}{T}$, the mean value of the rate $\langle r \rangle = \int r P(r|N) dr = \frac{N+1}{T}$, and the standard deviation $\sigma_r = \sqrt{\int (r^2 - r) P(r|N) dr} = \frac{\sqrt{N+1}}{T}$.

The equal-probability 1σ confidence interval $[\langle r \rangle - \sigma_r^-, \langle r \rangle + \sigma_r^+]$ may then be computed by solving the equations:

$$erfc(1) = \int_{\langle r \rangle}^{\langle r \rangle + \sigma_r^+} P(r|N) dr = \int_{\langle r \rangle - \sigma_r^-}^{\langle r \rangle} P(r|N) dr \tag{C.2}$$

The most significant consequence of this result is that we compute g_2 according to:

$$g_2 = \frac{2(N_2 + 1)N_0}{N_1^2} \tag{C.3}$$

Where the extra 1 in the numerator reflects the calculation of this appendix, and we have ignored corresponding offsets for N_0 and N_1 because we have many counts, so the distinction between N and $N+1$ is unimportant. A similar method should be used to compute quantities such as $\left\langle \frac{1}{N_2} \right\rangle$ and $\left\langle \frac{1}{N_2^A N_2^B} \right\rangle$, and their confidence intervals. While the former expression may be computed in closed form, the latter seems to require a numerical solution.

Appendix D

The Fabry-Perot Transmission

Spectrum

We briefly introduce how to calculate the cavity transmission spectrum in the absence of atoms, using only classical electromagnetic theory.

Consider an electric field of (scalar) amplitude E_{in} incident on a Fabry-Perot cavity, represented by a system of two high-reflectivity mirrors, as shown in figure (D.1). To determine the field everywhere, one can either compute the field in each of the three regions in the figure separately and match at the boundaries, or follow a wave-packet through the system as it reflects, repeatedly, off of the various surfaces.

Figure D.1: A Resonant Cavity.

The two approaches are equivalent, but the author prefers the latter.

The field which is transmitted through the first mirror has amplitude $E_{in}t_{12}$, and it then travels a distance L and is transmitted through the second mirror, yielding a transmitted field $E_{in}t_{12}t_{23}e^{ikL}$.

This is not the whole story, however, as the field could have reflected off of the second mirror, travelled back to the first, reflected off of the first, travelled back to the second, and *then* been transmitted. This yields a total field $E_{in}t_{12}^At_{23}^Be^{ikL}(1 + r_{22}^Be^{ikL}r_{22}^Ae^{ikL}$.

This is *still* not the whole story, as the light can bounce back and forth infinitely many times before exiting the cavity. Adding up all of these amplitudes and recognizing the geometric nature of the series yields:

$$\frac{E_{out}}{E_{in}} = \frac{t_{12}^At_{23}^Be^{ikL}}{1 - r_{22}^Ar_{22}^Be^{i2kL}} \tag{D.1}$$

The cavity transmission is maximized when $2kL = 2\pi N$, where N is any integer. To obtain the behavior near resonance we choose $k = \frac{2\pi N}{2L} + \frac{\delta}{c}$, expand the exponential in the denominator and simplify:

$$\frac{E_{out}}{E_{in}} = \frac{t_{12}^At_{23}^Be^{ikL}}{1 - r_{22}^Ar_{22}^B}\frac{1}{1 - i\frac{\delta}{\frac{c}{2L}}\frac{r_{22}^Ar_{22}^B}{1-r_{22}^Ar_{22}^B}} \tag{D.2}$$

Assuming the mirrors are lossless and identical and using the beamsplitter relations[111] gives:

$$\frac{E_{out}}{E_{in}} = \frac{e^{ikL}}{1 - i\frac{\delta}{\kappa/2}} \tag{D.3}$$

Where $\kappa = \frac{\Delta\nu_{FSR}}{\mathcal{F}}$ is the cavity power transmission full width at half maximum, $\Delta\nu_{FSR} = 2\pi\frac{c}{2L}$ is the cavity free spectral range, and $\mathcal{F} = 2\pi\frac{r_{22}^Ar_{22}^B}{1-r_{22}^Ar_{22}^B} \approx \frac{2\pi}{2T}$ is the cavity finesse. The free spectral range tells us the separation in frequency between adjacent

cavity transmission maxima, while the the finesse tells us the ratio of the separation between- to the width of- the maxima. The finesse contains the same information as the quality factor Q, but is smaller by a factor of $\frac{\omega_c}{\Delta\nu_{FSR}}$. This is sensible because the resolving power is not actually Q but $\mathcal{F}$, as the cavity has *many* transmission maxima, not just one.

If one wishes to include cavity mirror losses within the expressions, it is clear that within each pass through the cavity, an additional multiplicative factor of $(1 - \frac{1}{2}L_{cav})$ must be included. The algebra is grungy and not terribly interesting, and has the effect of reducing the peak cavity transmission from 1 down to approximately $\frac{T^2}{(T+L/2)^2}$[1] The cavity finesse is reduce to $\mathcal{F} = \frac{2\pi}{2T+L_{cav}}$, and the linewidth is increased accordingly. It is also clear that a photon in the cavity comes out the jth end of the cavity with a probability $P_j = \frac{T_j}{T_1+T_2+L_{cav}}$.
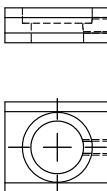
It is worth mentioning that in practice the two cavity mirrors never have identical transmissions, and so the transmitted fraction is given by $T_{cav} = \frac{4T_1T_2}{(T_1+T_2+L_{cav})^2}$. This expression is less than unity even in the absence of loss ($L_{cav} = 0$), $T_{cav} < 1$ unless $T_1 = T_2$. In practice this is one of the tools that we use to sort out the transmissions of the two mirrors which make up our Fabry-Perot cavity.

This method may also be used to incorporate the effect of atoms on cavity transmission as well. Including the absorption and indices of refraction of the atoms using linear dispersion theory, the quantum mechanically predicted vacuum rabi splitting may even be reproduced[130].

---
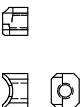
[1]There is technically a factor of $(1 - L_{cav})$ in the numerator. In practical cavities with $\mathcal{F} \geq 100$ this term is entirely negligible compared to the effect of the loss on the (nearly zero) denominator. As such we drop this and all other loss terms from the numerator.

Appendix E
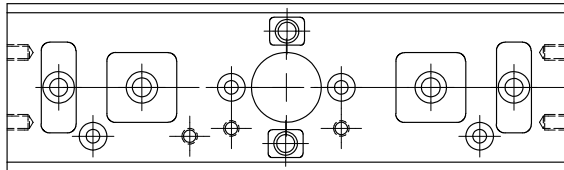
Machine Drawings of New Apparatus
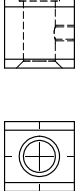
Collimator Lens Mount
Make 2
Material: 304L

Dipole Lens Mount
Make 2
Material: 304L

Baseplate
Make 2
Material: Macor

Mirrormount
Make 2
Material: 304L
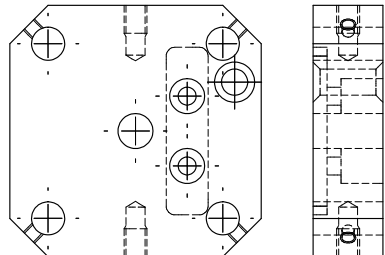
Mainplate
Make 1
Material: Macor

Summary

Scale 1:1

Vuletic Group, MIT

		DIMENSIONS ARE IN INCHES	NAME	DATE
		TOLERANCES:		
		FRACTIONAL ±	DRAWN	
		ANGULAR: MACH± BEND ±	CHECKED	
		TWO PLACE DECIMAL ±	ENG APPR.	
		THREE PLACE DECIMAL ±	MFG APPR.	
			Q.A.	
		MATERIAL	COMMENTS:	
		--		
		FINISH		
		--		
NEXT ASSY	USED ON			
APPLICATION		DO NOT SCALE DRAWING		

SIZE **A** DWG. NO. REV.

SCALE 1:1 WEIGHT: SHEET 1 OF 9

Mainplate (Holes Hidden)

Collimator Lens Mount Pocket

MirrorMount Pocket

Dipole Lens mount Pocket

Please Machine from Macor
Make 1

Fillet dimensions on pockets may be adjusted to closest convenient endmill, noting that the relevant chamfered component must fit into pocket, and that pockets must maintain Flat surfaces

One mount is offset by +.005 from midpoint, the other by -.005.
EXAMINE AT HIGH RESOLUTION, OR CALL.

Dipole Lens mount Pocket

MirrorMount Pocket

.155±.001
.030±.001
.030±.001
.030±.001
.155±.001

.065±.001
.065±.001
.065±.001

1.200±.001
.600±.001
.500±.001
.650±.001

.300±.001
.170±.001

R.063±.000
4.000±.001
R.063
R.031
.302±.001
.250
.010

.250±.001
.721±.001
.302±.001
.005
.785±.001
1.569±.001
.500±.001
.721±.001
.250±.001

Collimator Lens Mount Pocket

Scale 1:1
.650

			NAME	DATE	
		DRAWN			Vuletic Group, MIT
		CHECKED			
		ENG APPR.			
		MFG APPR.			
		Q.A.			
		COMMENTS:			

DIMENSIONS ARE IN INCHES
TOLERANCES:
FRACTIONAL±
ANGULAR: MACH±   BEND ±
TWO PLACE DECIMAL ±
THREE PLACE DECIMAL ±

MATERIAL   --

FINISH   --

NEXT ASSY   USED ON

APPLICATION   DO NOT SCALE DRAWING

SIZE DWG. NO.   REV.
A

SCALE:1:1   WEIGHT: SHEET 7 OF 9

Mainplate Hole Locations

All dimensions are to +/-0.001"
on this sheet

All holes in pockets are centered
in the pocket

Scale 2:1

Vuletic Group, MIT

Wiring Through hole ⌀.098
Wiring Through hole ⌀.098
⌀.225 Chamfer
#4-40 Loose-Fit Through Hole
#4-40 Loose-Fit Through Hole
⌀.225 Chamfer

⌀.198 Chamfer
⌀.500±.010

⌀.225 Chamfer
#4-40 Loose-Fit Through Hole
#4-40 Loose-Fit Through Hole
Wiring Through hole ⌀.098
#4-40 Loose-Fit Through Hole

#4-40 Tapped Hole

.500±.001
.350±.001
.150±.001

.150±.005

.150±.005
Wiring Through hole ⌀.098
⌀.198 Chamfer
#4-40 Tapped Hole
#4-40 Tapped Hole

⌀.198 Chamfer
#4-40 Tapped Hole
#4-40 Loose-Fit Through Hole
⌀.169 Chamfer

#4-40 Tapped Hole

All Chamfers designed at 45 Degrees, though this is not critical. If a more convenient tool exists from 35-55 Degrees, use it.

Mainplate Hole Dimensions

The dimensions of the chamfers on the 4-40 Loose-Fit through holes are not critical-- they are only there to ensure that the through hole do not have burrs- beyond that, they may be as small as is convenient for machining.

The dimensions of the holes and chamfers on the wiring through holes are also not critical. They may be adjusted to the nearest convenient tool size, but should not be reduced substantially, as they are important for ensuring that wires are not stripped.

Also note that wiring through holes are chamfered on both the top and bottom surfaces, while the #4-40 Loose Fit through holes are only chamfered on the top surface.

Scale 1.3:1

Vuletic Group, MIT

SIZE A | DWG. NO. | REV.
SCALE:1:1 | WEIGHT: | SHEET 8 OF 9

Dipole Lens Mount

.250±.001

R.120±.003

R.143 +.001 -.000

.181±.001

.250±.001

#4-40 Through Hole tapped to just below surface.
Hole must go through surface.

.040±.001

.125±.001

.100±.001

.200±.001

.040±.001

.080±.001

Please Machine from 304 Stainless
Make 2

Scale 8:1

Vuletic Group, MIT

	DIMENSIONS ARE IN INCHES TOLERANCES: FRACTIONAL ± ANGULAR: MACH± BEND ± TWO PLACE DECIMAL ± THREE PLACE DECIMAL ±		NAME	DATE
		DRAWN		
		CHECKED		
		ENG APPR.		
		MFG APPR.		
	MATERIAL --	Q.A.		
	FINISH --	COMMENTS:		

	NEXT ASSY	USED ON		DO NOT SCALE DRAWING
	APPLICATION			

PROPRIETARY AND CONFIDENTIAL
THE INFORMATION CONTAINED IN THIS DRAWING IS THE SOLE PROPERTY OF <INSERT COMPANY NAME HERE>. ANY REPRODUCTION IN PART OR AS A WHOLE WITHOUT THE WRITTEN PERMISSION OF <INSERT COMPANY NAME HERE> IS PROHIBITED.

SIZE **A** DWG. NO.

REV.

SCALE:21 WEIGHT: SHEET 5 OF 9

MirrorMount

Please Machine from 304 Stainless
Make 2

#4-40 Tapped Hole

#4-40 Tapped
Through Hole

Scale 4:1

ϕ.228±.001

.288±.001

.020±.001

.328±.010

.050±.020

ϕ.288 $^{+.001}_{-.000}$

ϕ.228±.003

.500±.001

.250±.001

.250±.001

.500±.001

.500±.001

.250±.001

.375±.001

.375±.001

.063±.001

.063±.001

Vuletic Group, MIT

	NAME	DATE
DRAWN		
CHECKED		
ENG APPR.		
MFG APPR.		
Q.A.		
COMMENTS:		

DIMENSIONS ARE IN INCHES
TOLERANCES:
FRACTIONAL ±
ANGULAR: MACH±   BEND ±
TWO PLACE DECIMAL   ±
THREE PLACE DECIMAL   ±

MATERIAL   --

FINISH   --

DO NOT SCALE DRAWING

NEXT ASSY	USED ON
APPLICATION	

SIZE	DWG. NO.	REV.
A		
SCALE:4:1	WEIGHT:	SHEET 6 OF 9

Collimator Lens Mount

ϕ .500 $^{+.001}_{-.000}$

R.188±.010

#4-40 Tapped Through Hole
(Tap to just below exposed surface, as threads on exposed circular surface will disrupt the surface flatness) Hole must go through surface

.140±.001

.325±.001

.650±.001

.750±.001

.375±.001

.250±.001

.070±.001

.110±.001

.070±.001

.510

.110

.070

.070

Please Machine from 304 Stainless
Make 2

Scale 2:1

Vuletic Group, MIT

			DIMENSIONS ARE IN INCHES		NAME	DATE
			TOLERANCES:			
			FRACTIONAL±	DRAWN		
			ANGULAR: MACH± BEND ±	CHECKED		
			TWO PLACE DECIMAL ±	ENG APPR.		
			THREE PLACE DECIMAL ±	MFG APPR.		
				Q.A.		
		MATERIAL --	COMMENTS:			
		FINISH --				

NEXT ASSY | USED ON

APPLICATION | DO NOT SCALE DRAWING

SIZE **A** | DWG. NO. | REV.

SCALE:2:1 | WEIGHT: | SHEET 4 OF 9

One of four through holes for alignment rods. ϕ .237 $^{+.001}_{-.000}$

VIEW Baseplate-Baseplate
SCALE 1 : 1

#4-40 Tapped Through Hole 1 of 4

#8-32 Tapped Hole 1 of 2

#4-40 Tapped Through Hole 2 of 4

.250±.010

.900±.010

Table mount hole 2

Alignment Rod 2 Hole

Alignment Rod 1 Hole

Alignment Rod Setscrew 1 of 4

.250±.005

Beam hole

Wiring Hole

Alignment Rod 4 Hole

Alignment Rod 3 Hole

Table mount hole 1

Mainplate mount hole 1

Mainplate mount Hole 2

Vuletic Group, MIT

ϕ .237 $^{+.001}_{-.000}$

ϕ .250±.010

1.800±.001

.900±.010

ϕ .250±.010

ϕ .237 $^{+.001}_{-.000}$

Loose #4-40 Through-hole

There are 4 such #4-40 Tapped Holes, for set-screws to hold alignment rods

.274±.001
1.800±.001

.900±.010

1.251±.001

#4-40 Tapped Hole

.194±.005

.274±.001

1.251±.001

.190

ϕ .237 $^{+.001}_{-.000}$

Loose #4-40 Through-hole

.550±.010

ϕ .250±.010, dimensions of chamfer on this edge (and companion edge) is non-critical, as it is used only to prevent wires from stripping.

Baseplate Frontside

Please machine from macor
MAKE 2

Scale 1:1

DIMENSIONS ARE IN INCHES
TOLERANCES:
FRACTIONAL±
ANGULAR: MACH±   BEND ±
TWO PLACE DECIMAL ±
THREE PLACE DECIMAL ±

MATERIAL   --

FINISH   --

PROPRIETARY AND CONFIDENTIAL
THE INFORMATION CONTAINED IN THIS DRAWING IS THE SOLE PROPERTY OF <INSERT COMPANY NAME HERE>. ANY REPRODUCTION IN PART OR AS A WHOLE WITHOUT THE WRITTEN PERMISSION OF <INSERT COMPANY NAME HERE> IS PROHIBITED.
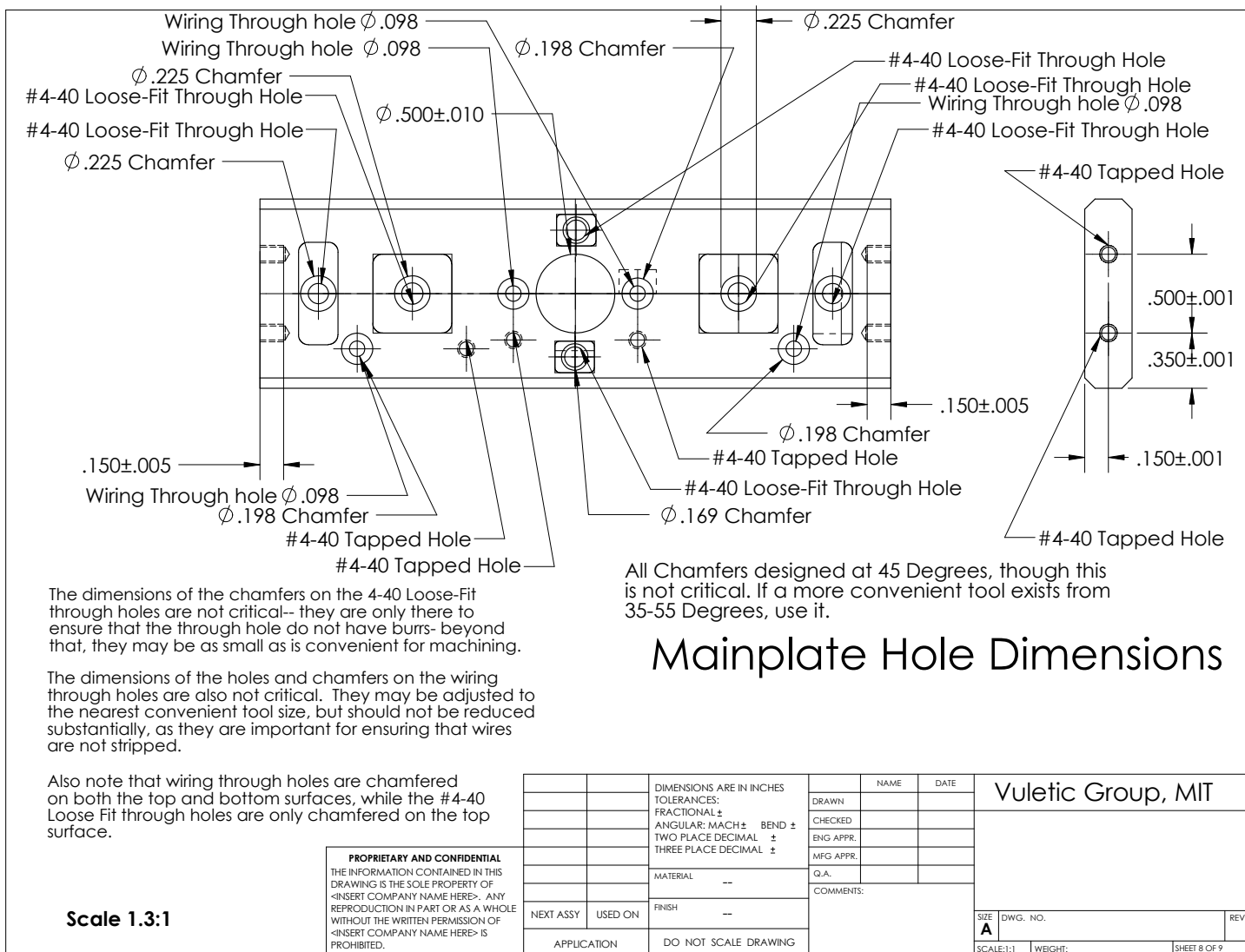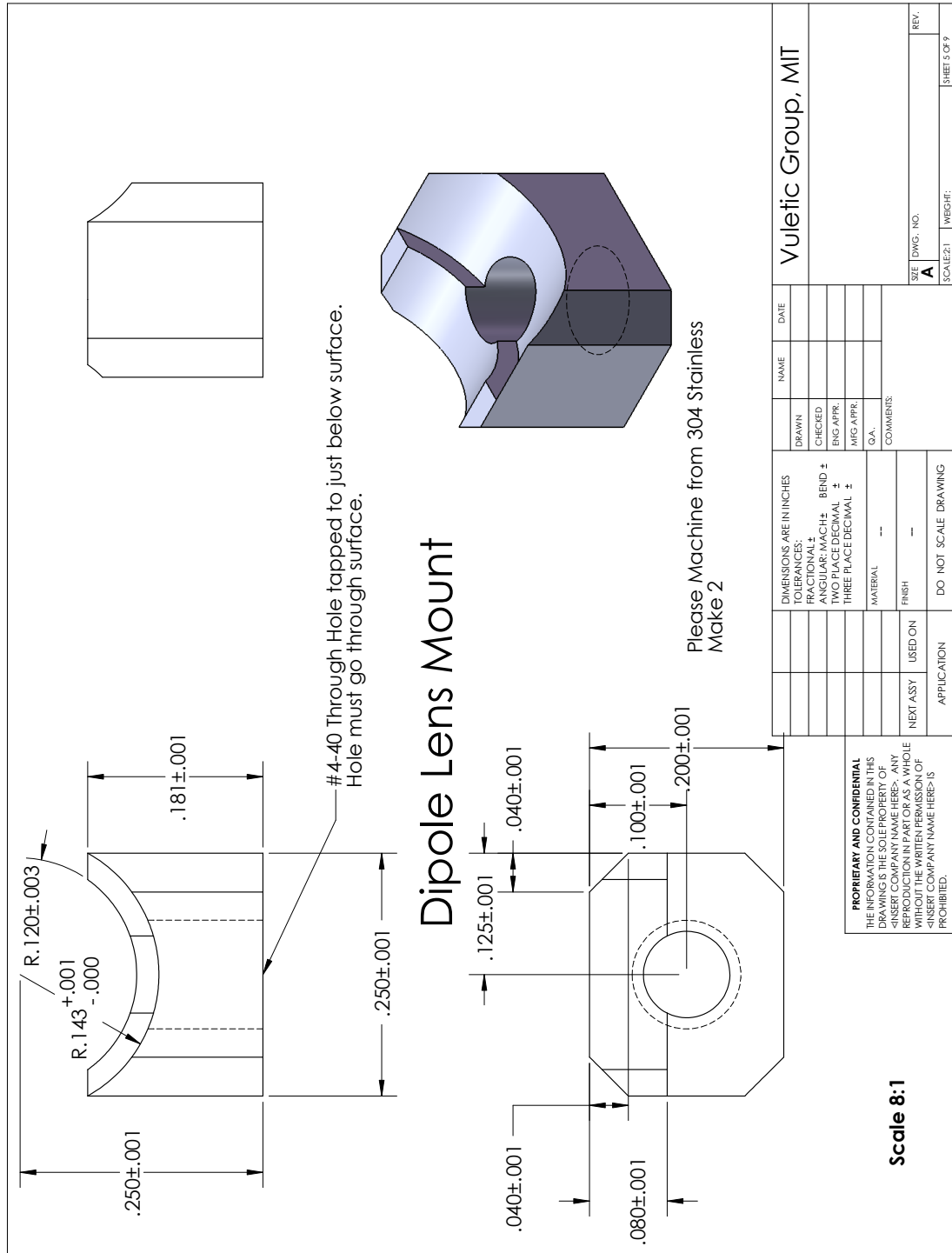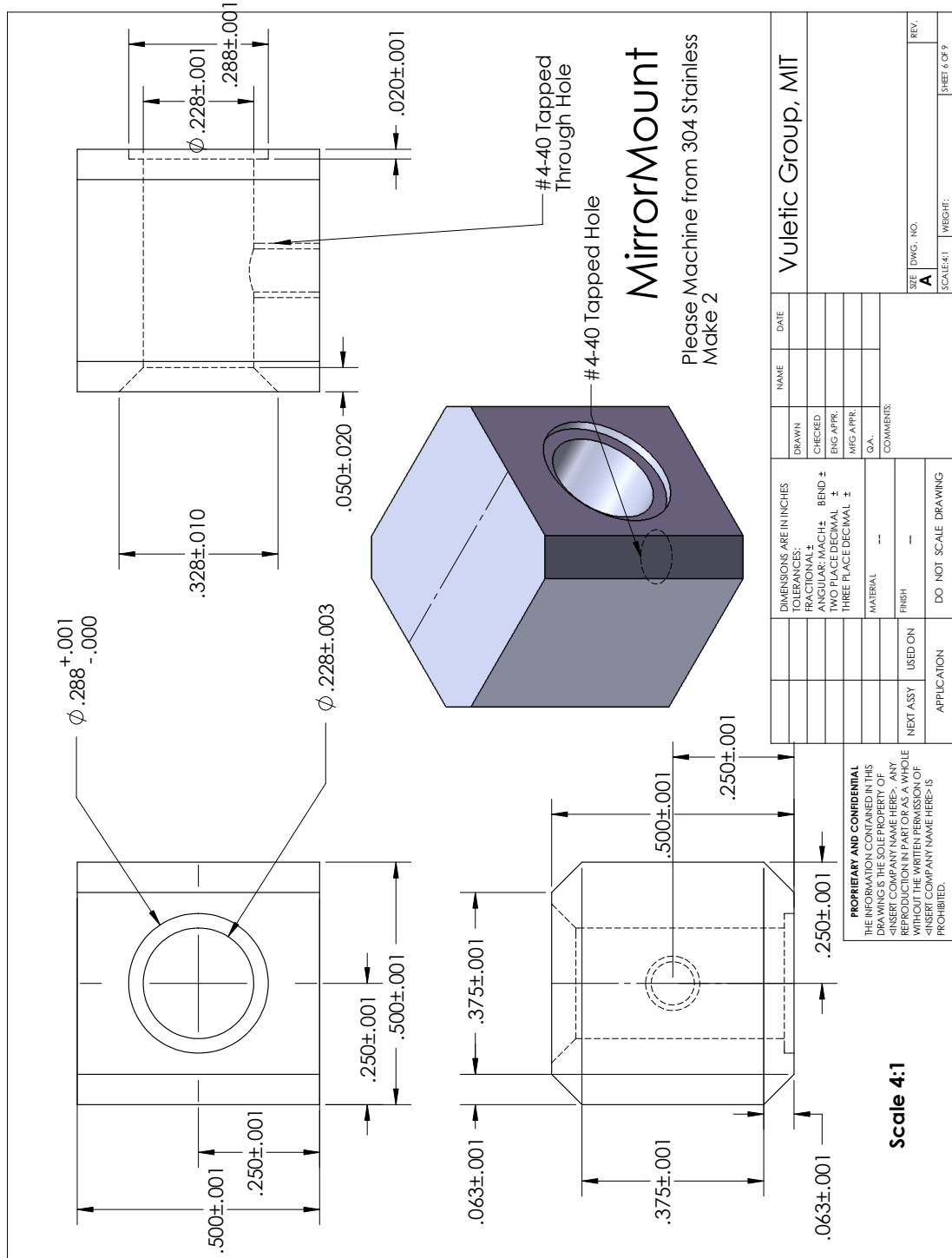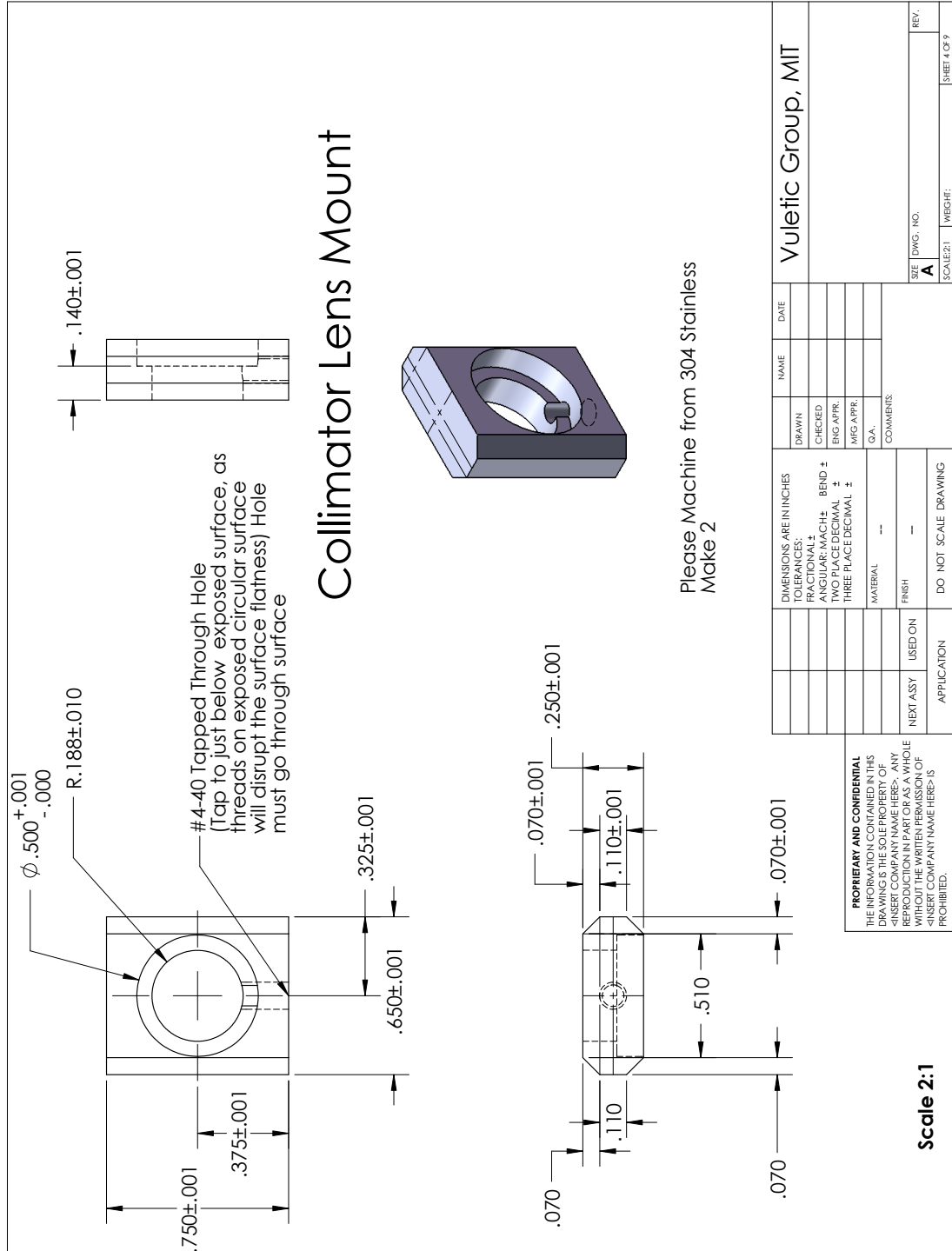
NAME   DATE
DRAWN
CHECKED
ENG APPR.
MFG APPR.
Q.A.
COMMENTS:

NEXT ASSY   USED ON
APPLICATION

DO NOT SCALE DRAWING

SIZE   DWG. NO.   REV.
A
SCALE:21   WEIGHT: SHEET 2 OF 9

Baseplate Backside and Cutaway to Pocket

#4-40 Tapped Through Hole 1 of 4

#8-32 Tapped Hole 1 of 2

#4-40 Tapped Through Hole 2 of 4

Pocket for Mainplate

#8-32 Tapped Hole 1 of 2

.300±.001

R.063±.001

.300±.001

.380±.001

.500±.001

.350±.001

#4-40 Through, Loose fit ⌀.129

.100±.001

.100±.003

1.200±.001

.350±.001

.356±.005

#4-40 Through, Loose fit ⌀.129

⌀.250±.010

⌀.250±.010

Scale 1:1

Vuletic Group, MIT

			NAME	DATE
		DRAWN		
		CHECKED		
		ENG APPR.		
		MFG APPR.		
		Q.A.		
		COMMENTS:		

DIMENSIONS ARE IN INCHES
TOLERANCES:
FRACTIONAL±
ANGULAR: MACH±   BEND ±
TWO PLACE DECIMAL ±
THREE PLACE DECIMAL ±

MATERIAL   --

FINISH   --

DO NOT SCALE DRAWING

NEXT ASSY	USED ON
APPLICATION	

SIZE **A**   DWG. NO.   REV.

SCALE:2:1   WEIGHT: SHEET 3 OF 9